New Synthetic Routes towards Well-Defined Polypeptides, Morphologies and Hydrogels

Dissertation
zur Erlangung des akademischen Grades
"doctor rerum naturalium"
(Dr. rer. nat.)
in der Wissenschaftsdisziplin „Polymer Science"

eingereicht an der
Mathematisch-Naturwissenschaftlichen Fakultät
der Universität Potsdam

angefertigt in den
Abteilungen für Kolloidchemie und Biomaterialien
Max-Planck-Institut für Kolloid- und Grenzflächenforschung
und dem
Institut für Chemie der Universität Potsdam

von
Charlotte D. Vacogne
Potsdam, Dezember 2016

Declaration

The enclosed research was conducted in the Department of Colloid Chemistry and Biomaterials at the Max Planck Institute of Colloids and Interfaces (MPIKG), and in the Institute of Chemistry at the University of Potsdam, under the supervision of Prof. Helmut Schlaad between July 2013 and November 2016. This thesis has not been submitted for any other qualifications at this or any other institution. This dissertation is the original work of the author and does not include any research that is the outcome of work done in collaboration with others, except where specifically indicated in the text and acknowledgements.

Eidesstattliche Erklärung

Die vorliegende Arbeit wurde in der Zeit von Juli 2013 bis November 2016 am Max-Planck-Institut für Kolloid- und Grenzflächenforschung in den Abteilungen Kolloidchemie und Biomaterialien (MPIKG), und an der Universität Potsdam im Institut für Chemie unter der Leitung von Prof. Helmut Schlaad angefertigt. Die Arbeit ist bisher an keiner anderen Hochschule eingereicht worden und wurde zudem selbständig und ausschließlich mit den angegebenen Mitteln angefertigt. Hiermit erkläre ich an Eides statt, dass ich die vorliegende Arbeit selbstständig verfasst und nur unter Zuhilfenahme der ausgewiesenen Quellen und Hilfsmittel angefertigt habe. Beiträge von Kooperationspartnern wurden explizit gekennzeichnet.

Referees

Prof. Dr. Helmut Schlaad (Universität Potsdam)
PD. Dr. Klaus Tauer (MPIKG)
Prof. Dr. Holger Frey (Johannes Gutenberg-Universität Mainz)

Defense

25th of April 2017
Grade awarded: summa cum laude

Potsdam, May 2017
Charlotte Vacogne

Abstract

There is a growing interest for functionalisable polypeptides for biomedical applications as such polymers can be tailored to achieve specific biocompatible, bioactive, stimuli-responsive or mechanical functions. Self-assembly is a greatly prized property as it can be used to generate biomimetic materials with microstructure and hierarchy that are particularly well-suited for tissue engineering or 3D cell culture applications. Because of their ability to self-assemble, block-copolymers and block-copolypeptides are hence very popular systems; however, biological proteins rarely rely on such block-like architectures to self-assemble. Statistical or random copolypeptides in comparison have received far less attention. Unlike block-copolymers, statistical copolymer properties are homogeneous and derive from the averaged properties of their constituent co-monomers. As such, they are promising candidates for the preparation of new types of (bio)materials.

This thesis describes the development and study of a series of statistical copolypeptides and materials prepared from them, as well as new routes to synthesise them. More precisely, copolypeptides of γ-benzyl-L-glutamate (BLG) and allylglycine (AG), noted P(BLG-co-AG), were investigated. This choice was mainly based on the ability for PBLG homopolymers to fold into α-helices that can self-assemble to form physical and thermoreversible gels at room temperature in helicogenic solvents such as toluene. AG was chosen as a functionalisable comonomer. The properties, composition and structure of these polypeptides were characterised. Their random architecture was confirmed by NMR, and their ability to form physical gels in toluene at low temperature (between -38 and -8 °C) was demonstrated by rheology. The gelation temperature was found to be affected by both the AG content and the chain length (n). Raman and FTIR spectroscopy were used to study the secondary structure of the polypeptides. For AG molar fraction lower than 26%, P(BLG-co-AG) were mostly α-helical, despite minor defects caused by the presence of AG and identified as portions of the α-helix that lacked intramolecular hydrogen bonds. A WAXS study showed that both P(BLG-co-AG) and PBLG α-helices were pseudo-hexagonally packed in the dry state. These results helped establish that P(BLG-co-AG) and PBLG have a similar conformation and packing behaviour, but that the presence of AG drastically modifies the gelation temperature and rheology of the polypeptides.

P(BLG-co-AG) organogels, stable at room temperature, were prepared by crosslinking AG moieties with dithiol crosslinkers. Robust organogels were prepared from very dilute P(BLG-co-AG) solutions (10 g·L^{-1} in toluene, THF or dioxane) despite rather short polymer chains ($50 < n < 220$). An SEM, TEM and WAXS study showed that, like PBLG, crosslinked P(BLG-co-AG) gels were composed of a network of fibres, themselves formed by pseudo-hexagonally packed α-helices. Moreover, an FTIR study confirmed that the conformation of P(BLG-co-AG), like PBLG, was α-helical in solution too (*i.e.,* in toluene and dioxane). These results indicate that P(BLG-co-AG) polypeptides behave similarly to PBLG in helicogenic solvents in that they fold into α-helices that aggregate in a head-to-tail and side-by-side fashion. By crosslinking these loosely bound aggregates, a fibrous network was formed, *i.e.,* an organogel. P(BLG-co-AG)-dioxane organogels

were the most robust gels produced and were thus used to prepare hydrogels by debenzylating the BLG units to yield L-glutamic acid (LGA) moieties. The resulting hydrogels retained the fibrous structure and were highly absorbent and pH-responsive. Most importantly, they were the first PLGA-based hydrogels to display such fibrous features. The pH responsiveness was the result of the helix-coil transition of PLGA and P(LGA-*co*-AG) polypeptides at acidic pH (~ 5 to 6).

Particles with highly regular spiral morphologies were obtained from PBLG- and P(BLG-*co*-AG)-toluene in water emulsions. A CD and Raman spectroscopic study demonstrated that the direction of these spirals was controlled by the chirality of the polypeptides. More specifically, PBLG and P(BLG-*co*-AG), which are composed of a majority of L residues and thus have a right-handed α-helical conformation, gave rise to particles exhibiting clockwise spirals. Vice-versa, PBDG and P(BDG-*co*-AG), synthesised for this particular study, which are composed of a majority of D residues and thus have a left-handed α-helical conformation, gave rise to particles exhibiting counterclockwise spirals. The transmission of the chirality from a molecular level (*i.e.*, polypeptide) to higher hierarchical levels (*i.e.*, particles of several microns diameter), is as yet not fully understood. Literature and SEM evidences suggested that it may occur *via* the existence of a chiral 'nano-twist' along the α-helix axis that is 'amplified' upon pseudo-hexagonal packing through crystallisation of liquid crystalline (LC) phases or fibre formation.

The aforementioned polypeptides were synthesised by ring opening polymerisation (ROP) of α-amino acid *N*-carboxyanhydrides (NCA), which typically uses primary amines as initiators in order to ensure that the polymerisation is controlled. Tertiary amines can be used to catalyse the ROP of NCA but the resulting polymerisation is uncontrolled. It was shown that primary ammonium chlorides and primary amines could be combined with tertiary amines to initiate a controlled ROP of NCA, provided the molar fraction of tertiary amines was below a certain threshold. A kinetic study by SEC and FTIR, complemented by NMR analyses, was used to produce time-conversion plots and to determine chain lengths and polydispersity indices (Đ) throughout the polymerisation reactions. The polymerisation rate could be controlled by the HCl to amine ratio and the polymerisation could even be paused and resumed by altering this ratio during the reaction.

Acknowledgements

am today without your scientific and moral support throughout this PhD, I am a better scientist for having been mentored by you.

Thank you to all my PhD fellows, at the MPIKG, IMPRS and UP, for having made this journey lighter and more enjoyable: Martina, Vale, Bahareh, Sonja, Evgenii, Ana, Livnat, Steffy, Sabine, Martin, Selina, Ulises, Anja, Monika, Vasil, Moritz, Kai, Joanna, Simon, Yongjun, Konrad, Elliot, Yan, etc. Thank you Sonja for drawing the beautiful α-helix and β-sheet that feature in my Chapter I, for feeding me ice cream and for the revolution attempt.

Finally, I would like to thank those closest to me, my sister Violaine, my brother Raphaël, my niece Cassia, Cannel, and my partner John. Vivi and Phinou, thank you for encouraging me to pursue my dreams and for being there when I need you. Cassia, thank you for making me a proud auntie. Cannel, I miss you every day, thank you for all the love, care and empathy you gave me, I am a better person because of you. John, thank you for providing me with daily love, support, patience and kindness.

Table of Contents

List of Abbreviations

Ac$_2$O	Acetic anhydride
AFM	Atomic force microscopy
AG	allylglycine (L, D or DL)
AMM	Activated monomer mechanism
ATR	Attenuated Total Reflectance
BG	γ-Benzylglutamate (L, D or DL)
Bn	Benzyl
BnA	Benzylamine Hydrochloride
BnA·HCl	Benzylamine Hydrochloride
B$_D$G	γ-Benzyl-D-glutamate
B$_L$G	γ-Benzyl-L-glutamate
CD	Circular Dichroism
d	*d*-spacing
DIPEA	Diisopropylethylamine (Hünig's base)
DMF	Dimethylformamide
DMSO	Dimethyl sulfoxide
DSC	Differential scanning calorimetry
ECM	Extracellular matrix
EtOH	Ethanol
FTIR	Fourier Transform Infrared Spectroscopy
G	Gibbs free energy
G*	Complex shear modulus
G′	Storage modulus
G″	Loss modulus
Gly	Glycine
GPC	Gel permeation chromatography (i.e., SEC)
h	hour
HexA	Hexylamine
HexDA	Hexamethylene diamine
HFIP	Hexafluoroisopropanol
Hyp	Hydroxyproline
IR	Infrared
LLeu	L-Leucine
LPhe	L-Phenylalanine

LC	Liquid crystalline (or liquid crystal)
M	Molar (mol·L^{-1})
M$_n$	Number average molecular weight
M$_W$	Weight average molecular weight
MalO	Maleic anhydride
MeOH	Methanol
min	minute
n	Chain length (*i.e.,* number of repeat units, degree of polymerisation)
NAM	Normal Amine Mechanisms
NCA	α amino acid *N*-carboxyanhydride
NMR	Nuclear magnetic resonance
p	Monomer conversion
PBLG	Poly(γ-Benzyl-L-glutamate)
PLG	Poly(L-glutamate)
PLGA	Poly(L-glutamic acid)
PPII	Polyproline type II
Pro	Proline
PS	Polystyrene
PyA	1-pyrenemethylamine
PyA·HCl	1-pyrenemethylamine hydrochloride
PyOH	1-pyrenemethanol
RI	Refractive index
ROP	Ring opening polymerisation
rt	Room temperature
s	second
S	Entropy
SEC	Size Exclusion Chromatography
SEM	Scanning electron microscopy
T$_g$	Glass transition temperature
T$_{gel}$	Gelation temperature
T$_m$	Melting temperature
TAB	1,2,3-Tris(aminomethyl)benzene
TAB·3HCl	1,2,3-Tris(aminomethyl)benzene trihydrochloride
TC	Tropocollagen
TEA	Triethylamine
TEM	Transmission electron microscopy

TFA	trifluoroacetic acid
THF	Tetrahydrofuran
Tol	Toluene
UV	Ultraviolet
vs.	Versus
WAXS	Wide angle X-ray Scattering
Đ	Polydispersity index
γ	Shear strain
ẏ	Shear strain rate
δ	NMR shift
ΔG	Gibbs free energy change
ΔH	Enthalpy change
ΔS	Entropy change
λ	Light wavelength
θ	Incident light angle
[θ]	Molar ellipticity (CD)
$[θ]_{MRE}$	Mean residue ellipticity (CD)
ν	Light frequency
η*	Complex viscosity

Chapter I

Introduction and Background

I.1   Introduction

Biological systems produce structural proteins that possess the ability to self-assemble into complex, yet highly ordered structures. These proteins are copolypeptides that derive their properties from the controlled sequences and compositions of their constituent amino acids.[1] The main function of structural proteins is to mechanically support tissues in the body and to provide structure for certain types of cells.[2,3] Most structural proteins are fibrous proteins, such as collagen, fibroin, elastin and keratin. As their name suggests, fibrous proteins self-assemble into fibres that confer stiffness and rigidity to otherwise-fluid biological components.[4,5] Such polypeptides are, therefore, of prime interest to the field of tissue engineering.[6] Although they can be extracted from biological samples, the recovery, purification and isolation of proteins is not straightforward.[7] In addition, their compositions and architectures are fixed, which ultimately limits the breadth of their applications. Being able to design and synthesise structural polypeptides is, therefore, of prime interest to the field of tissue engineering.[6,8]

Several methods exist for the synthesis of polypeptides, each of them with specific advantages and drawbacks.[1,9–11] While solid-phase synthesis produces sequence-controlled polypeptides that can truly mimic natural proteins, this technique is time-consuming and is not practical for the direct and large scale preparation of large polypeptides (> 100 residues).[1,12,13] The most economical process for the synthesis of long polypeptide chains is the ring opening polymerisation (ROP) of α-amino acid-N-carboxyanhydrides (NCA). This technique, however, does not allow for the preparation of sequence-controlled, hence truly biomimetic, polypeptides. Instead, the ROP of NCA can be used to synthesise bio-inspired polypeptides with carefully designed architectures and topologies (*e.g.*, linear, block, star), and that can self-assemble to form scaffolds or other complex structures (*e.g.*, gels, vesicles, micelles) of potential interest to the tissue engineering and biomedical field.[14,15] A widely used strategy to ensure effective self-assembly is the use of

1

block copolymer architectures, especially with blocks exhibiting contrasting secondary structures (*e.g.,* α-helical, coils, β-sheets) or with amphiphilic blocks.[16–19] Under these conditions, self-assembly proceeds through an interplay between microphase separation[20,21] (which is characteristic of block-copolymers), hydrophobic interactions, conformation specific assembly, liquid crystalline alignment, or even hydrogen bonding.[22–24] Intricate and complex microscopic structures, including worm-like gels, vesicles, flower micelles, can then be generated.[17,18,25] However, the level of synthetic complexity generally required to produce such systems, whose structures sometimes widely differ from natural protein structures and compositions, may challenge the actual applicability and practicality of the resulting materials.

It is worth noting that the secondary structure (*i.e.,* conformation) of most fibrous proteins plays a key role in their ability to self-assemble.[2,26] For instance, collagen fibres result from the organised assembly of right-handed triple helices, themselves formed by the assembly of polypeptide chains that exhibit a left-handed polyproline type II (PPII) conformation;[3] keratin filaments are composed of left-handed super-helices, themselves formed by coiled polypeptides that exhibit a mixture of motifs, including α-helices and β-sheets.[5] Therefore, a bio-inspired approach was chosen to synthesise structural polypeptides and fibrous networks, with a focus on architectures and compositions that would favour a secondary structure-driven assembly, without the assistance of the block architecture or self-assembly-inducing end groups. Poly(γ-benzyl-L-glutamate) (PBLG), a well-known synthetic polypeptides,[27] was thus selected as the model polymer for this study. Indeed, PBLG adopts an α-helical conformation in many organic solvents,[28] and under specific conditions, these helices self-assemble into fibrous networks, generating physical gels.[29] The debenzylation of its BLG side chains yields biocompatible poly(L-glutamatic acid) (PLGA); however, this now water soluble polypeptide no longer has the ability to self-assemble into complex structures.[30,31] By introducing comonomers in a statistical fashion (*i.e.,* statistical copolymers), some properties and functionalities (*e.g.,* reactivity towards click substrates, addition of basic amino acids) of PBLG and PLGA can be altered while preserving the overall α-helical conformation when the selected comonomer in sufficiently low molar fractions.[30–33] Functionalisable comonomers are particularly interesting as they allow for the synthesis of highly versatile copolypeptides whose properties can be easily tuned.[34] This doctoral work thus focused on the synthesis, characterisation and application of statistical copolypeptides of BLG and functionalisable allylglycine (AG), noted P(BLG-*co*-AG). More precisely, each chapter focused on the following topics:

- The synthesis of P(BLG-*co*-AG) polypeptides by controlled ROP of NCA with a random architecture, linear and star topologies, and different end groups is reported in Chapter II.

- The development of a novel and versatile controlled ROP of NCA, namely the primary ammonium-tertiary amine-mediated ROP of NCA, is reported in Chapter III.

- The effect of composition and architecture of P(BLG-*co*-AG) polypeptides on their secondary structure, physical gelation and long range organisation is reported in Chapter IV.

- A novel synthetic route to prepare fibrous organogels and hydrogels from P(BLG-*co*-AG) polypeptides and the study of the gel properties are reported in Chapter V.

- Novel and unique morphologies observed on microscopic P(B∟G-*co*-AG)-based particles are reported in Chapter VI.

I.2 Background

I.2.1 Ring Opening Polymerisation of Amino Acid *N*-Carboxyanhydrides

I.2.1.1 Amino Acid *N*-Carboxyanhydrides Synthesis

The synthesis of α-amino acid *N*-carboxyanhydrides (NCAs) was first reported by Leuchs et al. over 100 years ago.[10,35] The then called 'Leuchs's anhydrides' were originally synthesised by reacting an *N*-methoxy/ethoxycarbonyl amino acid chloride under vacuum at 70 °C to induce cyclisation (Scheme I.1a). Although the Leuchs method and its variations are still popular nowadays for the synthesis of *N*-substituted NCAs (NNCAs),[36] the Fuchs-Farthings method has since replaced the Leuchs method to synthesise NCAs.[37] The method was developed in 1950 by Farthing et al. and was adapted from the work performed by Fuchs 30 years before.[38] It consists of the direct phosgenation of α-amino acids (Scheme I.1b). Because of its acute toxicity, phosgene gas is rarely used nowadays; instead the safer bis(trichloromethyl)carbonate (triphosgene), which releases phosgene upon heating, is commonly used.[30,31,39]
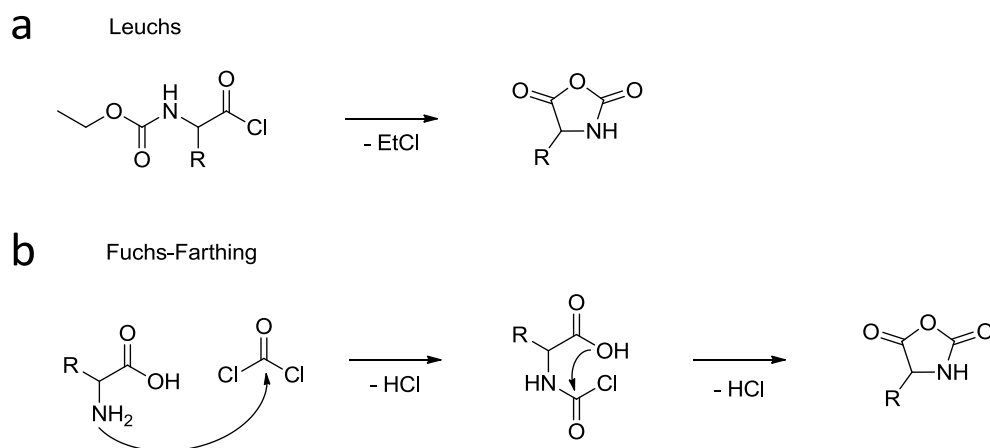
Scheme I.1 (a) the Leuchs method consists of heating *N*-ethoxycarbonyl amino acid chloride under vacuum at 70 °C to induce cyclisation; the precursor was traditionally synthesised by coupling carboethoxy chloride with an amino acid (originally glycine[35]), yielding carboethoxyamino acid, which was then converted to the corresponding acid chloride using thionyl chloride (SOCl$_2$); (b) the Fuchs-Farthing method consists of the phosgenation of an amino acid (in suspension in THF, at 50 °C) followed by its cyclisation.

The Fuchs-Farthing method was used for the synthesis of all types of NCAs used in this doctoral work (*i.e.*, B∟G, BᴅG, ∟AG, ᴅ∟AG, ∟Leu, ∟Phe).

I.2.1.2 Normal Amine and Activated Monomer Pathways

Since the late 1940s, NCA polymerisation has been the most common technique used for large-scale preparation of high molar mass polypeptides.[1,40] NCA polymerisations are traditionally initiated or catalysed

using nucleophiles and bases, respectively, the most common being amines and alcohols.[10] Depending on the type of initiator (I) and reaction conditions, the ring opening polymerisation (ROP) of NCA is known to mainly proceed *via* two different pathways, namely the 'normal amine' mechanism (NAM) and the 'activated monomer' mechanism (AMM) (Scheme I.2).[1,10] The NAM is a nucleophilic ring opening chain growth process where, provided side reactions are absent, the polymer grows linearly with the monomer conversion (p)[1] and a linear first order time conversion is expected.[41–43] The AMM takes place following the deprotonation (by a catalyst) of an NCA, which in turn becomes a nucleophile that initiates chain growth. Therefore, the NAM is favoured by nucleophilic initiators that are less basic than nucleophilic, such as primary amines, whereas the AMM is favoured by basic catalysts that are more basic than nucleophilic, such as sterically hindered secondary or tertiary amines, alkoxides, and thiols.[44]
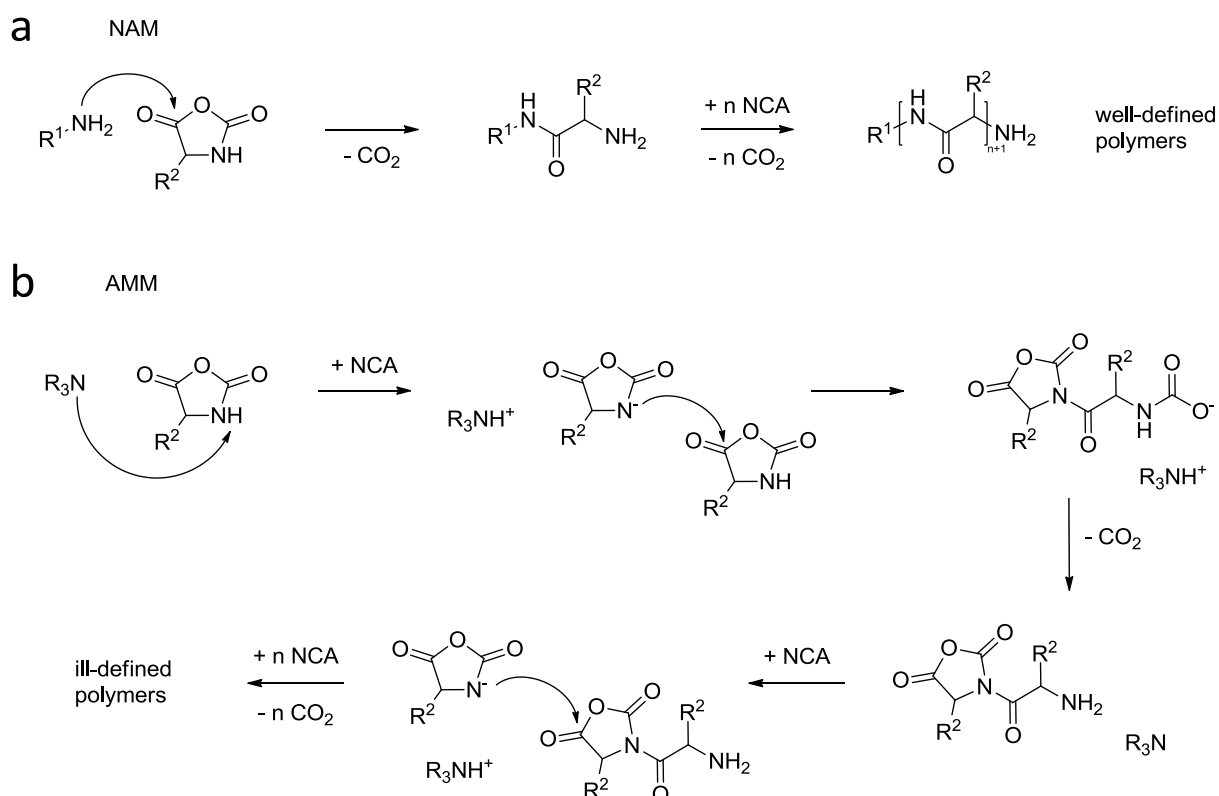
Scheme I.2 (a) Primary amine-initiated controlled ROP proceeding *via* the normal amine mechanism (NAM); typical terminating agents are anhydrides and acid chlorides. (b) Tertiary amine-catalysed uncontrolled ROP proceeding *via* the activated monomer mechanism (AMM); the tertiary amine is regenerated throughout the reaction and the growing polymer can add new NCAs on both the α- and ω-end.

The ROP of NCA catalysed by tertiary amines and the AMM were first reported by Ballard and Bamford,[45] and later refined by Bamford and Block[46] and by Szwarc in an exhaustive review.[46] Kricheldorf further extended the scope of base-catalysed ROP of NCA *via* the AMM by investigating the use of electrophilic cocatalysts in combination with tertiary amines.[47] As shown in Scheme I.2b, the base acts as a catalyst by deprotonating the NH of the NCA, thereby generating an NCA anion, which in turn acts as a nucleophilic initiator. The growing dimer then contains an *N*-acylated NCA α-end and either an amine anion ω-end or a primary amine ω-end if the catalyst has been regenerated (or in case of a proton transfer with

an NCA). At that point, the oligomer can add an NCA on either chain end, and the catalyst can 'activate' a new NCA. All these factors contribute towards a rapid propagation and monomer conversion, and the ensuing polymerisation is neither living nor controlled. The molar masses are generally large and broadly distributed (typically, Đ > 1.8). The AMM pathway is popular for the synthesis of very high molar mass polypeptides (typically, M_n > 100 kg·mol^{-1}), for instance for materials where a high level of chain entanglement is advantageous (*e.g.*, lyophilised materials, films).[48,49] Triethylamine (TEA) is a base that is very commonly used to induce the AMM pathway.[50,51]

Provided the initiation step is faster than the growing step, like in the case of sterically unhindered primary aliphatic amine initiators, and assuming the absence of side reactions (*e.g.*, dry solvent, unreactive pendant groups), the NAM pathway ensures a controlled ROP of NCA. Such a controlled polymerisation yields polypeptides with low dispersities (typically, Đ < 1.3), predictable molar masses (based on the [NCA]$_0$/[I]$_0$ feed ratio) and defined α- and ω-end groups (*i.e.*, initiated and terminated polypeptide ends, respectively). Some studies have even reported that 'living'-like polymerisation could be achieved under high vacuum or low temperatures.[42,52–54] Essentially, such conditions ensure the reduction of side reactions caused by impurities, either through a better purification of solvents and initiator solutions by high vacuum, or by reducing the activation barrier (E_a) for chain propagation (with respect to that of side reactions) *via* temperature reduction, thereby leading to a kinetically dominated chain propagation.[1]

It is, however, important to stress that side reactions in ROP of NCA are not solely caused by impurities. The main side reactions in ROP of NCA were in fact reported to be reactions with monomer, solvent, or polymer (*i.e.*, termination by reaction of the amine-end with an ester side-chain, attack of DMF by the amine-end, or chain transfer to monomer).[1,55–57] Therefore, in practice, the chain end (ω) (either the amine or intermediate carbamate) of the growing polymer can undergo a variety of side reactions, such as intramolecular termination, which is common for poly(γ-O-alkyl-L-glutamate)s (Scheme I.3), chain quenching by acids[58] or water.[1,10] In addition, NCA deprotonation may still occur, thereby making the AMM challenging to completely eliminate. As Deming explained it, a given system can switch back and forth between the NAM and the AMM many times during a polymerisation, a propagation step for one pathway being a side reaction for the other.[1]
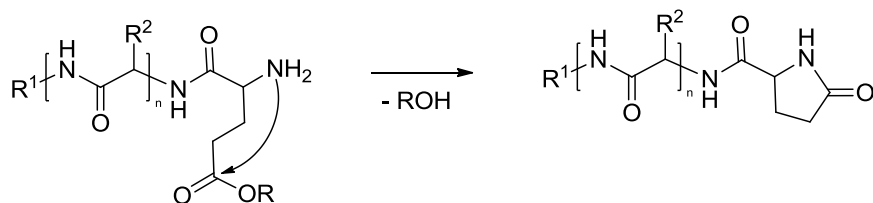
Scheme I.3 Intramolecular termination that is typical for poly(γ-O-alkyl-L-glutamate)s such as Poly(γ-benzyl-L-glutamate) (PBLG).

I.2.1.3   Other Pathways

A number of new approaches, developed over the past two decades, have been reported to achieve better control in ROP of NCA, especially for the purpose of synthesising well-defined and complex architectures

(*e.g.*, blocks, graft).[1] Notably, Deming demonstrated in 1997 that side reactions could be eliminated by the use of transition metal (*e.g.*, Co, Ni) complexes as active species to control the addition of NCA monomers to polymer chain-ends.[59] More precisely, he developed zerovalent nickel and cobalt initiators that led to 'living' ROP of NCA and high molecular weight polypeptides *via* the activation of NCAs into covalent propagating species.[1]

In 2007, Lu et al. reported a hexamethyldisilazane (HMDS)-mediated controlled NCA polymerisation.[60,61] *N*-trimethylsilyl amines were used to initiate NCA polymerisations, which proceeded *via* a trimethylsilyl carbamate (TMS-CBM) propagating group pathway. In this way, side reactions were avoided and effective functionalisation of the polypeptide end groups was achieved. Due to this unique pathway, such polymerisations do not require excessive monomer purification and offer a metal-free strategy for the convenient synthesis of homo- or block polypeptides with predictable molar masses and low dispersities.

Finally, an alternative to the primary amine-initiated ROP of NCA, the ammonium-mediated ROP of NCA, was developed by Dimitrov and Schlaad in 2003.[62] It consists of using ammonium chlorides (or amine hydrochlorides) as initiators, and was proposed to proceed *via* a dormant-active pathway, with the active species growing *via* the NAM pathway (See Scheme III.1c). Lutz further refined this method by using mixtures of ammonium chlorides and corresponding amines, allowing for the polymerisation of γ-benzyl-ʟ-glutamate (BʟG) *via* this method.[63] Since then, other studies have tested different counterions (*e.g.*, BF_4^-, TFA^-, Cl^-), initiators (*e.g.*, pyrene-, *n*-butyl-, PEG-ammoniums) and NCAs (*e.g.*, Z-ʟ-lysine, BʟG, β-benzyl-ʟ-aspartate).[64–67] Chapter III describes an alternative method to the ammonium-mediated ROP of NCA.

Despite all these more controlled methods, initiation with aliphatic primary amino groups remains a frequently used synthetic method for the preparation of complex architectures.[10] As the primary focus of this doctoral work is on statistical (random) copolypeptides and homopolypeptides, hence rather simple architectures, the more traditional amine- and a variation of the ammonium-initiated ROP of NCA methods were selected.

I.2.2   Structure of Polypeptides

A polypeptide chain is a type of linear polymer composed of a series of amino acids joined by peptide bonds, and each amino acid in a polypeptide chain is called a residue (*i.e.*, polypeptide repeat unit or peptide unit). Natural polypeptides are called proteins, which are generally categorised according to their structures and functions.[2] The protein structure is subdivided into four hierarchical levels: the primary structure (amino acid composition and sequence), the secondary structure (geometrical conformation of portions of the chain, *i.e.* structural motifs), the tertiary structure (3D shape of the protein), and the quaternary structure (arrangement of protein subunits into a larger complex).[68] Being less complex than proteins, non-sequence-controlled synthetic polypeptides are generally defined by their composition, architecture (*e.g.*, block, random), and their secondary structure (*i.e.*, conformation), which is often uniform throughout the entire chain or block; higher hierarchical levels are reached when polypeptides

self-assemble or aggregate, in which case, the phenomenon is generally referred to as supramolecular assembly.[13,69,70] This doctoral work being focused on synthetic polypeptides, this section presents the primary and secondary structures of polypeptides in general (*i.e.*, irrespective of their origin).

The primary structure of a protein is defined by the sequence of amino acids. There are 21 types of natural amino acids (*e.g.*, glutamic acid, aspartic acid, lysine, proline, glycine, and phenylalanine) and all of them are L amino acids, meaning that their α-carbon (*i.e.*, chiral centre) has an S configuration. A plausible explanation for this is that the selection of L over D was fixed early in evolutionary history.[2] As a result, only L natural amino acids are constituents of proteins. Synthetic polypeptides, on the other hand, can be prepared from a large variety of natural and unnatural amino acids, which can be D or L (*e.g.*, allylglycine, propargylglycine, benzylglutamate). The backbone of polypeptides has a unique geometry that differs from most carbon-based polymer backbones. As a result of the peptide-bond resonance structures, the peptide bond is planar, with six atoms lying in the same plane: the α-carbon and CO group of the first amino acid and the NH group and α-carbon of the adjacent amino acid (Figure I.1).[2]
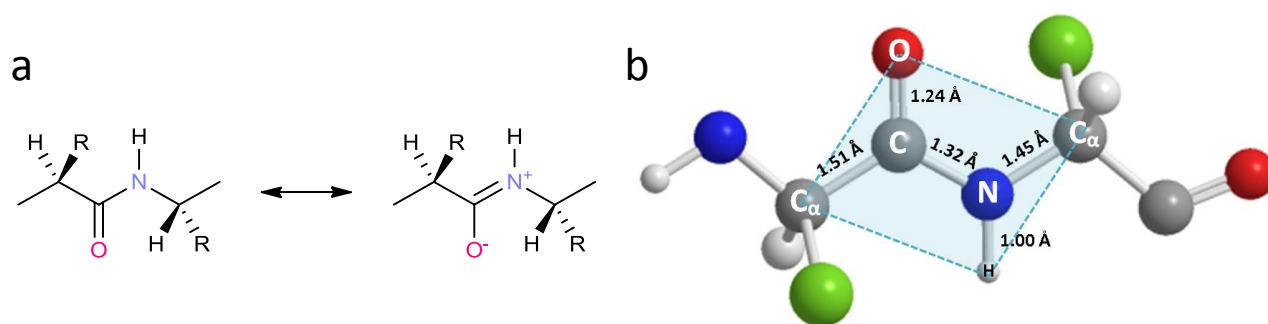
Figure I.1 (a) Peptide bond resonance structure (the peptide is in L configuration); (b) peptide bond plane containing six atoms (C_α, C, O, N, H, and C_α), the side chain (R) is represented by green balls (the model is in D configuration; these dimensions are also valid for the L configuration).

With regard to the configuration of the peptide bond, the *trans* form is almost always favoured because of steric hindrances (between adjacent pendant groups) that occur in the *cis* form. Despite these restrictions, polypeptides are endowed with some freedom of rotation between adjacent rigid units thanks to NC_α and $C_\alpha C$ being single bonds.[2] The rotations are specified by torsion angles (Φ and Ψ), also known as backbone dihedral angles, which vary depending on the nature of the adjacent peptide residues (Figure I.2). These angles are particularly important as they control the way proteins and polypeptides fold, and hence determine their secondary structures (*e.g.*, α-helix, β-sheet, β-turn) (Figure I.3). Ramachandran recognised that not all Φ and Ψ combinations are possible, mainly because of the principle of steric exclusion.[71] This consideration gave rise to the so-called Ramanchandran diagrams, which not only provide information on the allowed Φ and Ψ angles range, but also ascribes secondary structure corresponding to specific (Φ, Ψ) regions (Figure I.2b).
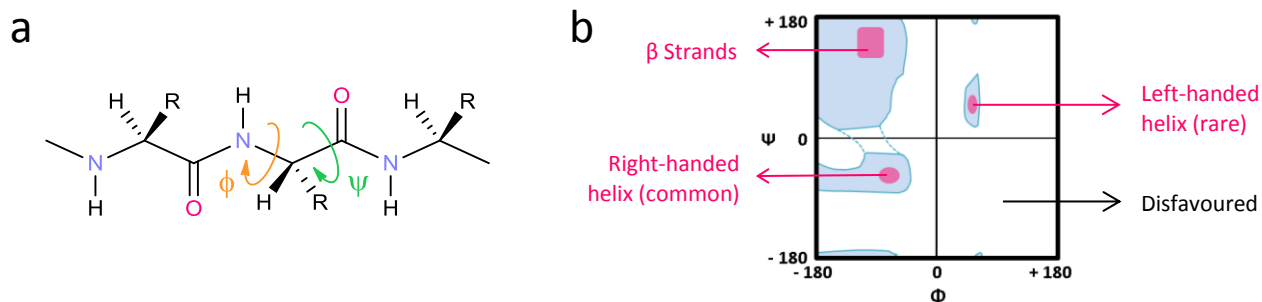
Figure I.2 (a) Adjacent peptide residues in a chain, with Φ the angle of rotation about the NC$_\alpha$ bond, and Ψ the angle of rotation about the C$_\alpha$C bond. (b) Ramachandran diagram showing the most favourable Φ and Ψ angle combinations, represented by regions of allowed conformations (blue), and within them, the regions favourable to right- and left-handed helices and β strands (pink).
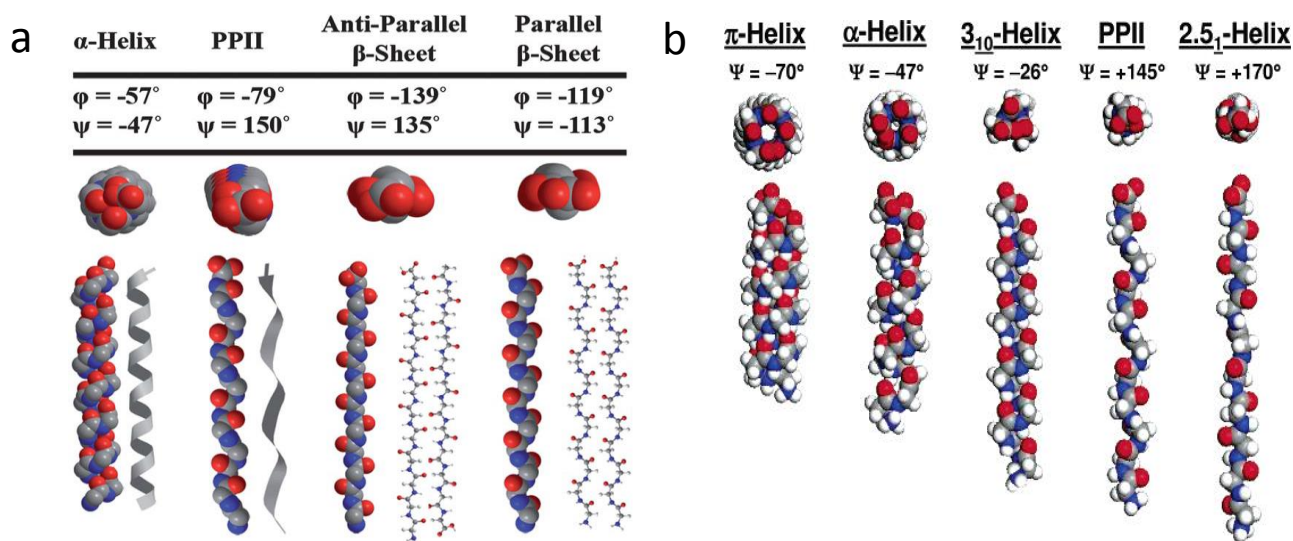
Figure I.3 Selected protein secondary structure conformations with corresponding Ramachandran angles, reprinted from (a) *Analyst, 137, Roach et al., Evolution of quantitative methods in protein secondary structure determination via deep-ultraviolet resonance Raman spectroscopy, 555-562, 2012,* with permission from The Royal Society of Chemistry,[68] and (b) *The Journal of Physical Chemistry B, 110, Mikhonin et al., Peptide Secondary Structure Folding Reaction Coordinate: Correlation between UV Raman Amide III Frequency, Ψ Ramachandran Angle, and Hydrogen Bonding, 1928-1943, 2006,* with permission from the American Chemical Society.[72]

There is a large variety of structural motifs and secondary structures available to proteins. They are controlled by Φ and Ψ angle combinations, which are themselves determined by the sequence and nature of amino acids that compose the proteins. The most common conformations are α-helices and β-sheets (Figure I.4). The α-helix is formed by a tightly coiled polypeptide chain, which is stabilised by regular intramolecular hydrogen bonds formed between C=O groups of amino acids (in position 'i') and N-H groups of amino acids on the fourth residue up (in position 'i+4'); such bonds are thus noted [i+4>i] (Figure I.5a).[2] As a result, the α-helix is defined by 3.6 residues per turn and a pitch of 0.54 nm, each residue being offset from its adjacent residues by a so-called translation of 0.15 nm along the helix axis and a rotation of 100°. The side chains point outward in an helical array. Due to the L configuration of natural amino acids, right-handed helices are energetically more favourable because there is less steric clash between side chains and backbones. Left-handed polyproline type II helices (PPII), which make up the collagen triple helices, are an

exception (3 residues per turn, Φ = -75°, Ψ = 150°). Other types of helices are defined by different intramolecular [i+n>i] hydrogen bonds, such as the π-helix (n = 5) or the 3_{10}-helix (n = 3). Unlike the α-helix, the β-sheet, also known as β pleated sheet, is stabilised by intermolecular hydrogen bonds (Figure I.5b). The β-sheet is composed of two or more extended polypeptide chains called β-strands, in which the distance between adjacent residues is 0.35 nm. The side chains of adjacent amino acids point in opposite directions, which are normal to the β-sheet plane. Neighbouring β-strands can run in opposite directions (antiparallel β-sheet) or in parallel directions (parallel β-sheet).
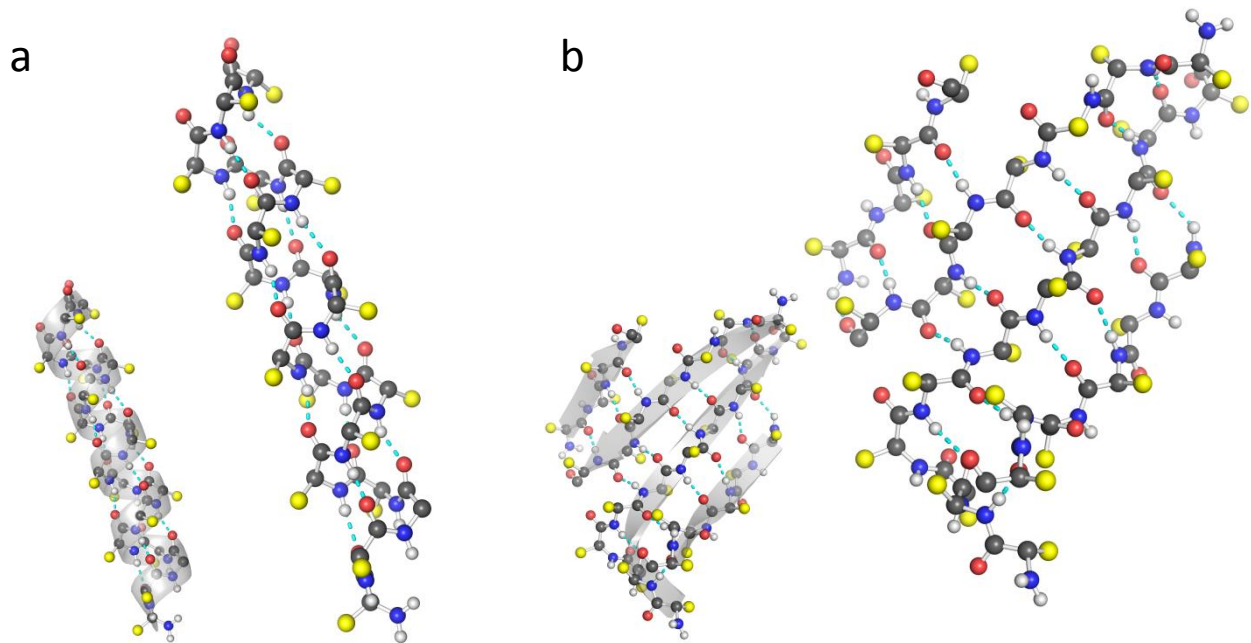
Figure I.4 Ball and stick models of (a) an α-helix motif and (b) an antiparallel β-sheet motif found in protein PDB ID: 1u9a. The dashed blue lines represent H bonds, and the different side chains are represented by yellow balls for simplicity. (*Journal of Biological Chemistry, 272, Tong et al, Crystal structure of murine/human Ubc9 provides insight into the variability of the ubiquitin-conjugating system, 1997, 21381-21387*). Models made with PyMOL Molecular Graphics System, Version 1.8 Schrödinger, LLC.
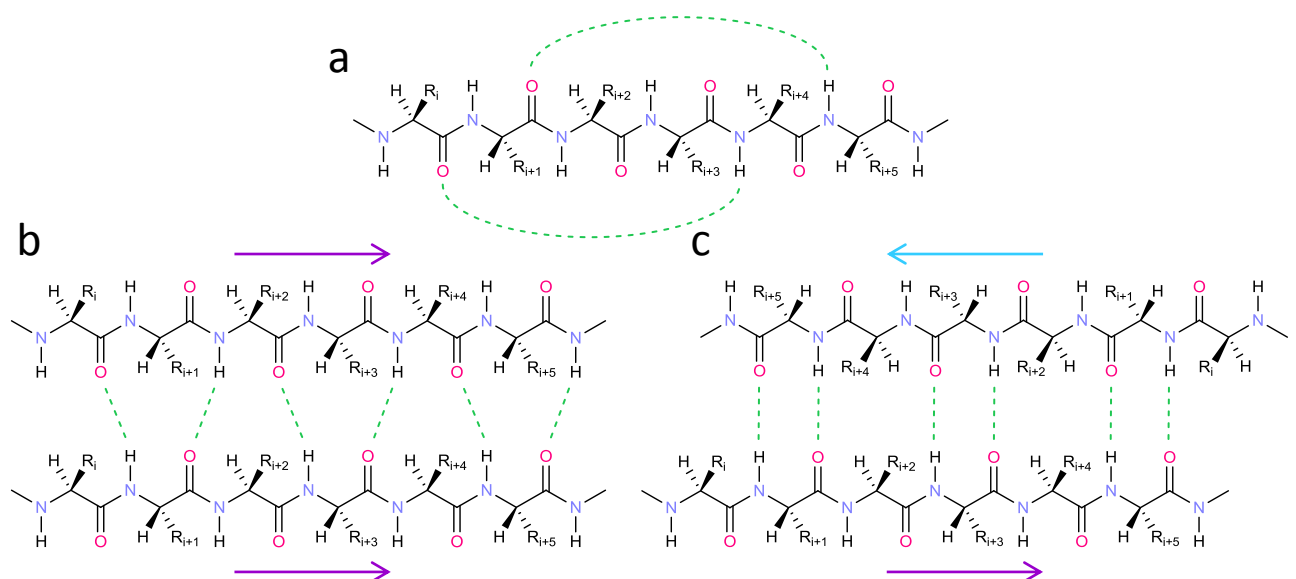
Figure I.5 Hydrogen bonding schemes for (a) a right-handed α-helix, (b) a parallel β-sheet, and (c) an antiparallel β-sheet. The hydrogen bonds are represented by green dashed lines.

I.2.3 Self-Assembly and Physical Gelation of Polypeptides

I.2.3.1 Protein Folding and Self-Assembly

Fibrous proteins are one of the major structural polymers in all types of load-bearing tissues, along with polysaccharides, such as cellulose (in plants) and chitin (insect cuticles).[73] The most common fibrous structural proteins include collagen, keratin and actin. The secondary structure of such proteins is essential to their ability to self-assemble and in turn provide structural support.[3,5] Let us consider collagen type I, which is the most abundant protein in mammals. The collagen helix is a right-handed triple helix formed by three parallel polypeptide chains (known as α-strands) in a left-handed, polyproline II-type (PPII) helical conformation, which are coiled about each other with a one-residue stagger (Figure I.6b).[3] This triple helix is a rod-shaped molecule, and is about 300 nm long and 1.5 nm in diameter. Each of its three constituent polypeptide strands is nearly 1000 residues long. The presence of glycine at every third residue in the amino acid sequence is responsible for the tight packing of PPII helices.[3] The repeating sequence is often noted (Gly, Xaa, Yaa). The sequence glycine-proline-hydroxyproline (Gly, Pro, Hyp) recurs frequently (Figure I.6a).[2,74,75] Unlike the α-helix, hydrogen bonds within a strand are absent; instead, the PPII helix is stabilised by the steric repulsion of the pyrrolidine rings of the Pro and Hyp residues. Intermolecular hydrogen bonds occur between the NH group of Gly residues and CO group of Xaa residues (typically Pro) of neighbouring strands within the triple helix (Figure I.6b).[3] The small Gly residues of each strand all lie in the core of the triple helix, while comparatively more bulky Pro and Hyp point outward.
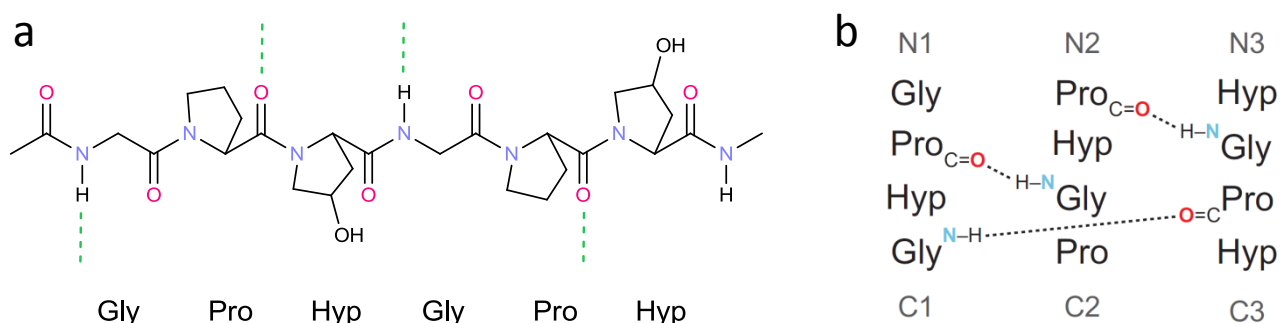
Figure I.6 (a) Collagen strand showing a typical (Gly, Pro, Hyp) collagen sequence, with intermolecular hydrogen bonds represented by green dashed lines. (b) Schematic illustration of the stagger between the three strands, with intermolecular hydrogen bonds represented by black dashed lines; reprinted from *Annual Review of Biochemistry, 78, Shoulders et al., Collagen Structure and Stability, 929-958, 2009,* with permission from Annual Reviews.[3]

Protein folding is the physical process by which a protein acquires its thermodynamically stable native structure (*i.e.*, secondary, tertiary and quaternary). It is a thermodynamically favoured process (*i.e.*, $\Delta G = \Delta H - T \cdot \Delta S < 0$), and is mainly driven by hydrophobic interactions.[76] Other forces, such as hydrogen bonding, ionic or van der Waals interactions, also contribute to the stabilisation of the formed structure. The hydrophobic effect is characterised by the transfer of non-polar amino acids from water into a non-polar medium that is preferably capable of hydrogen bonding,[76] which is the case with glycine residues in

the core of triple helix. The hydrophobic effect essentially reduces or eliminates the shells of ordered water molecules that form around hydrophobic regions or side chains of the protein, thereby leading to a positive contribution to the entropy of the system ($\Delta S \uparrow$). As for collagen, the preorganisation of the individual strands into a PPII conformation also contributes to reducing the entropic cost for collagen folding.[3]

In animals, individual collagen triple helices, known as tropocollagen (TC), assemble in a complex and hierarchical fashion, resulting in the formation of micro-fibrils, fibrils, macroscopic fibres and networks found in tendons, cartilage, bones, and basement membranes (Figure I.7).[3] The process by which TC self-assembles into well-ordered fibrils is known as fibrillogenesis, and has been shown to be entropically driven, the increase in entropy being associated with the loss of water molecules bound to the TC as it assembles.[77] Fibrillogenesis has been described as a nucleation-growth process, whereby the self-assembly is mediated by the interaction of C-terminal telopeptides (C-terminus) with specific binding sites on neighbouring TCs.[3] The resulting fibrils are further stabilised by intermolecular hydrogen bonds between hydroxyl groups of Hyp residues, most likely *via* a network of water bridges.[3,78] Micro-fibrils go on to further assemble into larger fibrils and also undergo enzymatic crosslinking.[79] Thanks to these processes, fibrils of type I collagen in tendon are up to 1 cm long and 500 nm wide.
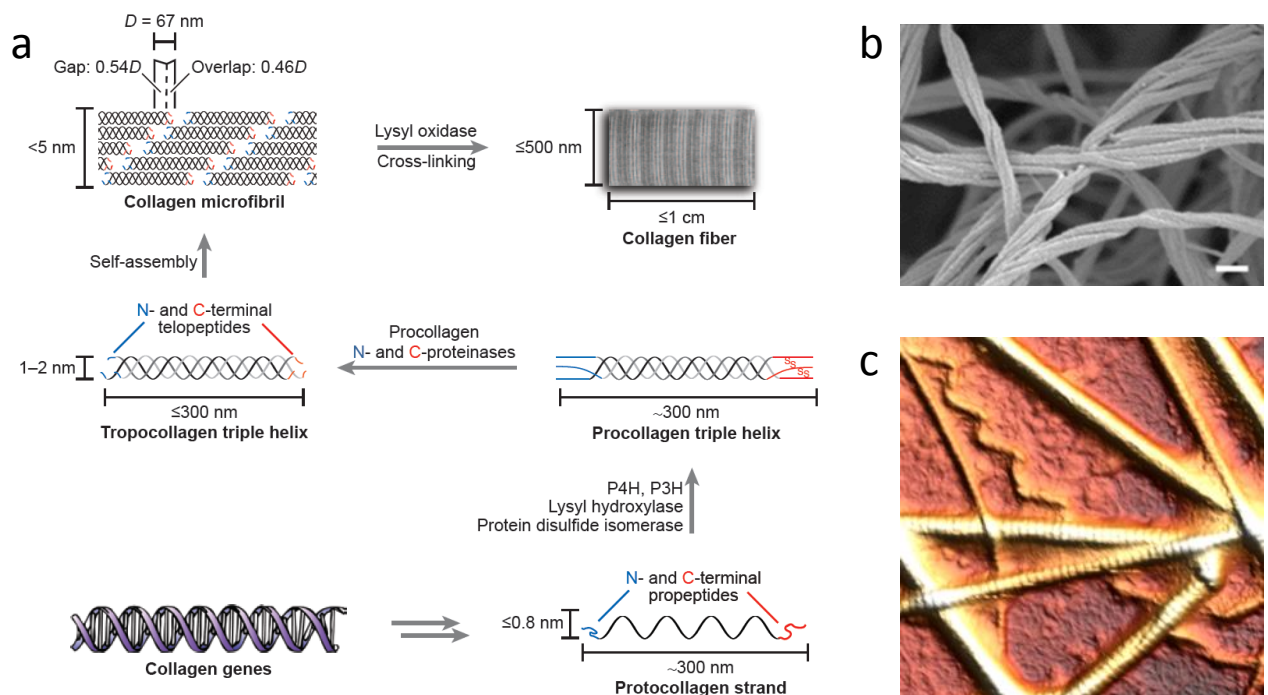
Figure I.7 (a) Biosynthetic route to a collagen fibre, which exhibits a characteristic D band of ~ 67 nm, which results from the staggered arrangement of triple helices along the fibril axis and the recurring end-to-end gaps; reprinted from *Annual Review of Biochemistry, 78, Shoulders et al., Collagen Structure and Stability, 929-958, 2009,* with permission from Annual Reviews.[3] (b) SEM image of the fibrous network of a dehydrated gel of collagen I exhibiting a characteristic bundling often found in collagen fibres (scale bar = 200 nm); reprinted from *Materials, 8, Moreno-Arotzena et al., Characterization of Fibrin and Collagen Gels for Engineering Wound Healing Models, 1636-1651, 2015,* with permission from MDPI.[80] (c) AFM image of insoluble collagen I fibrils dried from a suspension in 0.05M acetic acid (10 g·L^{-1}) and exhibiting the characteristic D band of ~ 67 nm (the fibril widths range between 100 and 300 nm).

I.2.3.2 Physical Gelation of Synthetic Polypeptides

Sequence-controlled polypeptides, typically prepared by solid-phase synthesis, are the only synthetic polymers that can reproduce the complexity of the primary and secondary structure of proteins.[13,81] As such, they also have the capacity to self-assemble in a similar fashion. Several studies have reported the synthesis of collagen-mimetic polypeptides and their ability to form collagen mimetic fibres and gels (Figure I.8a).[13,82,83] Simple synthetic homopolypeptides also have amino acid residue-controlled secondary structures, however, their ability to self-assemble in water in somewhat limited. There are two main reasons for this. First, in the context of self-assembly, water is a challenging solvent to work with as it is highly polar and disrupts hydrogen bonding, which are essential to the stabilisation of secondary structures.[69,84,85] The other reason pertains to the fact that homopolypeptides are composed of only one type of amino acid. In contrast, the primary structure of proteins can be seen as a carefully balanced combination of hydrophobic and hydrophilic, positively and negatively charged residues.[2] As such, proteins are 'designed' to be sufficiently hydrophilic to exist in water and sufficiently hydrophobic to fold and assemble into more complex structures. Poly(L-glutamatic acid) (PLGA), for instance, only exists in water as a randomly coiled polyanion as the electrostatic repulsions prevent its folding. Upon protonation, the polypeptide folds into an α-helix but becomes so hydrophobic that it precipitates.[30]
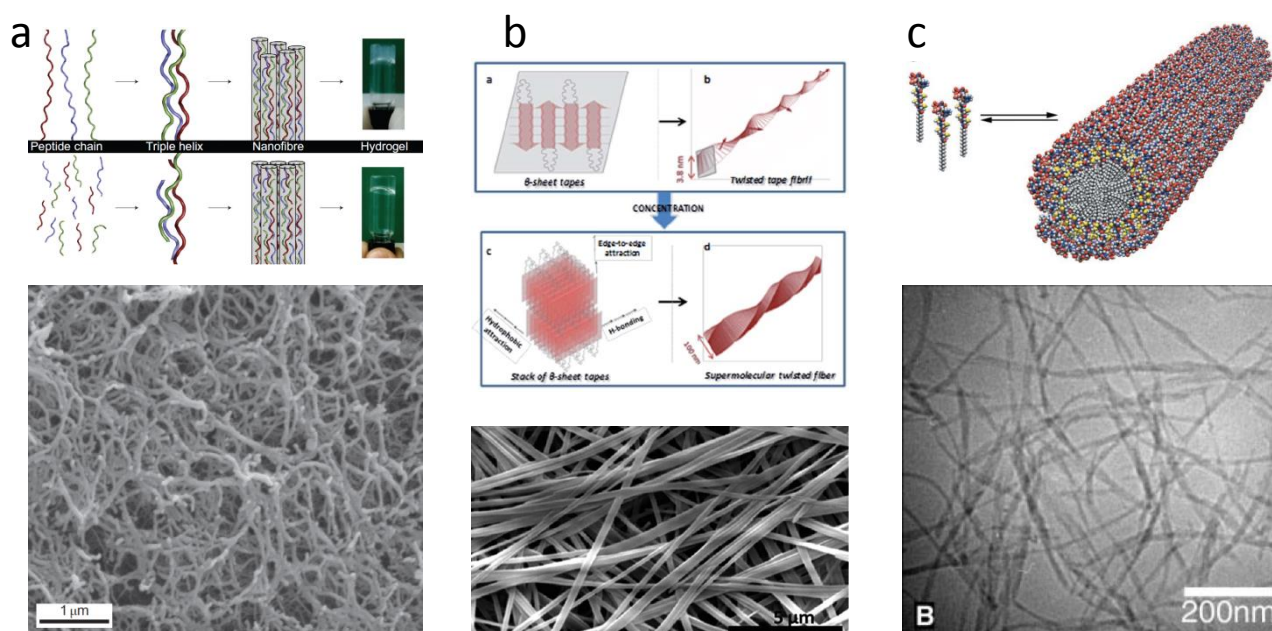
Figure I.8 (a) Self-assembly of collagen type I compared to that of collagen mimetic peptides, and SEM images of dried hydrogel; reprinted from *Nature Chemistry, 3, O'Leary et al., Multi-hierarchical self-assembly of a collagen mimetic peptide from triple helix to nanofibre and hydrogel, 821-828, 2011,* with permission from Macmillan Publishers Ltd.[13] (b) Schematic representation of the hierarchical self-assembly of the PAla–PGA–PAla triblock copolypeptide, and SEM images of freeze dried PAla–PGA–PAla gel samples; reprinted from *Soft Matter, 11, Popescu et al., Stimuli responsive fibrous hydrogels from hierarchical self-assembly of a triblock copolypeptide, 331-342, 2014,* with permission from the Royal Society of Chemistry.[18] (c) Schematic of the self-assembly of peptide amphiphile molecules into a cylindrical micelle, and TEM images of the hydrogel formed by self-assembled peptides; reprinted from *Science, 294, Hartgerink et al., Self-Assembly and Mineralization of Peptide-Amphiphile Nanofibers, 1684-1688, 2001,* with permission from AAAS.[86]

Based on this consideration, non-sequence controlled copolypeptides of two or more comonomers of different and contrasting properties represent simple, yet promising, alternatives for the preparation of bio-compatible self-assembled structures. Notably, block copolymers are particularly efficient at inducing self-assemblies. In simple terms, this architecture exploits the fact that different polymers usually do not like to mix.[19] In addition to unfavoured block A-block B interactions, differences in block-solvent interactions are exploited to further induce the segregation of blocks in solution,[24] thereby inducing a variety of self-assembled systems, including micelles, vesicles, ribbons, fibres and fibrous gels.[18,24,87] Typical block copolymer types include double hydrophilic, amphiphilic and dual conformation block (*e.g.*, rod-coil) copolymers.[17,19,22,88]

Physical polypeptide gels are of particular interest to tissue engineers as they are the macroscopic evidence of the formation of a supramolecular fibrous network, and fibrous networks are the structural scaffolds of most of the connective tissues and extracellular matrices in the body.[4,80,85] Their fibrous and porous architecture can provide mechanical support while allowing drugs and cells to diffuse in a water-rich environment, making them excellent biomedical candidates. A large variety of block copolypeptides have been shown to assemble into hydrogels (Figure I.8b).[16–18,89,90] Even small amphiphilic peptides have been shown to behave as hydrogelators (Figure I.8c).[23,70,84,91,92] However, despite a thorough literature search, there appear to be no examples of self-assembled statistical or random copolypeptide hydrogels, only examples of chemically crosslinked gels[93,94] or physical gels relying on moieties-inducing supramolecular assemblies (*e.g.*, fmoc, pyrene, PEG).[95–97] As pointed out by Deming, for a particular amino acid composition, amphiphilic block copolypeptides form hydrogels while random copolypeptides do not.[17]

In an effort to develop a new class of bio-inspired hydrogels, this doctoral work explored new synthetic routes to generate hydrogels from statistical (random) copolypeptides. In particular, the focus was put on BLG-based copolypeptides. PBLG can form physical gels, and it is a rod-like polypeptide like collagen, as such, it is an ideal model polymer for the preparation of bio-inspired materials.[98,99] The impact of comonomers substitution (*i.e.*, BLG to AG) in a polypeptidic organogelator (*i.e.*, PBLG) in particular was thoroughly investigated, the purpose of this systematic study being to guide the rational design of statistical copolypeptides for self-assembly and gelation purposes.

I.3 Selected Analytical Methods

I.3.1 Wide-Angle X-Ray Scattering

Wide-angle X-ray scattering (WAXS), also known as wide-angle X-ray diffraction (WAXD), is an X-ray-diffraction technique that is commonly used to determine the crystalline structure of polymers.[100,101] Like other X-ray techniques, including X-ray powder diffraction (XRD) and small-angle X-ray scattering (SAXS), WAXS is a non-destructive technique used to determine the atomic and molecular structure of a crystalline or semi-crystalline material by exposing it to a beam of incident X-rays and recording the specific angle 2θ

of the diffracted beam. This type of diffraction, known as Bragg diffraction, results from the constructive interference (*i.e.*, in-phase coherence) between electromagnetic waves reflected from different crystal planes (Figure I.9).[100] The resulting pattern provides information on the separation of crystallographic planes, or *d*-spacings, thereby allowing for the deduction of the crystal structure. Bragg's law, given by Equation I.1a, is used to calculate these characteristic dimensions or *d*-spacings. The results are generally reported in the form of a diffractogram of the scattered intensity (obtained from the integration of the 2D pattern) as a function of 2θ (typically for WAXS) or the scattering vector q (typically for SAXS) (Equation I.1b).

$$(a) \; n \cdot \lambda = 2 \cdot d \cdot \sin\theta \qquad\qquad (b) \; q = \frac{4 \cdot \pi \cdot \sin\theta}{\lambda} = \frac{2 \cdot \pi}{d}$$

Equation I.1 (a) Bragg's law, where *d* is the interplanar distance of the lattice planes in an ordered domain, θ is the scattering angle (*i.e.*, Bragg angle), n is a positive integer corresponding to the order of diffraction (first order diffraction, *i.e.* n = 1, generally provides the strongest peak intensities, but higher order reflections, *i.e.*, n > 1, are common in long-range ordered systems, such as collagen; see Figure I.11), and λ is the wavelength of the incident electromagnetic wave (typically, λ = 0.1542 nm). (b) Scattering vector q generally reported in nm^{-1} or $Å^{-1}$ and commonly used for SAXS data.

$$(a) \; (AB + BC + CD') - AE = DD' = n \cdot \lambda$$

$$(b) \; AB = BC = \frac{d}{\sin\theta}$$

$$(c) \; AE = CD' + AC \cdot \cos\theta$$

$$(d) \; AC = 2 \cdot AB \cdot \cos\theta = \frac{2 \cdot d \cdot \cos\theta}{\sin\theta}$$

$$(c) \; and \; (d) \; \rightarrow \; (e) \; AE = CD' + \frac{2 \cdot d \cdot (\cos\theta)^2}{\sin\theta}$$

$$(f) \; n \cdot \lambda = \frac{2 \cdot d \cdot (1 - (\cos\theta)^2)}{\sin\theta} = 2 \cdot d \cdot \sin\theta$$
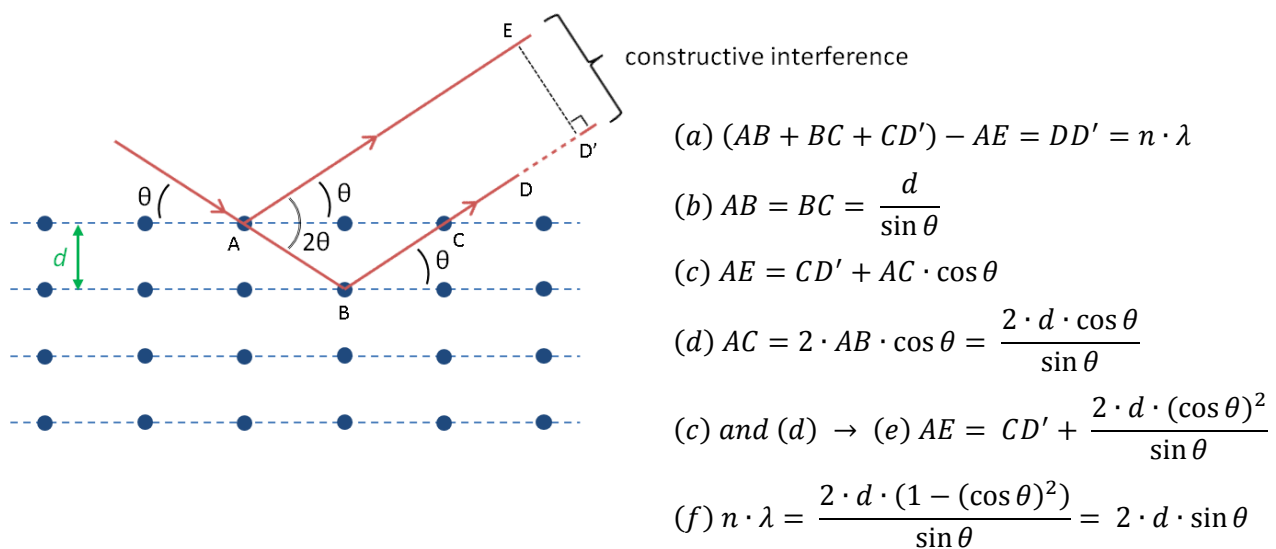
Figure I.9 (left) Bragg's law schematics, and (right) demonstration of the law, where (a) is the condition for the waves scattered by a 2θ angle to interfere constructively (*i.e.*, to be in phase) is that the path difference (DD') is λ times an integer, n; (b), (c), (d) and (e) show the trigonometric calculation of the lengths of the segments AB, BC, AE and AC (segments of the two paths of coherent waves scattered by the first two crystallographic planes), as a function of θ and *d*; (f) shows Bragg's law as derived from (a), (b) and (e).

It is worth noting that in WAXS, SAXS and XRD the electromagnetic wave is elastically scattered; more precisely, the energy is conserved and the wavelengths of the scattered and incident waves are the same.[100] This phenomenon is also known as Rayleigh scattering. More generally, scattering is the physical phenomenon that results from electromagnetic waves interacting with objects whose size is on the order of magnitude of their wavelength (*e.g.*, X-rays are scattered by electron clouds); following such an interaction, these waves are scattered in spatial directions. When the object encountered is ordered, the

waves scattered at specific 2θ angles are coherent, in which case the phenomenon is referred to as diffraction. In the context of X-ray studies, scattering and diffraction (a subset of the former) are thus used interchangeably.

Like the traditional XRD technique, WAXS is specifically suited to the analysis of Bragg peaks scattered to wide angles (*i.e.*, large 2θ), which are produced by nanometre- and sub-nanometre-sized structures. The two methods, however, differ in their set-up (Figure I.10). The detector and source (and hence the X-ray beam) in WAXS (and SAXS) are static. The beam penetrates the sample and is diffracted by an angle of 2θ onto the 2D detector located behind the sample. In this way, the diffraction is also measured across the entire 360° azimuthal or Chi angle (*X*) range. The resulting 2D pattern (in a (2θ, *X*) polar coordinate system) provides information about possible anisotropy in the sample (*e.g.*, alignment of crystallites and residual stress) (Figure I.11a).[102,103]
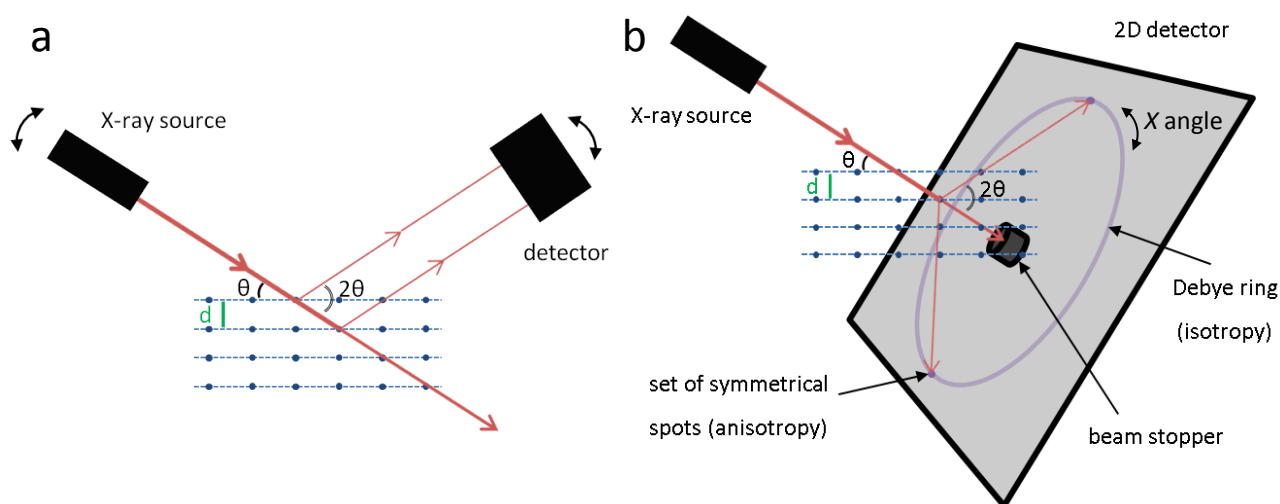
Figure I.10 Schematic representations of typical (a) XRD and (b) WAXS equipment set-ups; the X-rays are produced by accelerating electrons from a tungsten filament onto a copper target (λ (Cu-Kα) = 1.542 Å). In a WAXS measurement (b), crystalline domains in an otherwise isotropic sample generate Debye-Scherrer rings; if the crystalline domains are oriented over long distances, they generate symmetrical arcs and spots (for anisotropic and highly anisotropic samples, respectively); the axial symmetry simply results from the symmetry of constructively interfering waves.

If the sample is isotropic, uniform Debye-Scherrer rings are obtained (Figure I.11b). In any case, the scattering intensity is generally plotted, after *X* integration, as a function of the 2θ angle, which also allows maximisation of the intensity of the Bragg diffraction peaks, often referred to as Bragg peaks. This maximisation is particularly useful for samples like polymers, whose crystallinity or molecular order can be limited, often resulting in low signal to noise ratios in XRD measurements. Since WAXS (and SAXS) operate in 'transmission' (Figure I.10), the technique is not suited for X-ray-opaque samples such as metals. XRD, which operates in 'reflection', can be used to scan a broader 2θ range (typically, from 2 to 80°), which gives access to even wider 2θ angles than WAXS, but does so at a fixed *X* angle and requires larger sample quantities. A *Φ* and *X* scan is possible but requires longer running times. XRD is thus suited for highly crystalline inorganic samples.
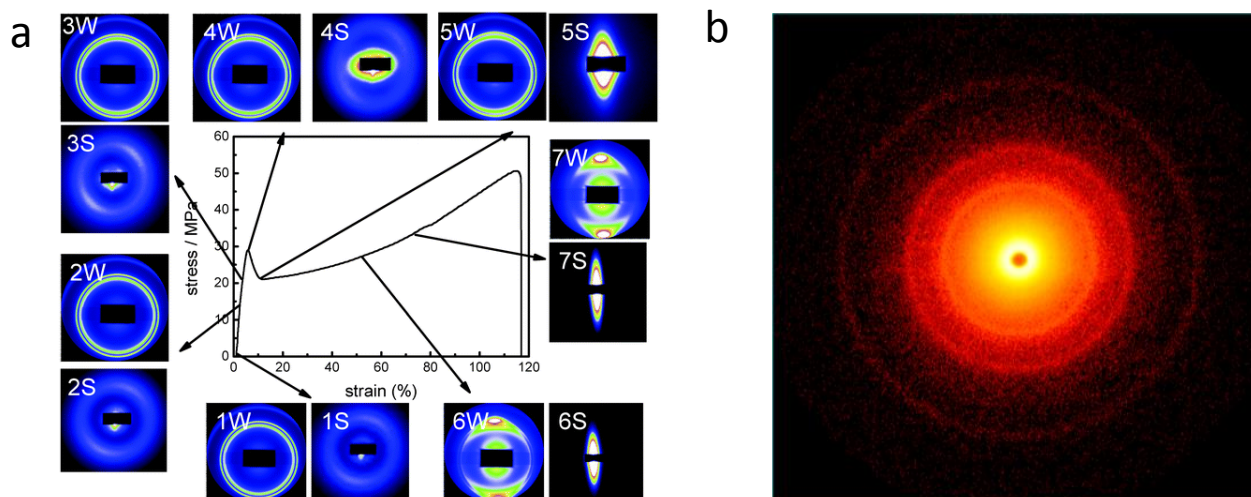
Figure I.11 Examples of WAXS and SAXS patterns of oriented and non-oriented samples. (a) Engineering stress–strain curves and selected 2D SAXS and WAXS patterns acquired during uniaxial tensile deformation of PVDF at 60 °C (the sample was stretched in a horizontal direction); reprinted from *CrystEngComm, 15, Guo et al., In-situ synchrotron SAXS and WAXS investigations on deformation and α–β transformation of uniaxial stretched poly(vinylidene fluoride), 1597-1606, 2013,* with permission from The Royal Society of Chemistry.[103] (b) Typical 2D SAXS pattern of an unoriented collagen type I film, showing uniform Debye-Scherrer rings corresponding to higher order diffractions of the classic D band (67 nm).

WAXS is essentially the same technique as SAXS (*i.e.*, X-ray scattering onto a 2D screen located behind the sample), only with the difference that the distance from sample to detector is shorter in WAXS and thus diffraction peaks at larger angles are observed.[100] This means that SAXS can detect larger *d*-spacings, and hence provide information about the molecular structure (up to ~ 80 nm) of the sample and its organisation at higher hierarchical levels.[104,105] Table I.1 provides typical sample to detector distances and corresponding *d*-spacing ranges.

Table I.1 Typical Sample to Detector Ranges for the Nanostar (Bruker) Instrument

Sample to detector distance (mm)	2θ (°)	d (nm)	Calibrant	WAXS or SAXS
1070	0.1 - 2.8	3 - 88*	silver behenate	SAXS
660	0.14 - 4.6	2 - 62*	silver behenate	SAXS
270	0.6 - 13.5	0.7 - 15*	silver behenate	SAXS
80	3 - 35	0.3 - 3*	corundum	WAXS
40	4 - 40	0.2 - 2*	corundum	WAXS

* The upper boundary for d depends on the size of the beam stopper, the sample-detector distance, and is apparatus-dependent (e.g., beam width, brand).

Additional information, like degree of crystallinity and average ordered domain size, can also be extracted from X-ray diffractograms (Equation I.2).[101,106] Macromolecules cannot pack as efficiently as low molecular weight compounds mostly due to chain entanglements. Polymers can therefore be completely amorphous or semi-crystalline (*i.e.*, containing both amorphous and crystalline domains). The crystalline phase produces Bragg peaks, whose sharpness varies essentially with the size of the ordered or crystalline

domain. The intensity of these peaks is proportional to the number of atoms that are found in the crystalline planes. The amorphous domains generate a diffuse halo caused by short-range 'order' between neighbouring chain segments, as there is a preferential distance amongst chain segments even in an amorphous material.[101] As crystalline layers grow thicker, the entangled amorphous layer becomes compressed, shifting the halo to a slightly higher scattering angle. Other amorphous materials, such as borosilicate glass and solvents, also generate amorphous halos. Due to the use of manually blown capillary glass holders with highly variable wall thicknesses, subtracting the capillary contribution to the amorphous halo can lead to unreliable results. In addition, the preparation of the samples involves some level of compaction, and compressive forces have been shown to affect the crystallinity of polymer samples.[107,108] For these reasons, together with the fact that the crystallinity index was non-essential to the present doctoral work, the degree of crystallinity of polypeptide samples was not quantified.

$$(a) \quad \tau = \frac{K \cdot \lambda}{\beta \cdot \cos\theta} \qquad\qquad (b)\ X_c = \frac{I_c}{I_a + I_c}$$

Equation I.2 (a) Scherrer equation, where τ is the mean size of the ordered domain, K is a dimensionless shape factor (0.9 to 1), is the X-ray wavelength (0.1542 nm), β is the line broadening at half the maximum intensity or full width at half maximum (FWHM), and θ is the Bragg angle.[109,110] (b) Crystallinity index (X_c) with I_a the area under the amorphous halo and I_c the area under the Bragg peaks corresponding to the crystalline domains.[101]

Should the degree of crystallinity be required for any future work, it is recommended than an ad hoc sample holder that does not induce sample compaction be used. In addition, for consistency, all samples should be freeze-dried from solutions of identical concentrations, volumes and in identical moulds. A PTFE mould that could also be used as a sample holder would represent an excellent solution.

I.3.2 Infrared and Raman Spectroscopy

I.3.2.1 Theory

Molecules can vibrate in many ways, which are called vibrational modes (*e.g.*, stretching, wagging, twisting). Amongst molecules with N atoms, linear molecules have 3N - 5 degrees of vibrational freedom, whereas nonlinear molecules have 3N - 6 degrees of vibrational freedom. Infrared (IR) and Raman spectroscopy techniques measure vibrational and rotational frequencies and the corresponding energy level differences or spacings (ΔE) in molecules. These measurements provide information on the types of bonds and functional groups present in a molecule.[111] In infrared spectroscopy, molecules absorb photons whose frequencies are characteristic of the molecular structure. More precisely, the frequency of the absorbed radiation (v_0) matches a vibrational frequency (v_m), which is associated with a particular mode of motion and a particular bond type (Figure I.12). In Raman spectroscopy, a photon of a specific wavelength (λ) excites the molecule, which is either in the ground vibrational state (*i.e.*, lowest vibrational energy level of the ground electronic state) or an excited vibrational state.[112] This interaction briefly promotes the

molecule to a so-called virtual energy state before the photon is elastically (*i.e.,* Rayleigh) or inelastically scattered. The inelastically scattered photon is either of lower (Stokes) or higher (anti-Stokes) energy than before the excitation. In either case, the resulting vibrational state of the molecule is different from the state that the molecule originally occupied. The difference in energy between the pre and post excitation states leads to a shift in the emitted photon's frequency (as $\Delta E = h \cdot c/\lambda = h \cdot v$, with h the Planck constant), which is the quantity measured by Raman spectroscopy (Figure I.12).
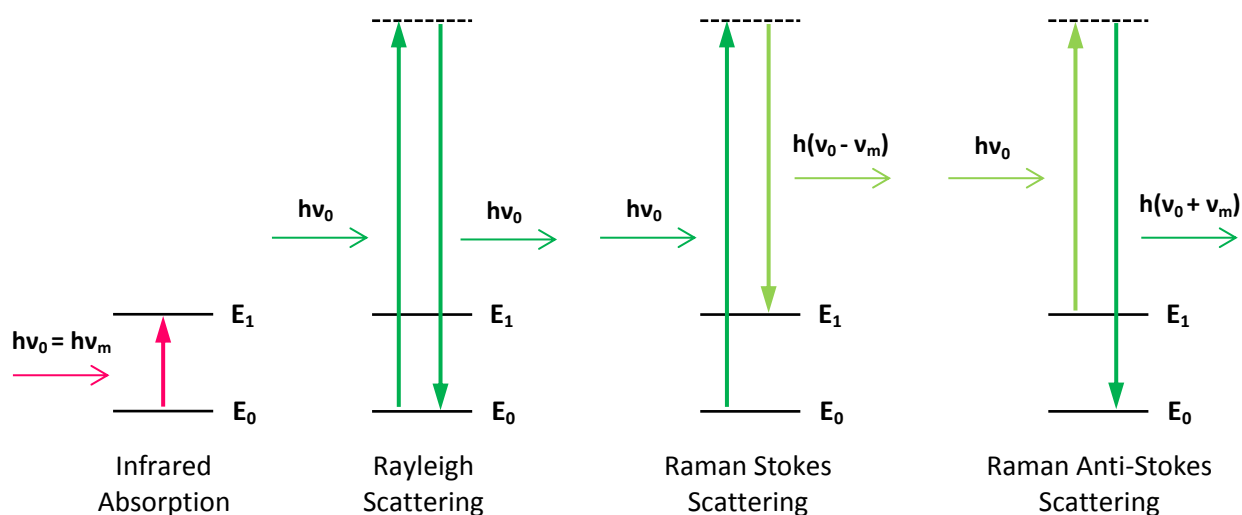
Figure I.12 Comparison of energy transitions between two molecular states: the ground state (E_0) and the first excited vibrational state (E_1), with v_0 the incident light frequency (infrared in the case of the absorption, a higher frequency such as green light in the case of the scattering), and v_m the vibrational molecular frequency ($v_m = c/\lambda_m$). Three possibilities of light scattering are represented: Rayleigh scattering (no energy exchange, incident and scattered photons have the same energy), Stokes Raman scattering (the molecule absorbs some energy, the scattered photon has less energy than the incident photon), and anti-Stokes Raman scattering (the molecule loses some energy, the scattered photon has more energy than the incident photon); the virtual energy state is represented by the dashed black line.

The Raman spectrum, therefore, shows the intensity of the inelastically scattered light as a function of its frequency difference ($\Delta v = v_0 - v_m$). Stokes and anti-Stokes peaks form a symmetric pattern around $\Delta v = 0$ (*i.e.,* Rayleigh line). The frequency shifts are symmetric because they correspond to the energy difference (hv_m) between the excited and ground states, which is the same for both scattering phenomena. However, the intensities vary because molecules are more likely to be found in their ground state than in an excited state; hence, Stokes transitions are more frequent than anti-Stokes transitions. Therefore, the Stokes scattering peaks are more intense than the anti-Stokes scattering peaks. In practice, Raman spectra usually combine both types of scattering (although some devices only retain the Stokes contribution) and display intensities as a function of Raman shifts ($\overline{v} = \Delta E/h \cdot c = 1/\lambda_0 - (1/\lambda_0 - 1/\lambda_m) = 1/\lambda_m$).

It is easy to understand from Figure I.12 that the excited states (and corresponding energy levels) are inherent to a particular molecule and not to the measurement method. Therefore, the set of Raman shifts displayed by the Raman spectrum should coincide with the set of wavenumbers ($1/\lambda_m$) displayed by the IR spectrum. Although the frequency (c/λ_m) corresponding to a specific vibrational state is unique regardless of the method used, the sets of frequencies that can be measured by IR or Raman can vary.

More precisely, some vibrational modes can be IR active and Raman inactive (or vice versa), or both IR and Raman active, or both IR and Raman inactive, and their relative peak intensities may also vary between Raman and IR spectra. This variance can be explained by the fact that the quantum mechanical (or spectroscopic) selection rules for IR and Raman processes are different. For a vibrational mode to be Raman active, it must involve a change in the polarisability of the molecule, whereas for it to be IR active, a dipole moment change is required.[111] As a result, less symmetric vibrations produce greater intensities in IR than in Raman, while more symmetric motions produce the strongest Raman and weakest IR intensities. In fact, for centrosymmetric molecules, the Raman active modes are IR inactive and vice versa; this is called the rule of mutual exclusion. The two techniques are, therefore, complementary.

I.3.2.2   Practical Aspects of ATR-FTIR and Raman Spectroscopy

Attenuated total reflectance or reflection (ATR) is a technique that enables samples to be analysed directly in the solid or liquid state without further preparation. Total internal reflection occurs when light travels from a high refractive index (n_1) medium to a low refractive index (n_2) medium at an incident angle below the critical angle (θ_c), determined by the Snell–Descartes law ($n_1 \cdot \sin\theta_1 = n_2 \cdot \sin\theta_2$, with $\theta_1 = \theta_c$ when $\theta_2 = 90°$). Under such conditions, an evanescent wave, which is an oscillating electromagnetic field whose energy is spatially concentrated in the vicinity of the interface, penetrates the n_2 medium. In an ATR accessory, a beam of infrared light travels through a dense crystal with a high refractive index (the ATR crystal) in such a way that it reflects at least once off the internal surface in contact with the sample (Figure I.13). This reflection generates evanescent waves that extend a few microns (depending on the wavelength) into the sample held in contact with the crystal. In regions of the infrared spectrum where the sample absorbs energy, the evanescent wave will be attenuated. Because of the nature of the evanescent wave and the conservation of energy law, the attenuated energy from each evanescent wave is 'passed back' to the IR beam, which then exits at the opposite end of the crystal and is analysed by the detector.
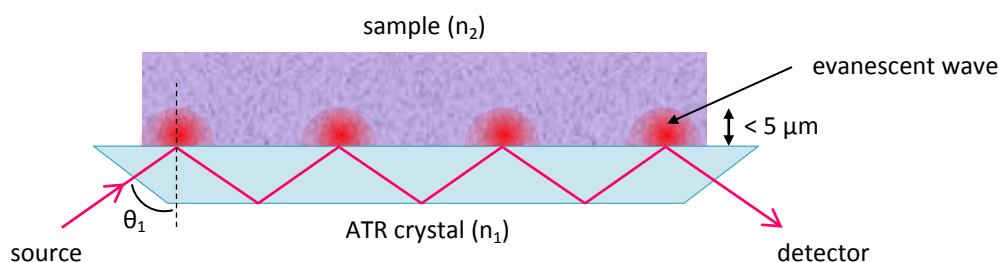
Figure I.13 Schematic ATR set up showing the total internal reflections and the resulting evanescent waves that penetrate the sample; this is enabled by a crystal with a high refractive index (n_1) and a carefully selected incident angle ($\theta_1 < \theta_c$).

Fourier transform infrared (FTIR) spectroscopy is a measurement technique for recording infrared spectra. The distribution of infrared light (*e.g.*, the different wavelengths) that passes through the sample is altered by an interferometer, which consists of a beam splitter and a static and moving mirror. The purpose of the interferometer is to generate constructive and destructive interferences as a function of the moving

mirror position, hence as a function of the IR wavelength. The recorded signal (*i.e.*, interferogram) is processed by Fourier transformation, which generates a typical intensity-wavenumber ($1/\lambda$ in cm^{-1}) FTIR spectrum.

In a typical Raman spectroscopic set up, a sample is illuminated with a laser beam (*e.g.*, green, λ = 532 nm). The electromagnetic radiation scattered from the sample is collected with a lens and processed by a monochromator. Elastically scattered photons (Rayleigh scattering), whose wavelength is the same as the laser and which represent more than 99.99% of all scattered light, are filtered out.[111] The remaining inelastically scattered photons (*i.e.*, < 0.1% of all scattered light) are dispersed onto a detector, and a typical intensity-Raman shift ($1/\lambda$ in cm^{-1}) Raman spectrum is generated.

I.3.3 Viscoelasticity and Rheology

Viscoelasticity is the property of materials that exhibit both viscous (*i.e.*, 'liquid-like') and elastic (*i.e.*, 'solid-like') characteristics when undergoing deformation in response to an applied force. The classical theory of elasticity deals with mechanical properties of solids, for which, in accordance with Hooke's law, stress (σ) is linearly proportional to strain (γ) at small deformations but independent of the rate of strain. The classical theory of hydrodynamics deals with properties of viscous liquids, for which, in accordance to Newton's law, the stress is directly proportional to the rate of strain but independent of the strain itself.[113] Both models are idealisations and are referred to as Hookean solid and Newtonian liquid, respectively (Equation I.3). For non-ideal materials, these equations do not fully describe the stress–strain–time relationship over the full range of response, as linear behaviour is generally only observed at very low strains and rates (referred to as the 'linear regime').[114,115] For instance, in the case of viscoelastic materials such as polymers and polymer melts and solutions, the shear moduli and viscosities are not constant and depend on strain rate, magnitude and time.

$$(a)\ \sigma = G \cdot \gamma \qquad (b)\ \sigma = \eta \cdot \frac{d\gamma}{dt} = \eta \cdot \dot{\gamma} \qquad (c)\ \gamma = \frac{x}{h}$$
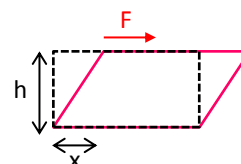
Equation I.3 (a) Shear stress for a Hookean solid as a function of shear modulus (G) and shear strain (γ); (b) shear stress for a Newtonian liquid as a function of dynamic viscosity (η) and shear rate ($\dot{\gamma}$); (c) shear strain as a function of the geometric parameters given by the schematic deformation (in shear mode) on the right. Note that in other deformation modes, the equations are still valid but typically use different symbols (*e.g.*, σ = E·ε in tensile or compressive mode, with E the young's modulus, and ε the tensile strain).

Viscoelasticity is typically studied using dynamic mechanical analysis (DMA), by applying a small oscillatory stress and measuring the resulting strain or vice versa. This type of measurement can be performed with a DMA analyser, which is best suited to samples that are more 'solid-like', or with a rheometer, which is best suited to samples that are more 'liquid-like'. Viscoelastic measurements belong to the discipline of rheology, which can be defined as the study of the deformation of matter with both solid and fluid characteristics (*i.e.*, viscoelastic materials) upon application of a force. In fact, the word 'rheology',

coined in 1929, was inspired by a quote by Heraclitus, "everything flows". Indeed, most materials flow but to different extents depending on how much force is applied and for how long.[116] In practice, a sinusoidal strain is applied to a sample and the resulting stress is measured, allowing for the determination of the complex modulus and other parameters (Equation I.4). For a purely viscous fluid (*i.e.*, Newtonian), there is a 90° phase lag (δ) of strain with respect to stress. For a perfectly elastic solid (*i.e.*, Hookean), strain and stress are in phase (δ = 0). For viscoelastic materials, the phase lag is somewhere between 0 and 90°.[113] Rheological measurements in oscillation mode, therefore, allow for the characterisation of the viscoelastic properties of a sample, in particular the loss modulus (G''), the storage modulus (G') and the complex viscosity (η*). A material is generally considered predominantly elastic (*i.e.*, solid-like) when G' > G''; likewise, is it considered predominantly viscous (*i.e.*, liquid-like) when G'' > G'.[17] This is particularly relevant when monitoring the progress of gelation or crosslinking (*e.g.*, polymer solutions or melts), which must be performed in oscillatory mode in order to limit the experimental disruption of the developing physical network.[17,87,90]

$$(a)\ \gamma(t) = \gamma_0 \cdot \cos(\omega t) = Re\big(\gamma_0 \cdot e^{i\omega t}\big) = Re(\gamma^*)$$

$$(b)\ \sigma(t) = \sigma_0 \cdot \cos(\omega t + \delta) = Re\big(\sigma_0 \cdot e^{i\omega t + \delta}\big) = Re(\sigma^*)$$

$$(c)\ G^* = \frac{\sigma^*}{\gamma^*} = \frac{\sigma_0}{\gamma_0} \cdot e^{i\delta} = \frac{\sigma_0}{\gamma_0} \cdot (\cos\delta + i\sin\delta) = G' + iG''$$

$$(d)\ G' = \frac{\sigma_0}{\gamma_0} \cdot \cos\delta \qquad\qquad (e)\ G'' = \frac{\sigma_0}{\gamma_0} \cdot \sin\delta$$

$$(f)\ \eta^* = \frac{\sigma^*}{\dot{\gamma}^*} = \frac{\sigma^*}{i\omega\gamma^*} = \frac{G^*}{i\omega} = \frac{G'}{i\omega} + \frac{G''}{\omega} = \frac{G''}{\omega} - \frac{iG'}{\omega} = \eta' - i\eta''$$

$$(g)\ \eta' = \frac{G''}{\omega} \qquad (h)\ \eta'' = \frac{G'}{\omega} \qquad (i)\ \tan\delta = \frac{G''}{G'}$$

Equation I.4 Equations that apply in a oscillatory experiment: (a) applied sinusoidal strain, with γ_0 the amplitude and $\omega = 2\pi\nu$ the angular frequency (rad·s^{-1}) which are fixed; (b) measured stress with a phase lag δ relative to the applied strain, with σ_0 the amplitude (Pa); (c) complex shear modulus (Pa); (d) storage modulus (Pa); (e) loss modulus (Pa); (f) complex viscosity (Pa·s); (g) dynamic viscosity (Pa·s); (h) real part of the complex viscosity related to the solid-like behaviour of the sample (Pa·s); (i) tan delta ranges between 0 and 1 and can be considered a measure of the material damping.

A variety of experiments can be used to fully characterise the properties of a viscoelastic sample. Rheometers can be operated in rotational (*i.e.*, steady flow) or oscillatory mode, in both shear and extension, allowing for such experiments to be performed. For instance, shear-thinning (*i.e.*, pseudoplastic), shear-thickening (*i.e.*, dilatant) and other non-Newtonian behaviours can be measured by shear stress-shear rate measurements (Figure I.14).[114,115] Shear thinning behaviour describes fluids whose viscosity decreases with the shear rate; it should be distinguished from thixotropy, which is a time-dependent shear thinning property (*i.e.*, viscosity decreases with time when stressed, then takes a fixed amount of time to return to its original state). Shear-thinning behaviour is common in polymer solutions and melts, as well as

colloidal systems like paint and nail polish. In contrast, shear thickening behaviour describes fluids whose viscosity increases with the shear rate, such as suspensions of corn starch in water. Bingham and Casson plastics require a finite yield stress before they begin to flow; typical examples include toothpaste and mayonnaise.
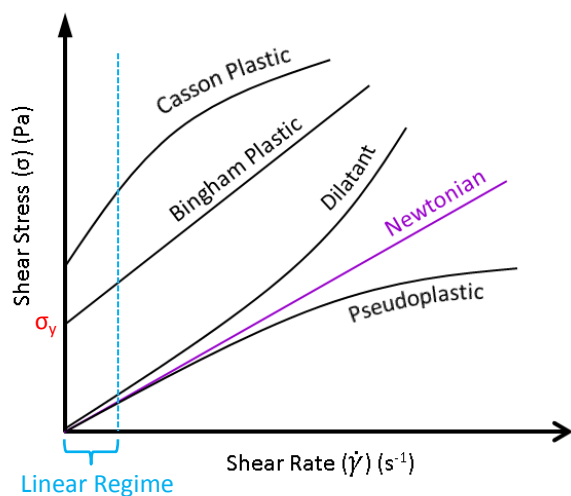
Figure I.14 Rheological behaviour or flow phenotype[115] of selected non-Newtonian fluids with shear stress as a function of shear rate; the typical Newtonian behaviour is represented in purple for comparison. Typically, dilatant and pseudoplastic fluids obey the 'power law' $\sigma = \eta_N \cdot \dot{\gamma}^n$, with η_N the zero shear (Newtonian) viscosity, $n > 1$ for a dilatant and $n < 1$ for a pseudoplastic. A Bingham body obeys $\sigma - \sigma_y = \eta \cdot \dot{\gamma}$, with σ_y the yield stress.

I.4   References

(1)   Deming, T. J. *Adv. Polym. Sci.* **2006**, *202*, 1–18.

(2)   Berg, J. M.; Tymoczko, J. L.; Stryer, L. *Biochemistry*, Sixth edit.; W. H. Freeman and Company: New York, **2007**.

(3)   Shoulders, M. D.; Raines, R. T. *Annu. Rev. Biochem.* **2009**, *78*, 929–958.

(4)   Jung, J. P.; Gasiorowski, J. Z.; Collier, J. H. *Biopolymers* **2010**, *94*, 49–59.

(5)   Hanukoglu, I.; Fuchs, E. *Cell* **1983**, *33*, 915–924.

(6)   Deming, T. J. *Prog. Polym. Sci.* **2007**, *32*, 858–875.

(7)   Schmidt, M. M.; Dornelles, R. C. P.; Mello, R. O.; Kubota, E. H.; Mazutti, M. A.; Kempka, A. P.; Demiate, I. M. *Int. Food Res. J.* **2016**, *23*, 913–922.

(8)   Krishna, O. D.; Kiick, K. L. *Biopolymers* **2010**, *94*, 32–48.

(9)   Katsoyannis, P. G. *The Chemistry of Polypeptides*; Katsoyannis, P. G., Ed.; Springer US: Boston, MA, **1973**; Vol. 1934.

(10)   Kricheldorf, H. R. *Angew. Chem. Int. Ed. Engl.* **2006**, *45*, 5752–5784.

(11)   Elmore, D. T. In *Amino Acids, Peptides and Proteins*; Royal Society of Chemistry: Cambridge, **1995**; pp 110–165.

(12)   Merrifield, R. B. *J. Am. Chem. Soc.* **1963**, *85*, 2149–2154.

(13)   O'Leary, L. E. R.; Fallas, J. A.; Bakota, E. L.; Kang, M. K.; Hartgerink, J. D. *Nat. Chem.* **2011**, *3*, 821–828.

(14)   Brulc, B.; Žagar, E.; Gadzinowski, M.; Słomkowski, S.; Žigon, M. *Macromol. Chem. Phys.* **2011**, *212*, 550–562.

(15)   Jing, P.; Rudra, J. S.; Herr, A. B.; Collier, J. H. *Biomacromolecules* **2008**, *9*, 2438–2446.

(16)   Deming, T. J. *Wiley Interdiscip. Rev. Nanomedicine Nanobiotechnology* **2014**, *6*, 283–297.

(17)   Nowak, A. P.; Breedveld, V.; Pakstis, L.; Ozbas, B.; Pine, D. J.; Pochan, D.; Deming, T. J. *Nature* **2002**, *417*, 424–428.

(18)   Popescu, M.-T.; Liontos, G.; Avgeropoulos, A.; Tsitsilianis, C. *Soft Matter* **2015**, *11*, 331–342.

(19)   Olsen, B. D.; Segalman, R. A. *Mater. Sci. Eng. R Reports* **2008**, *62*, 37–66.

(20)   Sanchez-Ferrer, A.; Mezzenga, R. *Macromolecules* **2010**, *43*, 1093–1100.

(21)   Rosales, A. M.; Segalman, R. A.; Zuckermann, R. N. *Soft Matter* **2013**, 8400–8414.

(22)   Bellomo, E. G.; Wyrsta, M. D.; Pakstis, L.; Pochan, D. J.; Deming, T. J. *Nat. Mater.* **2004**, *3*, 244–248.

(23)   Wang, J.; Liu, K.; Xing, R.; Yan, X. *Chem. Soc. Rev.* **2016**, *45*, 5589–5604.

(24)   Mai, Y.; Eisenberg, A. *Chem. Soc. Rev.* **2012**, *41*, 5969.

(25)   Gröschel, A. H.; Müller, A. H. E. *Nanoscale* **2015**, *7*, 11841–11876.

(26)   Matsumoto, A.; Chen, J.; Collette, A. L.; Kim, U.-J.; Altman, G. H.; Cebe, P.; Kaplan, D. L. *J. Phys. Chem. B* **2006**, *110*, 21630–21638.

(27)   Block, H. *Poly(gamma-benzyl-L-glutamate) and other glutamic acid containing polymers*; Gordon and Breach Science Publishers Ltd., **1983**.

(28)   Sakamoto, R. *Colloid Polym. Sci.* **1984**, *262*, 788–792.

(29)   Niehoff, A.; Mantion, A.; McAloney, R.; Huber, A.; Falkenhagen, J.; Goh, C. M.; Thünemann, A. F.; Winnik, M. A.; Menzel, H. *Colloid Polym. Sci.* **2013**, *291*, 1353–1363.

(30)   Krannig, K.-S.; Schlaad, H. *J. Am. Chem. Soc.* **2012**, *134*, 18542–18545.

(31)   Krannig, K.-S.; Sun, J.; Schlaad, H. *Biomacromolecules* **2014**, *15*, 978–984.

(32)   Huang, J.; Heise, A. *Chem. Soc. Rev.* **2013**, *42*, 7373–7390.

(33)   Huang, J.; Habraken, G.; Audouin, F.; Heise, A. *Macromolecules* **2010**, *43*, 6050–6057.

(34)   Brosnan, S. M.; Schlaad, H. *Polymer* **2014**, *55*, 5511–5516.

(35)   Leuchs, H. *Berichte der Dtsch. Chem. Gesellschaft* **1906**, *39*, 857–861.

(36)   Robinson, J. W.; Secker, C.; Weidner, S.; Schlaad, H. *Macromolecules* **2013**, *46*, 580–587.

(37)   Farthing, A. C.; Reynolds, R. J. W. *Nature* **1950**, *165*, 647–647.

(38)   Fuchs, F. *Berichte der Dtsch. Chem. Gesellschaft* **1922**, *55*, 2943–2943.

(39)   Krannig, K.-S.; Huang, J.; Heise, A.; Schlaad, H. *Polym. Chem.* **2013**, *4*, 3981–3986.

(40)   Woodward, R. B.; Schramm, C. H. *J. Am. Chem. Soc.* **1947**, *69*, 1551–1552.

(41)   Mavrogiorgis, D.; Bilalis, P.; Karatzas, A.; Skoulas, D.; Fotinogiannopoulou, G.; Iatrou, H. *Polym. Chem.* **2014**, *5*, 6256–6278.

(42)   Gibson, M. I.; Cameron, N. R. *J. Polym. Sci. Part A Polym. Chem.* **2009**, *47*, 2882–2891.

(43)   Zhao, W.; Gnanou, Y.; Hadjichristidis, N. *Biomacromolecules* **2015**, *16*, 1352–1357.

(44)   Zhang, X.; Oddon, M.; Giani, O.; Monge, S.; Robin, J.-J. *Macromolecules* **2010**, *43*, 2654–2656.

(45)   Ballard, D. G. H.; Bamford, C. H. *J. Chem. Soc.* **1956**, 381–387.

(46)   Szwarc, M. *Fortschritte der Hochpolymeren-Forschung*; Advances in Polymer Science; Springer-Verlag: Berlin/Heidelberg, **1965**; Vol. 4/1.

(47)   Kricheldorf, H. R.; Chemie, M. **1979**, *109*, 97–109.

(48)   Markland, P.; Amidon, G. L.; Yang, V. C. *Int. J. Pharm.* **1999**, *178*, 183–192.

(49)   Menzel, H.; Hallensleben, M. L. *Polym. Bull.* **1991**, *27*, 89–94.

(50)   Zhao, C.; He, P.; Xiao, C.; Gao, X.; Zhuang, X.; Chen, X. *J. Appl. Polym. Sci.* **2012**, *123*, 2923–2932.

(51)   Yang, Z.; Zhang, Y.; Markland, P.; Yang, V. C. *J. Biomed. Mater. Res.* **2002**, *62*, 14–21.

(52)   Aliferis, T.; Iatrou, H.; Hadjichristidis, N. *Biomacromolecules* **2004**, *5*, 1653–1656.

(53)   Vayaboury, W.; Giani, O.; Cottet, H.; Deratani, A.; Schué, F. *Macromol. Rapid Commun.* **2004**, *25*, 1221–1224.

(54)   Habraken, G. J. M.; Wilsens, K. H. R. M.; Koning, C. E.; Heise, A. *Polym. Chem.* **2011**, *2*, 1322.

(55)   Kricheldorf, H. R. *α-Aminoacid-N-Carboxyanhydrides and Related Materials*; Springer Berlin Heidelberg, **1987**.

(56)   Kricheldorf, H. R.; von Lossow, C.; Schwarz, G. *Macromolecules* **2005**, *38*, 5513–5518.

(57)   Kricheldorf, H. R.; Lossow, C. V.; Schwarz, G. *Macromol. Chem. Phys.* **2005**, *206*, 282–290.

(58)   Kricheldorf, H. R. In *Alpha-Aminoacid-N-Carboxy-Anhydrides and Related Heterocycles*; Springer Berlin Heidelberg, **1987**; pp 16–21.

(59)   Deming, T. J. *Nature* **1997**, *390*, 386–389.

(60)   Lu, H.; Cheng, J. *J. Am. Chem. Soc.* **2008**, *130*, 12562–12563.

(61)   Lu, H.; Cheng, J. *J. Am. Chem. Soc.* **2007**, *129*, 14114–14115.

(62)   Dimitrov, I.; Schlaad, H. *Chem. Commun.* **2003**, No. 23, 2944–2945.

(63)   Lutz, J.-F.; Schütt, D.; Kubowicz, S. *Macromol. Rapid Commun.* **2005**, *26*, 23–28.

(64)   Tang, H.; Zhang, D. *J. Polym. Sci. Part A Polym. Chem.* **2013**, *51*, 4489–4497.

(65)   Brulc, B.; Žagar, E.; Gadzinowski, M.; Słomkowski, S.; Žigon, M. *Macromol. Chem. Phys.* **2011**, *212*, 550–562.

(66)   Meyer, M.; Schlaad, H. *Macromolecules* **2006**, *39*, 3967–3970.

(67)   Conejos-Sánchez, I.; Duro-Castano, A.; Birke, A.; Barz, M.; Vicent, M. J. *Polym. Chem.* **2013**, *4*, 3182–3186.

(68)   Roach, C. A.; Simpson, J. V; JiJi, R. D. *Analyst* **2012**, *137*, 555–562.

(69)   Zayed, J. M.; Nouvel, N.; Rauwald, U.; Scherman, O. A. *Chem. Soc. Rev.* **2010**, *39*, 2806–2816.

(70)   Fichman, G.; Gazit, E. *Acta Biomater.* **2014**, *10*, 1671–1682.

(71)   Ramachandran, G. N.; Ramakrishnan, C.; Sasisekharan, V. *J. Mol. Biol.* **1963**, *7*, 95–99.

(72)   Mikhonin, A. V.; Bykov, S. V.; Myshakina, N. S.; Asher, S. A. *J. Phys. Chem. B* **2006**, *110*, 1928–1943.

(73)   Fratzl, P. In *Collagen*; Fratzl, P., Ed.; Springer US: Boston, MA, **2008**; pp 1–13.

(74)   Okuyama, K.; Miyama, K.; Mizuno, K.; Bächinger, H. P. *Biopolymers* **2012**, *97*, 607–616.

(75)   Ramshaw, J. A. M.; Shah, N. K.; Brodsky, B. *J. Struct. Biol.* **1998**, *122*, 86–91.

(76)   Dill, K. A. *Biochemistry* **1990**, *29*, 7133–7155.

(77)   Kadler, E.; Prockops, J. *J. Biol. Chem.* **1987**, *260*, 15696–15701.

(78)   Yannas, I. V. In *Biomaterials Science - An Introduction to Materials in Medecine*; Elsevier, **2004**; pp 127–128.

(79)   Eyre, D. R.; Weis, M. A.; Wu, J. *Methods* **2008**, *45*, 65–74.

(80)   Moreno-Arotzena, O.; Meier, J.; del Amo, C.; García-Aznar, J. *Materials (Basel).* **2015**, *8*, 1636–1651.

(81)   Lutz, J.-F.; Ouchi, M.; Liu, D. R.; Sawamoto, M. *Science* **2013**, *341*, 1238149-1–8.

(82)   Goodman, M.; Bhumralkar, M.; Jefferson, E. A.; Kwak, J.; Locardi, E. *Biopolymers* **1998**, *47*, 127–142.

(83)   Rele, S.; Song, Y.; Apkarian, R. P.; Qu, Z.; Conticello, V. P.; Chaikof, E. L. *J. Am. Chem. Soc.* **2007**, *129*, 14780–14787.

(84)   Estroff, L. A.; Hamilton, A. D. *Chem. Rev.* **2004**, *104*, 1201–1218.

(85)   Appel, E. A.; del Barrio, J.; Loh, X. J.; Scherman, O. A. *Chem. Soc. Rev.* **2012**, *41*, 6195–6214.

(86)   Hartgerink, J. D.; Beniash, E.; Stupp, S. I. *Science* **2001**, *294*, 1684–1688.

(87)   Fielding, L. A.; Lane, J. A.; Derry, M. J.; Mykhaylyk, O. O.; Armes, S. P. *J. Am. Chem. Soc.* **2014**, *136*, 5790–5798.

(88)   Brosnan, S. M.; Schlaad, H.; Antonietti, M. *Angew. Chem. Int. Ed. Engl.* **2015**, *54*, 9715–9718.

(89)   Song, B.; Song, J.; Zhang, S.; Anderson, M. A.; Ao, Y.; Yang, C.-Y.; Deming, T. J.; Sofroniew, M. V. *Biomaterials* **2012**, *33*, 9105–9116.

(90)   Breedveld, V.; Nowak, A. P.; Sato, J.; Deming, T. J.; Pine, D. J. *Macromolecules* **2004**, *37*, 3943–3953.

(91)   Fleming, S.; Ulijn, R. V. *Chem. Soc. Rev.* **2014**, *43*, 8150–8177.

(92)   Celis, S.; Nolis, P.; Illa, O.; Branchadell, V.; Ortuño, R. M. *Org. Biomol. Chem.* **2013**, *11*, 2839–2846.

(93)   Shirbin, S. J.; Karimi, F.; Chan, N. J.-A.; Heath, D. E.; Qiao, G. G. *Biomacromolecules* **2016**, *17*, 2981–2991.

(94)   Miyachi, Y.; Joke, K.; Oka, M.; Hayashi, T. *J. Biomater. Sci. Polym. Ed.* **1996**, *7*, 805–816.

(95)   Yu, L.; Fu, W.; Li, Z. *Soft Matter* **2015**, *11*, 545–550.

(96)   Maude, S.; Ingham, E.; Aggeli, A. *Nanomedicine* **2013**, *8*, 823–847.

(97)   Ryan, D. M.; Doran, T. M.; Nilsson, B. L. *Chem. Commun.* **2011**, *47*, 475–477.

(98)   Papadopoulos, P.; Floudas, G.; Klok, H.; Schnell, I.; Pakula, T. *Biomacromolecules* **2004**, *5*, 81–91.

(99)   Tipton, D. L.; Russo, P. S. *Macromolecules* **1996**, *29*, 7402–7411.

(100)   Kumar, C. S. S. R. *X-ray and Neutron Techniques for Nanomaterials Characterization*; **2016**.

(101)   Aboratory, S. P. L. In *X-Ray Scattering of Soft Matter*; Springer Berlin Heidelberg: Berlin, Heidelberg; pp 95–190.

(102)   Förster, S.; Timmann, A.; Schellbach, C.; Frömsdorf, A.; Kornowski, A.; Weller, H.; Roth, S. V; Lindner,

P. *Nat. Mater.* **2007**, *6*, 888–893.

(103) Guo, H.; Zhang, Y.; Xue, F.; Cai, Z.; Shang, Y.; Li, J.; Chen, Y.; Wu, Z.; Jiang, S. *CrystEngComm* **2013**, *15*, 1597–1606.

(104) Cai, Z.; Zhang, Y.; Li, J.; Xue, F.; Shang, Y.; He, X.; Feng, J.; Wu, Z.; Jiang, S. *Polymer* **2012**, *53*, 1593–1601.

(105) Nozue, Y.; Shinohara, Y.; Amemiya, Y. *Polym. J.* **2007**, *39*, 1221–1237.

(106) Kasai, N.; Kakudo, M.; Kasai, N.; Eroglu S., Toprak S., Urgan O, MD, Ozge E. Onur, MD, Arzu Denizbasi, MD, Haldun Akoglu, MD, Cigdem Ozpolat, MD, Ebru Akoglu, M. *X-ray diffraction by macromolecules*; **2005**; Vol. 33.

(107) Sobieraj, M. C.; Kurtz, S. M.; Rimnac, C. M. *Biomaterials* **2005**, *26*, 6430–6439.

(108) Worku, Z. A.; Aarts, J.; Van Den Mooter, G. *Mol. Pharm.* **2014**, *11*, 1102–1108.

(109) Babin Taton, D., Brinkman, M., Lecommandoux, S., J. *Macromolecules* **2008**, *41*, 1384–1392.

(110) Scherrer, P. *Nachrichten von der Gesellschaft der Wissenschaften zu Göttingen, Math. Klasse 2*, 98–100.

(111) Kiefer, W.; Laane, J. In *Analytical Applications of FT-IR to Molecular and Biological Systems*; Durig, J. R., Ed.; Springer Netherlands: Dordrecht, **1980**; Vol. 57, pp 537–577.

(112) *Handbook of Vibrational Spectroscopy*; Chalmers, J., Griffiths, P. R., Eds.; Wiley, **2001**.

(113) Ferry, J. D. In *Viscoelastic Properties of Polymers*; Wiley, **1980**; pp 1–30.

(114) Winkler, D.; Wilson, N. In *Rheology for Chemists*; Royal Society of Chemistry: Cambridge, **2015**; pp 1–13.

(115) Lenk, R. S. *Polymer Rheology*; Springer Netherlands: Dordrecht, **1978**.

(116) Janmey, P. A.; Schliwa, M. *Curr. Biol.* **2008**, *18*, R639–R641.

Chapter II

Synthesis and Characterisation of Polypeptides

II.1   Introduction

Poly(γ-benzyl-L-glutamate) (PBLG) is a well-known polypeptide, which, because of its rigid α-helical conformation, has been extensively studied as a model rod-like polymer.[1–3] Thanks to this well-defined secondary structure, PBLG has the ability to self-assemble into both fibrous physical gels and liquid crystalline phases.[4,5] The self-assembly of block copolypeptides has also been under extensive investigation in recent years,[6] and PBLG- and Poly(L-glutamate) (PLG) have been popular choices for blocks.[7–10] The self-assembly of statistical copolypeptides has been in comparison far less investigated.[11,12]

As mentioned in Chapter I, a main objective of this doctoral work is to investigate the self-assembly of statistical, and more specifically random, copolypeptides, with a view to producing novel bio-inspired materials. For that purpose, several series of copolypeptides of BLG and allylglycine (AG) with various compositions, lengths, and end groups were synthesised. The main focus was on statistical copolypeptides with linear architectures, but star architectures were also investigated. The traditional primary-amine initiated ring opening polymerisation (ROP) of α-amino acid *N*-carboxyanhydrides (NCA) and the novel primary ammonium-tertiary amine-mediated ROP of NCA (reported in Chapter III) were used to synthesise well-defined polypeptides.

It is important at that stage to distinguish between statistical and random copolymers. Although the terms are often used interchangeably, the random distribution is a special case of the statistical distribution. IUPAC defines a statistical copolymer as a macromolecule in which the sequential distribution of the monomeric units obeys known statistical laws (*e.g.*, Markovian statistics). In contrast, it defines a random copolymer as macromolecule in which the probability of finding a given monomeric unit at any given site in the chain is independent of the nature of the adjacent units (*i.e.*, true randomness). Therefore, when mixtures of monomers are polymerised together, the appropriate qualifier for the resulting

copolymers is 'statistical'. In order for a statistical copolymer to be called 'random', the random distribution has to be proven, for instance by calculating the reactivity ratios ($r_1 = r_2 = 1$ for true randomness, according to the Mayo-Lewis equation) and monitoring the growing chain composition.

Few studies have demonstrated the randomness of the statistical copolypeptides they synthesised. Huang et al. proved that statistical copolymers of BLG and DL-propargylglycine were random using MALDI-TOF.[11] More generally, NCA monomers are assumed to have similar reactivities hence ensuring a random-like distribution, and the resulting polypeptides are generally referred to as 'statistical'.[13,14] However, in practice, not all NCAs have the same reactivity.[15] For instance, as reported in Chapter III, L-phenylalanine NCA (LPhe-NCA) appears to be more reactive than BLG-NCA under the same polymerisation conditions. In this chapter, the study performed to establish the random distribution of a set of polypeptides, representative of the P(BLG-co-AG) series used in this doctoral work, is described. In addition, a selection of relevant analytical results are reported in order to present the typical methodology used in the present work to reliably determine compositions, chain lengths and end groups.

II.2 Experimental

II.2.1 Materials

The NCAs and initiators used for this study are gathered in Figure II.1. Other chemicals and solvents are listed in Appendix A. The synthesis of NCAs and statistical copolypeptides of γ-benzyl-L-glutamate (BLG) and allylglycine (AG), referred to as P(BLG$_x$-co-AG$_{1-x}$)$_n$ hereafter, as well as the procedure to debenzylate the BLG moieties to yield P(LG$_x$-co-AG$_{1-x}$)$_n$, are described in Appendix A.
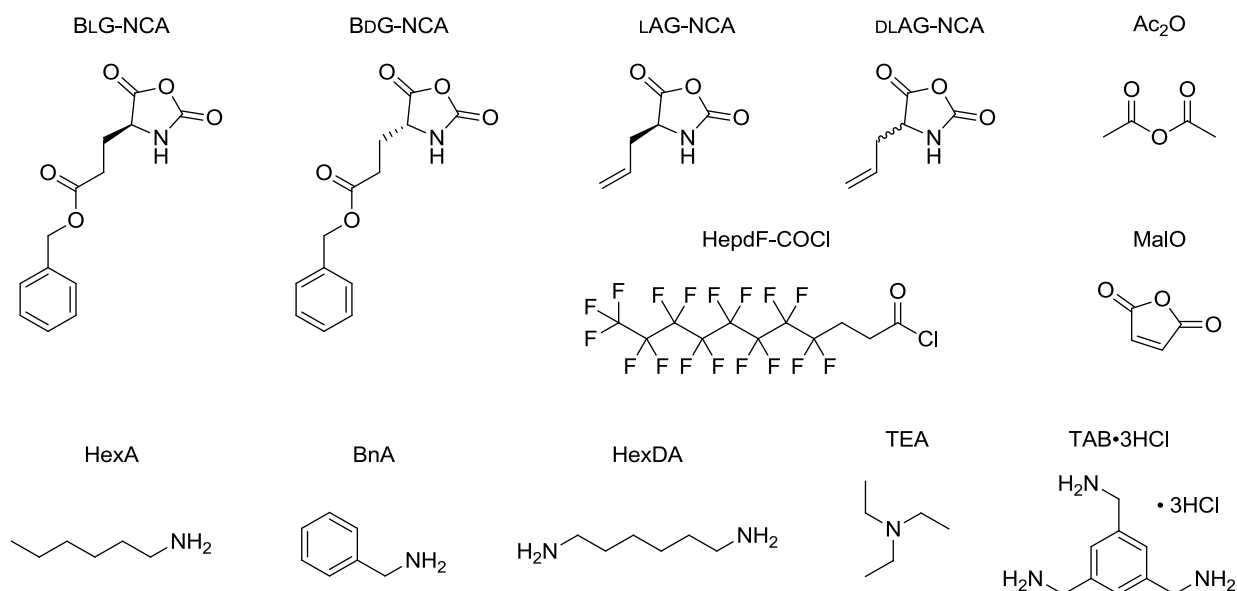
Figure II.1 List of NCAs, initiators and terminating agents discussed in this study: from left to right and top to down γ-benzyl-L-glutamate (BLG), γ-benzyl-D-glutamate (BDG), L-allyglycine (LAG), DL-allyglycine (DLAG), acetic anhydride (Ac$_2$O), heptadecafluoroundecanoyl chloride (HepdF-COCl), maleic anhydride (MalO), hexylamine (HexA), benzylamine (BnA), hexamethylene diamine (HexDA), 1-pyrenemethanol (PyOH), triethylamine (TEA), 1,2,3-tris(aminomethyl)benzene trihydrochloride (TAB·3HCl).

II.2.2 Methods

II.2.2.1 Copolymerisation Followed by ^{1}H-NMR

The ratio of BLG to AG repeat units was measured throughout the polymerisation reaction of different P(BLG$_x$-co-AG$_{1-x}$)$_n$ copolypeptides. For each reaction, samples were taken out at regular intervals, terminated by Ac$_2$O or MalO, precipitated and washed in methanol and diethyl ether, dried and finally measured by ^{1}H-NMR in TFA-d.

See Appendix A for all other analytical methods used here (i.e., NMR and SEC).

II.3 Results and Discussion

II.3.1 Polypeptide Compositions and End Groups Analysis

The polypeptides used in Chapter IV, V and VI were initiated by HexA and terminated by Ac$_2$O (Figure II.1 and II.2). Typical ^{1}H-NMR curves are displayed and analysed in Figure II.2 and II.3. An advantage of using HexA as an initiator is the large number of protons, hence peaks, corresponding to the hexyl α-end of the polypeptide, which helps to accurately determine the chain length (*n*). In comparison, for polypeptides initiated by BnA or TAB·3HCl, the ^{1}H-NMR peaks assigned to the α-end group are far smaller or hidden by the large benzyl peak from the BLG side chains. As a terminating agent with distinct proton shifts, MalO was therefore used to help to determine *n* with a greater degree of confidence (Figure II.4 and II.5). In addition, the resulting ω-end group (fumaric acid) can be functionalised by thiol-Michael addition.[16–19]
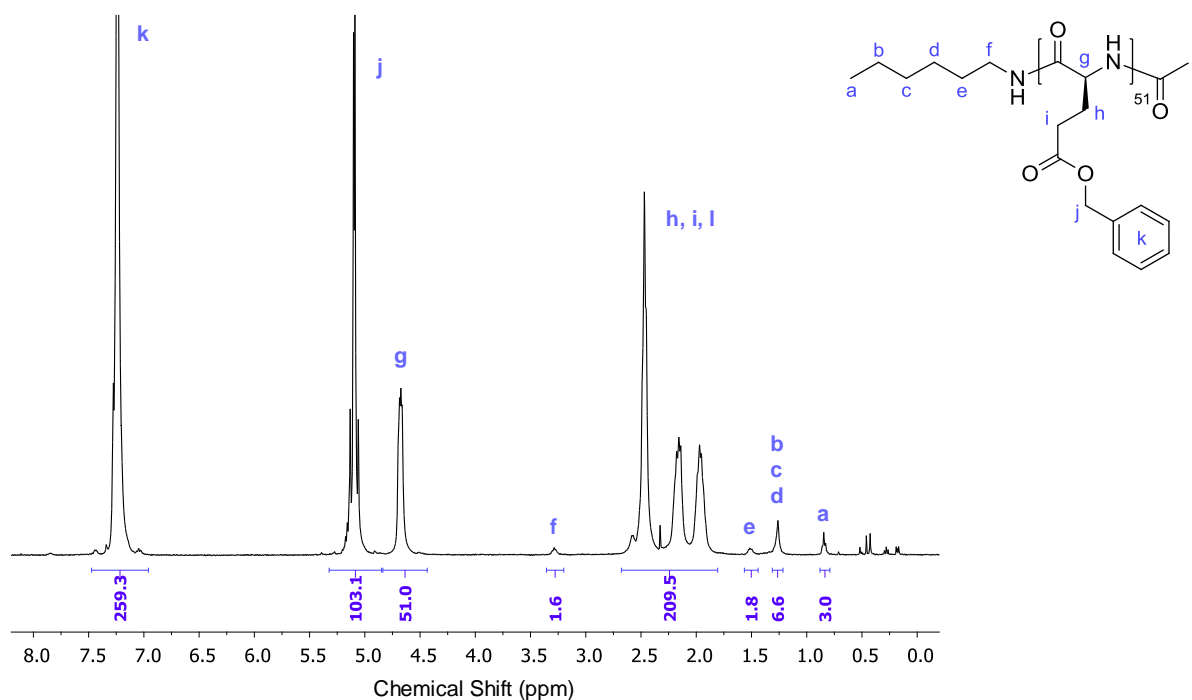
Figure II.2 ^{1}H-NMR spectrum (TFA-d, 400 MHz) of PBLG$_{51}$, initiated by HexA and terminated by Ac$_2$O after 5 days; the non-assigned peaks between 0 and 0.5 ppm correspond to silicone grease (Appendix B, P1).
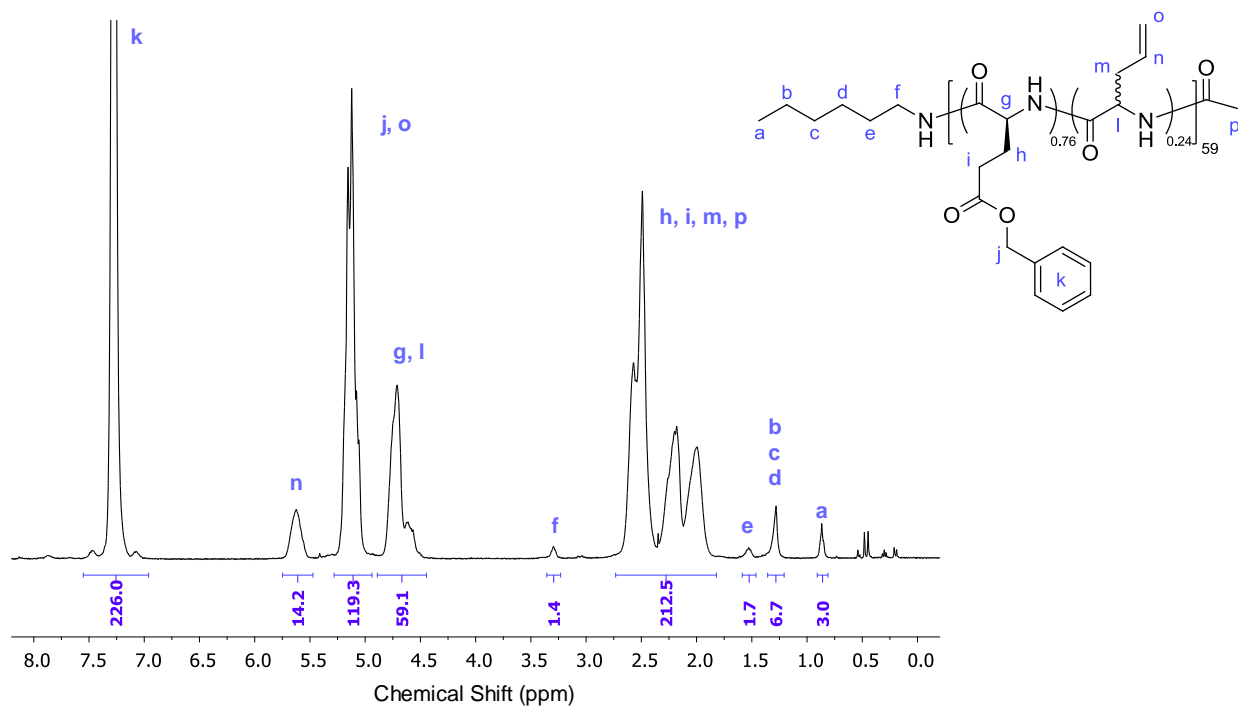
Figure II.3 ^{1}H-NMR spectrum (TFA-d, 400 MHz) of P(BLG$_{0.76}$-*co*-DLAG$_{0.24}$)$_{59}$, initiated by HexA and terminated by Ac$_2$O after 5 days; the non-assigned peaks between 0 and 0.5 ppm correspond to silicone grease (Appendix B, P2).
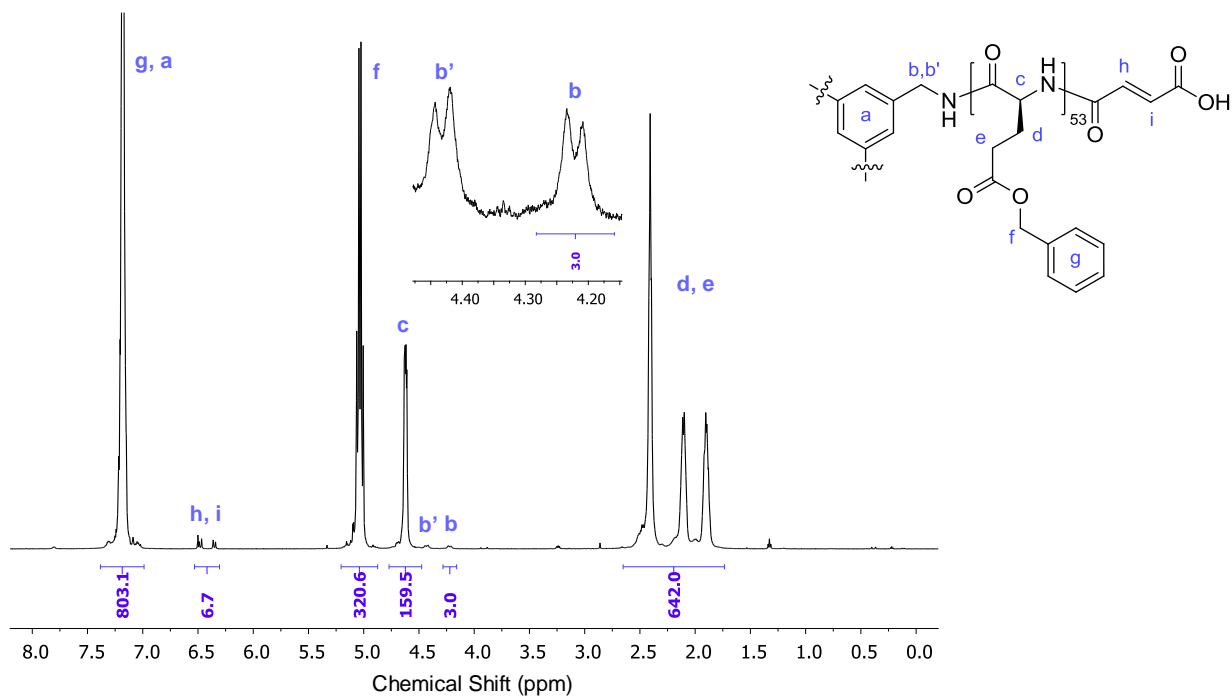
Figure II.4 ^{1}H-NMR spectrum (TFA-d, 600 MHz) of *star*-P(BLG$_{53}$)$_3$ initiated by TAB·3HCl/TEA (1:0.5 equiv. for 150 BLG-NCA equiv., DMF, rt) and terminated by MalO after 7 days; the final *n* of 160 was very close to the targeted *n* of 150; the non-assigned peaks at 1.3 and 3.2 ppm correspond to residual diethyl ether (Appendix B, P26).
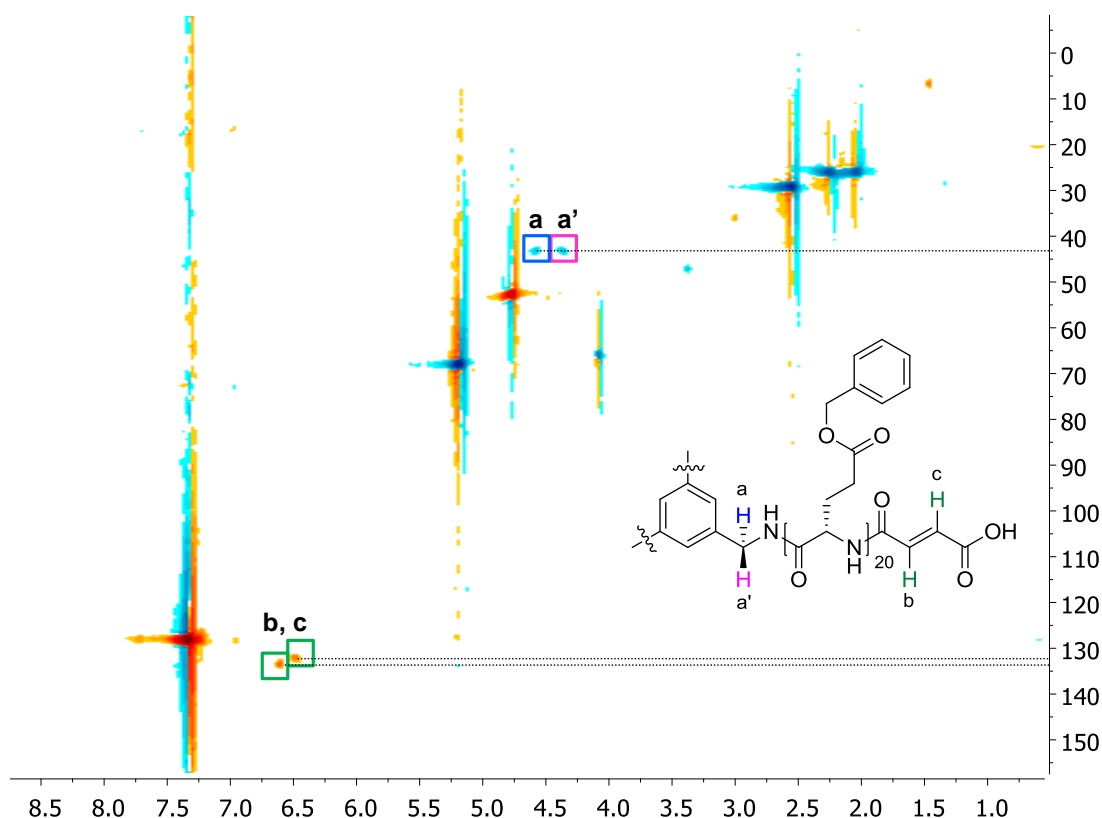
Figure II.5 Typical HSQC-NMR spectrum (x axis: ^{1}H chemical shift (ppm), y axis: ^{13}C chemical shift (ppm) of *star*-P(B$_L$G$_{20}$)$_3$ in TFA-d; the circled spots correspond to the colour-coded protons of the displayed polymer molecule (Appendix B, P33).

In order to confirm the assignment of the end group peaks, a series of polypeptides initiated by TAB·3HCl and terminated either by MalO and Ac$_2$O was investigated (Appendix B, P49 to P52, and P49-D to P52-D, Appendix A for chemical shifts). The polypeptides were analysed before and after the debenzylation of the B$_L$G unit, and following a dialysis against THF and H$_2$O, respectively. Both the α- and ω-end groups were successfully identified and assigned as shown in Figure II.4 and II5.

As described in Chapter I and III, primary-amine and primary-ammonium/tertiary amine-mediated ROP of NCA are controlled. This suggests that the chain growth of most polypeptides synthesised for this doctoral work proceeded *via* the normal amine mechanism (NAM) mainly. In practice, when the composition and n calculated from ^{1}H-NMR spectra match the initial monomer feed ratio and the targeted n, respectively, the polymerisation is generally considered controlled. However, since the activated monomer mechanism (AMM) yields polypeptides with *N*-acylated NCA (*i.e.*, *N*-acyl NCA) α-end groups, which cannot be detected by ^{1}H-NMR (Figure II.6), the characterisation of all polymers was complemented by an SEC analysis. From SEC traces, a unimodal and narrow distribution (*i.e.*, Đ < 1.3) and an apparent M$_n$ close to the M$_n$ calculated by ^{1}H-NMR, served to confirm the controlled nature of the polymerisation and validate the data (*e.g.*, composition and n) obtained from the ^{1}H-NMR spectra (Figure II.7).
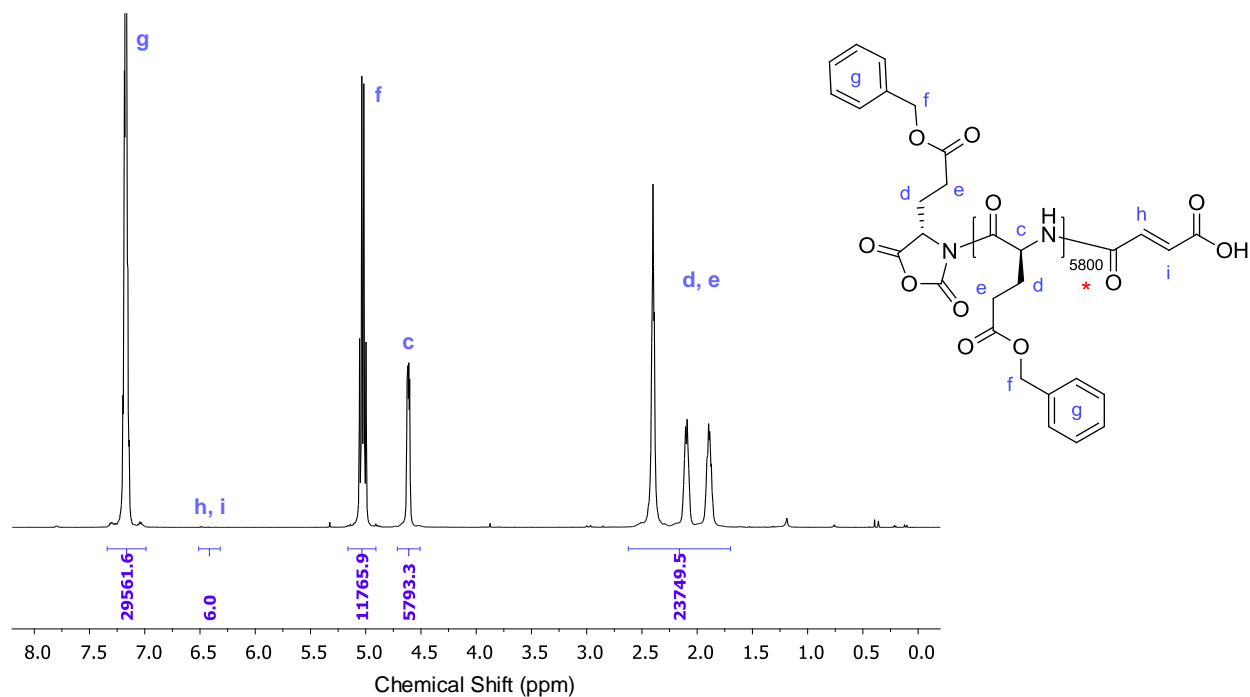
Figure II.6 ^{1}H-NMR spectrum (TFA-d, 600 MHz) of linear PBLG$_{5800*}$ catalysed by TEA (0.5 equiv. for 150 BLG-NCA equiv., DMF, rt) and terminated by MalO after 7 days; * the value for *n* should be regarded as an estimation as ^{1}H-NMR is unfit for the characterisation of large molar masses due to the low signal to noise ratio of the end groups at such low concentrations, in addition the molar mass distribution was broad (Đ > 1.8) (Appendix B, P27).
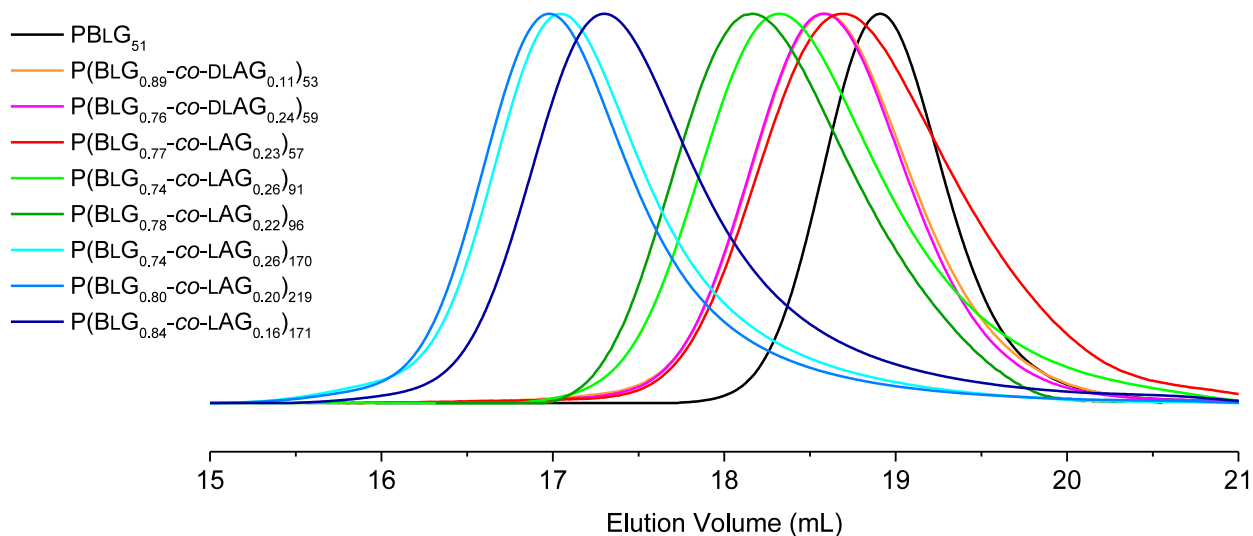
Figure II.7 Typical SEC (NMP, PMMA calibration) traces of P(BLG$_x$-*co*-AG$_{1-x}$)$_n$ polypeptides synthesised by controlled ROP of NCA; they are monomodal, Đ < 1.3 and their apparent M$_n$ are in line with those calculated from ^{1}H-NMR data (Appendix B, P1 to P4 and P12 to P16).

II.3.2   Copolymerisation

The final compositions of most P(BLG$_x$-*co*-AG$_{1-x}$)$_n$ copolypeptides were in good agreement with their monomer feed ratios and their final molar mass distributions were unimodal and narrow (Appendix B) (Figure II.7). Although this is a good indication of random distribution of the monomeric units within the polypeptide chains, this does not constitute absolute proof. True randomness also implies that the growing

chain composition is the same as the monomer feed ratio at all times throughout the chain growth. ^{1}H-NMR was used to monitor a series of copolymerisations of BLG- and AG-NCAs (Figure II.8). It showed that the BLG/AG molar ratio remained approximately constant and equal to the monomer feed ratio throughout the entire polymerisation. This indicates that the BLG and AG units are most likely randomly distributed within each polymer chain, and that the latter are hence not block or alternating copolymers. As such, all P(BLG$_x$-*co*-AG$_{1-x}$)$_n$ copolypeptides synthesised and studied in Chapter IV, V and VI, are most likely random copolypeptides. However, it has to be stressed that the dispersity being slightly broader for P(BLG$_x$-*co*-AG$_{1-x}$)$_n$ copolypeptides than for PBLG$_n$ homopolypeptides (Figure II.7), it cannot be excluded that the distribution of the monomeric units obeys a statistical law that slightly differs from true randomness. Regardless of the inherent statistical law regulating the distribution, based on the results obtained (Figure II.8), P(BLG$_x$-*co*-AG$_{1-x}$)$_n$ copolypeptides initiated by primary amines can be considered to be random-like.
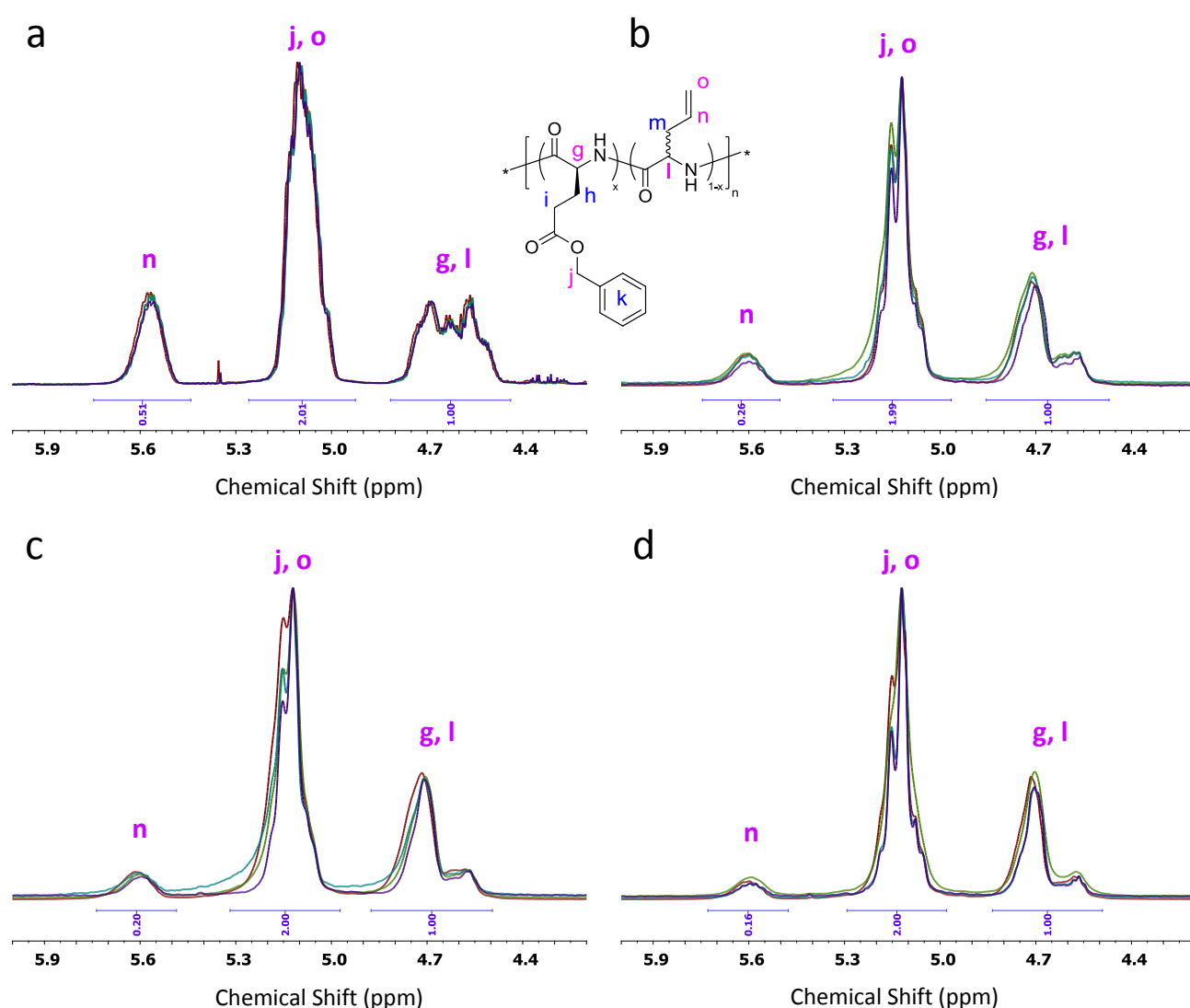
Figure II.8 [4.2 - 6 ppm] sections of ^{1}H-NMR spectra (TFA-d; 400 MHz for b, c, and d, and 600 MHz for a) corresponding to polymer samples taken during the polymerisation of (a) *"star"*-P((BLG$_{0.50}$-*co*-LAG$_{0.50}$)$_{73}$)$_2$, (b) P(BLG$_{0.74}$-*co*-LAG$_{0.26}$)$_{170}$, (c) P(BLG$_{0.80}$-*co*-LAG$_{0.20}$)$_{219}$, and (d) P(BLG$_{0.84}$-*co*-LAG$_{0.16}$)$_{171}$ (Appendix B, P40, P12, P13, and P14, respectively). Samples were collected at (a) (violet) 10 h, (blue) 24 h, (green) 32 h and (red) after termination; (b, c, d) (violet) 24 h, (blue) 48 h, (green) 72 h and (red) after termination; the samples were worked up as described in Section II.2.2.1; the spectra were normalised to the 5.0-5.3 ppm peak.

II.3.3 Post Polymerisation Modifications

One of the long term objectives of this doctoral work is to produce polypeptide-based materials for biomedical purposes. The debenzylation of the carboxylic ester functional group of the BLG side chains, therefore, represents an essential step towards that goal. The procedures are detailed in Appendix A and consist of the hydrolysis the carboxylic ester functional group in strong acidic conditions. Typical ^{1}H-NMR spectra of debenzylated polypeptides are displayed in Figure II.9 and II.10.
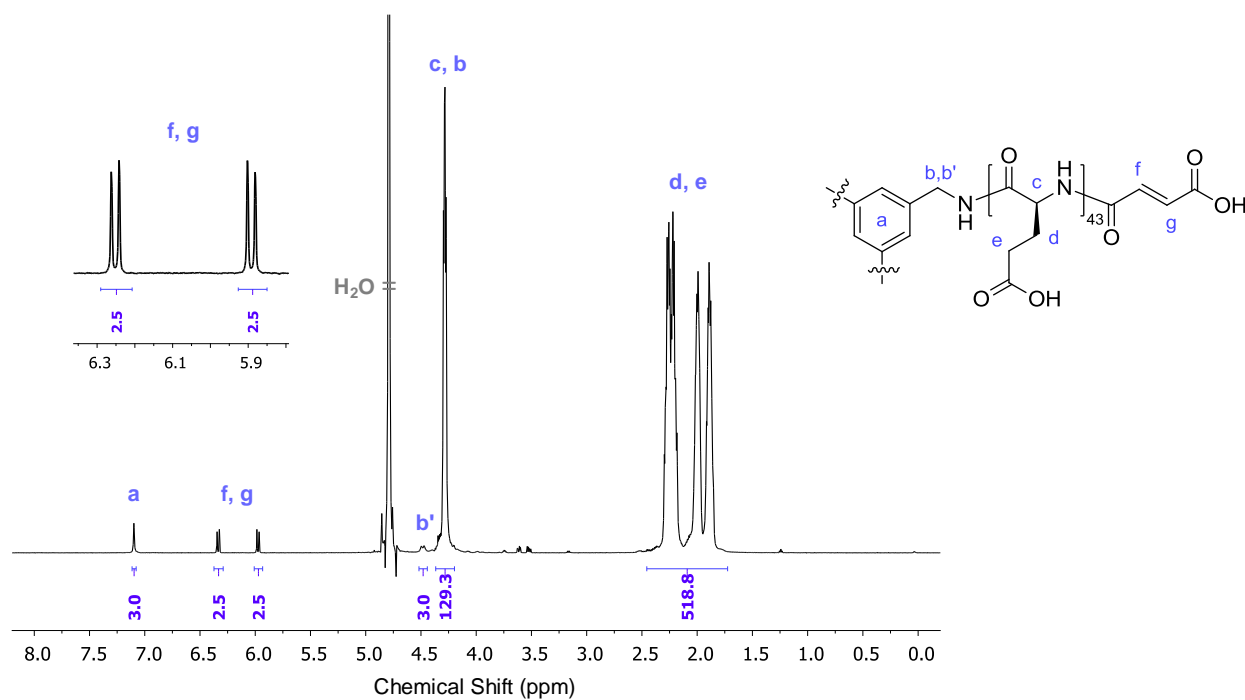
Figure II.9 ^{1}H-NMR spectrum (D$_2$O, 600 MHz) of (a) *star*-P(LG$_{43}$)$_3$, following the debenzylation of *star*-P(BLG$_{42}$)$_3$, initiated by TAB·3HCl/TEA (1:0.5 equiv. for 150 BLG-NCA equiv., DMF, rt) and terminated by MalO after 5 days (Appendix B, P49-D);
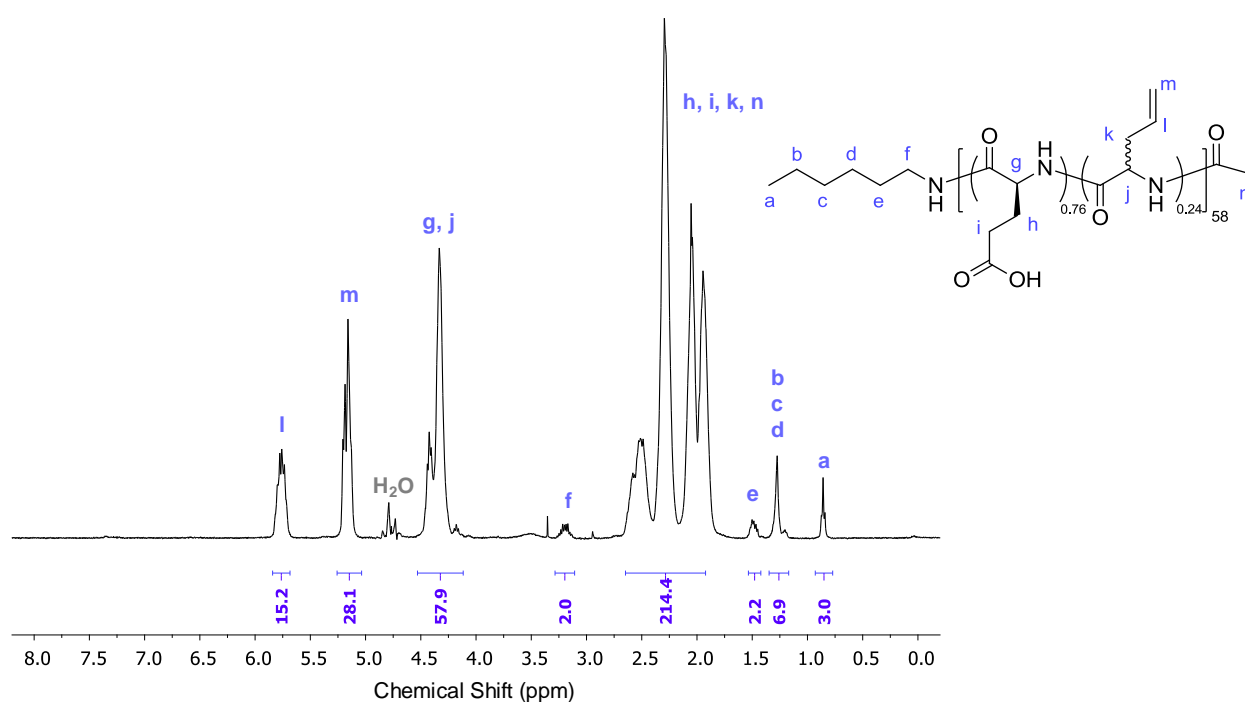
Figure II.10 ^{1}H-NMR spectrum (D$_2$O, 400 MHz, water suppression) of P(LG$_{0.76}$-*co*-DLAG$_{0.24}$)$_{58}$ following the debenzylation of P(BLG$_{0.76}$-*co*-DLAG$_{0.24}$)$_{59}$, initiated by HexA and terminated by Ac$_2$O after 5 days (Figure II.3) (Appendix B, P2-D).

It is worth noting that the chain length of the debenzylated polypeptides may vary slightly from their polypeptide precursors. This could be explained by the dialysis step, which is likely to cause some loss of the smaller chain fractions. For copolypeptides, the resulting composition (*i.e.,* BLG to AG molar fractions) remains constant, within the precision limits of the NMR measurement method.

II.3.4 Other Architectures

When initiating polymerisations with a difunctional initiator, the α-end group is at the centre of two growing chains, which once terminated yield symmetrical linear polymers with two identical ω-end groups. This type of polymer architecture is a two-armed star and the resulting polypeptides were noted *"star"*-(P(BLG$_x$-*co*-AG$_{1-x}$)$_n$)$_2$. The difunctional initiator used in this study was HexDA, and a typical ^{1}H-NMR spectrum is displayed in Figure II.11.
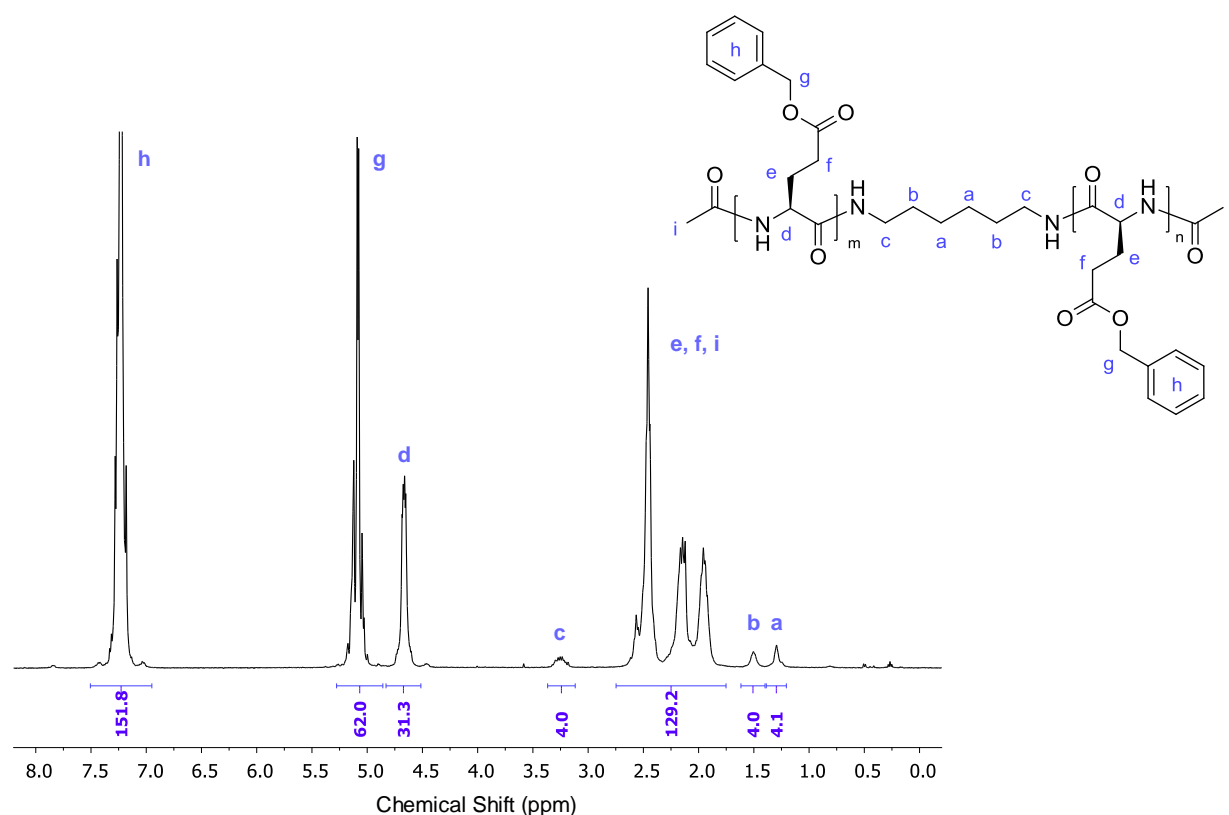
Figure II.11 ^{1}H-NMR spectrum (TFA-d, 400 MHz) of *"star"*-P(BLG$_{15}$)$_2$ initiated by HexDA and terminated by Ac$_2$O after 3 days (Appendix B, P18B).

This technique is particularly useful for the preparation of telechelic polypeptides or simply when both ends require the same functionality. For instance, fluorinated acyl chloride species can be used as terminating agents to end-cap polypeptides with hydrophobic moieties, with a view to preparing flower micelles-derived physical gels for instance.[20–22] A typical ^{19}F-NMR spectrum of a *"star"* PBLG$_n$ terminated by HepdF-COCl is displayed in Figure II.12.

The two- and three-armed star architecture was selected for two polypeptides, *star*-(PBLG$_{20}$)$_3$ and *"star"*-(P(BLG$_{0.50}$-*co*-LAG$_{0.50}$)$_{73}$)$_2$, studied in Chapter IV. The arms in *star*-(PBLG$_{20}$)$_3$ were chosen purposely short in order to study the effect of short chains on the polypeptide conformation. Free small chains are

challenging to work up and recover, however, the same chains as the arms of a star polymer can be more effectively recovered. As for *"star"*-(P(BLG$_{0.50}$-*co*-LAG$_{0.50}$)$_{73}$)$_2$, its polymerisation was followed in the context of the copolymerisation study reported in Section II.3.2. A difunctional initiator was, therefore, selected in order to maximise the recovery of the polymer at low conversions.
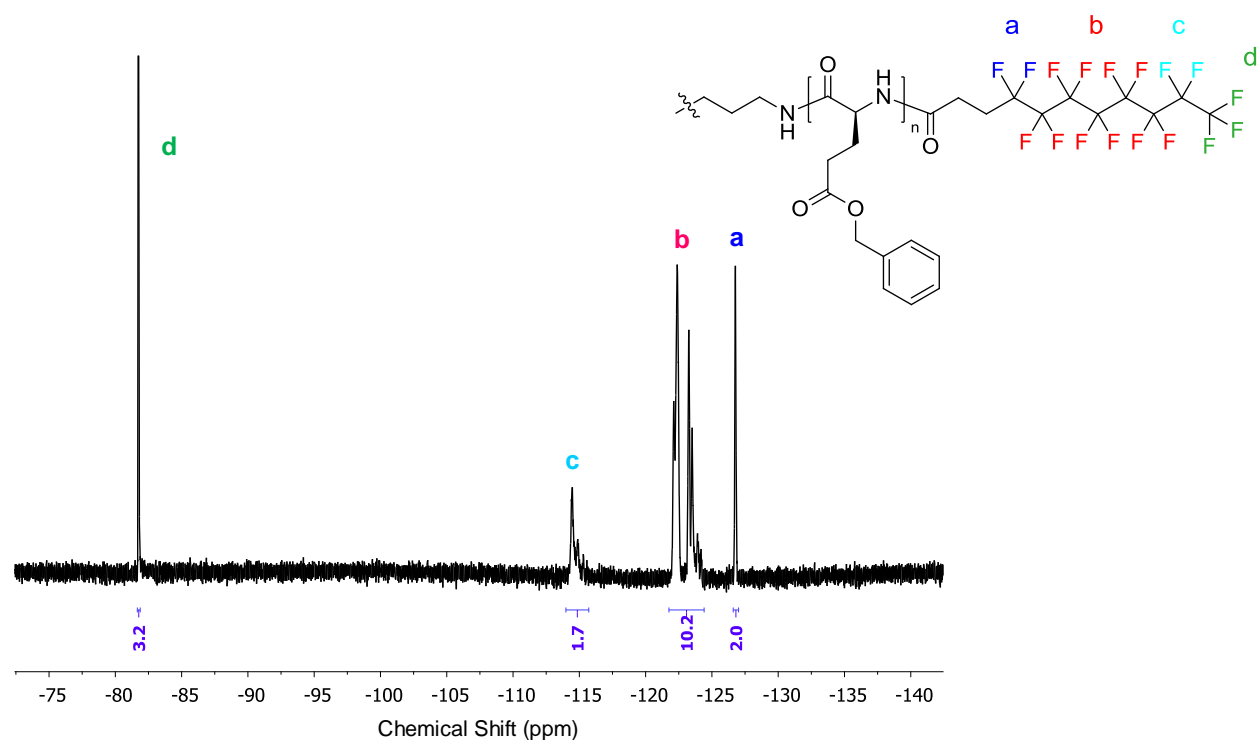
Figure II.12 ^{19}F-NMR spectrum (THF-d$_8$, 376 MHz) of *"star"*-P(BLG$_{15}$)$_2$ initiated by HexDA and terminated by HepdF-COCl after 3 days (Appendix B, P18A).

II.4   Conclusions

It was shown that a variety of P(BLG$_x$-*co*-AG$_{1-x}$)$_n$ copolypeptides, with different α- and ω-end groups, compositions and architectures could be synthesised with good precision and control by both the traditional ROP of NCA and the novel primary ammonium-tertiary amine-mediated ROP of NCA (reported in Chapter III). In addition, the typical methodology used to reliably determine the composition, architecture and chain length of said polypeptides was detailed.

Finally, it was demonstrated that the distribution of BLG and AG units in P(BLG$_x$-*co*-AG$_{1-x}$)$_n$ copolypeptides, synthesised and used in this doctoral work, was random-like. However, since true randomness requires the demonstration that the reactivity ratios for a set of comonomers are equal to 1 (*i.e.*, $r_1 = r_2 = 1$), and since not all polypeptides were tested, P(BLG$_x$-*co*-AG$_{1-x}$)$_n$ are referred to as statistical copolymers in the rest of this dissertation in order to comply with the definitions.

II.5   References

(1)   Block, H. *Poly(gamma-benzyl-L-glutamate) and other glutamic acid containing polymers*; Gordon and Breach Science Publishers Ltd., **1983**.

(2)   Flory, P. J. *Proc. R. Soc. London. Ser. A. Math. Phys. Sci.* **1956**, *234*, 73–89.

(3)   Kim, K. T.; Park, C.; Vandermeulen, G. W. M.; Rider, D. A.; Kim, C.; Winnik, M. A.; Manners, I. *Angew. Chem. Int. Ed.* **2005**, *44*, 7964–7968.

(4)   Papadopoulos, P.; Floudas, G.; Klok, H.; Schnell, I.; Pakula, T. *Biomacromolecules* **2004**, *5*, 81–91.

(5)   Niehoff, A.; Mantion, A.; McAloney, R.; Huber, A.; Falkenhagen, J.; Goh, C. M.; Thünemann, A. F.; Winnik, M. A.; Menzel, H. *Colloid Polym. Sci.* **2013**, *291*, 1353–1363.

(6)   Gangloff, N.; Luxenhofer, R. *Hierarchical Macromolecular Structures: 60 Years after the Staudinger Nobel Prize II*; Percec, V., Ed.; Advances in Polymer Science; Springer International Publishing: Cham, **2013**; Vol. 262.

(7)   Huang, J.; Bonduelle, C.; Thévenot, J.; Lecommandoux, S.; Heise, A. *J. Am. Chem. Soc.* **2012**, *134*, 119–122.

(8)   Gitsas, A.; Floudas, G.; Mondeshki, M.; Butt, H. J.; Spiess, H. W.; Iatrou, H.; Hadjichristidis, N. *Biomacromolecules* **2008**, *9*, 1959–1966.

(9)   Olsen, B. D.; Segalman, R. A. *Mater. Sci. Eng. R Reports* **2008**, *62*, 37–66.

(10)   Sánchez-Ferrer, A.; Mezzenga, R. *Macromolecules* **2010**, *43*, 1093–1100.

(11)   Huang, J.; Habraken, G.; Audouin, F.; Heise, A. *Macromolecules* **2010**, *43*, 6050–6057.

(12)   Krannig, K.-S.; Sun, J.; Schlaad, H. *Biomacromolecules* **2014**, *15*, 978–984.

(13)   Krannig, K.-S.; Schlaad, H. *J. Am. Chem. Soc.* **2012**, *134*, 18542–18545.

(14)   Krannig, K.-S.; Sun, J.; Schlaad, H. *Biomacromolecules* **2014**, *15*, 978–984.

(15)   Kricheldorf, H. R.; Chemie, M. **1979**, *109*, 97–109.

(16)   Stolz, R. M.; Northrop, B. H. *J. Org. Chem.* **2013**, *78*, 8105–8116.

(17)   Hoyle, C. E.; Lowe, A. B.; Bowman, C. N. *Chem. Soc. Rev.* **2010**, *39*, 1355–1387.

(18)   Chan, J. W.; Hoyle, C. E.; Lowe, A. B.; Bowman, M. *Macromolecules* **2010**, *43*, 6381–6388.

(19)   Nair, D. P.; Podgórski, M.; Chatani, S.; Gong, T.; Xi, W.; Fenoli, C. R.; Bowman, C. N. *Chem. Mater.* **2014**, *26*, 724–744.

(20)   Jeong, Y.-I.; Nah, J.-W.; Lee, H.-C.; Kim, S.-H.; Cho, C.-S. *Int. J. Pharm.* **1999**, *188*, 49–58.

(21)   Kujawa, P.; Watanabe, H.; Tanaka, F.; Winnik, F. M. *Eur. Phys. J. E* **2005**, *17*, 129–137.

(22)   Tanaka, F. *J. Non. Cryst. Solids* **2002**, *307–310*, 688–697.

Chapter III

Primary Ammonium/Tertiary Amine-Mediated Controlled Ring Opening Polymerisation of Amino Acid *N*-Carboxyanhydrides

This chapter contains results and material that have been published and are hereby reproduced by permission of the Royal Society of Chemistry (See Appendix C for the list of publications).

III.1 Introduction

Achieving good control over polymerisation reactions is essential for the synthesis of well-defined polymers. Typically, anionic, cationic, controlled radical (CRP), and ring opening polymerisation (ROP) techniques are used to synthesise polymers with predetermined composition, functionality, molar mass, and low dispersity.[1] These properties are essential in the fields of self-assembly and biomimicry. Self-assembled and biomimetic supramolecular assemblies, such as micelles, vesicles, hydrogels and hierarchical scaffolds, are often developed for biomedical or materials science applications.[2–6] In this context, polypeptides are very interesting polymers, not only because they can be designed to be biocompatible and biodegradable, but also because they can be synthesised in a controlled manner by ROP of amino acid *N*-carboxyanhydrides (NCAs).[7,8]

The non-metal catalysed ROP of NCA is known to proceed *via* two distinct pathways, namely the normal amine mechanism (NAM) and the activated monomer mechanism (AMM) (Scheme III.1a and b).[9] The NAM is favoured by the use of nucleophilic initiators such as primary amines and yields well-defined polypeptides. The AMM is favoured by non-nucleophilic bases, such as tertiary amines, and yields polypeptides with high molar mass and dispersity. Although the choice of initiator can influence the NCA polymerisation pathway, it is challenging to completely supress the AMM. Over the past two decades, considerable advances in controlled NCA polymerisation have been realised. The effort was mostly aimed at the elimination of side reactions, notably the AMM, by using transition metal catalysts,[10] silazane[11] and ammonium salts[12] as initiators, by lowering the reaction temperature[13] and by applying high vacuum techniques.[14] Also primary/tertiary amine organocatalytic systems have been reported to promote an accelerated amine mechanism through monomer activation (AAMMA).[15,16]

a NAM

b AMM

c

d $R^1NH_3^+Cl^-$ + R_3N $\rightleftharpoons$ R^1NH_2 + R_3NH^+ Cl^-
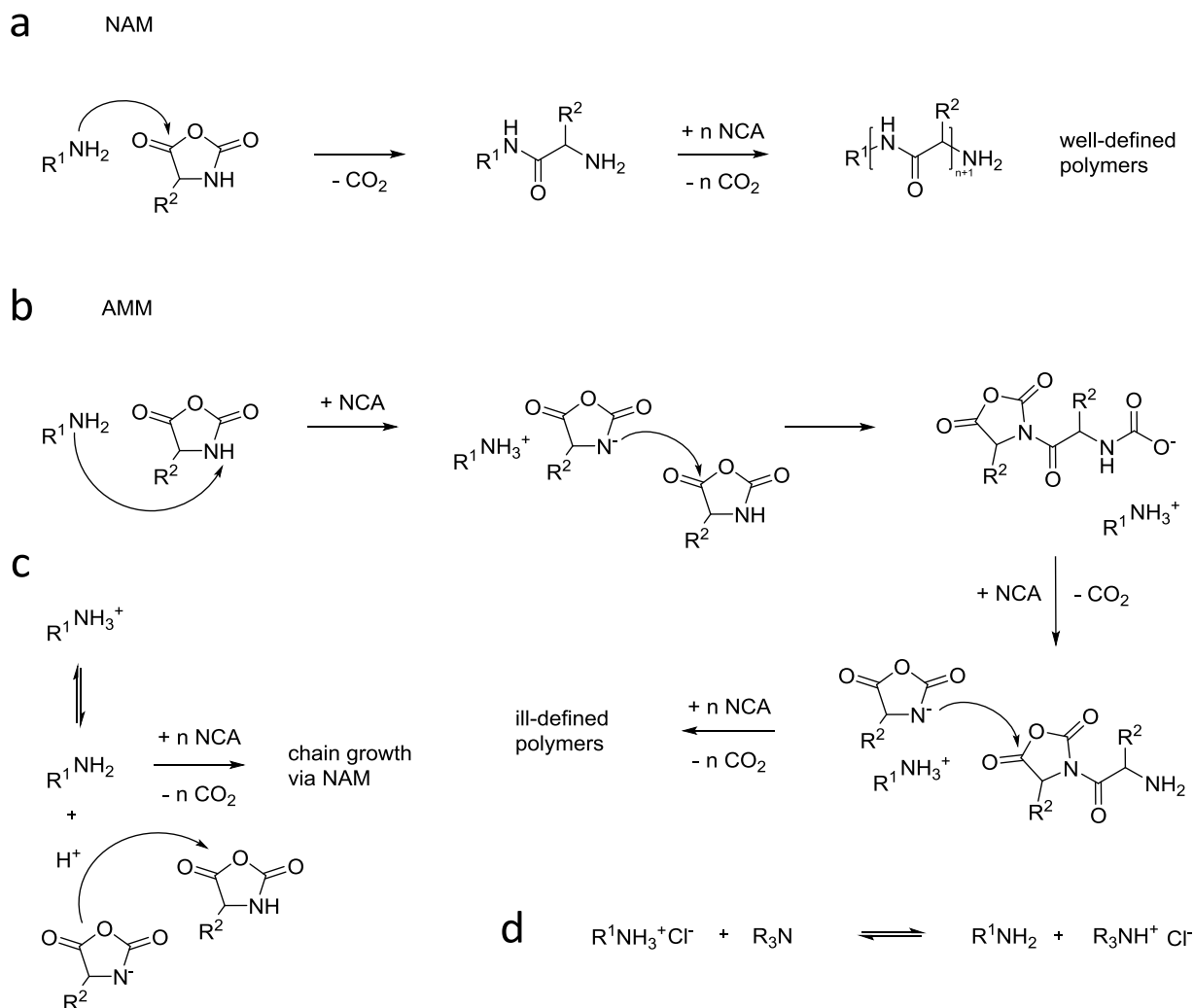
Scheme III.1 (a) Normal amine mechanism (NAM), (b) activated monomer mechanism (AMM), (c) mechanism for the ammonium-mediated ring opening polymerisation[12] and (d) primary/tertiary amine-ammonium equilibrium.

Ammonium salts are attractive alternatives to amines as initiators for ROP of NCA as they are more stable, easier to handle and to purify. Schlaad et al.[12] postulated that the ammonium-mediated ROP mechanism may involve an equilibrium between dormant (ammonium) and active (amine) ω-chain ends (Scheme III.1c), leading to a controlled propagation like in living cationic polymerisation or nitroxide-mediated radical polymerisation. It was suggested that the protons introduced *via* the ammonium salts would protonate NCA anions and thereby suppress the AMM.[12,17,18] However, this technique proved ineffective for hydrophobic NCAs, possibly as a result of this equilibrium being too far shifted to the ammonium side due to a more apolar reaction medium.[19,20] For instance, γ-benzyl-L-glutamate (BLG) NCA could only be polymerised by a mixture of the ammonium salt and its corresponding primary amine,[17] thus somehow defeating the initial purpose of using the ammonium salt as the sole initiator. Being able to establish an alternative ammonium-mediated ROP without the need for the corresponding amine would be extremely beneficial because – aside from the aforementioned advantages – ammonium salts, especially the chlorides, are easier to synthesise and more readily available for purchase than their amine counterparts.

Since the use of a primary amine in combination with its corresponding ammonium salt for the polymerisation of BLG-NCAs was solely aimed at shifting the dormant-active equilibrium to allow the polymerisation to proceed (Scheme III.1c), a question arose as to whether a catalyst could serve the same purpose. In an effort to establish a more versatile variant of the ammonium-mediated polymerisation, an investigation into catalysts that could be universally used in combination with any ammonium salt initiator was undertaken. Since tertiary amines are less good nucleophiles than they are basic,[21] mixtures of primary ammonium salts and tertiary amines were examined (Scheme III.1d). As mentioned earlier, tertiary amines like triethylamine (TEA) are typically used as catalysts to promote an uncontrolled polymerisation of NCAs *via* the AAM in order to obtain long polypeptides within very short timeframes; but as a drawback, such polypeptides also exhibit high dispersities (typically, Đ > 2) and no defined end groups.[7,22] Despite this, well-defined polymers with narrow molar mass distributions and predefined end groups were obtained. The degree of robustness, versatility and limits of this promising new controlled ROP of NCA was sought and the findings are reported and discussed in this chapter.

III.2 Experimental

III.2.1 Materials

In order to determine the versatility of this new ROP of NCA, different primary ammoniums, primary amines, tertiary amines, primary alcohol and NCAs very tested and compared (Figure III.1). Their synthesis along with other chemicals and solvent used are detailed in Appendix A.
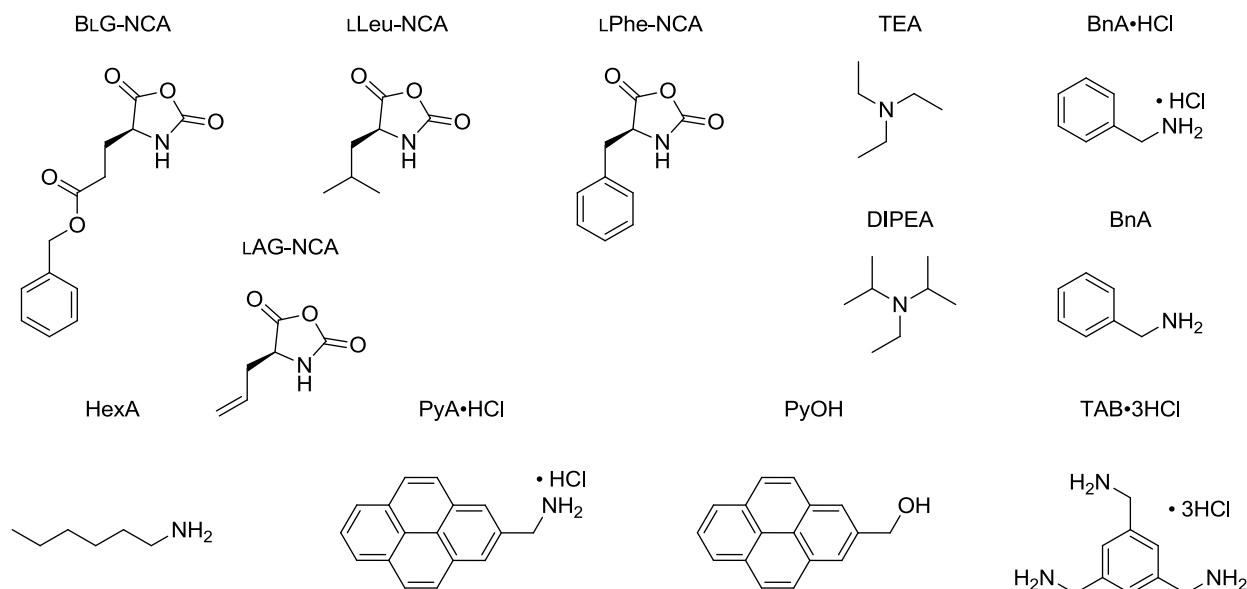
Figure III.1 List of NCAs and initiators compared in this study: from left to right and top to down γ-benzyl-L-glutamate (BLG), L-allylglycine (LAG), L-leucine (LLeu) and L-phenylalanine (LPhe) NCAs, triethylamine (TEA), benzylamine hydrochloride (BnA·HCl), diisopropylethylamine (DIPEA, *a.k.a.* Hünig's base), benzylamine (BnA), hexylamine (HexA), 1-pyrenemethylamine hydrochloride (PyA·HCl), 1-pyrenemethanol (PyOH), 1,2,3-Tris(aminomethyl)benzene trihydrochloride (TAB·3HCl).

III.2.2 Methods to Monitor Reaction Progress

Several methods exist to monitor NCA polymerisation kinetics, such as ^{1}H-NMR,[23] MALDI-TOF MS,[24] FTIR[25], HPLC[23] and SEC.[14] The main limitation of ^{1}H-NMR comes from the tendency of the NH peak to shift as a result of concentration changes, and most importantly the integration of this peak showed that it is not quantitative due to its ability to undergo rapid proton exchange in many solvents.[26] The advantage of MALDI-TOF MS and SEC is that these techniques provide both molar mass and dispersity (Đ). While MALDI-TOF MS is best-suited for short polypeptides (typically, M_n < 5 kg·mol^{-1}), SEC is a very versatile technique that suits polymers of a broad range and degree of polymerisation provided they are soluble in the eluent.[27,28] Unless otherwise specified, all polymerisations were run at room temperature (rt), in DMF and with an initial NCA concentration of 100 g·L^{-1}. Regardless of the method used to follow the kinetics, molar masses were regularly controlled during the polymerisation and after the termination by both ^{1}H-NMR and SEC, and so were the dispersities (by SEC).

III.2.2.1 Monomer Conversion Followed by SEC

For the aforementioned reasons, SEC was selected as one of the main techniques to follow the kinetics of NCA polymerisations. In order to extract a concentration from a peak area, an internal standard was used. By using a pre-established calibration curve (Figure III.2), the ratio of the area under the polymer peak to that of the internal standard in SEC elugrams, provided the polymer concentration (wt %), from which the monomer conversion (p) was deducted. For this method to be reliable, it is necessary that the growing polymer and internal standard peaks do not overlap; in other words, the internal standard ought to be either a small molecule or a high molar mass polymer.

In order to avoid of the challenges associated with the integration of peaks at high elution volumes (*e.g.*, presence of impurities, solvent or monomer peaks), a high molar mass polystyrene standard was selected. Polystyrene was chosen for its solubility in the SEC eluent (NMP), and for its inert chemical nature as it did not contain reactive functional groups, neither in the pendant groups (benzyl group) or along the backbone, nor at the α and ω chain ends since such SEC standards are typically synthesised by anionic polymerisation. Since side reactions caused by the internal standard are unlikely, the latter could be added either (i) directly to the polymerisation medium, or (ii) in controlled amounts to know volumes sampled from the reaction medium. Different internal standards were compared (Appendix B) and a polystyrene SEC standard of Mw = 1,815,000 g·mol^{-1} and referred to as PS2M was selected for the present study.

A calibration curve was prepared using a series of solutions composed of PBLG$_{51}$/PS2M (x:y) in 2.5 mL DMF, with x = 15 mg for all solutions, and y = 1, 3, 5, 10, 15, 30, and 60 mg (Figure III.2), as well as a control solution composed of 15 mg of PS2M only. The calibration ratios (x:y) were chosen to cover as much of the expected conversion range as possible: the amount of internal standard used for each polymerisation sample was always calculated so that [PS2M] = 0.1[NCA]$_0$. Thus, at t = 0, the amount of

PS2M present in the reaction medium is infinitely larger than that of the polymer; for a complete conversion, the amount of PS2M would be 10 times lower than that of the polymer.
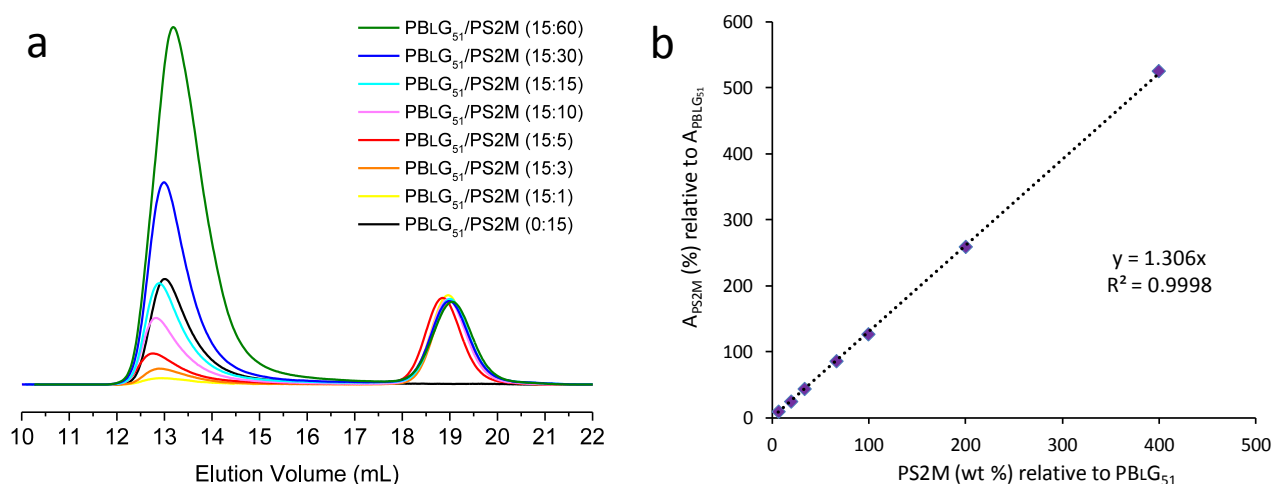
Figure III.2 (a) SEC traces of the PBLG$_{51}$/PS2M calibration series (weight ratios in bracket); (b) calibration curve of the PBLG$_{51}$/PS2M calibration series where the PS2M/PBLG$_{51}$ ratio of the areas under the elution peaks extracted from (a) are plotted as a function of the PS2M/PBLG$_{51}$ weight ratios.

This technique presents some drawbacks: (i) the need for an SEC internal standard, which is costly and requires additional steps as part of the samples preparation; (ii) the presence of low molar mass impurities (*e.g.*, unreacted NCA, terminating agent) at high elution volumes prevents the accurate quantification of molar mass, dispersity and of the conversion for low molar mass polymers, that is at the beginning of the polymerisation; and (iii) when used not in-line, this technique is extremely time consuming and labour intensive due to the sample preparation mostly.

III.2.2.2 Monomer Conversion Followed by FTIR

With SEC, the monomer conversion (p) is indirectly calculated from the polymer concentration, which does not account for potential side reactions, whereas FTIR directly measures the monomer consumption. The absorbance peaks (1850-1855 cm^{-1} and 1785-1790 cm^{-1}) of the carbonyl bonds (C=O stretch) of NCAs (*e.g.*, BLG, LLeu and LPhe) do not overlap with absorbance peaks of the corresponding polymers (Figure III.3a). The 1850-1855 cm^{-1} and the 1785-1790 cm^{-1} peaks were assigned by Kricheldorf to the (C-)C=O and the (N-)C=O groups, respectively.[29] This assignment was mostly based on the fact that 2-thioxooxazolidine-5-ones (TOOs), which possess only one carbonyl group, (C-)C=O, only exhibit one carbonyl band at 1850 cm^{-1}.

The peak at 1785-1790 cm^{-1} is larger, and as such, less likely to incur measurement error than the smaller 1850-1855 cm^{-1} peak; it was, therefore used to monitor the monomer conversion. The calibration series were composed of NCA solutions in DMF of concentration ranging from 0 to 100 g·L^{-1} (Figure III.3b and Appendix A). In order to ensure that the presence of polypeptides did not affect the calibration curve in any way, a control calibration series of BLG-NCA/PBLG$_{51}$ (x:y with x and y ranging from 0 to 10 and x+y=1) solutions in DMF of total concentration ranging from 0 to 100 g·L^{-1} was measured and yielded an almost identical calibration curve to that of the calibration series using BLG-NCA alone.

No internal standards were used: the area under the fitted 1785-1790 cm^{-1} peak is directly related to the NCA concentration in DMF. The consistency of the method was confirmed by a coefficient of determination (R-squared) close to 1 and almost identical linear regression equations obtained for two repeats. This consistency relied on a systematic processing of the spectra as described in Appendix A. The calibration curves for LLeu and LPhe are also available in Appendix A.
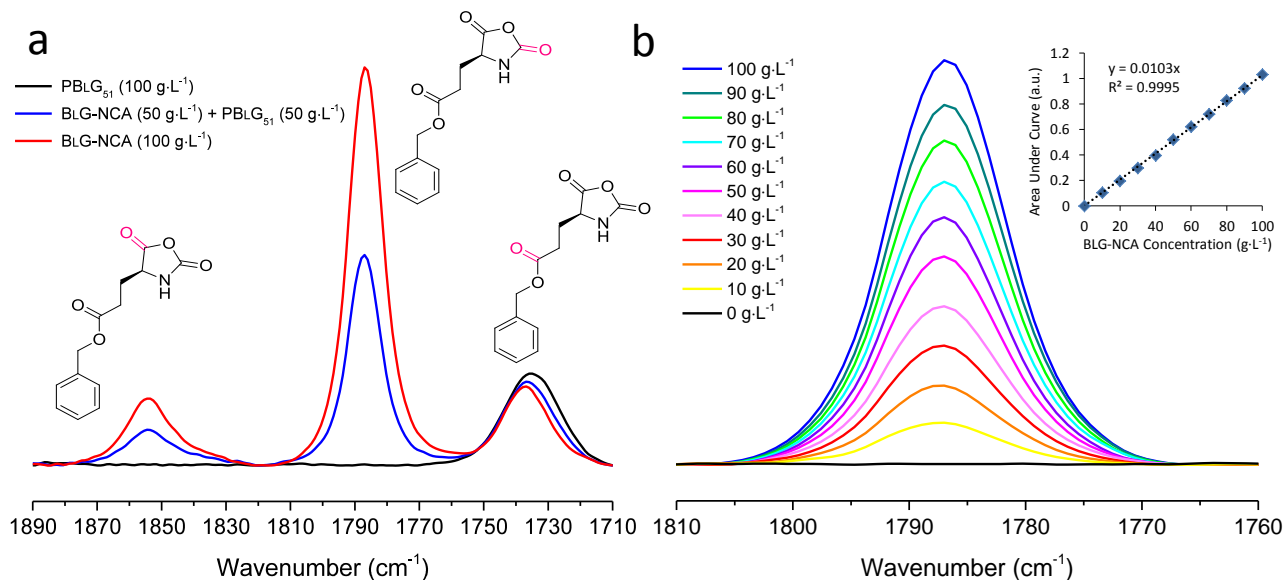
Figure III.3 (a) FTIR absorbance peaks (C=O stretch) in the 1710-1890 cm^{-1} region of solutions of BLG-NCA and PBLG$_{51}$ in DMF (DMF background subtracted), and corresponding carbonyl groups (in pink). (b) FTIR absorbance peaks of BLG-NCA (N-)C=O stretch from the BLG-NCA calibration series; (insert) calibration curve of the NCA calibration series where the area under the 1785-1790 cm^{-1} fitted peaks is plotted as a function of the BLG-NCA concentration.

See Appendix A for all analytical methods used here (i.e., NMR, SEC and FTIR).

III.3   Results and Discussion

III.3.1   Primary Ammonium/Tertiary Amine-Mediated NCA Polymerisation

1,2,3-Tris(aminomethyl)benzene (TAB) is an amine that can be used as a trifunctional initiator for ROP of NCA but is only available for purchase in the form of its trihydrochloride salt (TAB·3HCl).[30] It was, therefore, chosen as a candidate to test the primary ammonium/tertiary amine-mediated ROP of NCA. The efficacy of TAB·3HCl as an initiator for the polymerisation of BLG-NCA was initially investigated. The monomer conversion and dispersity were followed by SEC (Section III.2.2.1) and the molar mass by ^{1}H-NMR (Appendix B). The polymerisation was very slow with only 13% conversion after seven days at room temperature (rt) (Figure III.4a), and 48% conversion after seven days at 50 °C (Figure III.4b). In contrast, the polymerisation of BLG-NCA initiated by a 1:0.5 mixture of TAB·3HCl and TEA at room temperature led to low dispersities (< 1.08) with 67% conversion achieved after five days (Figure III.4c). The reaction was stopped after seven

days and the polymers were worked up and analysed by ^{1}H-NMR. End group analysis showed that the number-average molar mass (M_n) closely matched the targeted molar mass (Appendix B).

In order to assess whether TEA was solely responsible for this faster and controlled ROP, a 'reference' polymerisation was run and followed by SEC (Figure III.4d) and ^{1}H-NMR (Appendix B). For this reference reaction, a solution of TEA was used to initiate the polymerisation of BLG-NCA; for comparison purposes, the TEA/NCA$_0$ ratio was the same as for the polymerisation shown in Figure III.4c (*i.e.*, 0.5:150). The SEC traces and ^{1}H-NMR spectra showed that the polymerisation was clearly uncontrolled (M_n > 77 kDa, Đ > 2), thereby indicating that the AMM was the dominant mechanism (Scheme III.1d). These results confirmed that TAB·3HCl and TEA, when used as an initiator mixture, have a synergistic effect on the polymerisation of BLG-NCA in that it proceeds in a controllable fashion. It was, therefore, postulated that the NAM is the dominant mechanism in the primary ammonium/tertiary amine-mediated ROP of NCA. However, as suggested by Scheme 1d, the occurrence of the AAM could not be completely excluded.
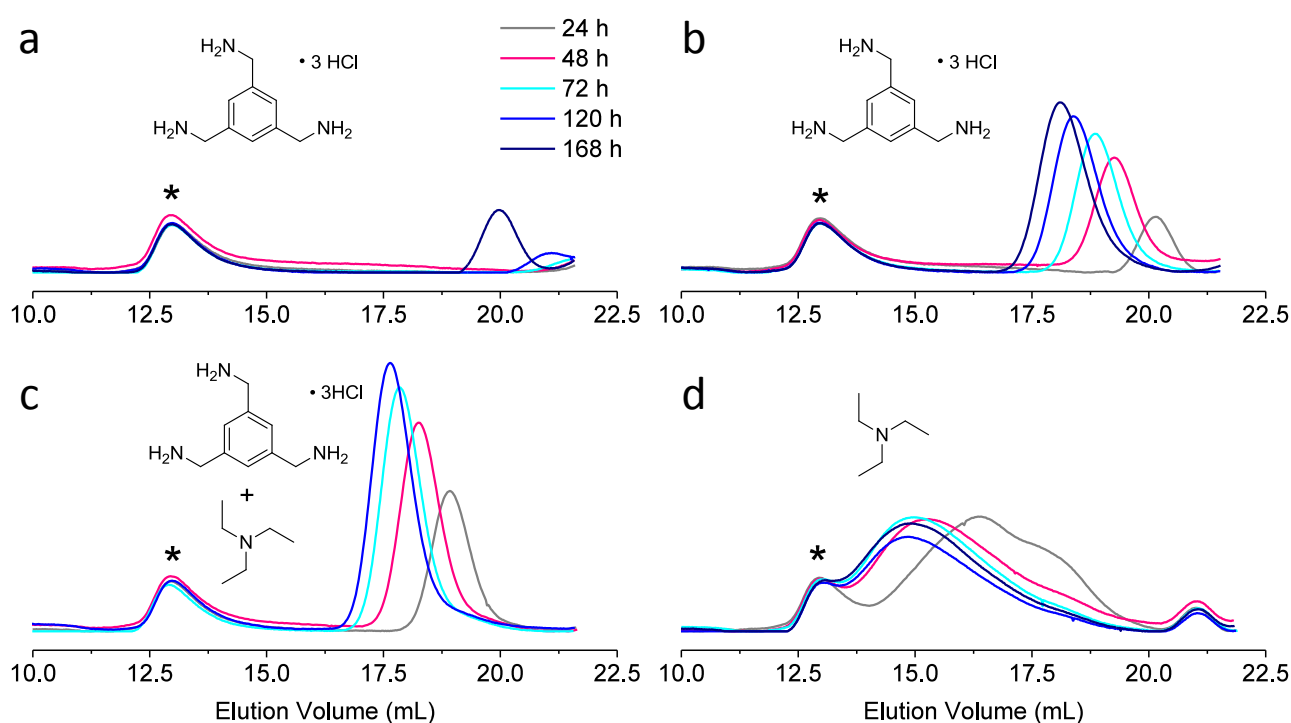
Figure III.4 SEC traces of the polymerisations of BLG-NCA (150 equiv.) in DMF (60 g·L^{-1}) initiated by (a) TAB·3HCl (1 equiv.), rt; (b) TAB·3HCl (1 equiv.), 50 °C; (c) TAB·3HCl/TEA (1:0.5 equiv.), rt; and (d) TEA (0.5 equiv.), rt; * peak of the high molar mass polystyrene (PS2M; 2 MDa) used as internal standard for calculating the monomer conversion (Section III.2.2.1) (Appendix B, P25-28).

III.3.2   Effect of the Primary Ammonium/Tertiary Amine Ratio

In order to study the robustness and limits of this primary ammonium/tertiary amine polymerisation, a polymerisation series of BLG-NCA initiated with mixtures of 1-pyrenemethylamine hydrochloride (PyA·HCl) (1 equiv.) and TEA (0 to 1.5 equiv.) in different ratios (Figure III.5) was followed. PyA·HCl was chosen to allow for the tracking of pyrene end groups using the UV detector set at λ = 340 nm (noted UV$_{340nm}$).[31–33] The results, summarised in Table III.1, reveal that the rate of polymerisation increased with increasing

amounts of TEA. For all PyA·HCl/TEA ratios, except 1:1.5, the polypeptides exhibited very low dispersities (< 1.1) and the final molar masses were close to the target (Appendix B), indicating that the primary ammonium/tertiary amine-mediated polymerisations proceeded in a controlled manner. Moreover, SEC analysis by RI and UV$_{340nm}$ detection allowed to conclude qualitatively that the polypeptide fractions carried a pyrene unit (the only species present in the polymerisation medium that absorb at 340 nm), which is supportive of the NAM. In the case of the uncontrolled polymerisation, *i.e.* PyA·HCl/TEA = 1:1.5, the polypeptide chains, but not all, were labelled with pyrene (Figure III.5f). This result suggests that although the AMM seems to be the predominant mechanism in this one case, pyrene species were still incorporated in polymer chains, probably *via* the addition of PyA-initiated chains to *N*-acylated NCA chain ends, indicating that the NAM also played a role.
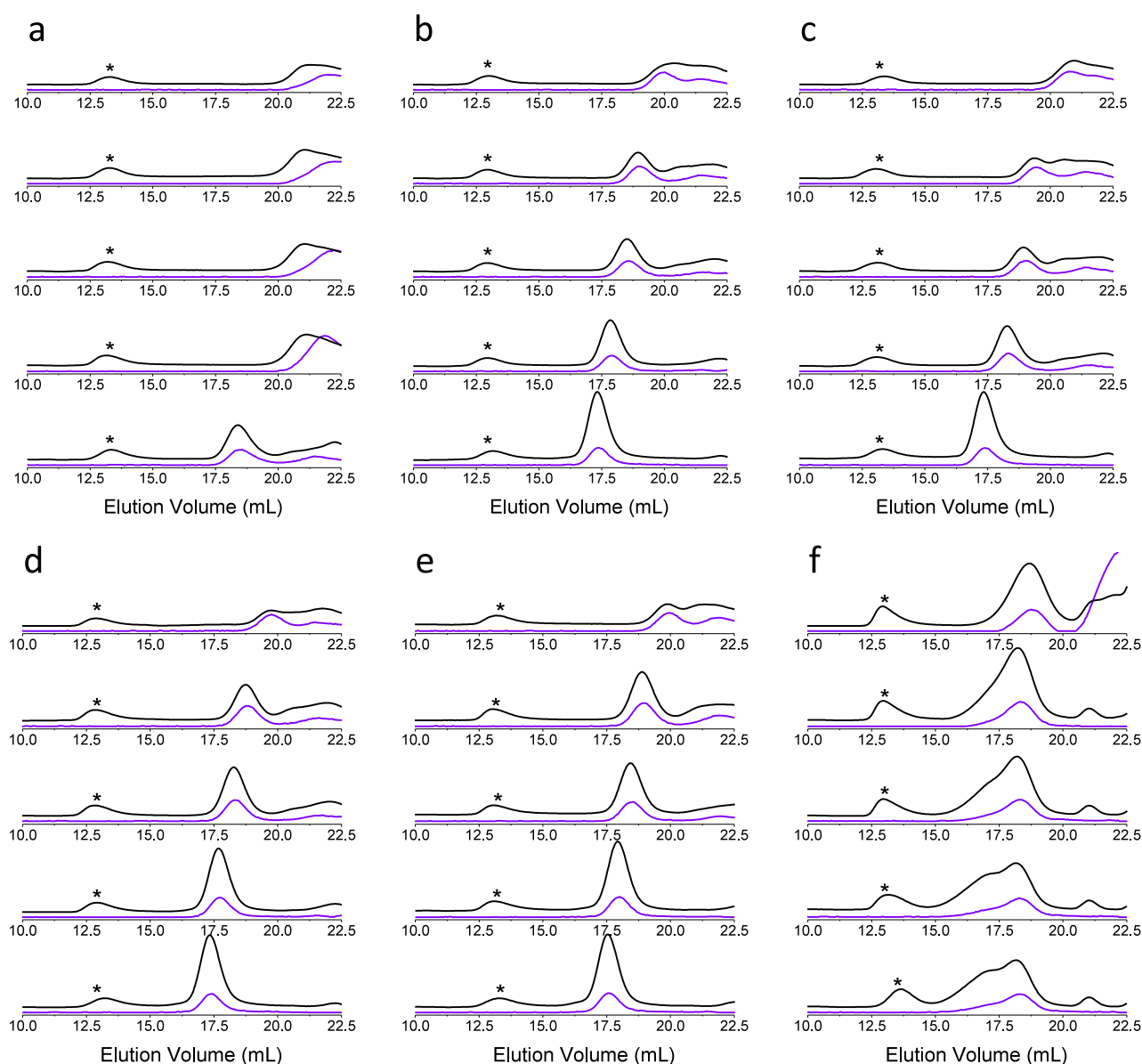
Figure III.5 SEC traces (RI in black, UV$_{340nm}$ in purple) of polymerisations of B$_L$G-NCA (150 equiv.) in DMF initiated by PyA·HCl/TEA in the following ratios: (a) 1:0, (b) 1:0.5, (c) 1:0.7, (d) 1:0.9, (e) 1:1.1, (f) 1:1.5; each set of traces corresponds to samples taken at (top to bottom) 2 h, 6 h, 8 h, 24 h and (a to e) 120 h / (f) 168 h; the peak (*) corresponds to the high molar mass polystyrene (PS2M, 2 MDa) used as internal standard for calculating the monomer conversion (Section III.2.2.1) (Appendix B, P34 and P41).

Table III.1 Results (determined by SEC) of the series polymerisations of BLG-NCA (150 equiv.) at room temperature initiated by PyA·HCl/TEA mixtures (molar ratio 1:x, x = 0 to 1.5) (Appendix B, P34 and P41).

PyA·HCl/TEA	1:0	1:0.2	1:0.5	1:0.7	1:0.9	1:1.1	1:1.5
24 h - conversion	-	37%	50%	70%	80%	88%	94%
- dispersity (Đ)	-	1.12	1.07	1.07	1.07	1.07	1.90
120 h - conversion	25%	77%	86%	95%	96%	99%	100%
- dispersity (Đ)	1.06	1.10	1.08	1.07	1.08	1.08	1.90

Interestingly, for all PyA·HCl/TEA initiator mixtures ranging from 1:0 to 1:1.1, a secondary UV_{340nm} (and RI) absorption peak (or hump) was generally observed at high elution volumes (> 20 mL) and disappeared with time as the polymerisation proceeded, leaving a narrow and monodispersed final molar mass distribution (Figure III.5a to e). This observation could be explained by the coexistence of both NAM and AMM, as a consequence of the equilibrium shown in Scheme III.1d, where the AMM plays a determining role in the early stages of the polymerisation and the NAM progressively takes over, provided that the initial TEA/PyA·HCl ratio is under a certain limit (< 1.5) (Figure III.5f). Thus, it was hypothesised that tertiary amines (*e.g.*, TEA) would initially generate *N*-acylated NCA oligomers through the AMM (Scheme III.1b) but that primary ammonium chlorides (*e.g.*, PyA·HCl), present in greater quantities, would regulate the propagation by (i) favouring the NAM, causing *N*-acylated NCA oligomers to be progressively incorporated at the ω-end of other growing chains (hence the disappearance of the secondary RI peaks), and (ii) supplying protons to prevent the AMM from dominating throughout the propagation (Scheme III.1c), thereby ensuring the incorporation of any unreacted primary ammonium initiators either *via* 'normal' initiation or *via* the reaction with α-ends of *N*-acylated NCA oligomers, causing the secondary UV_{340nm} peak to disappear over time (Scheme III.2).
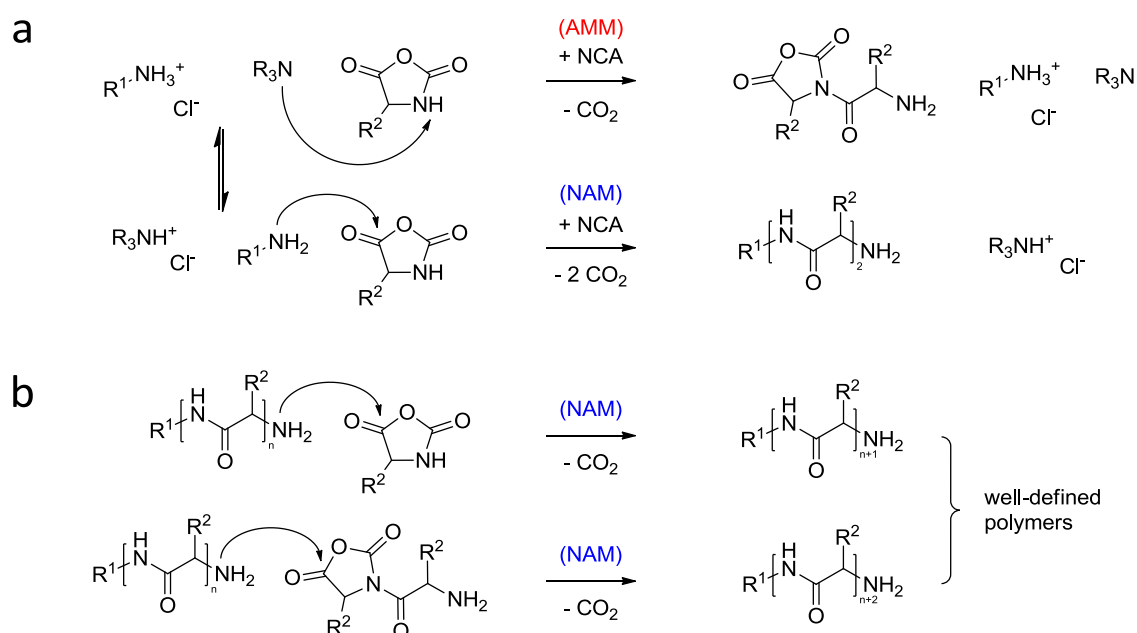
Scheme III.2 Proposed mechanisms responsible for the controlled nature of the primary ammonium/tertiary amine-mediated ROP of NCA. (a) Initiation and early propagation stages, during which the AMM (faster than the NAM) is expected to predominate. (b) Propagation stage showing how the NAM becomes the predominant mechanism and how the *N*-acylated α-ends are consumed.

Based on these results, it was postulated that NAM and AMM coexist during the initiation and – the entirety or part of – the propagation of the primary ammonium/tertiary amine-mediated ROP of NCA. A higher tertiary amine/primary ammonium chloride ratio clearly led to a faster propagation, but the controlled nature of the reaction was lost above a certain threshold ratio, which, in the case of TEA/PyA·HCl system is between 1.1:1 and 1.5:1. The dormant-active mechanism proposed by Schlaad et al. for the ammonium-mediated ROP of NCA[12] may also play a role in the overall mechanism of primary ammonium/tertiary amine-mediated ROP of NCA. Thus, another determining factor - potentially affecting the propagation rate - to consider was the total amines (both primary and tertiary) to HCl ratio. Supposedly, the higher this ratio is, the more active species (*e.g.*, ω-end amines) are present in the polymerisation medium and able to engage in either NAM or AMM; the lower this ratio is, the more dormant species (*e.g.*, ω-end ammonium salts) are present in the polymerisation medium (Scheme III.1c).

III.3.3   Dormant-Active Equilibrium

The primary ammonium salt/tertiary amine equilibrium (Scheme III.1d) suggests that the ratio of total amines (both primary and tertiary) to HCl (*i.e.*, amine/HCl ratio) should affect the polymerisation rate. Large amine/HCl ratios should lead to higher concentrations of active amine chain ends, thereby inducing a higher polymerisation rate (R_p) as it is a function of the concentration of active species. However, for too large tertiary amine/HCl ratio the controlled nature of the reaction is lost, as illustrated by the polymerisation initiated by TEA/PyA·HCl = 1.5:1 (Table III.1). Likewise, low amine/HCl ratios should lead to higher concentrations of dormant ammonium chain ends according to Scheme III.1c, potentially resulting in an inhibition of the polymerisation for [HCl] > [amine] as in Figure III.4a.

In order to validate this dormant-active model, the PyA·HCl/TEA (1:0.5) initiated polymerisation of BLG-NCA was repeated, and HCl was added (1 equiv. with respect to the initially introduced TEA) 24 h following the initiation. At that stage, the amine/HCl ratio was hence adjusted to 1 (*i.e.*, [HCl] = [amine]), thereby shifting the equilibrium to the dormant side. At 81 h, TEA was added (1 equiv. with respect to HCl added at 24 h), and the reaction was allowed to run for another 87 h. The SEC analysis showed that the polymerisation was 'paused' following the addition of HCl at 24 h as neither the monomer conversion (Figure III.6a) nor the molar mass of the polymer (Figure III.6b) increased between 24 h and 81 h. After 81 h, both molar mass and conversion started to increase again, indicating that the polymerisation 'resumed' following the addition of TEA. These results extend the dormant-active mechanism from the ammonium-mediated ROP of NCA to the primary ammonium/tertiary amine-mediated ROP of NCA. They also confirm that the control in primary ammonium/tertiary amine-mediated ROP of NCA should be viewed as the result of a synergistic combination of primary amine, tertiary amine and HCl species, within a certain molar fraction range.
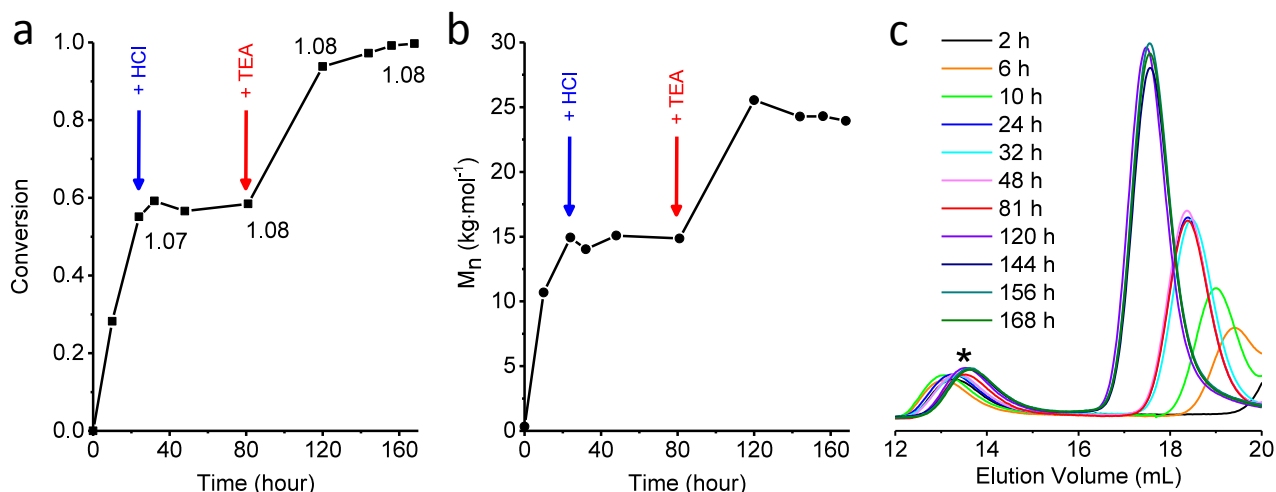
Figure III.6 Polymerisation of BʟG-NCA (150 equiv.) in DMF initiated by PyA·HCl/TEA (1:0.5 equiv.), paused at 24 h by adding HCl and resumed at 81 h by adding TEA; (a) time-conversion plot and dispersities (at 24 h, 81 h, 120 h, and 168 h) determined by SEC (Section III.2.2.1), (b) number-average molar mass determined by SEC as a function of time, (c) corresponding SEC traces; the peak (*) is a high molar mass polystyrene (PS2M; 2 MDa) internal standard (Appendix B, P43); .

Although the existence of a dormant-active equilibrium as part of the primary ammonium/tertiary amine mechanism was demonstrated, the complete mechanism is likely to be more complex. As suggested by the results reported in Section III.3.2, in particular the secondary UV_{340nm} peak observed by SEC (Figure III.5) and the loss of control for the largest tertiary amine fractions, it is likely that the chain growth proceeds *via* a mixed NAM-AMM mechanism. In addition, the predominance of one mechanism over the other greatly depends on the primary/tertiary amine and amine/HCl ratios, and thus may vary throughout the chain growth process. As aforementioned, the initiation and early propagation stage is likely dominated by the AMM, while the NAM takes over in a later propagation stage (Scheme III.2), provided the fraction of tertiary amine is sufficiently low. It should also be stressed that the amine-ammonium equilibrium likely depends on solution pH and solvent polarity, making a prediction of the reaction kinetics challenging.[21]

III.3.4   Comparison of NCAs and Tertiary Amines

In order to assess the versatility of this primary ammonium/tertiary amine-mediated ROP of NCA, it was tested with another bulky tertiary amine, diisopropylethylamine (DIPEA, Hünig's base), and two other hydrophobic NCAs, ʟ-leucine (ʟLeu) and ʟ-phenylalanine (ʟPhe) NCAs. Since PʟLeu and PʟPhe could not be analysed by SEC due to their poor solubility in organic solvents (*e.g.*, NMP, THF), the monomer conversion was followed by FTIR for all reactions (Section III.2.2.2). The time-conversion plots for the polymerisation of BʟG-NCA, ʟLeu-NCA, and ʟPhe-NCA, initiated by benzylamine (BnA), benzylamine hydrochloride (BnA·HCl), BnA·HCl/TEA, and TEA are shown in Figure III.7. Most importantly, the polymerisations of ʟLeu-NCA and BʟG-NCA when initiated by BnA·HCl were very slow (< 15% conversion after 32 h), as expected, and were both considerably faster with BnA·HCl/TEA as an initiator mixture (respectively, 63% and 77% conversion after 32 h), almost or as fast as with BnA. All PBʟG samples exhibited low dispersities, except for those initiated by TEA only, further confirming the controlled nature of BnA·HCl/TEA-initiated ROP of NCA.
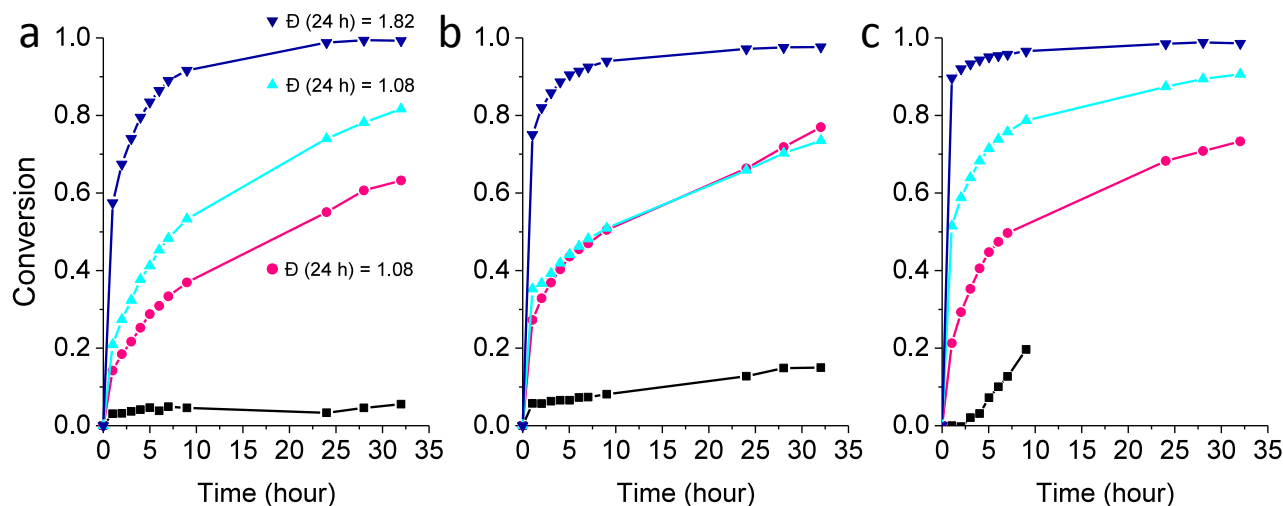
Figure III.7 Time-conversion plots for the polymerisations of (a) BLG-NCA (100 equiv.), (b) LLeu-NCA (100 equiv.) and (c) LPhe-NCA (100 equiv.) in DMF initiated by ■ BnA·HCl (1 equiv.), ● BnA·HCl/TEA (1:0.5 equiv.), ▲ BnA (1 equiv.), and ▼ TEA (0.5 equiv.). Monomer conversions were determined by FTIR spectroscopy (Section III.2.2.2); PBLG dispersities at 24 h were determined by SEC (Appendix B, P44-46).

The polymerisation of LPhe-NCA using the same initiators followed similar trends, with the exception of BnA·HCl, for which the conversion progressed more rapidly than in the case of BLG-NCA and LLeu-NCA. LPhe-NCA was the most reactive of all three NCAs tested. As such, the regular sampling of the reaction medium for kinetic analysis may have led to the introduction of small amounts of water molecules, despite the use of purged syringes and dried glassware, which may have sufficed to induce polymerisation. In fact, even control solutions of BLG-NCAs subjected to regular sampling were found to react after a certain amount of time (typically > 48 h). Despite this, since all the polymerisation series depicted in Figure III.7 were run in parallel and treated in the same way, the collected results and their comparison were considered consistent and reliable.

The primary ammonium/tertiary amine-mediated ROP of NCA was also successful with the other tertiary amine tested. The amino group in DIPEA (Hünig's base) is more sterically hindered than in TEA (Figure III.1), hence even less nucleophilic, and has a similar basicity (pKa ~ 10.6-10.7 for both, in water). As such, DIPEA was expected to have a similar effect as TEA when used in combination with a primary amine hydrochloride to initiate an ROP of NCA. Table III.2 shows that both reactions, which were run in parallel and under the same conditions, were controlled, as indicated by the low dispersities (< 1.09), and showed very similar molar masses throughout the entire polymerisation. The conversion differed only slightly as it was larger for the PyA·HCl/DIPEA- than for the PyA·HCl/TEA-initiated polymerisation. Although repeats would be necessary to confirm the significance of this difference, a possible explanation could be that (i) the ammonium chloride-amine equilibrium constant likely varies with the nature of the tertiary amine (Scheme III.1d), leading to a shift towards active growing chains, or (ii) DIPEA might be slightly more basic than TEA, resulting in the consumption of more monomers *via* the AMM during the initiation and early stages of the propagation.

Table III.2 Results of the series of polymerisations of BLG-NCA (150 equiv.) at room temperature initiated by PyA·HCl/TEA and PyA·HCl/DIPEA (1:0.5) (Appendix B, P41-50 and P42). The target M_n was ~ 33,000 g·mol^{-1} (*i.e.*, 150 repeat units). Conversions, dispersity and M_n were measured by SEC (Section III.2.2.1).

PyA·HCl / Tertiary Amine (1:0.5)		10 h	24 h	32 h	48 h	81 h	120 h	168 h
TEA	Conversion	24%	50%	60%	68%	81%	86%	91%
	Dispersity (Đ)	1.05	1.07	1.07	1.08	1.08	1.08	1.09
	M_n (g·mol^{-1})	11,200	16,100	18,200	21,600	25,000	26,500	27,200
DIPEA	Conversion	32%	63%	64%	81%	88%	96%	-
	Dispersity (Đ)	1.06	1.08	1.08	1.08	1.08	1.09	-
	M_n (g·mol^{-1})	11,100	16,700	19,700	22,800	25,200	26,300	-

The primary ammonium/tertiary amine-mediated ROP of NCA proceeds in a similar and controlled fashion regardless of the type of NCA, primary ammonium salt and tertiary amine used. This is a strong evidence that the polymerisation kinetics is controlled by the common denominator between the different experiments, that is the primary amine/tertiary amine/HCl molar ratio.

III.3.5   Kinetics and Mechanism

Ring opening polymerisations are a type of chain growth polymerisations; the ω-end of the chains acts as an active centre. Unlike free radical polymerisations, the active centres of NCA ring-opened polymers are not free radicals but primary amines and thus cannot undergo termination *via* disproportionation or combination. Termination, transfer and side reactions can still occur, for instance as a result of the presence of *N*-acylated NCA α-ends (through AMM, Scheme III.1), contaminants (*e.g.*, nucleophiles, electrophiles, acids or bases), or even through backbiting (*e.g.*, ester pendant groups, backbone amide residues).[34] By working in dry and inert conditions, with high purity reagents and solvents, and with NAM-inducing initiators (*e.g.*, unhindered primary amines), ROP of NCA can reach a level of control that resembles that of living polymerisations.[14,35]

As for ammonium-mediated ROP of NCA, Schlaad et al. proposed that an excess of protons in the reaction medium contributes to the suppression of the AMM and induced a dormant-active equilibrium of the active centre (Scheme III.1), thereby safeguarding the controlled nature of the polymerisation.[12,18] In the present study, due to the ineffective initiation of BLG-NCA by ammonium chlorides, the addition of tertiary amines was implemented as a way to enable the initiation by freeing primary amines through the equilibrium described in Scheme III.1d. The results discussed in the aforementioned sections demonstrated that the ROP of NCA remains largely controlled for ammonium chloride/tertiary amine ratios (x:y) comprised between 1:0 and at least 1:1.1. The fact that 'y' can approach and exceed 1 equiv. without causing the AMM to predominate and the control to be lost, causing a substantial rise of both dispersity and molar mass, is an exceptional result. This suggests that NAM and AMM can coexist but that the presence of primary ammonium chloride species, even in smaller quantities than tertiary amines, can cause

the NAM to prevail over the AMM. In order to test this hypothesis, a kinetic analysis of the series of polymerisations reported in Section III.3.4 was undertaken.

In an 'ideal' case of controlled ROP of NCA, *i.e.*, either *via* NAM-only or dormant-active equilibrium (Scheme III.3), and under the assumptions of steady state and absence of side reactions, the rate equations can be resolved and simplified into linear functions of time, ln(1/(1-p))(t) (Equation III.1). A deviation from linearity would imply that the ideal mechanism assumptions are incorrect or incomplete, in which case 'non-ideal' models would be considered, such as a dormant-active-NAM-AMM coexistence model.
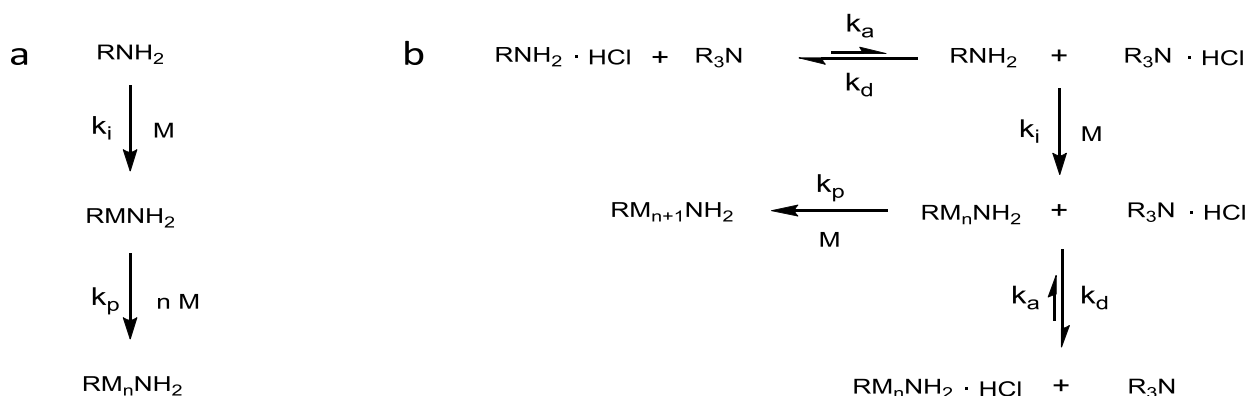
Scheme III.3 ROP of NCA proceeding *via* (a) NAM in the absence of side-reactions, and (b) dormant-active equilibrium, with the propagation step following the NAM; with M the monomer (NCA) or monomeric unit.

$(a1)$ $R_p = -\dfrac{d[M]}{dt} = k_p[RM_nNH_2][M]$

$(a2)$ $\dfrac{d[M]}{[M]} = -k_p[RM_nNH_2]dt = -k_p[RNH_2]_0 dt$

$(a3)$ $\displaystyle\int_0^t \dfrac{d[M]}{[M]} = -k_p[RNH_2]_0 \int_0^t dt$

$(a4)$ $\ln\left(\dfrac{[M]_0}{[M(t)]}\right) = \ln\left(\dfrac{1}{1-p}\right) = \underbrace{k_p[RNH_2]_0}_{\text{constant}} t$

$(b1)$ $K = \dfrac{k_a}{k_d} = \dfrac{[RM_nNH_2][R_3N \cdot HCl]}{[RM_nNH_2 \cdot HCl][R_3N]}$

$(b2)$ $[RM_nNH_2] = [RNH_2]_0 = K\dfrac{[RNH_2 \cdot HCl]_0[R_3N]_0}{[R_3N \cdot HCl]_0}$

$(b3)$ $R_p = k_p[M][RM_nNH_2] = -\dfrac{d[M]}{dt}$

$(b4)$ $\dfrac{d[M]}{[M]} = -k_p K\dfrac{[RNH_2 \cdot HCl]_0[R_3N]_0}{[R_3N \cdot HCl]_0}dt$

$(b5)$ $\ln\left(\dfrac{[M]_0}{[M(t)]}\right) = \underbrace{\dfrac{k_p K[RNH_2 \cdot HCl]_0[R_3N]_0}{[R_3N \cdot HCl]_0}}_{\text{constant}} t$

Equation III.1 Resolved polymerisation rate (R_p) equations for an ideal controlled ROP of NCA (a) initiated by a primary amine (RNH_2) and proceeding *via* NAM (Scheme III.1a), (b) initiated by a primary ammonium/tertiary amine system (RNH_2/R_3N) and proceeding *via* the proposed dormant-active equilibrium (Scheme III.1c) and a NAM-controlled propagation; where p is the conversion, [M] the NCA concentration, k_p the rate constant for propagation, K the equilibrium constant for the amine hydrochloride equilibrium, and RM_nNH_2 the growing chains. In order for the equations to be solved, a number of assumptions were made: (a2 and b2) in order for the concentration of growing chains to equal the initial initiator concentration, a fast and quantitative initiation was assumed; (a and b) the absence of side reactions, transfer or termination was assumed; (b1) steady-state was assumed.

The kinetic study showed that all ln(1/1-p)(t) plots (also known as first order time conversion plots) exhibited a slight concave curvature at low conversions before 'straightening up', which is indicative of a faster conversion in the early propagation stages. This phenomenon was observed not only for primary ammonium/tertiary amine- but also for the more traditional primary amine-initiated ROP of NCA (Figure III.8). Most importantly, this result indicates that none of the studied polymerisations proceeded *via* a NAM-only or dormant-active mechanism (Scheme III.3, Equation III.1), thereby supporting a 'non-ideal' propagation model. As pointed out by Deming et al., the abundance of potential reactions in ROP of NCA makes it difficult to achieve a living polymerisation system where only chain propagation occurs, even when using only primary amines as initiators.[34] In other words, a ln(1/1-p)(t) plot deviating from linearity is more expectable than a linear one. Nevertheless, both primary ammonium/tertiary amine- and primary amine-initiated ROP of NCA yielded polymers with predictable molar masses and end groups (Appendix B), pointing towards the NAM as the prevailing mechanism. In order to determine whether the AMM also occurred and was the main cause for the non-linear ln(1/(1-p))(t) plots, tertiary amine-initiated polymerisations were examined.
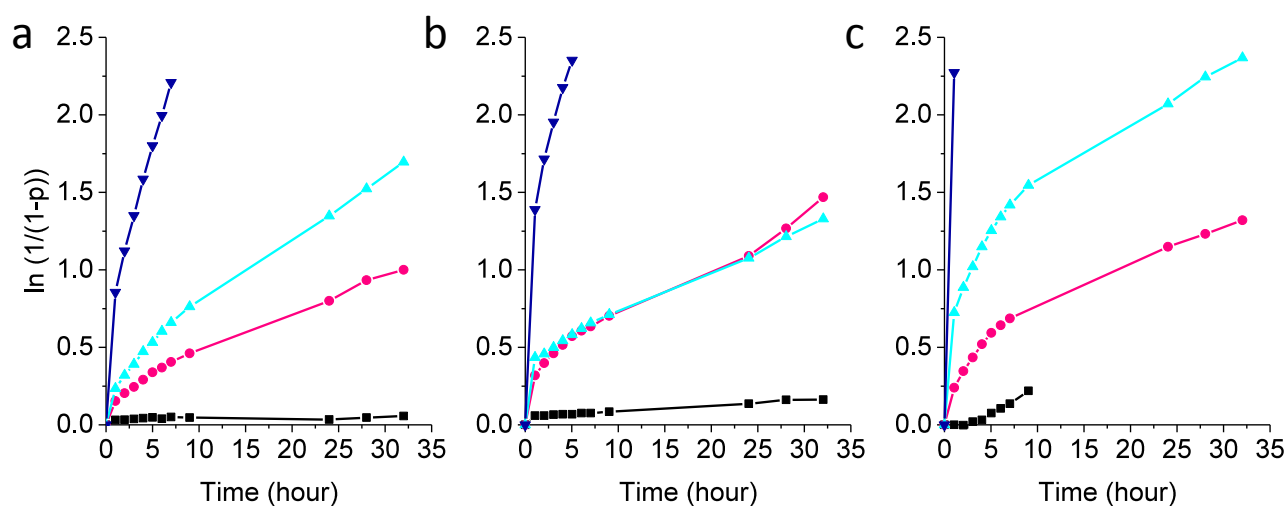
Figure III.8 First order time conversion plots for the polymerisations of (a) BʟG-NCA (100 equiv.), (b) ʟLeu-NCA (100 equiv.) and (c) ʟPhe-NCA (100 equiv.) in DMF initiated by ■ BnA·HCl (1 equiv.), ● BnA·HCl/TEA (1:0.5 equiv.), ▲ BnA (1 equiv.), and ▼ TEA (0.5 equiv.). Monomer conversions were determined by FTIR spectroscopy (Section III.2.2.2) (Appendix B, P44-46).

Tertiary amine-initiated ROP of NCA are known to proceed *via* the AMM, a mechanism that enables the rapid achievement of high conversions and large molar masses, albeit with broad distributions, principally due to the regeneration of the tertiary amine and the existence of active *N*-acylated species at the α-end of all chains.[36–38] This mechanism was well illustrated by the steep aspect (i.e., large slope) of ln(1/(1-p))(t) plots of TEA-initiated ROP of BʟG-, ʟLeu-NCA and ʟPhe-NCA (Figure III.8) and large dispersities (Figure III.7).[38] In light of these considerations, it could be rationally postulated that for primary ammonium/tertiary amine- and primary amine-initiated ROP of NCA, both NAM and AMM co-exist, with the AMM predominating in the early stages of propagations, as indicated by initially rapid conversions.

To provide further evidence to the NAM-AMM coexistence model, initiator mixtures of primary and tertiary amines without hydrochloric acid were investigated. A polymerisation series of BʟG-NCA initiated by mixtures of BnA (1 equiv.) and TEA (0 to 1.5 equiv.) in different ratios was followed by FTIR (Figure III.9). As the fraction of TEA increased, the dispersity increased and the ln(1/(1-p))(t) plots became gradually more 'concave'. Based on and molar mass results, the control is lost when TEA exceeded 0.5-0.8 equiv. relative to BnA. This result is coherent with the observation that PyA·HCl/TEA-initiated ROP of NCA became uncontrolled when TEA exceeded 1.5 equiv. relative to PyA·HCl (Section III.3.2). Moreover, the ROP of BʟG-NCA initiated with BnA/TEA (1:0.5 equiv.) generated very similar time-conversion plots, molar masses dispersities as when initiated with BnA·HCl/TEA (1:1.5 equiv.) (Figure III.10). These results further consolidate the hypothesis according to which NAM and AMM coexist during the chain growth of both primary ammonium/tertiary amine- and primary amine-initiated ROP, and that the NAM is the prevailing mechanism, ensuring the controlled nature of the polymerisation, as long as the tertiary amines remains under about 1.5 equiv. and 0.5 equiv. relative to primary ammonium salts and primary amines, respectively.

Figure III.9 Time-conversion and first order time conversion plots for the polymerisations of BʟG-NCA (100 equiv.) in DMF initiated by ▲ BnA (1 equiv.), ■ BnA/TEA (1:0.5 equiv.), ● BnA/TEA (1:0.8 equiv.), ▼ BnA/TEA (1:1 equiv.), and ◆ BnA/TEA (1:1.5 equiv.). Monomer conversions were determined by FTIR spectroscopy (Section III.2.2.2); the polymer dispersities at 24 and 25 h were determined by SEC (Appendix B, P47-A, P47-E and P55 series).

The accelerating effect of the addition of a tertiary amine in the ROP of NCA was also tested for hydroxyl initiators, which are known to be less efficient initiators than amines (due to their lower nucleophilicity). For that purpose, ROP of BʟG-NCA was initiated with 1-pyrenemethanol (PyOH)/TEA (1:0.5 equiv.) but resulted in an uncontrolled polymerisation (Đ(25 h) = 2.32; conversion > 95% after 5 h). In comparison, when PyOH was used alone, the conversion remained under 5% after 25 h (Appendix B).

Interestingly, the present study somewhat corresponds to a form of negative control experiment that could have been used by Zhao et al. to support their hypothesis of a monomer activation (AAMMA) mechanism in the case of initiators comprising of both primary and tertiary amines.[15] Zhao et al. ruled out the possibility that the NAM and the AMM could coexist and lead to a controlled polymerisation, instead proposing a new mechanism (AAMMA), involving the activation of NCAs with the tertiary amines present at the α-end of each polymer. The advantage of using a mixture of primary and tertiary amines is that their ratios can be precisely set, which allowed for the observation of a gradual and smooth transition from a controlled to an uncontrolled polymerisation (Figure III.9). This, together with the study performed on primary ammonium/tertiary amine-initiated ROP of NCA (Sections III.3.1 to III.3.4), point toward a NAM-AMM coexistence model. In order to validate this hypothesis, negative controls shall be investigated using mixtures of primary, secondary and tertiary amines, and comparing them to equivalent molecules composed of multiple amino groups in future studies.

III.3.6   Effect of NCA Concentration, Temperature and Copolymerisation

In order to understand how other parameters, such as temperature and concentration affect the primary ammonium/tertiary amine-initiated ROP of NCA, a series polymerisations was followed by FTIR (Figure III.10). The BnA·HCl/TEA ratios were kept within the pre-established range to maintain the polymerisation controlled. Interestingly, a close to linear $\ln(1/(1-p))(t)$ plot was obtained when a lower concentration of NCA was used, 50 g·L^{-1} instead of 100 g·L^{-1} (used in the rest of this study) and 200 g·L^{-1} (whose plot further deviated from linearity). This may indicate that using a lower NCA concentration lowers the incidence of side reactions and/or the AMM. Indeed, the AMM is likely to be associated with reaction orders greater than 1 with respect to NCAs (Scheme III.1b), and would be more affected by a change of NCA concentration than the NAM and dormant-active mechanisms, which are first order reactions with respect to NCAs (Scheme III.3 and Equation III.1).

Higher temperatures led to $\ln(1/(1-p))(t)$ plots composed of a steeper slope in the early propagation stage (2 to 8 h), before 'straightening up'. The ammonium/amine equilibrium as well as the propagation and reaction rates for both the AMM and the NAM are likely to vary with the temperature. Therefore, the complexity of the primary ammonium/tertiary amine-initiated ROP of NCA, in terms of the number of different co-existing mechanisms (*e.g.*, AMM, NAM and dormant-active mechanism) and equilibriums (*e.g.*, amine/ammonium), does not allow to make an informed conclusion based on the only three temperatures tested (rt, 50 and 80 °C).
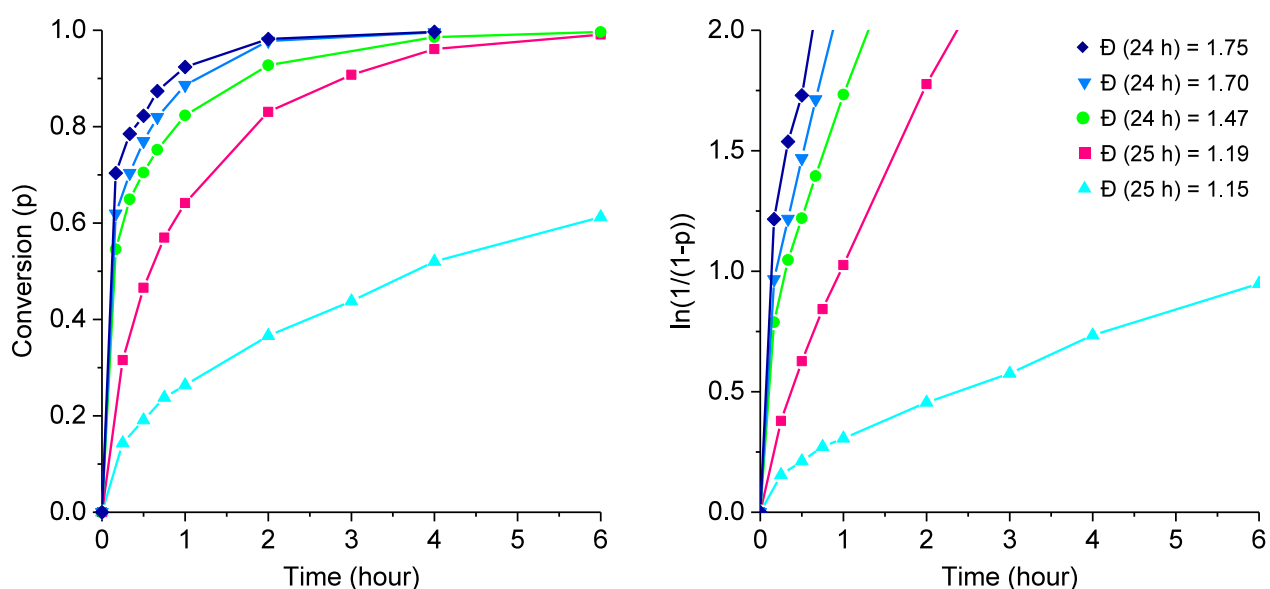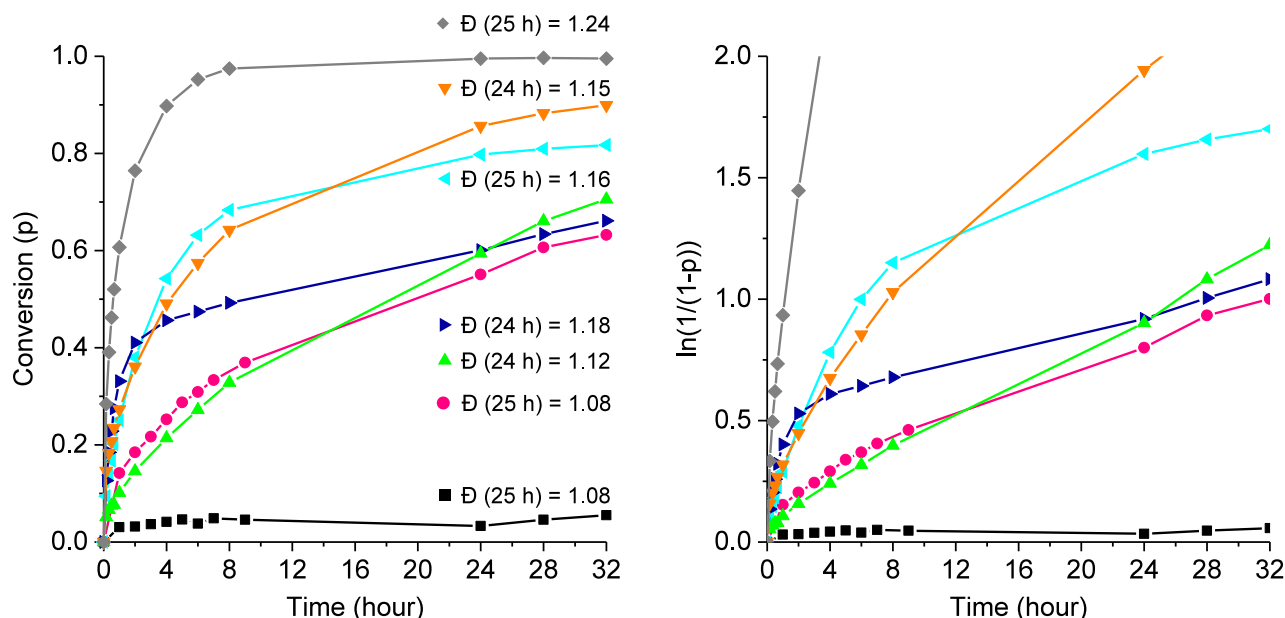
Figure III.10 Time-conversion and first order time conversion plots for the polymerisations of BʟG-NCA (100 equiv.) in DMF initiated by ■ BnA·HCl (1 equiv.), ● BnA·HCl/TEA (1:0.5 equiv.), ◄ BnA·HCl/TEA (1:0.5 equiv.) and maintained at 50 °C, ► BnA·HCl/TEA (1:0.5 equiv.) and maintained at 80 °C, ▲ BnA·HCl/TEA (1:0.5 equiv.) with $[NCA]_0$ = 50 g·L^{-1}, ▼ BnA·HCl/TEA (1:0.5 equiv.) with $[NCA]_0$ = 200 g·L^{-1}, and ◆ BnA·HCl/TEA (1:1.5 equiv.). Monomer conversions were determined by FTIR spectroscopy (Section III.2.2.2); the polymer dispersities at 24 and 25 h were determined by SEC (Appendix B, P44-B, P44-C, P57 series and P58).

In order to conclude with certainty on the reactions involved in the primary ammonium/tertiary amine-mediated ROP of NCA and quantify their individual involvement at different stages of the chain growth, more data and repeats are required. To do so, the kinetic parameters of the NAM and dormant-active mechanism ought to be extracted from 'near ideal' ln(1/(1-p))(t) plots, and ln(1/(1-p))(t) plots corresponding to reactions proceeding solely *via* the AMM ought to be fitted, in order to establish a polymerisation rate equation and extract its corresponding parameters. To identify these equations and parameters, a series of polymerisations with different NCA concentrations and initiator mixtures are required. A more comprehensive study would require in addition to vary additional parameters including counter-ions, solvents, temperatures and target molar masses. Complementing the kinetic study with additional analyses of the reaction medium over time by ^{1}H-NMR spectroscopy and mass spectrometry, in carefully selected solvents, may help identify the species present in the early propagation stages.

In addition, it cannot be excluded that the secondary structures of the growing polymer chains may have an effect on the kinetics. Indeed, some studies on the kinetics of ROP of NCA (mostly in dioxane) initiated by primary amines have reported that initially slow polymerisations became faster once the growing oligomers had reached a sufficient length (~ 8 repeat units for PBʟG);[39] this would appear to be the opposite phenomenon to what was observed in DMF.[40–42] Different hypotheses were then proposed to explain this two-tier phenomenon.[43–45] The latter was principally ascribed it to a change in conformation that occurs once a certain degree of polymerisation has been reached: either (i) a random coil to α-helical transition occurs and the acceleration in the polymerisation rate results from a facilitated addition of NCAs to the growing chain enabled by well-positioned hydrogen bonds,[46,47] or (ii) initially aggregated β-sheets

propagate slowly due to their limited solubility and intermolecular hydrogen bonding but change conformation above a certain degree of polymerisation, leading to rapidly growing random coils.[26,48] It therefore seems appropriate that any future work is supplemented with analyses of the secondary structure, for instance by CD spectroscopy.

Finally, the primary ammonium/tertiary amine-mediated ROP of NCA was used to copolymerise BLG- and LAG-NCAs (Appendix B, P49 to P52, and P49D to P52D). A small systematic error, whereby the BLG molar fraction was slightly larger than the monomer feed (*i.e.*, the target), was observed. This discrepancy might be caused by an experimental error or it may indicate that the incorporation of BLG was favoured over that of LAG. The latter case may be characteristic of the AMM contribution. The copolymerisation of different NCAs using this new ROP of NCA technique thus requires further investigations and may incidentally help with the study of its overall mechanism and the quantification of the different contributing reactions (*e.g.*, NAM, AMM, dormant-active).

III.4   Conclusions

A novel and versatile way of controlling ROP of NCA (*e.g.*, BLG-, LLeu- and LPhe-NCA) by using an initiator system composed of a primary ammonium salt (*e.g.*, TAB·3HCl, PyA·HCl and BnA·HCl) and a tertiary amine (*e.g.*, TEA and DIPEA) was reported. The rate of polymerisation could be controlled by varying the primary ammonium salt to tertiary amine ratio, and the polymerisation could even be paused and resumed by the addition of HCl and TEA, respectively. The control was preserved even for TEA fractions as high as 1.5 equiv. relative to the primary ammonium salt. This result is exceptional as tertiary amines favour the AMM, *i.e.*, the mechanism responsible for uncontrolled polymerisations resulting in large polypeptides with broadly distributed molar masses. Primary amines, on the other hand, favour the NAM, *i.e.*, the mechanism responsible for controlled polymerisations. Controlled ROP of NCA are often thought to proceed *via* a NAM-only pathway, excluding the occurrence of the AMM,[15] although, as pointed out by Deming, a system can switch back and forth between the NAM and the AMM many times during a polymerisation, even when initiated by primary amines.[9] In fact, the kinetic studies carried out in this study showed that even primary amine-initiated ROP of NCA did not produce perfectly linear first order time conversion plots, which is normally expected for a NAM-only mechanism, and is thus indicative of side-reactions. The large slope of the plots in the early stages of the polymerisation, reminiscent of the TEA-initiated polymerisation plots, suggests that the AMM might have contributed to the overall reaction. Based on these considerations, it was hypothesised that both NAM and AMM contribute to the overall mechanism of the newly established primary ammonium/tertiary amine-mediated ROP of NCA and also to the more traditional primary amine-initiated ROP of NCA. More precisely, it was proposed that the rapid monomer conversion in the early stages of the polymerisation is enabled by the AMM, while the NAM prevails for the remaining of the propagation, thereby maintaining the polymerisation controlled.

This hypothesis was further supported by the polymerisation series initiated by mixtures of primary amines (*e.g.*, BnA) and tertiary amines (*e.g.*, TEA). Indeed, these polymerisations remained controlled even for initiator mixtures of up to 0.8 equiv. of TEA relative to BnA. Moreover, there was no sharp increase, rather a gradual increase of the dispersity with increasing TEA mole fraction. This result further highlights the fact that the level of control of the ROP of NCA can be finely tuned by the initiator mixture, more precisely by the primary amine/tertiary amine molar ratio, through a fine balance between two mechanisms, namely the NAM and the AMM. This outcome hence reveals a notion of gradual decrease or increase of control, rather than a 'black or white' model. As such, the control of primary ammonium/tertiary amine-mediated ROP of NCA is directly related the ratio of primary amine/tertiary amine/Brønsted-Lowry acid (*e.g.*, hydrochloric acid), with the tertiary amine essentially acting as a catalyst. Although all aforementioned evidences suggest that both the NAM and the AMM coexist throughout the primary ammonium/tertiary amine-mediated and primary amine/tertiary amine-initiated ROP of NCA, only the identification of the actual reactions kinetics and their parameters would constitute an irrefutable proof of such a model. However, this is a complex task as such polymerisation reactions involve several interdependent pathways and acid-base equilibria, which are sensitive to parameters including temperature, counter ions and secondary structure of the growing chain.

Therefore, as future work, a comprehensive study is recommended to determine accurate rate equations, extract kinetic parameters, and finally establish a complete mechanistic model. In addition, since the AMM is known to favour stereospecificity[48,49] (*i.e.*, tacticity resulting from the copolymerisation of D and L monomers) and to be affected by the nucleophilicity of *N*-acylated NCA chain ends[50] (which may vary with the nature of the NCA), the copolymerisation of NCAs by primary amine/tertiary amine-initiated ROP of NCA ought to be thoroughly investigated, particularly in terms of the resulting comonomer composition and distribution.

III.5 References

(1)   O'Reilly, R. K. *Polym. Int.* **2010**, *59*, 568–573.

(2)   Stuart, M. A. C.; Huck, W. T. S.; Genzer, J.; Müller, M.; Ober, C.; Stamm, M.; Sukhorukov, G. B.; Szleifer, I.; Tsukruk, V. V; Urban, M.; Winnik, F.; Zauscher, S.; Luzinov, I.; Minko, S. *Nat. Mater.* **2010**, *9*, 101–113.

(3)   Deming, T. J. *Prog. Polym. Sci.* **2007**, *32*, 858–875.

(4)   Balazs, A. C.; Emrick, T.; Russel, T. P. *Science* **2006**, *314*, 1107–1111.

(5)   Brosnan, S. M.; Schlaad, H.; Antonietti, M. *Angew. Chem. Int. Ed. Engl.* **2015**, *54*, 9715–9718.

(6)   Mabire, A. B.; Robin, M. P.; Willcock, H.; Pitto-Barry, A.; Kirby, N.; O'Reilly, R. K. *Chem. Commun.* **2014**, *50*, 11492–11495.

(7)   Kricheldorf, H. R. *Angew. Chem. Int. Ed. Engl.* **2006**, *45*, 5752–5784.

(8)   Hadjichristidis, N.; Iatrou, H.; Pitsikalis, M.; Sakellariou, G. *Chem. Rev.* **2009**, *109*, 5528–5578.

(9)   Deming, T. J. *Adv. Polym. Sci.* **2006**, *202*, 1–18.

(10)   Deming, T. J. *Nature* **1997**, *390*, 386–389.

(11)   Lu, H.; Cheng, J. *J. Am. Chem. Soc.* **2007**, *129*, 14114–14115.

(12)   Dimitrov, I.; Schlaad, H. *Chem. Commun.* **2003**, No. 23, 2944–2945.

(13)   Vayaboury, W.; Giani, O.; Cottet, H.; Deratani, A.; Schué, F. *Macromol. Rapid Commun.* **2004**, *25*, 1221–1224.

(14)   Aliferis, T.; Iatrou, H.; Hadjichristidis, N. *Biomacromolecules* **2004**, *5*, 1653–1656.

(15)   Zhao, W.; Gnanou, Y.; Hadjichristidis, N. *Chem. Commun.* **2015**, *51*, 3663–3666.

(16)   Zhao, W.; Gnanou, Y.; Hadjichristidis, N. *Biomacromolecules* **2015**, *16*, 1352–1357.

(17)   Lutz, J.-F.; Schütt, D.; Kubowicz, S. *Macromol. Rapid Commun.* **2005**, *26*, 23–28.

(18)   Meyer, M.; Schlaad, H. *Macromolecules* **2006**, *39*, 3967–3970.

(19)   Brulc, B.; Žagar, E.; Gadzinowski, M.; Słomkowski, S.; Žigon, M. *Macromol. Chem. Phys.* **2011**, *212*, 550–562.

(20)   Tang, H.; Zhang, D. *J. Polym. Sci. Part A Polym. Chem.* **2013**, *51*, 4489–4497.

(21)   Kanzian, T.; Nigst, T. A.; Maier, A.; Pichl, S.; Mayr, H. *European J. Org. Chem.* **2009**, *2009*, 6379–6385.

(22)   Peng, H.; Ling, J.; Zhu, Y.; You, L.; Shen, Z. *J. pol* **2012**, *50*, 3016–3029.

(23)   Zelzer, M.; Heise, A. *J. Polym. Sci. Part A Polym. Chem.* **2014**, *52*, 1228–1236.

(24)   Wong, S.; Kwon, Y. J. *J. Polym. Sci. Part A Polym. Chem.* **2015**, *53*, 280–286.

(25)   Mavrogiorgis, D.; Bilalis, P.; Karatzas, A.; Skoulas, D.; Fotinogiannopoulou, G.; Iatrou, H. *Polym. Chem.* **2014**, *5*, 6256–6278.

(26)   Gibson, M. I.; Cameron, N. R. *J. Polym. Sci. Part A Polym. Chem.* **2009**, *47*, 2882–2891.

(27)   Trathnigg, B. In *Encyclopedia of Analytical Chemistry*; John Wiley & Sons, Ltd: Chichester, UK, **2006**; pp 8008–8034.

(28)   Russell, D. H.; Edmondson, R. D. *J. Mass Spectrom.* **1997**, *32*, 263–276.

(29)   Kricheldorf, H. R. In *Alpha-Aminoacid-N-Carboxy-Anhydrides and Related Heterocycles*; Springer Berlin Heidelberg, **1987**; pp 16–21.

(30)   Grawe, T.; Schrader, T.; Zadmard, R.; Kraft, A. *J. Org. Chem.* **2002**, *67*, 3755–3763.

(31)   Sardar, R.; Shem, P. M.; Pecchia-Bekkum, C.; Bjorge, N. S.; Shumaker-Parry, J. S. *Nanotechnology* **2010**, *21*, 345603.

(32)   Guo, X.; Zhang, D.; Zhou, Y.; Zhu, D. *Chem. Phys. Lett.* **2003**, *375*, 484–489.

(33)   Kim, K. T.; Park, C.; Vandermeulen, G. W. M.; Rider, D. A.; Kim, C.; Winnik, M. A.; Manners, I. *Angew. Chemie Int. Ed.* **2005**, *44*, 7964–7968.

(34)   Cheng, J.; Deming, T. J. *Top. Curr. Chem.* **2012**, *310*, 1–26.

(35)   Odian, G. In *Principles of polymerization*; **2004**; pp 578–581.

(36)   Matsuoka, S.; Kikuno, T.; Takagi, K.; Suzuki, M. *Polym. J.* **2010**, *42*, 368–374.

(37) Chanda, M. *Introduction to Polymer Science and Chemistry: A Problem-Solving Approach*, Second Edi.; CRC Press, **2013**.

(38) Cosani, A.; D'Este, G.; Peggion, E.; Scoffone, E. *Biopolymers* **1966**, *4*, 595–599.

(39) Block, H. *Poly(gamma-benzyl-L-glutamate) and other glutamic acid containing polymers*; Gordon and Breach Science Publishers Ltd., **1983**.

(40) Lundberg, R. D.; Doty, P. *J. Am. Chem. Soc.* **1957**, *79*, 3961–3972.

(41) Coombes, J. D.; Katchalski, E. *J. Am. Chem. Soc.* **1960**, *82*, 5280–5285.

(42) Mori, H.; Iwata, M.; Ito, S.; Endo, T. *Polymer* **2007**, *48*, 5867–5877.

(43) Idelson, M.; Blout, E. R. *J. Am. Chem. Soc.* **1957**, *79*, 3948–3955.

(44) Hasegawa, E.; Shibata, T.; Takeuchi, H.; Tsuchida, E. *Eur. Polym. J.* **1977**, *13*, 669–672.

(45) Rinaudo, M.; Domard, A. *Biophys. J.* **1976**, *15*, 2185–2199.

(46) Weingarten, H. *J. Am. Chem. Soc.* **1958**, *80*, 352–355.

(47) Williams, F. D.; Brown, R. D. *Biopolymers* **1973**, *12*, 647–654.

(48) Williams, F. D.; Eshaque, M.; Brown, R. D. *Biopolymers* **1971**, *10*, 753–765.

(49) Kricheldorf, H. R.; Mang, T. *Die Makromol. Chemie* **1981**, *182*, 3077–3098.

(50) Kricheldorf, H. R.; Chemie, M. **1979**, *109*, 97–109.

Chapter IV

Secondary Structure and Physical Gelation of Polypeptides

This chapter contains results and material that have been published and are hereby reproduced by permission of the American Chemical Society (See Appendix C for the list of publications).

IV.1   Introduction

The rapidly growing interest in biomimetic and bio-inspired materials is driven by the increasing need for highly functional and efficient materials such as those found in nature (*e.g.*, nacre, spider silk, or mussel glue), which often outweigh even the best synthetic materials.[1–3] As part of the search for biomimetic materials, substantial effort has been dedicated to the study of structure-property relationships of biological samples, with a view to synthetically replicating such relationships.[4] Similarly, bio-inspired materials aim to recreate structures, functions, or properties observed in biological samples, yet with a view to synthesising novel or more performant materials.[5] The complexity of natural polymers (*e.g.*, sequence control, composition, or branching) is such that, driven by synthetic limitations, a common approach for the design of bio-inspired polymers often consists in simplifying their composition and architecture, while maintaining some key biological properties (*e.g.*, secondary structure, functional groups, biocompatibility, etc.) in order to aim for the targeted bio-inspired property, structure, or function.[6,7] As such, bio-inspired polymers often need modifying and redesigning to further adjust or improve their properties. A systematic approach to do so is by establishing design rules through the study of structure-property relationships.

Collagen is a protein which, owing to its ability to form fibres, plays a crucial structural and mechanical role in the many tissues it is found in (*e.g.*, cartilages, tendons, or bones).[8] Its structure-property relationships have been extensively studied,[9,10] and collagen-mimetic peptides, generally produced by cost-intensive solid phase synthesis, hence received much attention from synthetic chemists.[11–13] Simpler bio-inspired approaches consist in replicating only some essential characteristics that give collagen its ability to form complex structures.[14] In particular, the secondary structure of collagen

strands is essential to their ability to form triple helices, which in turn self-assemble into fibrils and fibres, which are stabilised by both hydrogen-bonding and enzymatic crosslinking.[9,15]

Poly(γ-benzyl-L-glutamate) (PBLG) is a synthetic polypeptide whose α-helical secondary structure enables it to self-assemble into fibres, which in turn trap solvent, resulting in a physical gel. A physical gel is more generally defined as a solid-like gel stabilised by non-convalent bonds (*i.e.*, as opposed to a chemical gel).[16,17] The stiffness of the α-helices causes PBLG to abide by the Flory phase diagram for rigid rod-like polymers.[18] As such, PBLG undergoes physical gelation upon reduction of the temperature and forms liquid crystalline phases at high concentrations, in helicogenic solvents such as toluene, benzylalcohol, m-cresol or DMF.[19–24] PBLG, whose carboxylic ester functions can be easily deprotected to yield biocompatible PLGA, therefore, represents an attractive polymer precursor for the preparation of bio-inspired and biomedical fibrous gels or materials. Copolymerising BLG with functionalisable comonomers such as allylglycine (AG) or propargylglycine significantly extends the versatility of PBLG by making it functionalisable[7,25–27] and crosslinkable.[28,29] Notably, the bio-related applications of debenzylated and functionalised BLG-based copolymers has recently received a great deal of attention.[26,27,30,31] Although the aggregation[32–35] and gelation[24,36–38] of PBLG in helicogenic solvents like dioxane and toluene, respectively, is well known, that of such BLG-based copolymers has yet to be explored.

The introduction of AG comonomers - which promote β-sheet rather than α-helical conformations[39] - into PBLG is expected to alter the structure and properties of the polypeptide.[27,28] Indeed, it was previously shown that substituting BLG for AG moieties causes a reduction of the helicity of poly(L-glutamic acid-*co*-allylglycine) (P(LG-*co*-AG)) (*i.e.*, debenzylated P(BLG-*co*-AG)).[27] Unlike PBLG, however, PLGA and derivatives (*i.e.*, P(LG-*co*-AG)) do not undergo gelation. Characterising and comparing the gelation and rheological properties of P(BLG-*co*-AG) in relation to their secondary structures and organisation would allow for the establishment of structure-property relationships, thereby leading to a better understanding of the physical impact of the substitution of BLG for AG in PBLG. Such a study may even help predict the behaviour and properties of other polypeptide gelators or rod-like polymers,[39–41] and to design rules for the preparation and tuning of PBLG- and PLGA-based gels and the like.

IV.2 Experimental

IV.2.1 Materials

The synthesis of statistical copolypeptides of γ-benzyl-L-glutamate (BLG) and allylglycine (AG), referred to as P(BLG$_x$-*co*-AG$_{1-x}$)$_n$ hereafter, is described in Chapter II and Appendix A, and the copolymers used for this study are gathered in Table IV.1. Homopolymer PBLG$_{51}$ is used as the reference polymer. Other chemicals and solvents used for this study are gathered in Appendix A.

Table IV.1 Molecular Characteristics of Polypeptides Used in Chapter IV (Appendix B, P1 to P4, P12 to P16, P33, P40, and P59)

Sections	Polymer	γ-Benzyl-L-glutamate (BLG)		Allylglycine (AG)		M_n^a	n^a	$Đ^{app}$
		Mole fraction[a]	Configu-ration	Mole fraction[a]	Configu-ration	(kg·mol⁻¹)		$(M_w/M_n)^b$
A IV.3.1 to IV.3.4	PBLG$_{51}$	100%	L	-	-	11.3	51	1.09
	P(BLG$_{0.89}$-co-DLAG$_{0.11}$)$_{53}$	89%	L	11%	DL	11.0	53	1.18
	P(BLG$_{0.76}$-co-DLAG$_{0.24}$)$_{59}$	76%	L	24%	DL	11.4	59	1.16
	P(BLG$_{0.77}$-co-LAG$_{0.23}$)$_{57}$	77%	L	23%	L	11.1	57	1.25
	P(BLG$_{0.74}$-co-LAG$_{0.26}$)$_{91}$	74%	L	26%	L	17.2	91	1.21
	P(BLG$_{0.78}$-co-LAG$_{0.22}$)$_{96}$	78%	L	22%	L	18.6	96	1.13
	P(BLG$_{0.74}$-co-LAG$_{0.26}$)$_{170}$	74%	L	26%	L	31.9	170	1.28
	P(BLG$_{0.80}$-co-LAG$_{0.20}$)$_{219}$	80%	L	20%	L	42.8	219	1.23
	P(BLG$_{0.84}$-co-LAG$_{0.16}$)$_{171}$	84%	L	16%	L	34.2	171	1.28
B IV.3.2	PBLG$_{159}$	100%	L	-	-	35.0	159	1.21
	star-(PBLG$_{20}$)$_3$	100%	L	-	-	13.6	60	1.13
	"star"-(P(BLG$_{0.50}$-co-LAG$_{0.50}$)$_{73}$)$_2$	50%	L	50%	L	23.4	146	1.27

[a] M_n = number-average molar mass. n = number-average degree of polymerisation. Determined by ^{1}H-NMR (Appendix A).
[b] $Đ^{app}$ = M_w/M_n = ratio of weight over number-average molar mass (dispersity). Determined by SEC (PMMA calibration) (Appendix A).

IV.2.2 Methods

IV.2.2.1 Preparation of Physical Gels

Thermoreversible gels were prepared by dissolving the copolypeptides in toluene, to achieve concentrations between 4 and 50 g·L⁻¹ (*i.e.*, 0.4 to 5% w/v), at 60 °C (for PBLG$_{51}$) or at room temperature (for P(BLG$_x$-*co*-AG$_{1-x}$)$_n$) and cooling the mixtures down to room temperature or to -40 °C, respectively.

IV.2.2.2 Rheology

Rheological measurements were performed on a DHR-3 rheometer (TA Instruments), using a parallel plate-plate set-up in oscillation mode (frequency = 1 Hz). A Dual Stage Peltier Plate was used as lower plate and temperature controller. The upper geometry was a 40 mm diameter plate and the measurement gap was set to 500 µm for all experiments. Typically, 0.6 mL of a P(BLG$_x$-*co*-AG$_{1-x}$)$_n$-toluene solution (20 g·L⁻¹) was sandwiched between the plates at room temperature and confined in a controlled atmosphere chamber. The latter was equipped with a toluene reservoir in order to saturate the atmosphere with toluene vapours, to prevent the samples from drying, especially at the atmosphere-exposed edge. The cooling rate of the temperature ramp was set to -3 K·min⁻¹, from 30 °C to -40 °C for the copolymers, and from 60 °C to 0 °C for the homopolymer. In order to avoid damaging the developing gel, the strain was set to 0.5%. Additionally, the axial force control was turned on. This feature accounts for the shrinkage of the sample during cooling and gelation and adjusts the measurement gap to maintain an optimally filled sample.

See Appendix A for all other analytical methods used here (i.e., NMR, FTIR, Raman, WAXS, DSC, CD, AFM and TEM).

IV.3 Results and Discussion

IV.3.1 Physical Gelation

Upon dissolving PBLG$_{51}$ in hot toluene (typically at 60 °C, and down to 1 g·L^{-1}) and cooling it down to room temperature, the solution set into a solid-like physical gel. This behaviour is typical of PBLG$_n$ polymers, noted PBLG hereafter for simplicity. PBLG gels are thermoreversible and therefore melt again upon increasing the temperature. The microstructure of PBLG gels is well known: it is composed of a solvent trapping sheaf-like network of entangled fibres or bundles of fibrils, themselves formed by aggregated α-helical PBLG chains (Figure IV.1).[19,24,37,42] As reported in the literature[43] and attested by Figure IV.1, these bundles range in width between under 10 nm and 100 nm.
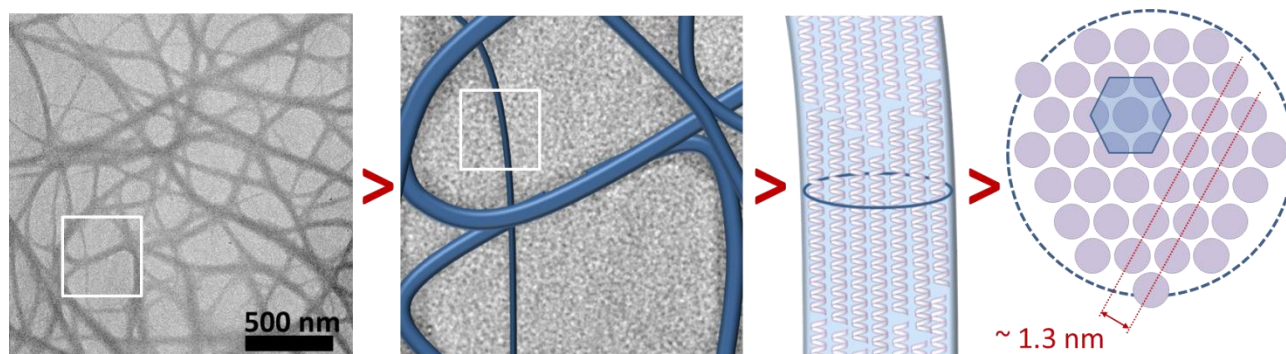

Figure IV.1 TEM micrograph of a 4 g·L^{-1} (*i.e.*, 0.4% w/v) organogel of PBLG$_{51}$ in toluene (scale bar = 500 nm), schematic microstructure of the fibres that compose its network, and schematic fibril cross-section showing a typical pseudo-hexagonal packing of the rod-like α-helices (of ~ 1.5 nm diameter[44]) with a typical *d*-spacing of approximately 1.3 nm.

The gelation mechanism, which will be discussed in greater details in Section IV.3.4, has been the topic of many studies over the past decades and gave rise to a variety of models.[19,24,36–38,45,46] Irrespective of the mechanism, a prerequisite for the gelation to occur is that the solvent be helicogenic and poor.[47] Unlike PBLG, all studied P(BLG$_x$-*co*-AG$_{1-x}$)$_n$ copolymers (Table IV.1A) are soluble in toluene at room temperature, which suggests that the substitution of some BLG for AG moieties is responsible for the enhanced solubility in toluene. However, as suggested by the relatively high viscosity of the P(BLG$_x$-*co*-AG$_{1-x}$)$_n$-toluene solutions[35] (Table IV.2) and by their FTIR spectra (Figure IV.2), toluene is clearly a helicogenic solvent for these copolymers too. Furthermore, most of them underwent thermoreversible physical gelation at lower temperatures, typically below 0 °C, which confirms that toluene is a poor solvent for P(BLG$_x$-*co*-AG$_{1-x}$)$_n$ at sufficiently low temperatures. Physical gelation was initially confirmed by vial inversion tests and by means of mechanical disruption with spatulae. However, the actual quantification of the gelation temperatures and other gel properties would be necessary to accurately determine the physico-chemical impact of monomer substitutions on helical polypeptides. Although indirect methods can be used to monitor chemical or physical changes that are indicative of a physical gelation (*e.g.*, NMR[48] or DSC[49]), an unambiguous method to measure the liquid-solid transition, which defines gelation, is rheology.[50]
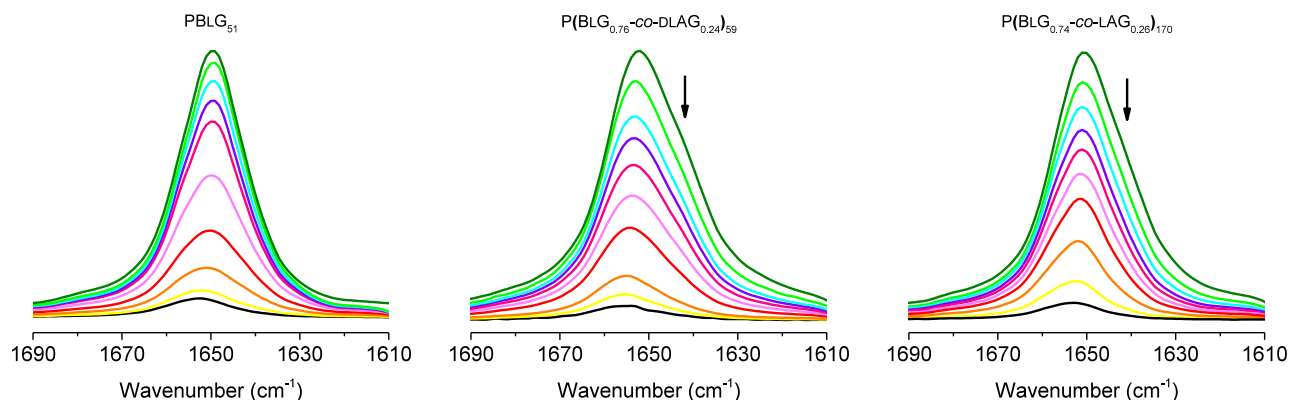
Figure IV.2 Amide I bands from FTIR spectra of P(BLG$_x$-co-AG$_{1-x}$)$_n$-toluene (50 g·L^{-1}) solutions (bottom, black spectra) that were left to dry (coloured spectra) until a film was formed (top, dark green spectra). The bands are composed of a main peak at ~ 1650 cm^{-1}, which is indicative of an α-helical conformation; the shoulder at ~ 1640 cm^{-1} (indicated by an arrow), more pronounced for the copolymers, corresponds to the α' peak, also observed in Raman spectroscopy and discussed in Section IV.3.2 and IV.3.3.

P(BLG$_x$-co-AG$_{1-x}$)$_n$-toluene gels and their mechanical properties were rheologically characterised by monitoring the evolution of the storage and loss moduli with temperature (Figure IV.3). The moduli cross-over, that is where storage and loss moduli are equal, corresponds to the physical gelation, and as such provided both gelation and melting temperature (T_{gel} and T$_m$, respectively) and the Young's modulus of the formed gel (under the dynamic conditions used) (Table IV.2). It is worth noting that the hysteresis between gelation and melting temperatures is consistent with previous studies on PBLG.[43] The gelation temperature is generally lower than the melting temperature, and their values depend on the thermal history, a characteristic with will be discussed in Section IV.3.4. This behaviour is also observed for P(BLG$_x$-co-AG$_{1-x}$)$_n$ copolypeptides, suggesting that the gels are of similar nature.

Table IV.2 Rheological Properties of PBLG and P(BLG$_x$-co-AG$_{1-x}$)$_n$ Polypeptides in Toluene

Polymer	Cross-over Modulus (Stiffness)[a] (Pa)	Complex Viscosity (η*) at 20 °C [a] (mPa·s)	Cross-over Temperature (T_{gel})[a] (°C)	Melting Temperature (T$_m$)[a] (°C)
PBLG$_{51}$	5	5900	39[#]	37
P(BLG$_{0.89}$-co-DLAG$_{0.11}$)$_{53}$	26	520	-26	2
P(BLG$_{0.76}$-co-DLAG$_{0.24}$)$_{59}$	27	630	-38	-36
P(BLG$_{0.77}$-co-LAG$_{0.23}$)$_{57}$	30	150	-27	-8
P(BLG$_{0.74}$-co-LAG$_{0.26}$)$_{91}$	96	780	-35	-17
P(BLG$_{0.78}$-co-LAG$_{0.22}$)$_{96}$	54	620	-23	-3
P(BLG$_{0.74}$-co-LAG$_{0.26}$)$_{170}$	158	2270	-23	-6
P(BLG$_{0.80}$-co-LAG$_{0.20}$)$_{219}$	444	3000	-12	8
P(BLG$_{0.84}$-co-LAG$_{0.16}$)$_{171}$	331	1450	-8	13

[a] Determined by rheometry. [#] Based on the shape of the G' and G" curves in Figure IV.3, there is a possibility that the T_{gel} actually lies at 10 °C.
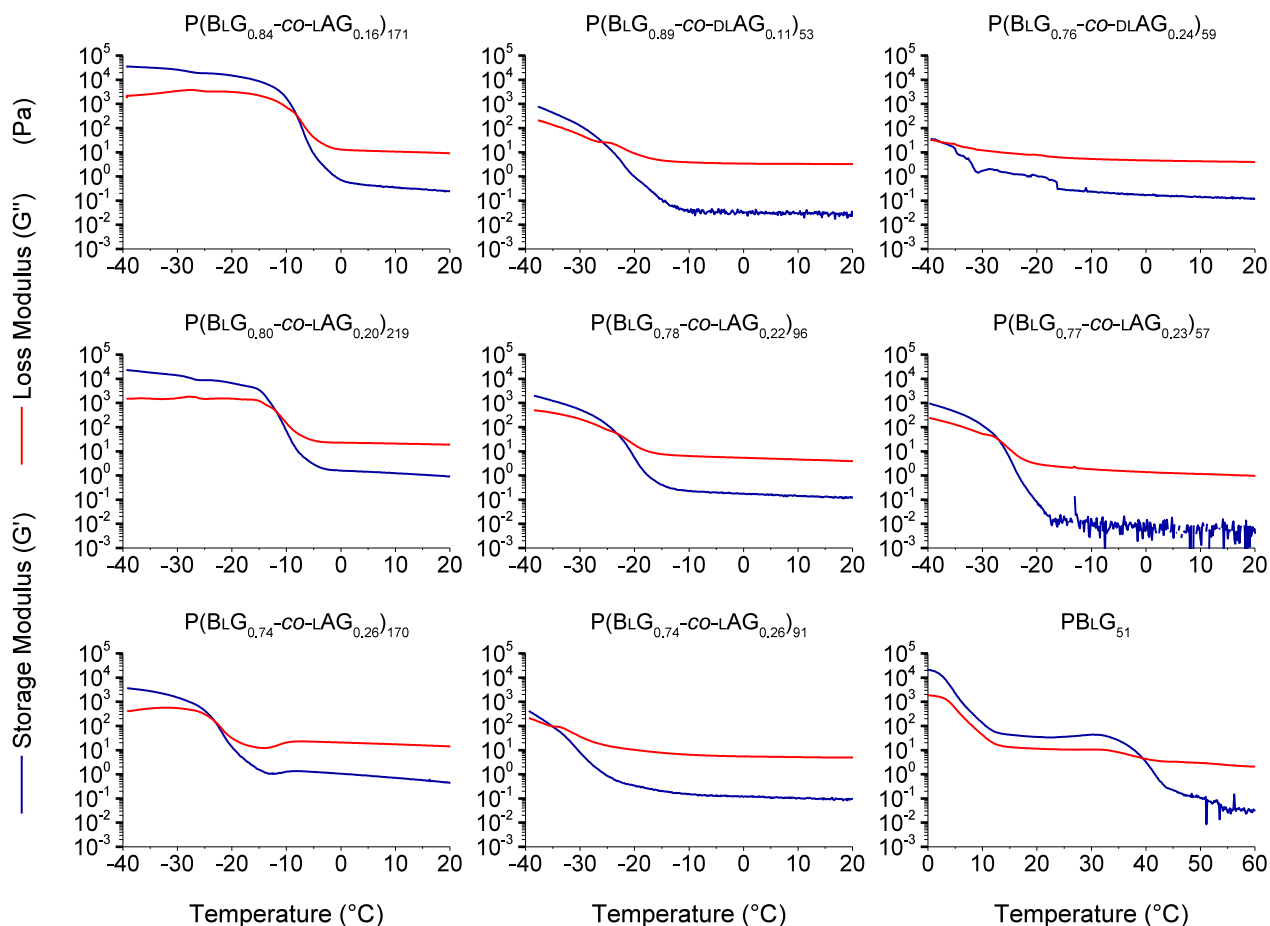
Figure IV.3 Storage and loss moduli as a function of temperature of $P(\text{BLG}_x\text{-}co\text{-}AG_{1-x})_n$ in toluene (20 g·L^{-1}) during cooling (-3 K·min^{-1}). The noise observed for some samples results from the sensitivity limits of the apparatus at the chosen low strain. As for PBLG$_{51}$, it cannot be excluded that the sharp rise of G' at 39 °C might be the result of partial drying due to the need for the analysis to be performed at higher temperatures, and that the T_{gel} actually lies at 10 °C, when both G' and G'' increase.

From the analysis of the eight copolypeptides (Table IV.1A), it was possible to show clear correlations between rheological properties (*e.g.*, viscosity, modulus, and gelation temperature) and copolypeptide compositions and chain lengths (Figure IV.4). The cross-over modulus (Figure IV.4a) and the complex viscosity (η^* at 20 °C) (Figure IV.4b) increased with increasing chain length (*n*) but remained mostly unaffected by the BLG content over the range studied (74 to 89 mol%). Interestingly, the cross-over modulus, which corresponds to the stiffness of the organogel, correlated well with the swelling ratios of the corresponding hydrogels, as later reported in Chapter V. More precisely, the stiffer the organogel, the lower the swelling ratio of the hydrogel. In this context, a lower swelling ratio could, therefore, be interpreted as being the result of a stiffer, more robust, fibrillar network, hence a less deformable gel.

On the other hand, the gelation temperature was found to increase with both increasing chain length and BLG mole fraction (Figure IV.4c). This trend could be explained by (*i*) a better solubility of AG than BLG in toluene, as initially suggested by the good solubility of $P(\text{BLG}_x\text{-}co\text{-}AG_{1-x})_n$ in toluene, and (*ii*) a decreasing solubility of copolypeptide chains with increasing chain length (Equation IV.1). The latter can be explained by the fact that the entropic contribution (ΔS_{mix}) decreases with increasing *n*, resulting in a larger

free energy of mixing (ΔG_{mix}) and hence higher T_{gel} (*i.e.*, when ΔG_{mix} = 0).[51] Interestingly, P(BLG$_{0.76}$-*co*-DLAG$_{0.24}$)$_{59}$ did not fit this trend (Figure 4c) as its gelation temperature (T_{gel} = -37 °C) was lower than expected. In contrast, P(BLG$_{0.77}$-*co*-LAG$_{0.23}$)$_{57}$ which is virtually identical to P(BLG$_{0.76}$-*co*-DLAG$_{0.24}$)$_{59}$ with the exception of the configuration of the AG moieties, gelled at a relatively higher temperature of -27 °C and fit the trend reported in Figure IV.4c, pointing to the configuration of AG (L vs. DL) as the cause for discrepancy. More generally, since the secondary structure of polypeptides is dictated by not only the nature (*e.g.*, type of amino acid) but also the configuration (*i.e.*, L or D) of the repeat units,[52] this result suggests that the relatively lower gelation temperature of all P(BLG$_x$-*co*-AG$_{1-x}$)$_n$-toluene systems may be explained not only by the better solubility of AG in toluene but also by its configuration. In order to refine this hypothesis, an in-depth study of the secondary structure of P(BLG$_x$-*co*-AG$_{1-x}$)$_n$ polymers was carried out.
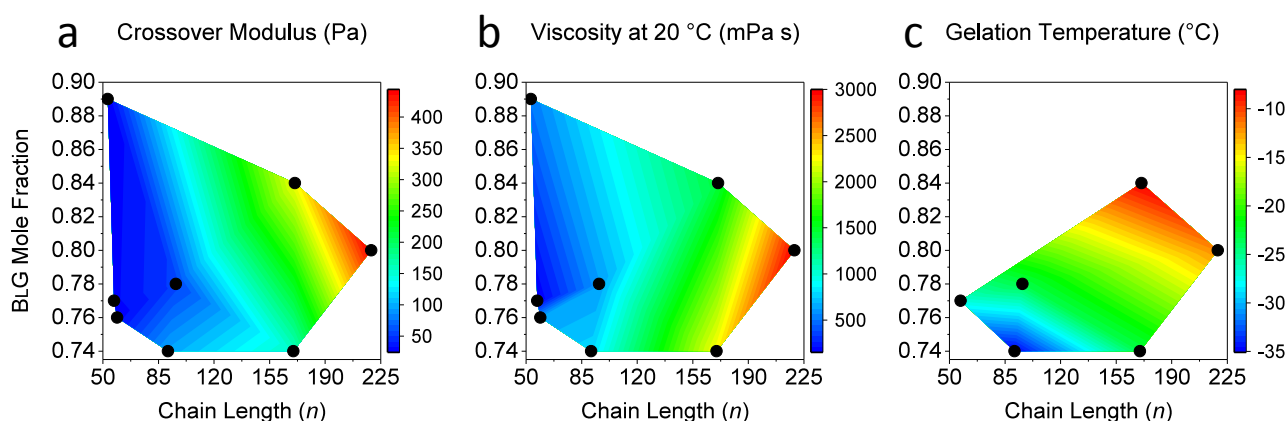

Figure IV.4 Contour maps showing (a) cross-over modulus and (b) viscosity of P(BLG$_x$-*co*-**AG**$_{1-x}$)$_n$ in toluene (20 g·L^{-1}), and (c) gelation temperature of P(BLG$_x$-*co*-**LAG**$_{1-x}$)$_n$ in toluene (20 g·L^{-1}), as a function of chain length (x axis) and mole fraction of BLG units (y axis). (a and b) The horizontal color gradient is indicative of the dependency of the crossover modulus and the viscosity with the degree of polymerisation; (c) the diagonal color gradient is indicative of the dependency of the gelation temperature with both degree of polymerisation and molar concentration of BLG units.

$$(a) \qquad \Delta G_{mix} = \Delta H_{mix} - T \cdot \Delta S_{mix}$$

$$(b) \qquad 1 - x = AG\ (mol\%)\ \uparrow \Rightarrow\ \Delta H_{mix} \downarrow \qquad\qquad n \uparrow \Rightarrow\ \Delta S_{mix} \downarrow$$

Equation IV.1 (a) Gibbs free energy of mixing for P(BLG$_x$-*co*-LAG$_{1-x}$)$_n$ and (b) expected dependencies of its enthalpic and entropic components with the chain length (n) and the copolymer composition (AG mole fraction).

IV.3.2   Secondary Structure

Raman spectroscopy is an established technique for identifying and quantifying secondary structures in proteins.[53] In particular, the composition of the Amide I band (located between 1620 and 1680 cm^{-1}), which is assigned to the C=O stretch (vC=O) of the amide group, is indicative of the polypeptide conformation. Upon the deconvolution of Amide I bands, overlapping peaks were identified and their respective contribution towards the conformation of P(BLG$_x$-*co*-AG$_{1-x}$)$_n$ polypeptides was investigated (Figure IV.5).
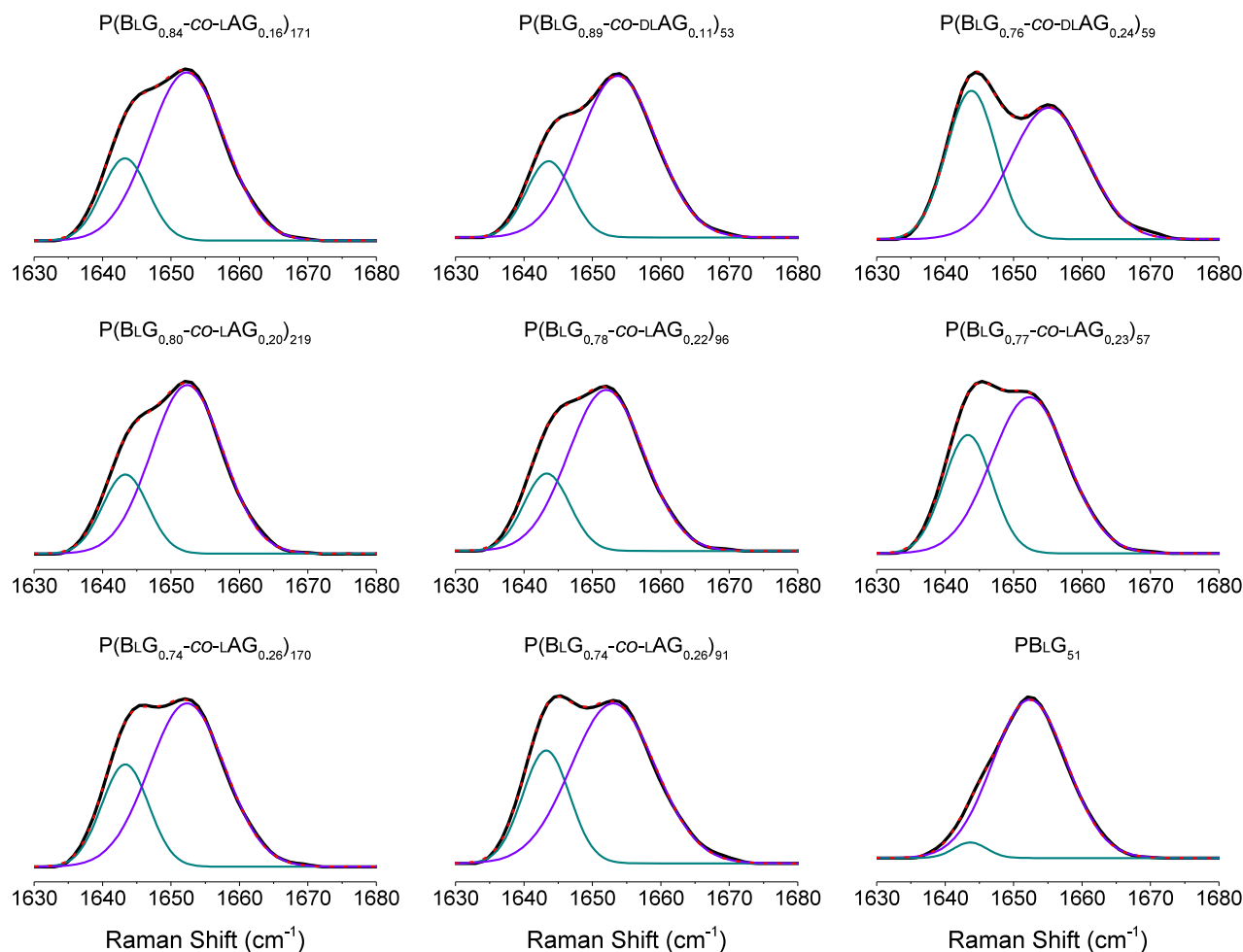
Figure IV.5 Amide I bands (black) from Raman spectra of P(BLG$_x$-*co*-AG$_{1-x}$)$_n$ polymers, composed of a main peak (α peak, violet) at approximately 1653 cm^{-1} that corresponds to an α-helical conformation,[53,54] and a second peak (α' peak, green) at approximately 1643 cm^{-1}, the exact nature of which is discussed in this study; the dashed red curve represents the cumulative fit.

The Raman spectrum of reference polymer PBLG$_{51}$ exhibits a main peak at 1653 cm^{-1} that can be safely ascribed to an α-helical conformation.[55] A very small contribution of a peak at 1643 cm^{-1} might have been deemed insignificant (or within measurement error) if it was not for the Amide I band of P(BLG$_x$-*co*-AG$_{1-x}$)$_n$ copolypeptides. The latter consists of a combination of an α-helix peak (in the 1652 to 1655 cm^{-1} range) and peak at ~ 1643 cm^{-1}, which could not be identified from the current literature and was arbitrarily noted α'. The role of the AG residues in the presence and prominence of the α' peak is confirmed by a clear correlation between this peak and the molar fraction of AG (Figure IV.6a), as well as by the relative ratio of the Amide I band to a reference peak of BLG units (Figure IV.6b). Former studies have demonstrated that for statistical copolymers of BLG - as the major comonomer (*i.e.*, > 66 mol%) and L/DL-AG, the AG units acted as defects and that the overall secondary structure of the statistical copolymer was driven by that of the BLG units (*i.e.*, α-helical);[31] this, despite the fact that poly-AG homopolymers or blocks are known to form β–sheets.[39,56] The ability for BLG units to impose an α-helical conformation was also demonstrated in other statistical copolymers of similar BLG to comonomer (*e.g.*, propargylglycine) ratios.[57] For these reasons, it can be postulated that DL- and L-AG units only have a limited impact on the overall conformation

of P(BLG$_x$-*co*-AG$_{1-x}$)$_n$ polypeptides. They may result in a small amount of 'defects' - the nature of which will be discussed in Section IV.3.3 - in an otherwise BLG-driven α-helical conformation. This is consistent with the fact that DL-AG units lead to larger α' peaks than L-AG; indeed, the presence of D-residues is expected to disrupt the L-driven right handed α-helical geometry (*e.g.*, P(BLG$_{0.76}$-*co*-DLAG$_{0.24}$)$_{59}$ vs. P(BLG$_{0.77}$-*co*-LAG$_{0.23}$)$_{57}$). The small contribution of the α' peak in the Amide I band of homopolymer PBLG$_{51}$ and its virtually non-existent contribution in longer polymer PBLG$_{159}$ (Figure IV.8 and IV9), both support this hypothesis as it has been reported that model polymer PBLG can exhibit loose ends and defects.[58–60] This would explain why shorter copolypeptides exhibit larger α' peaks (*e.g.*, P(BLG$_{0.77}$-*co*-LAG$_{0.23}$)$_{57}$ vs. P(BLG$_{0.78}$-*co*-LAG$_{0.22}$)$_{96}$).
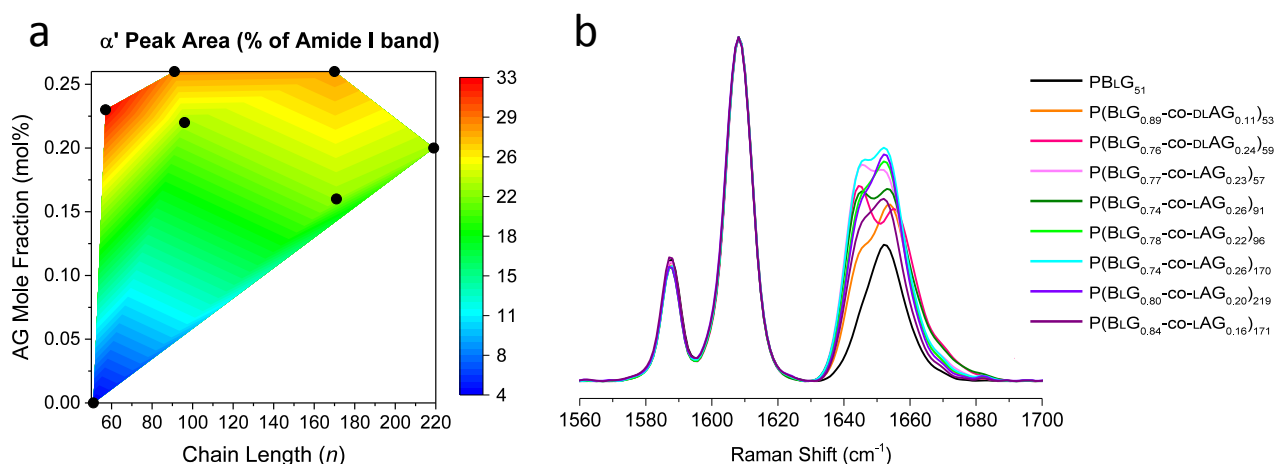

Figure IV.6 (a) Contour map showing the fraction of surface area occupied by the α' peak relative to the Amide I band (Raman) of P(BLG$_x$-*co*-**LAG**$_{1-x}$)$_n$ polypeptides, as a function of chain length (x axis) and mole fraction of BLG units (y axis). The color gradient is largely vertical, which is indicative of a strong dependency of this α' peak area with the AG mole fraction. (b) Amide I band of dry PBLG and P(BLG$_x$-*co*-AG$_{1-x}$)$_n$ copolypeptides after baseline correction and normalisation to the 1610 cm^{-1} peak, which corresponds to the ν(C-C) of the phenyl group of the BLG moiety;[61–65] since the Amide I band (1620 - 1680 cm^{-1}) of P(BLG$_x$-*co*-AG$_{1-x}$)$_n$ copolypeptides comprises the ν(C=O) peaks of BLG and AG residues, its area, relative to the 1610 cm^{-1} peak, increases with increasing AG content.

The proposed hypothesis, by which the contribution of the α' conformation towards the overall conformation may be small, seems to contrast with the large area occupied by the α' peak within the Amide I band in the Raman spectra of P(BLG$_x$-*co*-AG$_{1-x}$)$_n$ polypeptides (Figure IV.5). It is, thus, important to stress that in IR or Raman spectroscopy, relative peak heights cannot be used, without prior calibration, as direct measurements of the molar ratio of functional groups, their configurations or the conformations that they favour. Indeed, the quantum mechanical selection rules for Raman spectroscopy (*i.e.*, polarisability change) are such that some vibrations are more or less Raman active, resulting in stronger or weaker peaks, irrespective of relative mole fractions.[66] Likewise, these rules are different for infrared spectroscopy (*i.e.*, dipole moment change), which is here illustrated by a smaller α' peak, relative to the α peak, in FTIR spectra (Figure IV.7). As a result of the deconvolution process performed on FTIR and Raman spectra, smaller peaks are likely to be tinged with a greater margin of error than larger peaks. This was a major driver for the choice of Raman spectroscopy to compare the secondary structures of the polypeptides.
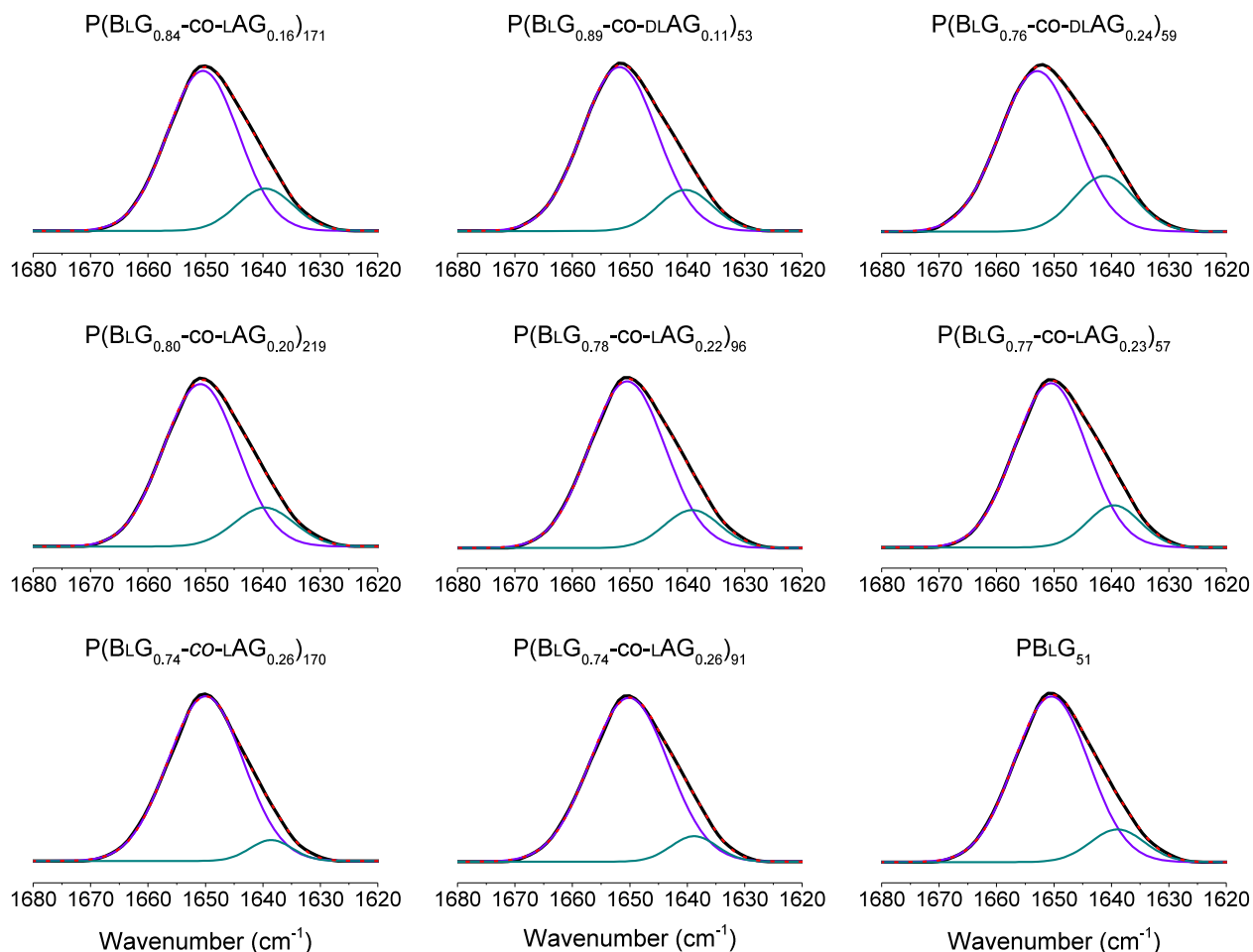
Figure IV.7 Amide I bands from FTIR spectra of PBLG and P(BLG$_x$-co-AG$_{1-x}$)$_n$ polymers, composed of a main peak (α helix, violet) at ~ 1650 cm^{-1} that correspond to an α-helical conformation, and a secondary peak (α' conformation, green) at ~ 1640 cm^{-1}, the exact nature of which is discussed in this study; the dashed red curve represents the cumulative fit.

In order to rule out the β-sheet as a possible conformation for the series of polymers used in this study (Table IV.1A), both a PBLG and a P(BLG$_x$-co-AG$_{1-x}$)$_n$ polymer were designed in order to purposely generate the β-sheet conformation and identify its peaks (Table IV.1B). The following polymers were synthesised (see Chapter II): (a) a three-armed star PBLG noted *star*-(PBLG$_{20}$)$_3$ and (b) a two-armed star P(BLG$_x$-co-AG$_{1-x}$)$_n$ noted "*star*"-(P(BLG$_{0.50}$-co-LAG$_{0.50}$)$_{73}$)$_2$. The choice of such designs in order to generate β-sheets is explained hereafter. α-Helices consist of 3.6 residues per turn; as such, a minimum number of residues is required for this conformation to simply exist, which has been estimated to be about 8-10 residues for PBLG; below this minimum threshold, PBLG is known to fold into β-sheets.[67] Since a short linear PBLG would have been technically difficult to precipitate and work up, the star architecture was selected for (a). The polymerisation reaction was terminated as soon as the polymer was long enough to be precipitated, which turned out to be 20 repeat units per arm. At such arm length, and because of the intrinsic molecular weight distribution of synthetic polymers, a mixture of α-helices and β-sheets was to be expected.[59] As for the design of (b), AG moieties are known to favour β-sheets.[39,56] However, the low solubility of high-AG content P(BLG$_x$-co-AG$_{1-x}$)$_n$ copolymers in most good solvents for PBLG (*e.g.,* DMF and TFA), precisely because of this conformation, called for a 50-50 mol% comonomer mixture compromise.

The deconvolution of the Raman (Figure IV.8) and FTIR (Figure IV.9) spectra of these polymers led to the following observations: (i) the conformation of both polymers ((a) and (b)) was a mixture of α-helix, β-sheet and the aforementioned α' conformation; and (ii) relative to the α-helical conformation (violet peak), "*star*"-(P(BLG$_{0.50}$-*co*-LAG$_{0.50}$)$_{73}$)$_2$ (b) exhibited a larger proportion of β-sheets than *star*-(PBLG$_{20}$)$_3$ (a).

star-P(BLG$_{20}$)$_3$ (a)   "*star*"-P((BLG$_{0.50}$-*co*-LAG$_{0.50}$)$_{73}$)$_2$ (b)   PBLG$_{159}$

Raman Shift (cm^{-1})

Figure IV.8 Amide I bands (black) from Raman spectra of P(BLG$_x$-*co*-AG$_{1-x}$)$_n$ polymers, exhibiting some or all of the following peaks: a peak at ~ 1653 cm^{-1} (α-helix,[65,68] violet), a peak at ~ 1643 cm^{-1} (α' conformation, green), a peak at ~ 1670 cm^{-1} (β-sheet,[53,62,65,68] orange), and a peak at ~ 1660 cm^{-1} (possibly β-turn[65], neon green); the dashed red curve represents the cumulative fit.

star-(PBLG$_{20}$)$_3$ (a)   "*star*"-(P(BLG$_{0.50}$-*co*-LAG$_{0.50}$)$_{73}$)$_2$ (b)   PBLG$_{159}$
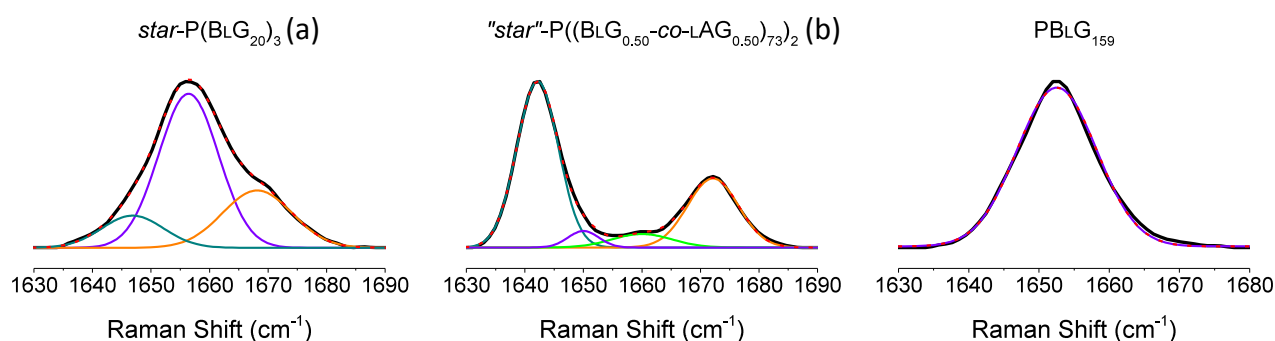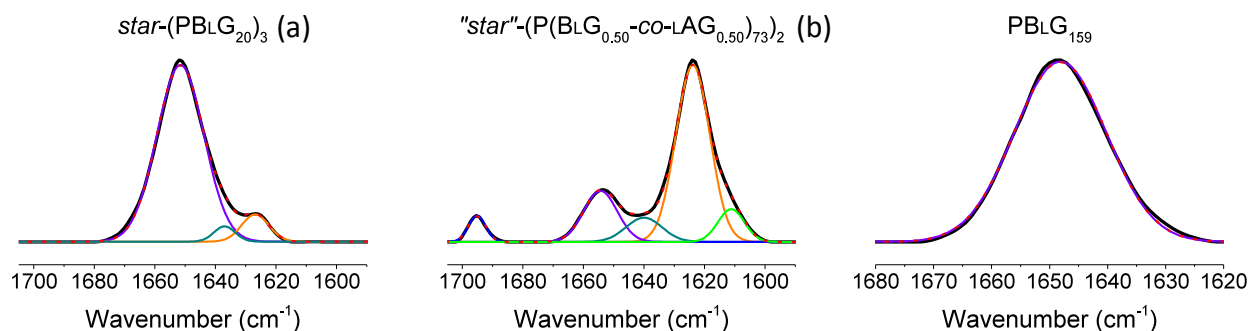
Wavenumber (cm^{-1})

Figure IV.9 Amide I bands (black) from FTIR spectra of P(BLG$_x$-*co*-AG$_{1-x}$)$_n$ polymers, exhibiting some or all of the following peaks: a peak at ~ 1648-1653 cm^{-1} (α-helix,[53,61] violet), a peak at ~ 1640 cm^{-1} (α' conformation, green), a peak at ~ 1625 cm^{-1} (β-sheet - main peak,[62,69,70] orange), a peak at ~ 1695 cm^{-1} (β-sheet - secondary peak,[39,44,61] or β-turn[62] or random coil,[70] blue), and a peak at ~ 1610 cm^{-1} (possibly the ν(C-C) of the phenyl group made Raman active as a result of angle constraints in β-sheet conformation,[62,64] neon green); the dashed red curve represents the cumulative fit.

It is worth noting that the α/α' peak intensity ratio (*i.e.*, I$_α$/I$_{α'}$) - which is highly dependent on the spectroscopic technique used (*e.g.*, FTIR versus Raman) as previously discussed (Figure IV.5 versus Figure IV.7) - varied in a consistent fashion across polymers ((a) and (b)) and spectroscopic techniques. In other words, I$_α$/I$_{α'}$(a) > I$_α$/I$_{α'}$(b) for both FTIR and Raman measurements, and I$_α$/I$_{α'}$(FTIR) > I$_α$/I$_{α'}$(Raman) for both (a) and (b) polymers. A similar trend was observed for the α/β peak intensity ratio: I$_α$/I$_β$(a) > I$_α$/I$_β$(b) for both FTIR and Raman measurements, and I$_α$/I$_β$(FTIR) > I$_α$/I$_β$(Raman) for both (a) and (b) polymers. These observations demonstrate that FTIR and Raman are robust and consistent techniques, which when used complementarily, allow to reliably identify mixtures of conformations as well as provide qualitative relative contributions. In addition, both techniques showed that the α' peak was particularly prominent when a larger proportion of β-sheets, with respect to α-helices, was observed (b). Such a mixture of α and β conformations within one polymer is likely to lead to a certain disorder, especially in the vicinity of

conformational transitions. This supports the hypothesis by which the α' peak may be ascribed to an unordered conformation or defect, as sometimes suggested in the literature.[65,71] Most importantly, this comparative work demonstrates that a β-sheets contribution towards the overall conformation of P(BLG$_x$-co-AG$_{1-x}$)$_n$ polypeptides can be largely excluded, at least for 1-x < 0.26 and n > 50 (Table IV.1A).

CD spectroscopy, a well-established technique for the identification and quantification of secondary structures,[72–75] was used in order to determine the relative contribution of α-helices and random coils towards the total conformation of P(BLG$_x$-co-AG$_{1-x}$)$_n$ polypeptides in solution. The solvent used was a known helicogenic solvent for PBLG, HFIP.[67] The CD spectra of three selected P(BLG$_x$-co-AG$_{1-x}$)$_n$ copolypeptides - including P(BLG$_{0.76}$-co-DLAG$_{0.24}$)$_{59}$, whose Raman Amide I band exhibited the largest α' peak - and of model homopolypeptide PBLG$_{51}$ showed two minima at 208 nm and 222 nm, which are characteristic of the α-helical conformation (Figure IV.10).[76] Interestingly, no significant difference between the copolymers and the reference (PBLG$_{51}$) was observed, suggesting that the α-helical conformation is largely predominant. FTIR, Raman, and CD spectroscopy, therefore, allowed to conclude with confidence that all P(BLG$_x$-co-AG$_{1-x}$)$_n$ polypeptides listed in Table IV.1A are mainly α-helical under the conditions studied (*i.e.*, BLG molar fraction > 0.74, dry state, and semi-dilute solutions in toluene and HFIP).
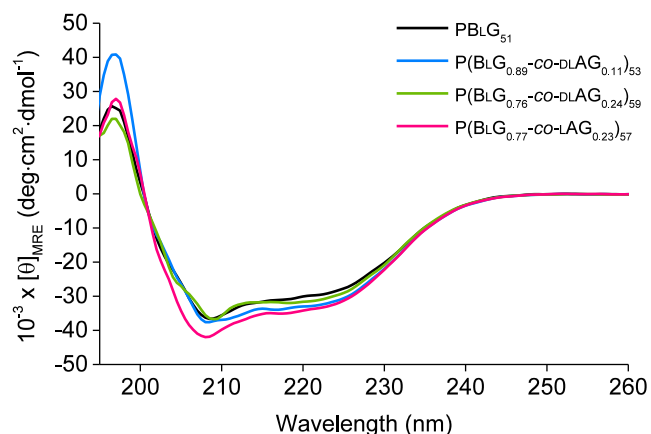

Figure IV.10 CD spectra of PBLG$_{51}$ and P(BLG$_x$-co-AG$_{1-x}$)$_n$ copolypeptides in HFIP at 0.2 g·L^{-1}; the two minima at 208 and 222 nm and their relative intensities are characteristic of an α-helical conformation in organic solvents.[76–79] The variations in intensity fall within the measurement uncertainty and error.

Despite having identified the secondary structure of all studied P(BLG$_x$-co-AG$_{1-x}$)$_n$ polypeptides (Table IV.1), and despite having established a clear correlation between the AG units and the α' peak in Raman spectroscopy, the exact nature of the α' conformation remains to be elucidated. It should, however, be highlighted that P(BLG$_{0.76}$-co-DLAG$_{0.24}$)$_{59}$, which stood out from the gelation temperature trend for P(BLG$_x$-co-LAG$_{1-x}$)$_n$ (Figure IV.4, right), also exhibited the largest α' peak contribution in both Raman (Figure IV.5) and FTIR spectroscopy (Figure IV.7). Interestingly, its enantiomerically pure counterpart, P(BLG$_{0.77}$-co-LAG$_{0.23}$)$_{57}$, showed both a higher gelation temperature and smaller α' peak contribution. Therefore, all things being equal, DLAG units have a greater effect than LAG on both the gelation temperature and the size of the α' peak. In other words, introducing geometric irregularities (*e.g.*, DAG units) causes P(BLG$_x$-co-AG$_{1-x}$)$_n$ to further deviate from the PBLG model. This observation indicates that the α' peak may actually be ascribed to a conformational defect, which was also hypothesised earlier following the comparative analysis of β-sheets by FTIR and Raman. This will serves as a basis for the elucidation of the α' conformation, discussed in the following Section (IV.3.3).

IV.3.3   Elucidation of the α' Conformation

The geometry of the α-helix, that is 3.6 residues per turn and a pitch of 0.54 nm, is controlled and stabilised by regular intramolecular hydrogen bonds formed between C=O groups of amino acid residues (in position 'i') and N-H groups on the fourth amino acid residue up (in position 'i+4'); such bonds are thus noted [i+4>i].[52] Since the secondary structure of P(BLG$_x$-*co*-AG$_{1-x}$)$_n$ copolymers has been established as being mostly α-helical (Section IV.3.2), and that FTIR, Raman and CD spectroscopy measurements allowed to exclude a β-sheet contribution,[80–82] one may thus conclude that the α' peak results only from a minor disruption of the model α-helix due to the presence of AG moieties.

This disruption may have no effect on the overall geometry of the α-helix, which would imply either that (*a*) [i+4>i] intramolecular hydrogen bonds,[83] a prerequisite for α-helices,[52] are present along the entire backbone, but undergo a shift to a slightly lower vC=O vibrational energy for carbonyls that belong to AG units, or that (*b*) AG units cause a change in dihedral angles,[52] more pronounced when racemic mixtures are used, such that intramolecular hydrogen bonds simply cannot form whenever C=O or N-H are within or directly adjacent to one or more AG units (Figure IV.11). Alternatively the presence of AG moieties could cause minute geometrical alterations of the α-helix, such as (*c*) looser or tighter helical portions[84] resulting in either [i+5>i] (*i.e.*, π-helix[85]) or [i+3>i] (*i.e.*, 3$_{10}$-helix[83,86]) intramolecular hydrogen bonds, respectively, or (*d*) local kinks or defects caused by the absence of intramolecular hydrogen bonds in the vicinity of AG units (Figure IV.11). The option (*a*) implies that the size of the α' peak should be proportional to the AG mole fraction, and therefore, does not justify the differences observed between DLAG and LAG. The option (*c*) would necessarily result in a number of non-hydrogen-bonding carbonyls at the physical boundary between two types of helices, which would generate a third peak that was observed neither in infrared nor in Raman spectroscopy. This further supports the hypothesis by which α' corresponds to non-hydrogen-bonding carbonyls, that is option (*b*) or (*d*). This hypothesis is also consistent with the presence of a small α' peak in the Amide I band of homopolymer PBLG$_{51}$, as it is common for the extremities of α-helices to be 'loose' and composed of non-hydrogen-bonding carbonyls.[52,67]

(a)   **(b)**   **(c)**   **(d)**
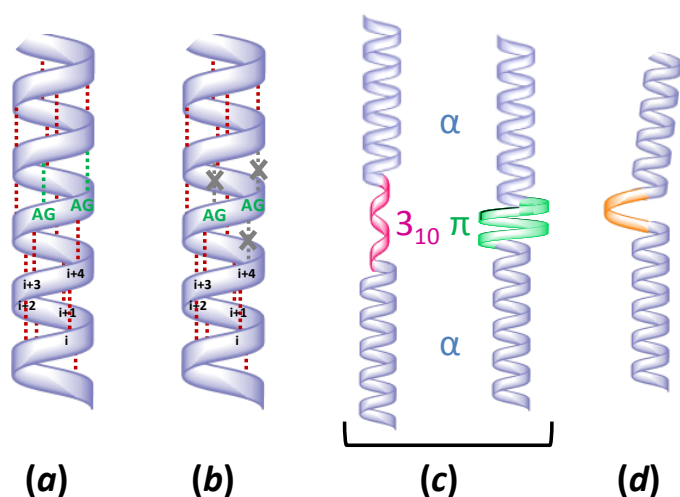
Figure IV.11 Schematic representations of possible disruptions of α-helical PBLG as a consequence of the substitution of some BLG with AG moieties (in the 11 to 26 mol% range): (*a*) the vibrational energy of intramolecular hydrogen bonded (red dashed lines) carbonyls decreases slightly within AG moieties (green dashed lines); (*b*) the presence of AG moieties prevents the formation of some intramolecular hydrogen bonds (grey dashed lines); (*c*) the presence of AG moieties results in a tightening or loosening of the helix in places, thereby generating 3$_{10}$- or π-helical portions; (*d*) is similar to (*b*) but with defects resulting from the lack of intramolecular hydrogen bonds.

Based on this model, the lower gelation temperature of $P(BLG_{0.76}-co-DLAG_{0.24})_{59}$ compared to $P(BLG_{0.77}-co-LAG_{0.23})_{57}$ could be explained by the fact that fewer intramolecular hydrogen bonds result in a slightly more flexible helix in toluene, with a greater degree of freedom, thereby entropically favoring its solubility (*i.e.*, larger ΔS_{mix}). In the solid state, WAXS analysis of $P(BLG_x-co-AG_{1-x})_n$ copolymers from Table IV.1a and homopolymer $PBLG_{51}$ revealed almost identical spectra, which is indicative of a similar kind of arrangement or packing (Figure IV.12). The WAXS diffractograms of these polypeptides showed peaks at 2θ = 6-7° and 17°. The first peak was assigned to a *d*-spacing of 1.3-1.4 nm corresponding to a pseudo-hexagonal packing of helices,[19,87–89] while the second 'peak', or shoulder, corresponds to a typical α-helical pitch of 0.5 nm (Equation IV.2a).[19] This result suggests that homopolymer $PBLG_{51}$ and statistical copolymers $P(BLG_x-co-AG_{1-x})_n$ can both self-assemble or aggregate in a similar fashion, that is a pseudo-hexagonal packing of α-helices (Figure IV.1). This result supports the option (*b*), at least in the dry state. The decreasing pseudo-hexagonal *d*-spacing (in the 2θ range of 6-7°) with increasing AG content, could be explained by the fact that introducing less bulky comonomers like AG moieties results in helices with a smaller mean diameter, hence leading to smaller *d*-spacings (Figure IV.13). To refine this explanation, one could postulate that the space freed by the substitution of some BLG with AG moieties may allow BLG pendant groups to rearrange along the axis of the α-helix in a more compact fashion. Future research could include a modeling study aimed towards determining the packing of $P(BLG_x-co-AG_{1-x})_n$ copolymers and their pendant groups, relative to adjacent copolymers, in a pseudo hexagonal arrangement.

"*star*"-P((BLG_{0.50}-*co*-LAG_{0.50})_{73})_2

P(BLG_{0.84}-*co*-LAG_{0.16})_{171}

P(BLG_{0.80}-*co*-LAG_{0.20})_{219}

P(BLG_{0.74}-*co*-LAG_{0.26})_{170}

P(BLG_{0.78}-*co*-LAG_{0.22})_{96}

P(BLG_{0.74}-*co*-LAG_{0.26})_{91}

P(BLG_{0.77}-*co*-LAG_{0.23})_{57}

P(BLG_{0.76}-*co*-DLAG_{0.24})_{59}

P(BLG_{0.89}-*co*-DLAG_{0.11})_{53}

PBLG_{51}

2θ (deg)
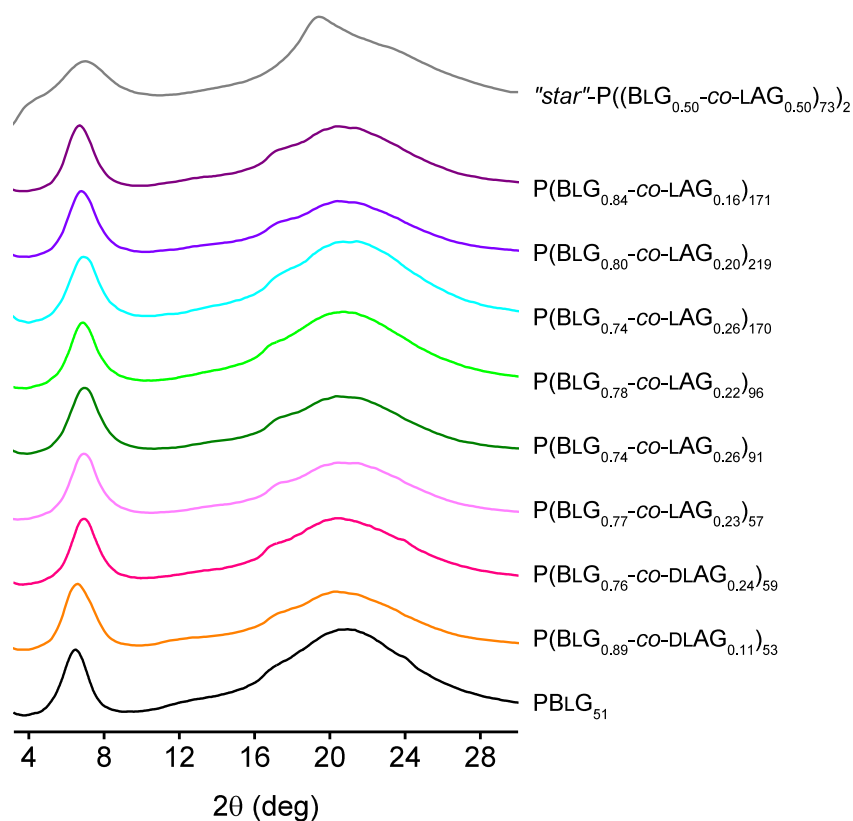
Figure IV.12 WAXS diffractograms of the following lyophilised polymers: (coloured curves) PBLG and $P(BLG_x-co-AG_{1-x})_n$ copolypeptides from Table IV.1; the peak at 6–7° (~ 1.3-1.4 nm) corresponds to the pseudo-hexagonal arrangement of α-helical polymers; the shoulder at 17° (~ 0.5 nm) corresponds to the α-helical pitch; and (grey curve) "*star*"-(P(BLG_{0.50}-*co*-AG_{0.50})_{73})_2 whose conformation is a mixture of α-helices and β-sheets; the shoulder at 4° (~ 2.2 nm) corresponds to the inter-lamellar distance and the peak at 19° (~ 0.46 nm) corresponds to the inter-chain spacing between adjacent chains within a lamella (or sheet).[70,90] The broad peak centred around 21° is the amorphous halo, resulting from the glass capillary and the measured polymers.

Figure IV.13 Close up of the [4 to 10°] 2θ range derived from the full diffractograms displayed in Figure IV.12 (a) WAXS peaks (tip from 6.4° to 6.9°) corresponding pseudo-hexagonal *d*-spacings ranging between 1.37 nm (PBLG$_{51}$) and 1.27 nm (P(BLG$_{0.74}$-*co*-LAG$_{0.26}$)$_{91}$), and (b) scatter distribution showing a good linear correlation between *d*-spacing and BLG content.

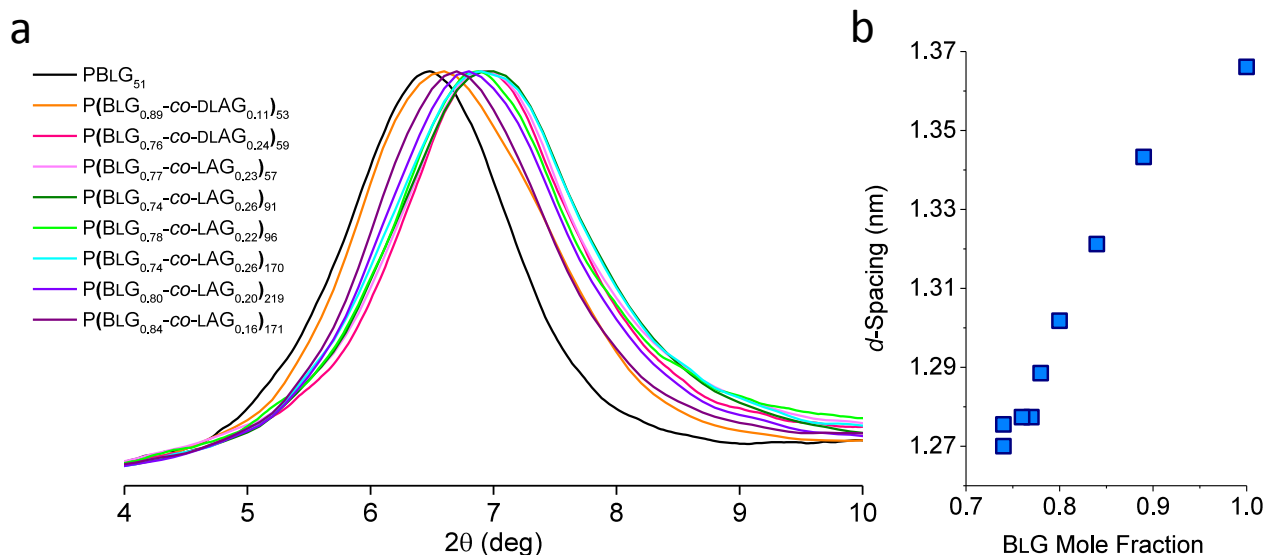It is worth noting that the full width at half maximum (FWHM) of the WAXS peaks corresponding to the pseudo-hexagonal *d*-spacing is similar amongst all analysed polypeptides (Figure IV.13). By using the Scherrer equation (Equation IV.2b)[89,91], an estimate of the size of pseudo-hexagonally ordered α-helices domains (*e.g.*, bundles, fibrils) can be extracted. More precisely, the Scherrer formula provides a lower boundary value on the size of the analysed crystalline or ordered particle. The value of ~ 8 nm (which equals n x 1.3 nm with n the number of side-by-side α-helices across the bundle widths), obtained using this equation and the line broadening (FWHM) of the WAXS peaks, indicates that the bundles are made of at least n = 6 α-helices across. The studied polypeptides are endowed with a dispersity (Đ) that is typical of synthetic polymers, resulting in the absence of order or repeat distances along the fibril's long axis (Figure IV.14b) like in the case of collagen (Figure IV.14a). Indeed, collagen fibres display a regular stripy pattern of 67 nm (D-band)[9] generated by the highly ordered enzyme-mediated assembly[15] of α-strands into triples helices, and by the self-assembly of these triple helices into fibrils; unlike synthetic polymers, the strands (and by extension, the helices) have a unimodal size distribution (300 nm long for a diameter 1.5 nm), which enables the recurrence of this D-band pattern (Section I.2.3.1).[8]

$$(a) \qquad n \cdot \lambda = 2 \cdot d \cdot sin\theta \qquad\qquad (b) \qquad \tau = \frac{K \cdot \lambda}{\beta \cdot cos\theta}$$

Equation IV.2 (a) Bragg's law, where *d* is an interplanar distance of lattice planes in an ordered domain, θ is the scattering angle (*i.e.*, Bragg angle), n is a positive integer corresponding to the reflection order (first order, *i.e.* n = 1, generally provide the strongest reflections, but higher order reflections, *i.e.*, n > 1, are frequent in long-range ordered systems, such as collagen), and λ is the wavelength of the incident wave (in the case of WAXS, X-ray with λ = 0.1542 nm); (b) Scherrer equation, where τ is the mean size of the ordered domain, K is a dimensionless shape factor (0.9), λ is the X-ray wavelength (0.1542 nm), β is the line broadening at half the maximum intensity or full width at half maximum (FWHM), and θ is the Bragg angle.
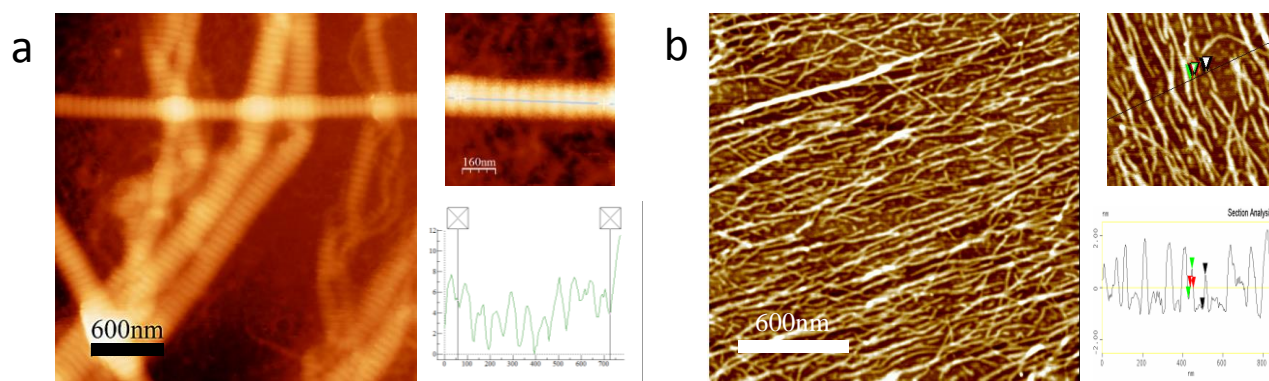
Figure IV.14 AFM images of (a) (left) dried 10 g·L^{-1} collagen (insoluble, type I, from bovine Achilles tendon) suspension in 0.05 M acetic acid together with (right) single fibre analysis and measured D-band value of 67±2 nm, typical for collagen; (b) (left) dried PBLG$_{51}$-toluene gel (4 g·L^{-1}) with (right) fibres analysis , showing typical diameters of 10 to 30 nm.

IV.3.4   Physical Gelation Mechanism

As pointed out by a recent study by Niehoff et al.,[19] there is to date no clear consensus on the exact gelation mechanism of PBLG. Three gelation mechanisms have been proposed: (*a*) incomplete spinodal decomposition resulting in jammed polymer-rich fibres,[24,37] (*b*) nucleation growth from crystal solvates,[22,36,38,45] and (*c*) liquid-liquid phase separation (*via* path *a* or *b*), followed by crystallisation in the concentrated phase.[46,92,93] Irrespective of the mechanism, a prerequisite for the gelation to occur is that the solvent be helicogenic and poor; that is, a solvent where the α-helical conformation is favoured and where the aggregation of α-helices occurs under certain conditions.[47,94] Although the mechanism is not completely agreed upon, most studies acknowledge that, in helicogenic solvents, PBLG abides by the Flory diagram for rod-like polymers, whereby gelation occurs as the decreasing temperature causes the system to cross the isotropic to isotropic/liquid crystalline (LC) threshold (Figure IV.15a).[24,36–38,60,92,95–98] The formation of intra-hydrogen bonds in polypeptides such as PBLG not only generates α-helical conformations but also reduces chain flexibility.[92] This explains why α-helical polypeptides behave as a rigid rods. [58,60]

As attested by cross-polarised light microscopy pictures, concentrated solutions of PBLG$_{51}$ in toluene - which set into a gel at room temperature - were strongly birefringent, which is indicative of the presence of a liquid crystalline phase, most likely in the 'broad biphasic' phase. The pictures of concentrated solutions of PBLG$_{51}$ in dioxane and TFA exhibited a somewhat milder birefringence, indicative of some order, possibly the narrow biphasic or LC regions.[87] Indeed, the Flory diagram and its transition temperatures and concentration depends on several factors including the solvent, the type of polymer and its length (n). Although the nature and properties of the liquid phases are not the focus of this study, it is important to stress that liquid crystalline (or lyotropic) PBLG solutions have been reported to be of nematic,[24,42,60,99,100] columnar[87,101,102] and cholesteric (*i.e.*, chiral nematic)[24,60,92,97,101,103] nature. It has also been reported that the nature of the liquid crystalline phase varies with both solvent and concentration.[60,97,101] This could also explain why the aspect of PBLG$_{51}$ in toluene differs from that in dioxane and TFA in cross-polarised microscopy (Figure IV.15b, c and d).
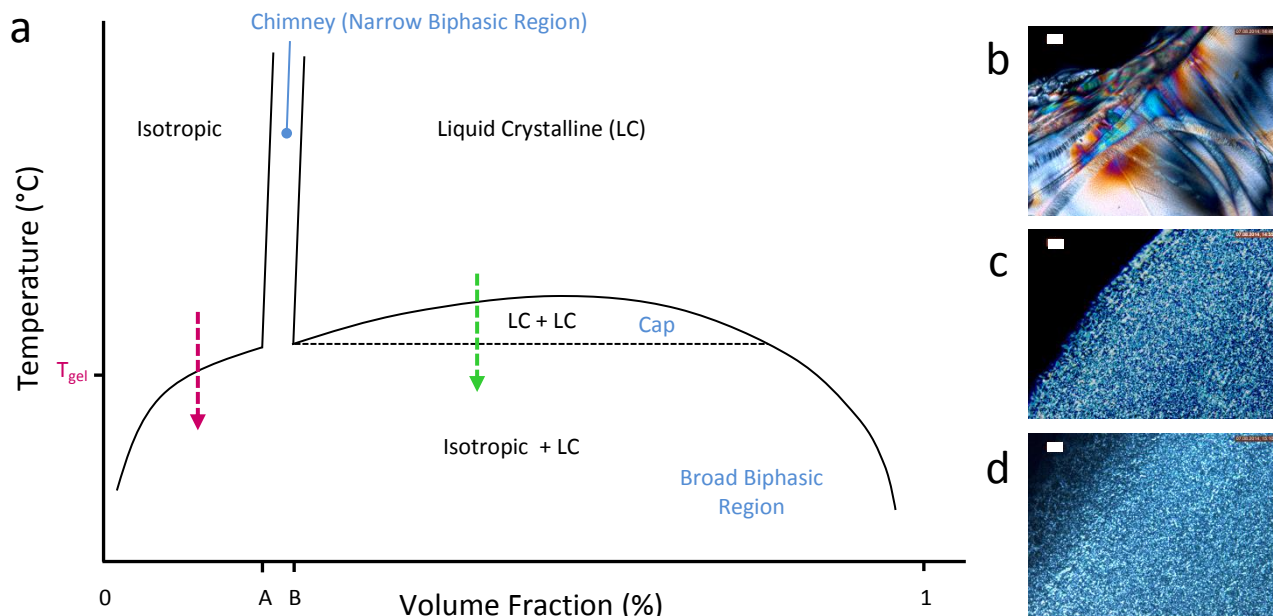
Figure IV.15 (a) Schematic of a typical Flory phase diagram for rod-like polymers such as PBLG, with terminology for the different phases (in black) and for the corresponding parts of the diagram (in blue); the concentrations A and B, *i.e.*, Robinson A and B points, correspond to transitions between the isotropic, narrow biphasic and LC phases; the dotted arrows show typical paths to generate gels either from dilute and isotropic solutions (red) or from concentrated and LC solutions (green). (right) Cross-polarised light microscopy (transmission) of ~ 100 g·L^{-1} solutions of PBLG$_{51}$ in (b) toluene (scale bar = 60 μm), (c) dioxane (scale bar = 30 μm), and (d) TFA (Scale bar = 30 μm).

The present study showed that the analysed P(BLG$_x$-*co*-AG$_{1-x}$)$_n$ copolymers are structurally similar to PBLG and also that they behave similarly in solution in that they form α-helices, and arrange pseudo-hexagonally upon gelation (upon decreasing the temperature). Based on these considerations, P(BLG$_x$-*co*-AG$_{1-x}$)$_n$ copolymers, like PBLG, should logically abide by the Flory phase diagram too, only with an isotropic to isotropic-liquid crystalline threshold shifted to lower temperatures (*i.e.*, lower T$_{gel}$, Section IV.3.2). The physical gelation of these polypeptides was analysed by rheometry, which is the most direct technique to distinguish between solid-like and liquid-like materials. Other methods, such as NMR and DSC, are also commonly used to monitor gelation. The measurement of gelation by NMR relies on the formation of a solid-like gel network (*i.e.*, gelators within a supramolecular system and hence with fewer degrees of freedom and fewer interactions with the solvent).[48,104,105] Physical gelation generally relies on the formation or breaking of non-covalent bonds (first order transition), which can be measured by DSC.[43,49,106] The indirect nature of such measurements implies that the gelation temperature may not be accurately determined. However, such measurements serve as complementary techniques to rheometry and help to better understand gelation mechanisms.

During a physical gelation, gelators are incorporated in a supramolecular solid-like network, which can cause line broadening, loss of spectral resolution, and signal disappearance in ^{1}H-NMR measurements.[48,104,105] This phenomenon was observed in a temperature-sweep ^{1}H-NMR experiment for dilute solutions of P(BLG$_x$-*co*-AG$_{1-x}$)$_n$ polypeptides in toluene-d$_8$ (Figure IV.16 and B.47). The disappearance of the benzyl peak, noted k, and the gelation temperature measured by rheology followed a similar trend

(Table IV.2 and B.5), therefore confirming that peak disappearance in ^{1}H-NMR spectra can be used to predict gelation temperatures of P(BLG$_x$-co-AG$_{1-x}$)$_n$-toluene systems, and probably of other physical gelators too. The benzyl peaks, however, disappeared at temperatures globally lower that the T$_{gel}$ measured by rheology. One could argue that if the gelation is indeed driven by phase separation, free polymers are still present in the polymer-poor (isotropic) phase, and likewise, fibres are still solvent-swollen just after the polymer rich phase kinetically froze into a self-supporting fibrous network.[46,87] This suggests that gelation may occur prior to complete NMR peak disappearance. Other aspects to consider for this discrepancy might also be cooling rates and solvate-solvent interactions, possibly affected by the use of deuterated solvents.
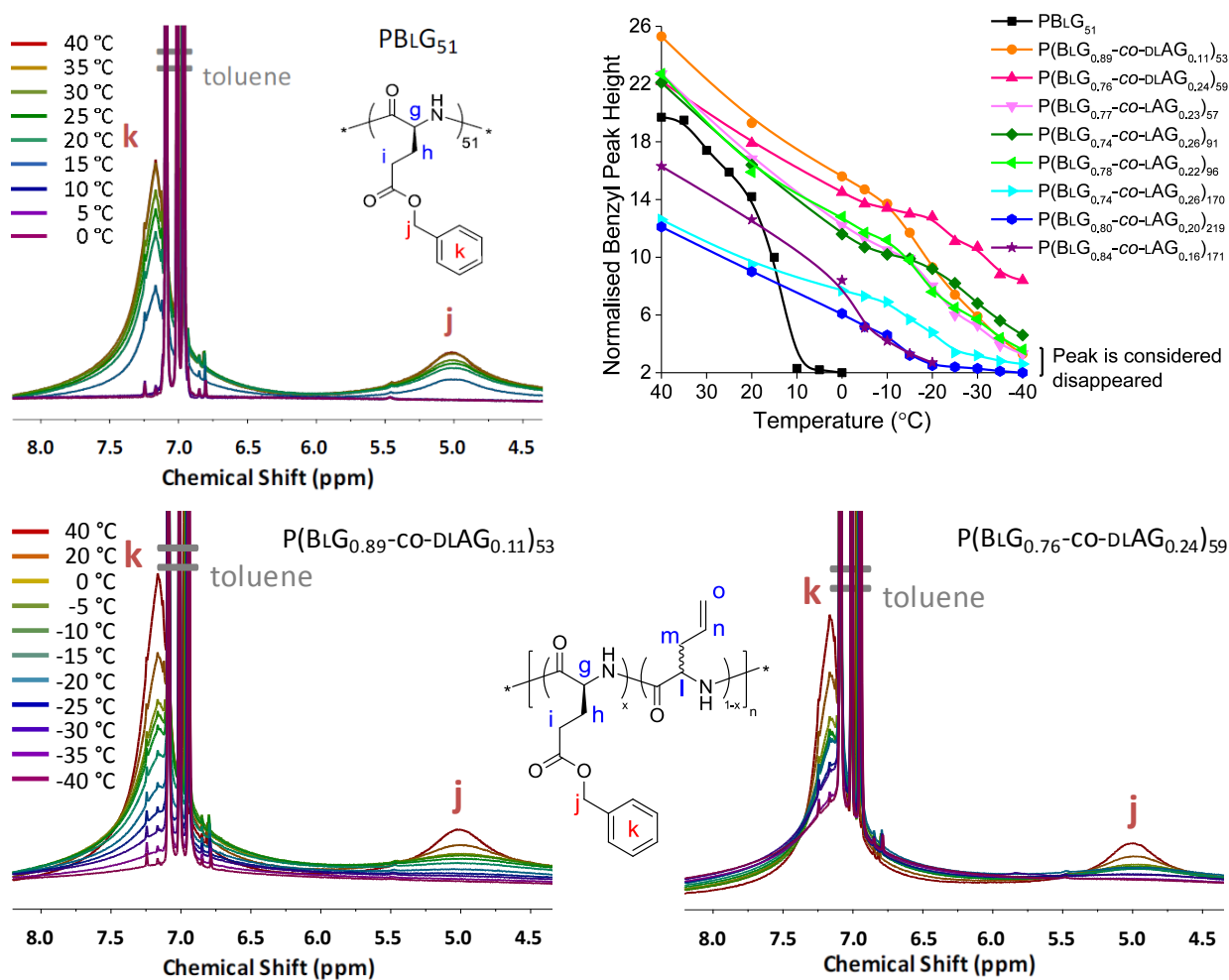
Figure IV.16 [4.5 - 8 ppm] Portions of ^{1}H-NMR spectra of P(BLG$_x$-co-AG$_{1-x}$)$_n$-toluene-d$_8$ solutions (20 g·L^{-1}): (top left) PBLG$_{51}$; the spectra were acquired at incrementally decreased temperatures, from 40 °C to 0 °C; (bottom) P(BLG$_x$-co-AG$_{1-x}$)$_n$; the spectra were acquired at incrementally decreased temperatures, from 40 °C to -40 °C (the spectra of all other analysed copolypeptides can be found in Appendix B, Figure B.47); all spectra were normalised to the toluene signal at 7.01 ppm. (top right) Benzyl peak height (taken at 7.16 ppm) extracted from all these NMR spectra and showing how it disappears as a function of the temperature.

The measurement of physical gelations by DSC is generally permitted by the occurrence of crystallisation, either as a result of or as a driving force for gelation.[107] The model whereby physical gelation is driven by crystallisation is questionable in the case of PBLG as well as other systems.[108] Indeed, the

crystallisation of solutes, which proceeds *via* a nucleation and growth mechanism, is generally a slow process and does not necessarily give rise to an interconnected network.[87,108] The most popular mechanism for the gelation of PBLG depicts a liquid-liquid phase separation, *via* spinodal decomposition, into bi-continuous polymer- and solvent-rich phases, followed by rod alignment and crystallisation in the polymer rich phase, which prevents the phase separation from proceeding to completion, thereby leaving a kinetically frozen yet continuous PBLG-rich network surrounded by a solvent-rich phase, *i.e.*, a gel.[92] In that context, the crystallisation of PBLG in the polymer-rich phase occurs as a result of the increased polymer concentration in that phase.

It should be stressed that in toluene, PBLG as well as $P(BLG_x\text{-}co\text{-}AG_{1-x})_n$ copolymers, adopt an α-helical conformation (Figure IV.2), even at high temperatures.[19,35,44] Hence, the presently discussed crystallisation does not refer to the intramolecular hydrogen bonding and ensuing chain folding into α-helices, but to the organised arrangement of α-helices with respect to one another. As the phase separation begins and the polymer concentration rises in the polymer-rich phase, entropy dictates that rigid rod-like molecules arrange side by side. The Onsager theory explains this phenomenon by the fact that a parallel arrangement of rigid rods maximises the translational entropy.[92,109] As the phase separation continues, and the polymer concentration in the polymer-rich phase further increases, crystallisation takes place. The crystallisation may generate polymer-solvent co-crystals or even pure polymer crystals, in which adjacent BLG moieties interact *via* π-π interactions.[24,46] The former option (co-crystals) is more consistent with weak WAXS reflection observed for PBLG gels as reported in the literature[43] and in Chapter V. Countless studies have reported crystallisation exotherms (in the cooling stage) as well as melting endotherms (in the heating stage), from DSC measurements of PBLG solutions.[22,43,44,99,110] These first order transitions were simply attributed to gelation and gel melting phenomena.[47,99] Such explanation however lacks details and somewhat fails to define the true nature of the gelation. Since the substitution of BLG with AG moieties was shown earlier to effectively tune the gelation temperature of α-helical polypeptides (Section IV.3.1), a DSC analysis was conducted in an attempt to better understand the gelation of PBLG polymers and the like.

As expected, the heat flow curves of solutions of $PBLG_{51}$ in toluene exhibited exothermic peaks (as the temperature decreased) and endothermic peaks (as the temperature increased), whereas $P(BLG_x\text{-}co\text{-}AG_{1-x})_n$ copolymers, which also undergo physical gelation, did not (Figure IV.17a). It could be argued that the small perturbations observed in the heat flow curves of toluene solutions of $P(BLG_{0.77}\text{-}co\text{-}LAG_{0.23})_{57}$, $P(BLG_{0.74}\text{-}co\text{-}LAG_{0.26})_{170}$, and $P(BLG_{0.89}\text{-}co\text{-}DLAG_{0.11})_{53}$ (onsets between -10 and -20 °C), may in fact be attenuated exothermic peaks corresponding to their respective gelation. However, unlike $PBLG_{51}$, no endothermic peak was observed during the heating stage. The attenuated exotherms could be explained by the fact that random copolymers do not crystallise as readily as homopolymers due to their reduced stereoregularity,[109,111–113] and the seemingly non-existent melting might be explained by the lack of resolution of the apparatus. Nevertheless, the difference of magnitude between the pronounced

exothermic peak for $PBLG_{51}$-toluene and the perturbations for $P(BLG_x\text{-}co\text{-}AG_{1-x})_n$-toluene (lack of perturbation in the case of $P(BLG_{0.76}\text{-}co\text{-}DLAG_{0.24})_{59}$) strongly contrast with the equally pronounced viscoelastic transitions for both homo- and copolypeptides (Figure IV.3). This observation is more consistent with a phase-separation-driven gelation mechanism followed by a more or less pronounced crystallisation, rather than a crystallisation-driven gelation.[114] The fact that $PBLG_{51}$-toluene systems form a gel even at high cooling rates (over 40 °C·min^{-1}), also supports this mechanism (Figure IV.17b). In addition, these perturbations were not observed for $P(BLG_x\text{-}co\text{-}AG_{1-x})_n$ concentrations of 20 g·L^{-1} and below, probably due to the detection limit of the apparatus. This was the determining factor for the use of 50 g·L^{-1} for this DSC study, which unfortunately limits direct comparisons with rheological and NMR results.
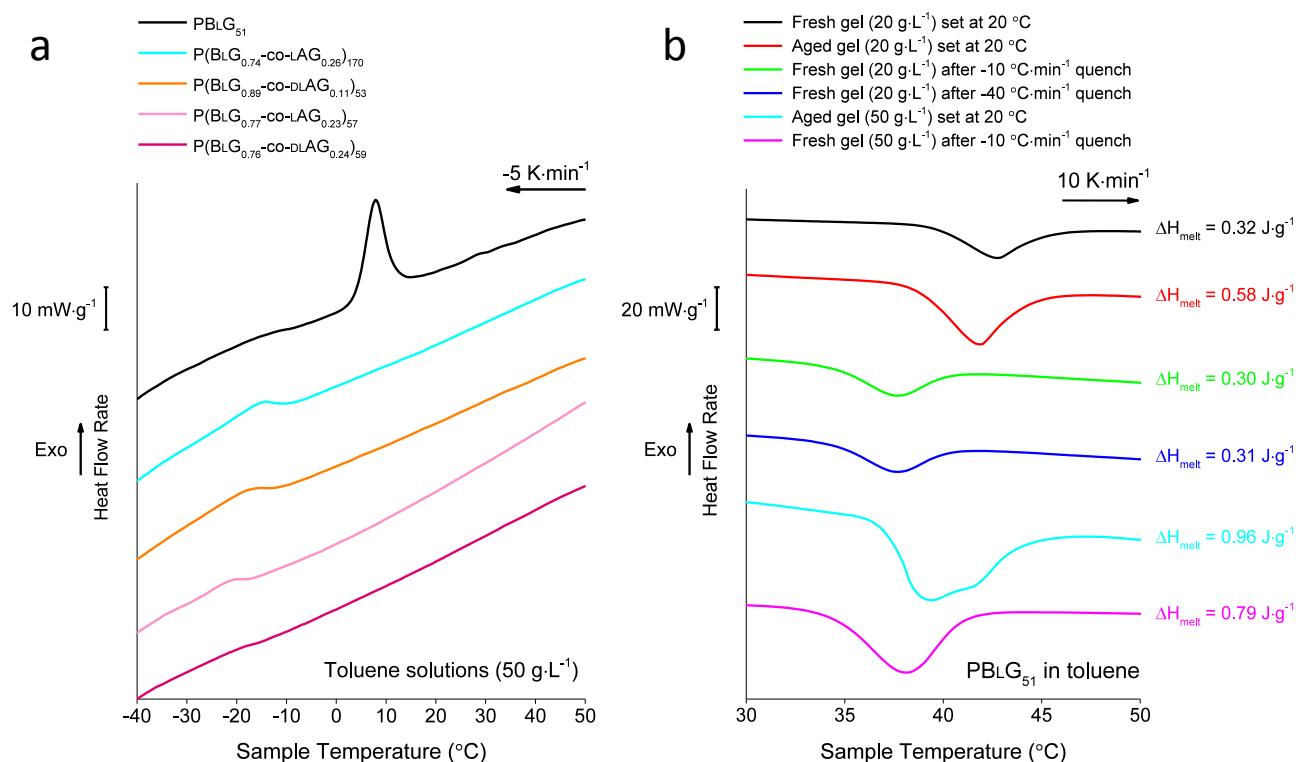

Figure IV.17 (a) Heat flow rate curves of $P(BLG_x\text{-}co\text{-}AG_{1-x})_n$ copolymers and $PBLG_{51}$ in toluene during the cooling stage (from 60 °C to -40 °C). (b) Heat flow rate curves of $PBLG_{51}$ in toluene during the heating stage and measured enthalpies of melting (ΔH_m). From top to bottom: (black) freshly prepared gel that was set at room temperature; (red) 2-week old gel that was set at room temperature and store at 4 °C; (green) same gel as the latter after a -10 °C·min^{-1} quench from 60 °C to -40 °C; (blue) same gel as the latter after a -40 °C·min^{-1} quench from 60 °C to -40 °C; (cyan) aged gel that was set that was set at room temperature and store at 4 °C; (pink) same gel as the latter after a -40 °C·min^{-1} quench from 60 °C to -40 °C. All curves were normalised to the weight of the samples, that is that of the gels and not the polymer content of those gels; this is well illustrated in (b) as the 50 g·L^{-1} gel (pink curve) requires around 2.5 times more energy to melt than the 20 g·L^{-1} gel (green curve) (whose polymer concentration is 2.5 times less) following the same heating and cooling treatment.

Aged $PBLG_{51}$-toluene gels exhibited larger endothermic peaks than freshly prepared ones (Figure IV.17b). The aspect of these gels also evolved with time: freshly prepared $PBLG_{51}$-toluene gels that were set at room temperature (for concentrations between 4 and 50 g·L^{-1}) or at 4 °C (for concentrations between 1 and 4 g·L^{-1}) were initially always clear and transparent, and generally turned cloudy after a few weeks

(Figure IV.18). As mentioned earlier, PBLG gels most likely correspond to a non-equilibrium kinetically frozen state[106] of an incomplete phase separation, followed by polymer-polymer or polymer-solvent (co)crystallisation in the polymer-rich phase, resulting in a continuous fibrous and rigid network surrounded by a solvent-rich phase (Figure IV.1). It is possible that free polymers remain in the solvent-rich phase and progressively aggregate and crystallise onto the polymer fibres, thickening them to the point where visible light is scattered, resulting in both a cloudy appearance and the need for more heat (to melt larger aggregates). In addition, PBLG$_{51}$-toluene gels that were allowed to set at room temperature exhibited melting peaks at higher temperatures (T_m) than PBLG$_{51}$-toluene gels quenched to lower temperatures (Figure IV.17b). Although complementary studies would be required to confidently conclude on this result, one could postulate that this discrepancy has something to do with the fraction of solvent molecules trapped in the polymer-rich phase, which is possibly affected by the cooling rate, and would result in more or less solvent-polymer and polymer-polymer interactions, and hence different T_m. The quench may also result in a disordered packing of adjacent helices,[43] which may be an additional factor affecting the T_m. In any case, the ageing of PBLG gels is yet another evidence supporting the fact that these gels are assembled structures trapped in a metastable state (*i.e.*, kinetically frozen) slowly evolving towards thermodynamic equilibrium (*e.g.*, PBLG crystals).[106]

Figure IV.18 Aged PBLG$_{51}$-toluene gel (4 g·L^{-1}) sample (with stirring bar) that underwent partial melting, thereby exhibiting (left, lid side) a two-week old gel with a cloudy aspect, and (right, glass bottom side) a freshly set and transparent gel, also corresponding to the initial aspect of the entire sample when first prepared.

The DSC curve, in the heating stage, of an aged PBLG$_{51}$-toluene gel (50 g·L^{-1}) clearly displayed two endothermic peaks (Figure IV.17b). This double melting has been previously reported for concentrated (*i.e.*, > 20 g·L^{-1}) PBLG solutions in helicogenic solvents.[43,44,99,110] A number of explanations were proposed for that phenomenon, including (i) the coexistence of different solid phases in the gel (*e.g.*, crystal solvates, liquid crystal phase, isotropic domain),[43,99] (ii) the coexistence of fibres of bimodal sizes,[99] and (iii) a multi-stage process consisting in the fragmentation of polymer bundles making up the gel network into elementary fibrils, followed by the dissociation of the latter.[44] As observed by Cohen et al., a double melt and its characteristics (*e.g.*, peak ratio, T_m) vary with the thermal history of the sample and its concentration,[43] and probably also depends on the PBLG molar mass as well as the solvent.[93] In this study, a double endotherm was observed to occur mainly in the case of aged gels. As previously mentioned, the aging of PBLG gels is accompanied with an increase in cloudiness, which implies an increasing number of visible light scatterers. This is most likely the result of an increased fibre thickness and / or density (*via* the addition of free polymers or the depletion of solvent molecules). Whichever phenomenon is responsible for the cloudiness, it is a slow process, and may therefore not have proceeded to completion by the time aged gel samples

were measured, thereby generating inhomogeneities in the gel network (*e.g.*, different fibre diameters or densities), resulting in a two-step melting process. An in-depth study involving PBLG samples of different molar masses, together with a thorough follow up of the aging process by DSC, TEM (to assess the size distribution of fibres), SAXS and visible light transmission, is highly recommended to validate this postulate.

Finally, it might be interesting to note that the melting enthalpy of PBLG$_{51}$-toluene gels (between 0.30 and 0.58 J·g^{-1} for 20 g·L^{-1} gels) is very close to that of gelatin-water gels (0.73 J·g^{-1} for 15 g·L^{-1} gels).[115] However, the gelation of gelatin and PBLG proceed *via* different routes. Gelatin is denatured collagen, which consists mostly of individual polypeptide chains that originally made up the collagen triple helices. Upon melting gelatin in water and decreasing the temperature past the denaturation nature of collagen (43 °C, in a 20% solution),[115] these polypeptide chains fold into polyproline II (PPII) helices, which bond with one another *via* the formation of triple-helical coiled coils.[116] This results in triple-helical fibres of at least three polypeptide chains across, held together by hydrogen bonds. PBLG gels, on the other hand, result from the formation of fibres (or bundles or fibrils) in which α-helices mainly interact *via* π-π stacking. As calculated in Section IV.3.3, and reported in the literature, fibrils are composed of 4 to 10 α-helices across.[19,24] Since the binding energy range of H-bonds in collagen (-1.4 to -2 kcal·mol^{-1})[9] and that of π-π interactions (-2 to -3 kcal·mol^{-1})[117] overlap, a similar melting enthalpy turns out to be logical.

IV.4   Conclusions

A series of statistical P(BLG$_x$-*co*-AG$_{1-x}$)$_n$ copolymers, with 0.74 < *x* < 1 and 50 < *n* < 220, were synthesised and characterised by rheology, Raman, FTIR, CD spectroscopy, and WAXS, in solution and in the dry state. While PBLG$_{51}$ underwent physical gelation in toluene at room temperature, all P(BLG$_x$-*co*-AG$_{1-x}$)$_n$ copolypeptides gelled at lower temperatures. Their gelation temperature (T_{gel}) was found to decrease with increasing AG mole fraction, which most likely resulted from the toluene being a better solvent for AG than for BLG. Furthermore, their T_{gel} increased with increasing chain length (*n*), which was explained by a smaller contribution of the entropy of mixing for longer chains. Like PBLG$_{51}$, P(BLG$_x$-*co*-AG$_{1-x}$)$_n$ copolymers exhibited a mostly α-helical secondary structure in toluene as well as in the dry state, and a pseudo-hexagonal arrangement. This indicates that the gel microstructure and the gelation mechanism of P(BLG$_x$-*co*-AG$_{1-x}$)$_n$ copolymers and of PBLG are very similar, within the range of parameters studied. This result is remarkable as it demonstrates that statistical copolypeptides can gel without the assistance of blocks or self-assembly-inducing end group moieties.[18] This work may also lead the way towards design rules for statistical copolypeptide hydrogelators, which would set a precedent in the field of self-assembled polypeptide hydrogels, currently dominated by block and sequence-controlled architectures.

Furthermore, through this study, the Amide I band of P(BLG$_x$-*co*-AG$_{1-x}$)$_n$ copolypeptides was elucidated. Notably, the second peak (α') observed in the Amide I band, which increased with the AG mole fraction (all the more with DLAG), was ascribed to non-hydrogen bonding carbonyls. Interestingly, the

stiffness of the P(BLG$_x$-co-AG$_{1-x}$)$_n$-toluene organogels showed a good correlation with the swelling ratios of the corresponding hydrogels, investigated in Chapter V. Therefore, this comprehensive study allowed not only to characterise and quantify the physical effect of introducing non-α-helix-promoting monomers (*e.g.*, AG) into α-helical systems (*i.e.*, PBLG), but also to predict the properties of P(BLG$_x$-co-AG$_{1-x}$)$_n$-derived hydrogels. As such, it offers a methodological procedure for the study of structure-property relationships of similar (co)polypeptide systems.

Finally, a comparative study of the gelation of PBLG and P(BLG$_x$-co-AG$_{1-x}$)$_n$ in toluene by DSC and NMR provided a new insight into the gelation of rod-like polypeptides and its underlying mechanism. The results were consistent with a phase separation-driven gelation. The aging of PBLG gels indicated that these gels are in a non-equilibrium state. These observations support the model by which the continuous fibrous network – responsible for the mechanical strength of the gels – is the results of a kinetically frozen spinodal decomposition that did not proceed to completion, possibly as a result of rod jamming in the polymer-rich phase. The rheological and structural study showed that once the differences between P(BLG$_x$-co-AG$_{1-x}$)$_n$ and PBLG were quantified and explained, both polymers were in fact similar at many levels (*e.g.*, physical gelation, secondary structure, packing). Yet, the DSC analysis of their gelation in toluene showed rather different thermodynamical behaviours, which were interpreted as a more or less pronounced crystallisations following the gelation step. Therefore, the study of the physical gelation of P(BLG$_x$-co-AG$_{1-x}$)$_n$ copolymers, by DSC and possibly ITC, may represent a great opportunity to better understand the gelation mechanism of rod-like PBLG polymers and the like. For instance, a new series of P(BLG$_x$-co-LAG$_{1-x}$)$_n$ with $0.01 < 1-x < 0.10$ may be synthesised in order to help better understand whether the first order gelation peak simply disappears or gradually morphs into the small perturbations observed for $0.11 < 1-x < 0.26$. In order to provide more conclusive evidences regarding the kinetically frozen spinodal decomposition mechanism, wet-cell TEM monitoring of the gel formation might also be considered.

IV.5   References

(1)   Lee, B. P.; Messersmith, P. B.; Israelachvili, J. N.; Waite, J. H. *Annu. Rev. Mater. Res.* **2011**, *41*, 99–132.

(2)   Luz, G. M.; Mano, J. F. *Philos. Trans. R. Soc. A Math. Phys. Eng. Sci.* **2009**, *367*, 1587–1605.

(3)   Heim, M.; Keerl, D.; Scheibel, T. *Angew. Chemie Int. Ed.* **2009**, *48*, 3584–3596.

(4)   Guan, Z. *Polym. Int.* **2007**, *56*, 467–473.

(5)   Vullev, V. I. *J. Phys. Chem. Lett.* **2011**, *2*, 503–508.

(6)   Zhao, Y.; Sakai, F.; Su, L.; Liu, Y.; Wei, K.; Chen, G.; Jiang, M. *Adv. Mater.* **2013**, *25*, 5215–5256.

(7)   Bonduelle, C.; Lecommandoux, S. *Biomacromolecules* **2013**, *14*, 2973–2983.

(8)   Stenzel, K. H.; Miyata, T.; Rubin, A. L. *Annu. Rev. Biophys. Bioeng.* **1974**, *3*, 231–253.

(9)   Shoulders, M. D.; Raines, R. T. *Annu. Rev. Biochem.* **2009**, *78*, 929–958.

(10)   Fratzl, P. In *Collagen*; Fratzl, P., Ed.; Springer US: Boston, MA, **2008**; pp 1–13.

(11)   Goodman, M.; Bhumralkar, M.; Jefferson, E. A.; Kwak, J.; Locardi, E. *Biopolymers* **1998**, *47*, 127–142.

(12)   O'Leary, L. E. R.; Fallas, J. A.; Bakota, E. L.; Kang, M. K.; Hartgerink, J. D. *Nat. Chem.* **2011**, *3*, 821–828.

(13)   Rele, S.; Song, Y.; Apkarian, R. P.; Qu, Z.; Conticello, V. P.; Chaikof, E. L. *J. Am. Chem. Soc.* **2007**, *129*, 14780–14787.

(14)   Zhang, Z.; Liu, B.; Zhang, Y.-W.; Hwang, K.-C.; Gao, H. *Carbon N. Y.* **2014**, *77*, 1040–1053.

(15)   Eyre, D. R.; Weis, M. A.; Wu, J. *Methods* **2008**, *45*, 65–74.

(16)   Flory, P. J. *Faraday Discuss. Chem. Soc.* **1974**, *57*, 7–18.

(17)   Appel, E. A.; del Barrio, J.; Loh, X. J.; Scherman, O. A. *Chem. Soc. Rev.* **2012**, *41*, 6195–6214.

(18)   Kim, K. T.; Park, C.; Vandermeulen, G. W. M.; Rider, D. A.; Kim, C.; Winnik, M. A.; Manners, I. *Angew. Chemie Int. Ed.* **2005**, *44*, 7964–7968.

(19)   Niehoff, A.; Mantion, A.; McAloney, R.; Huber, A.; Falkenhagen, J.; Goh, C. M.; Thünemann, A. F.; Winnik, M. A.; Menzel, H. *Colloid Polym. Sci.* **2013**, *291*, 1353–1363.

(20)   Russo, P. S.; Magestro, P.; Miller, W. G. **1987**; Vol. 3, pp 152–180.

(21)   Oikawa, H.; Nakanishi, H. *J. Chem. Phys.* **2001**, *115*, 3785–3791.

(22)   Hill, A.; Donald, A. M. *Mol. Cryst. Liq. Cryst. Inc. Nonlinear Opt.* **1987**, *153*, 395–404.

(23)   Miller, G.; Goebel, K. D.; Miller, W. G. **1961**, *221*, 64–69.

(24)   Shukla, P. *Polymer* **1992**, *33*, 365–372.

(25)   Franz, N.; Klok, H.-A. *Macromol. Chem. Phys.* **2010**, *211*, 809–820.

(26)   Brosnan, S. M.; Schlaad, H. *Polymer* **2014**, *55*, 5511–5516.

(27)   Krannig, K.-S.; Schlaad, H. *J. Am. Chem. Soc.* **2012**, *134*, 18542–18545.

(28)   Vacogne, C. D.; Brosnan, S. M.; Masic, A.; Schlaad, H. *Polym. Chem.* **2015**, *6*, 5040–5052.

(29)   Pang, X.; Chu, C.-C. *Polymer* **2010**, *51*, 4200–4210.

(30)   Krannig, K.-S.; Huang, J.; Heise, A.; Schlaad, H. *Polym. Chem.* **2013**, *4*, 3981–3986.

(31)   Krannig, K.-S.; Sun, J.; Schlaad, H. *Biomacromolecules* **2014**, *15*, 978–984.

(32)   Gupta, A. K.; Dufour, C.; Marchal, E. *Biopolymers* **1974**, *13*, 1293–1308.

(33)   Gupta, A. K.; Strazielle, C.; Marchal, E.; Benoit, H. *Biopolymers* **1977**, *16*, 1159–1165.

(34)   Gupta, A. K. *J. Polym. Sci. Polym. Lett. Ed.* **1979**, *17*, 47–53.

(35)   Chakrabarti, S.; Miller, W. G. *Biopolymers* **1984**, *23*, 719–734.

(36)   Tipton, D. L.; Russo, P. S. *Macromolecules* **1996**, *29*, 7402–7411.

(37)   Tohyama, K.; Miller, W. G. *Nature* **1981**, *289*, 813–814.

(38)   Tadmor, R.; Khalfin, R. L.; Cohen, Y. *Langmuir* **2002**, *18*, 7146–7150.

(39)   Zou, J.; Zhang, F.; Chen, Y.; Raymond, J. E.; Zhang, S.; Fan, J.; Zhu, J.; Li, A.; Seetho, K.; He, X.; Pochan, D. J.; Wooley, K. L. *Soft Matter* **2013**, *9*, 5951–5958.

(40)   Popescu, M.-T.; Liontos, G.; Avgeropoulos, A.; Tsitsilianis, C. *Soft Matter* **2015**, *11*, 331–342.

(41)   Suzuki, M.; Hanabusa, K. *Chem. Soc. Rev.* **2010**, *39*, 455–463.

(42) Cai, C.; Lin, J.; Zhuang, Z.; Zhu, W. In *Controlled Polymerization and Polymeric Structures*; Springer, **2013**; pp 159–199.

(43) Cohen, Y.; Dagan, A. *Macromolecules* **1995**, *28*, 7638–7644.

(44) Prystupa, D. A.; Donald, A. M. *Macromolecules* **1993**, *26*, 1947–1955.

(45) Floudas, G.; Papadopoulos, P.; Klok, H.-A.; Vandermeulen, G. W. M.; Rodriguez-Hernandez, J. *Macromolecules* **2003**, *36*, 3673–3683.

(46) Tadmor, R.; Dagan, A.; Cohen, Y. *Macromol. Symp.* **1997**, *114*, 13–22.

(47) Izumi, Y.; Takezawa, H.; Kikuta, N.; Uemura, S.; Tsutsumi, A. *Macromolecules* **1998**, *31*, 430–435.

(48) Shapiro, Y. E. *Prog. Polym. Sci.* **2011**, *36*, 1184–1253.

(49) Nishinari, K. *Colloid Polym. Sci.* **1997**, *275*, 1093–1107.

(50) Estroff, L. A.; Hamilton, A. D. *Chem. Rev.* **2004**, *104*, 1201–1218.

(51) Higgins, J. S.; Lipson, J. E. G.; White, R. P. *Philos. Trans. R. Soc. A Math. Phys. Eng. Sci.* **2010**, *368*, 1009–1025.

(52) Berg, J. M.; Tymoczko, J. L.; Stryer, L. *Biochemistry*, Sixth edit.; W. H. Freeman and Company: New York, **2007**.

(53) Li-Chan, E. C. Y.; Ismail, A. A.; Sedman, J.; Van de Voort, F. R. *Handbook of Vibrational Spectroscopy*; Chalmers, J. M., Griffiths, P. R., Eds.; Wiley, **2001**.

(54) Koenig, J. L.; Frushour, B. *Biopolymers* **1972**, *11*, 1871–1892.

(55) Chen, M. C.; Lord, R. C. *J. Am. Chem. Soc.* **1974**, *96*, 4750–4752.

(56) Guinn, R. M.; Margot, A. O.; Taylor, J. R.; Schumacher, M.; Clark, D. S.; Blanch, H. W. *Biopolymers* **1995**, *35*, 503–512.

(57) Huang, J.; Habraken, G.; Audouin, F.; Heise, A. *Macromolecules* **2010**, *43*, 6050–6057.

(58) Muroga, Y.; Nagasawa, M. *Biopolymers* **1998**, *45*, 281–288.

(59) Floudas, G.; Spiess, H. W. *Macromol. Rapid Commun.* **2009**, *30*, 278–298.

(60) Wu, L.; Müller, E. A.; Jackson, G. *Macromolecules* **2014**, *47*, 1482–1493.

(61) Koenig, J. L.; Sutton, P. L. *Biopolymers* **1971**, *10*, 89–106.

(62) Iconomidou, V. A.; Chryssikos, G. D.; Gionis, V.; Willis, J. H.; Hamodrakas, S. J. *Insect Biochem. Mol. Biol.* **2001**, *31*, 877–885.

(63) Wilser, W. T. *J. Chem. Phys.* **1975**, *62*, 720.

(64) Profit, A. A.; Vedad, J.; Saleh, M.; Desamero, R. Z. B. *Arch. Biochem. Biophys.* **2015**, *567*, 46–58.

(65) David, C.; D'Andrea, C.; Lancelot, E.; Bochterle, J.; Guillot, N.; Fazio, B.; Maragò, O. M.; Sutton, A.; Charnaux, N.; Neubrech, F.; Pucci, A.; Gucciardi, P. G.; de la Chapelle, M. L. *Vib. Spectrosc.* **2012**, *62*, 50–58.

(66) Kiefer, W.; Laane, J. In *Analytical Applications of FT-IR to Molecular and Biological Systems*; Durig, J. R., Ed.; Springer Netherlands: Dordrecht, **1980**; Vol. 57, pp 537–577.

(67) Block, H. *Poly(gamma-benzyl-L-glutamate) and other glutamic acid containing polymers*; Gordon

and Breach Science Publishers Ltd., **1983**.

(68)   Rousseau, M.; Beaulieu, L.; Lefe, T.; Paradis, J.; Asakura, T.; Pe, M. *Biomacromolecules* **2006**, No. 7, 2512–2521.

(69)   Kotharangannagari, V. K.; Sánchez-Ferrer, A.; Ruokolainen, J.; Mezzenga, R. *Macromolecules* **2012**, *45*, 1982–1990.

(70)   Tang, H.; Zhang, D. *J. Polym. Sci. Part A Polym. Chem.* **2013**, *51*, 4489–4497.

(71)   Pelton, J. T.; McLean, L. R. *Anal. Biochem.* **2000**, *277*, 167–176.

(72)   Greenfield, N.; Fasman, G. D. *Biochemistry* **1969**, *8*, 4108–4116.

(73)   Chou, P. Y.; Fasman, G. D. *Biochemistry* **1974**, *13*, 222–245.

(74)   Johnson, W. C. *Proteins* **1990**, *7*, 205–214.

(75)   Charney, E.; Milien, J. B.; Yamaoka, K. *J. Am. Chem. Soc.* **1970**, *92*, 2657–2664.

(76)   Parrish, J. R.; Blout, E. R. *Biopolymers* **1971**, *10*, 1491–1512.

(77)   Formaggio, F.; Toniolo, C. *Chirality* **2010**, *22*, E30–E39.

(78)   Mazzier, D.; Maran, M.; Polo Perucchin, O.; Crisma, M.; Zerbetto, M.; Causin, V.; Toniolo, C.; Moretto, A. *Macromolecules* **2014**, *47*, 7272–7283.

(79)   Conejos-Sánchez, I.; Duro-Castano, A.; Birke, A.; Barz, M.; Vicent, M. J. *Polym. Chem.* **2013**, *4*, 3182–3186.

(80)   Guerette, P. A.; Hoon, S.; Ding, D.; Amini, S.; Masic, A.; Ravi, V.; Venkatesh, B.; Weaver, J. C.; Miserez, A. *ACS Nano* **2014**, *8*, 7170–7179.

(81)   Maiti, N. C.; Apetri, M. M.; Zagorski, M. G.; Carey, P. R.; Anderson, V. E. *J. Am. Chem. Soc.* **2004**, *126*, 2399–2408.

(82)   He, X.; Fan, J.; Zhang, F.; Li, R.; Pollack, K. A.; Raymond, J. E.; Zou, J.; Wooley, K. L. *J. Mater. Chem. B* **2014**, *2*, 8123–8130.

(83)   Lakhani, A.; Roy, A.; De Poli, M.; Nakaema, M.; Formaggio, F.; Toniolo, C.; Keiderling, T. A. *J. Phys. Chem. B* **2011**, *115*, 6252–6264.

(84)   Mikhonin, A. V.; Bykov, S. V.; Myshakina, N. S.; Asher, S. A. *J. Phys. Chem. B* **2006**, *110*, 1928–1943.

(85)   Weaver, T. M. *Protein Sci.* **2000**, *9*, 201–206.

(86)   Jacob, C. R.; Luber, S.; Reiher, M. *J. Phys. Chem. B* **2009**, *113*, 6558–6573.

(87)   Jahanshahi, K.; Botiz, I.; Reiter, R.; Thomann, R.; Heck, B.; Shokri, R.; Stille, W.; Reiter, G. *Macromolecules* **2013**, *46*, 1470–1476.

(88)   McKinnon, A. J.; Tobolsky, A. V. *J. Phys. Chem.* **1968**, *72*, 1157–1161.

(89)   Babin Taton, D., Brinkman, M., Lecommandoux, S., J. *Macromolecules* **2008**, *41*, 1384–1392.

(90)   Li, S.-T.; Lin, Y.-C.; Kuo, S.-W.; Chuang, W.-T.; Hong, J.-L. *Polym. Chem.* **2012**, *3*, 2393.

(91)   Scherrer, P. *Nachrichten von der Gesellschaft der Wissenschaften zu Göttingen, Math. Klasse 2*, 98–100.

(92)   Horton, J. C.; Donaldt, A. M. *Polymer.* **1991**, *32*, 2418–2427.

(93)   Korenaga, T.; Oikawa, H.; Nakanishi, H. *J. Macromol. Sci. Part B* **1997**, *36*, 487–501.

(94)   Tsuboi, K.; Marcelletti, E.; Matsumoto, H.; Ashizawa, M.; Minagawa, M.; Furuya, H.; Tanioka, A.; Abe, A. *Polym. J.* **2012**, *44*, 360–365.

(95)   Chester, A. N.; Martellucci, S. *Phase Transitions in Liquid Crystals*; Martellucci, S., Chester, A. N., Eds.; NATO ASI Series; Springer US: Boston, MA, **1992**; Vol. 290.

(96)   Minato, K.-I.; Ohkawa, K.; Yamamoto, H. *Macromol. Biosci.* **2006**, *6*, 487–495.

(97)   Miller, W. G.; Wu, C. C.; Wee, E. L.; Santee, G. L.; Rai, J. H.; Goebel, K. G. *Pure Appl. Chem.* **1974**, *38*, 37–58.

(98)   Deming, T. J. *Adv. Mater.* **1997**, *9*, 299–311.

(99)   Jackson, C. L.; Shaw, M. T. *Polymer* **1990**, *31*, 1070–1084.

(100)   Erman, B.; Bahar, I.; Navard, P. *Macromolecules* **1989**, *22*, 358–364.

(101)   Yen, C.; Edo, S.; Oka, H.; Tokita, M.; Watanabe, J. *Macromolecules* **2008**, *41*, 3727–3733.

(102)   Lee, H.; Sheu, H.; Jeng, U.; Huang, C.; Chang, F.-C. *Macromolecules* **2005**, *38*, 6551–6558.

(103)   Livolant, F.; Bouligand, Y. *J. Phys.* **1986**, *47*, 1813–1827.

(104)   Yu, G.; Yan, X.; Han, C.; Huang, F. *Chem. Soc. Rev.* **2013**, *42*, 6697.

(105)   Yan, X.; Xu, D.; Chi, X.; Chen, J.; Dong, S.; Ding, X.; Yu, Y.; Huang, F. *Adv. Mater.* **2012**, *24*, 362–369.

(106)   Wang, J.; Liu, K.; Xing, R.; Yan, X. *Chem. Soc. Rev.* **2016**, *45*, 5589–5604.

(107)   Shi, X.; Bin, Y.; Hou, D.; Men, Y.; Matsuo, M. *Polym. J.* **2014**, *46*, 21–35.

(108)   Adams, D. J.; Morris, K.; Chen, L.; Serpell, L. C.; Bacsa, J.; Day, G. M. *Soft Matter* **2010**, *6*, 4144.

(109)   Matsuyama, A. In *Encyclopedia of Polymer Blends, Volume 1: Fundamentals*; Wiley-VCH Verlag GmbH & Co. KGaA: Weinheim, Germany, **2010**; pp 45–100.

(110)   Hill, A.; Donald, A. M. *Polymer* **1988**, *29*, 1426–1432.

(111)   Natta, G. *J. Polym. Sci.* **1959**, *34*, 531–549.

(112)   Sanchez, I. C.; Eby, R. K. *Macromolecules* **1975**, *8*, 638–641.

(113)   Nicholson, J. W. In *The Chemistry of Polymers*; RSC Publishing, **2006**; pp 40–53.

(114)   Leung, L. M.; Koberstein, J. T. *Macromolecules* **1986**, *19*, 706–713.

(115)   Tsereteli, G. I.; Smirnova, O. I. *Polym. Sci. U.S.S.R.* **1991**, *33*, 2112–2118.

(116)   te Nijenhuis, K. *Colloid Polym. Sci.* **1981**, *259*, 1017–1026.

(117)   Tauer, T. P.; Derrick, M. E.; Sherrill, C. D. *J. Phys. Chem. A* **2005**, *109*, 191–196.

Chapter V

From the Self-Assembly of Polypeptides to Fibrillar Hydrogels

This chapter contains results and material that have been published and are hereby reproduced by permission of the Royal Society of Chemistry (See Appendix C for the list of publications).

V.1   Introduction

Polypeptide-based hydrogels are becoming increasingly important biomedical materials[1–4] as they provide a biomimetic, porous, and hydrophilic environment, ideal to support cell colonisation[5] and drug delivery.[4,6] There are many examples of hydrogels used in medicine that are derived from natural polypeptides, such as soluble collagen,[7] gelatin,[8,9] and fibrin.[10] These proteins have predefined structures, compositions, and sequences,[11] which confer advantages such as biocompatibility and bioactivity but fundamentally limits the extent to which they can be chemically modified or processed to fit specific application needs.[12] These limitations can be overcome by the use of synthetic polypeptides, whose chain lengths, compositions (*e.g.*, sequence controlled, block or random copolymers, and natural or non-natural amino acids) and secondary structures (*e.g.*, α-helices and β-sheets) can be adapted. Owing to their secondary structure, synthetic polypeptides can behave as macromolecular building blocks and self-assemble to form supramolecular assemblies (*e.g.*, fibres, gels, or liquid crystals).[1–3,13] Notably, their composition, architecture and topology can be tailored to generate biocompatible supramolecular gels with tuneable properties (*e.g.*, density, porosity, microstructure)[14–16] and high swelling ratios.[17–23] As such, synthetic polypeptides offer a versatile approach towards structural[24] and stimuli responsive[9,25] medical hydrogels.[26]

Typically, sequence-controlled polypeptides are synthesised by solid-phase synthesis.[27,28] The advantage of this technique is the complete control over the polypeptide sequence and chain length, hence allowing to synthesise truly biomimetic macromolecules. However, this technique produces polypeptides in lab scale quantities (< 1 g) and with low chain lengths (< 50 repeat units). A cost effective route for the synthesis of longer polypeptides in larger quantities is the ring opening polymerisation (ROP) of α-amino acid *N*-carboxyanhydride (NCA). Poly(γ-benzyl-L-glutamate) (PBLG) is one of the most common and studied polypeptides synthesised by ROP.[1,29] Additionally, the carboxylic ester moieties of PBLG can be

debenzylated to generate its biocompatible counterpart, poly(L-glutamic acid) (PLGA, hydrophobic) under acidic conditions and poly(L-glutamate) (PLG, hydrophilic) under neutral and basic conditions.[30–32] The popularity of PBLG and PLGA can be attributed to a relatively inexpensive α-amino acid precursor, L-glutamic acid γ-benzyl ester, and also to their ability to fold into α-helices. PLGA undergoes a helix-to-coil transition at pH ~ 5-6,[1,33,34] making it an attractive candidate for stimuli-responsive bio-systems.[1,33,35–38] Notably, the rod-like α-helical conformation[25,39], pH-responsiveness[36–38] and good solubility at neutral and high pH[13] of PLGA have been exploited in block copolymers used for vesicles and hydrogels. PLGA and PLG, however, do not self-assemble into physical hydrogels as the hydrophobicity of PLGA α-helices causes them to precipitate from water.[43] The formation of long range order or supramolecular assemblies from α-helical building blocks in water is challenging as water disrupts hydrogen bonds, essential to the stabilisation of secondary structures.[4,44] That is why PLGA-based hydrogels are generally prepared by (*i*) chemical crosslinking using water soluble carbodiimides[17] or diamines,[18,19] (*ii*) blending with cationic polymers,[20,21] (*iii*) self-assembly of PLGA-based block copolymers,[21] and (*iv*) lyophilisation.[17]

Unlike PLGA, PBLG α-helices can assemble in a head-to-tail (*i.e.*, end-to-end) and side-by-side fashion[29,45,46] and generate long range order in helicogenic organic solvents. At high concentrations (over 10 wt%, *i.e.*, 100 g·L^{-1}), PBLG self-assembly yields lyotropic phases.[47] In dilute systems (down to 0.1 wt%, *i.e.*, 1 g·L^{-1}) and in 'poor' solvents, such as toluene, benzyl alcohol, or dioxane-water mixtures,[48] PBLG self-assembly yields a continuous network of solvent-trapping fibrils and fibrillar bundles (*i.e.*, fibres) forming physical organogels.[47,48] In these fibrils, composed of typically 4 to 10 PBLG α-helices across, all helices are oriented parallel to the fibrils' long axis.[46,49,50] PBLG helices and fibres are stabilised by intramolecular hydrogen bonding (favoured by aprotic solvents),[11] dipole-dipole interaction of the PBLG helices (favoured by non-polar solvents),[45,51,52] and π-π stacking of the outward-pointing pendant benzyl groups.[53] These organogels exhibit attractive features, including a robust fibrous network and a high porosity.[48] In contrast, the physical gelation of β-sheets, differs from α-helices in that self-assembly occurs in a side-by-side fashion upon intermolecular hydrogen bonding.[54] Inspired by PBLG supramolecular assemblies, a few studies circumvented the challenging self-assembly of PLGA in water by chemically crosslinking lyotropic phases of concentrated PBLG solutions and deprotecting their carboxylic acid functions to yield liquid crystalline (LC) chemical gels.[25,26] The highly concentrated solutions used (25 wt%) led to dense gels with low porosity and limited swelling in the presence of water.[18] Besides, the crosslinking treatment that reacted multifunctional amines with benzyl ester side groups, was extremely time-consuming (> 3 days) and was non-specific to the position and number of crosslinks.[18,19,55]

In order to overcome these obstacles and achieve biocompatible fibrillar networks, a new route to prepare highly absorbent, porous, and stimuli-responsive PLGA/PLG-based hydrogels was explored. This was achieved by synthesising (*via* ROP of NCA) statistical copolymers of BLG and allylglycine (AG) of relatively low molar masses (*e.g.*, down to 11 kDa),[43,56] and photo-crosslinking gelation followed by the deprotection of the carboxylic acid functions. BLG was chosen as the main monomer in order to ensure α-

helical conformation, and AG as the co-monomer, as it can be functionalised or crosslinked under UV light using fast and quantitative thiol-ene click chemistry.[43,57,58] The ability for dilute solutions of P(BLG-*co*-AG) copolymers in 1,4-dioxane, toluene, and THF (down to 10 g·L^{-1}, *i.e.* 1% w/v) to form robust and highly porous UV-crosslinked organogels is reported herein. The α-helical conformation of P(BLG-*co*-AG) and their self-assembly into supramolecular fibre-like aggregates was shown to be essential to the preparation of crosslinked organogels from dilute solutions. Finally, the debenzylation of their carboxylic acid functions led to pH-responsive and highly absorbent fibrous hydrogels that have great potential as extracellular matrices for application in 3D cell culture and regenerative medecine.[16]

V.2   Experimental

V.2.1   Materials

In order to prepare polyglutamate-based hydrogels, statistical copolypeptides of γ-benzyl-l-glutamate (BLG) and allylglycine (AG), referred to as P(BLG$_x$-*co*-AG$_{1-x}$)$_n$ hereafter, were synthesised and used as precursors. Their synthesis is described in Chapter II and Appendix A, and the specific copolymers used for this study are gathered in Table V.1.

Table V.1 Molecular Characteristics of Polypeptides Used in Chapter V (Appendix B, P1 to P4, and P12 to P16)

Sections	Polymer	γ-Benzyl-L-glutamate (BLG)		Allylglycine (AG)		M_n[a]	n[a]	Đ^{app}
		Mole fraction[a]	Configu-ration	Mole fraction[a]	Configu-ration	(kg·mol^{-1})		(M$_w$/M$_n$)[b]
A	PBLG$_{51}$	100%	L	-	-	11.3	51	1.09
V.3.1 to V.3.5	P(BLG$_{0.89}$-*co*-DLAG$_{0.11}$)$_{53}$	89%	L	11%	DL	11.0	53	1.18
	P(BLG$_{0.76}$-*co*-DLAG$_{0.24}$)$_{59}$	76%	L	24%	DL	11.4	59	1.16
	P(BLG$_{0.77}$-*co*-LAG$_{0.23}$)$_{57}$	77%	L	23%	L	11.1	57	1.25
	P(BLG$_{0.74}$-*co*-LAG$_{0.26}$)$_{91}$	74%	L	26%	L	17.2	91	1.21
	P(BLG$_{0.74}$-*co*-LAG$_{0.26}$)$_{170}$	74%	L	26%	L	31.9	170	1.28
B	P(BLG$_{0.78}$-*co*-LAG$_{0.22}$)$_{96}$	78%	L	22%	L	18.6	96	1.13
V.3.3	P(BLG$_{0.80}$-*co*-LAG$_{0.20}$)$_{219}$	80%	L	20%	L	42.8	219	1.23
	P(BLG$_{0.84}$-*co*-LAG$_{0.16}$)$_{171}$	84%	L	16%	L	34.2	171	1.28

[a] M_n = number-average molar mass. n = number-average degree of polymerisation. Determined by ^{1}H-NMR (Appendix A).
[b] Đ^{app} = M_w/M_n = ratio of weight- over number-average molar mass (dispersity). Determined by SEC (PMMA calibration) (Appendix A).

Benzophenone and 1,9-nonanedithiol were used as photo-initiator and crosslinker, respectively, for the preparation of photo-crosslinked organogels (Figure V.1). Trimethylolpropane tris(3-mercaptopropionate) was also tested as a crosslinker, and Michler's ketone as a photo-initiator, in Section V.3.3 (Figure V.1). Other chemicals and solvents used for this study are listed in Appendix A.
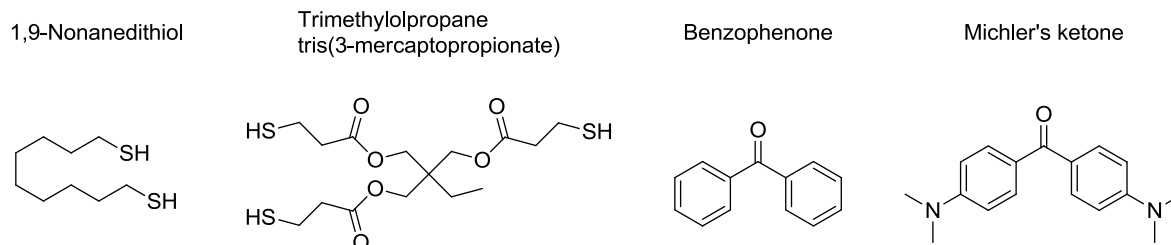
| 1,9-Nonanedithiol | Trimethylolpropane tris(3-mercaptopropionate) | Benzophenone | Michler's ketone |

Figure V.1 (left) Multifunctional thiol crosslinkers and (right) type II photo-initiators used in this study.

V.2.2 Methods

V.2.2.1 Organogel Preparation

Thermoreversible physical gels of $PBLG_{51}$ were prepared by dissolving it in toluene (typically, 4 to 10 $g \cdot L^{-1}$, *i.e.*, 0.4 to 1% w/v) at 60 °C for 45-60 min and cooling the mixture down to room temperature. In order to prepare crosslinked $P(BLG_x\text{-}co\text{-}AG_{1-x})_n$ gels, the copolypeptides were dissolved in toluene, THF or 1,4-dioxane (typically, 10 to 50 $g \cdot L^{-1}$, *i.e.*, 1 to 5 % w/v) at 60 °C in a glass vial. Then the crosslinker 1,9-nonanedithiol (typically 0.75 equiv. relative to AG units) and type II photoinitiator benzophenone (typically, 1 $g \cdot L^{-1}$) were added. The mixture was then argon or nitrogen purged for 10 min and exposed to UV radiation (Heraeus TQ 150 Hg-lamp 150 W) for 20 to 30 min. To prepare 'cold-crosslinked' toluene gels, the vials were plunged in a -77 °C cooling bath and positioned upside-down to ensure UV-exposure through the bottom glass wall of the vials.

V.2.2.2 Hydrogel Preparation

In order to prepare hydrogels, dioxane gels were dried under high vacuum and immersed in a TFA/anisole/MSA (45:10:45 vol%) solution (deprotection route A) or in a TFA/HBr (75:25 vol%) solution (deprotection route B), with HBr in acetic acid (37 vol%); 5 mL of deprotection solution per 20 mg of dried organogel. As toluene is harder to remove, toluene-based gels were simply immersed as such in the aforementioned deprotection solutions. The mixtures were gently shaken in ice for 30 min and then at room temperature for another 30 min. The gels were washed with diethyl ether and immersed in a $NaHCO_3$-saturated aqueous solution for 12 h. The gels were then dialysed against distilled water for 48 h.

V.2.2.3 Swelling Ratio Measurement

In order to quantify their swelling ratio (SR), the hydrogels were weighed following the debenzylation stage, in their swollen state (*i.e.*, loaded with Millipore water), as well as after the freeze-drying. The swelling ratio was then calculated using the following equation, $SR = (m_H - m_D)/m_D$, with m_H the mass of the hydrated (*i.e.*, swollen) hydrogel and m_D its dry mass.

See Appendix A for all analytical methods used here (i.e., CD, FTIR, Raman, WAXS, AFM, SEM and TEM).

V.3 Results and Discussion

V.3.1 Photo-Crosslinking Gelation

As discussed in Chapter IV, all analysed $P(BLG_x$-co-$AG_{1-x})_n$ copolypeptides were shown to, once dissolved in toluene, formed physical gels at temperatures ranging from -38 °C to -8 °C. In addition, they were shown to be α-helical, hence rod-like, like PBLG. The physical gelation theory of rod-like polymers suggests that such gels comprise of a network of entangled or connected fibres, which was demonstrated by TEM for PBLG (Figure IV.1 and V.2a) and supported by indirect evidences for $P(BLG_x$-co-$AG_{1-x})_n$ in Chapter IV, but with no direct SEM or TEM evidence.[49,52,59,60] Since $P(BLG_x$-co-$AG_{1-x})_n$-toluene physical gels only exist at low temperatures, photo-crosslinking of the allyl functional groups with dithiol crosslinkers was investigated as a way of fixing the physical network in order to allow for the handling and characterisation of the copolypeptides-based gels at room temperature.

UV-crosslinking by thiol-ene chemistry was selected as it is well known for being rapid (< 1 h) and nearly quantitative.[58] As it was desirable to ensure that the physical gel network was preserved during the process, $P(BLG_x$-co-$AG_{1-x})_n$-toluene systems (5 to 50 $g \cdot L^{-1}$) were crosslinked at -77 °C, $i.e.$, below their gelation temperature (Table IV.2) and above the melting point of toluene (- 95 °C) (Figure V.2b). This 'cold crosslinking' procedure was successful for $P(BLG_x$-co-$AG_{1-x})_n$-toluene systems for which the proportion of AG was greater than 23% ($i.e.$, 1-x > 0.23), but failed for $P(BLG_{0.89}$-co-$DLAG_{0.11})_{53}$. This can be imputed to the fact that a minimum number of crosslinking moieties ($i.e.$, 'ene' form AG units) is required to readily fix and stabilise the gel microstructure, in the same way that a construction scaffold requires a minimum number of clamps to hold it together. All crosslinked $P(BLG_x$-co-$AG_{1-x})_n$-toluene gels showed partial shrinkage and a tendency to plastically deform when handled (Figure V.3a). This indicates that the gel microstructure of $P(BLG_x$-co-$AG_{1-x})_n$-toluene systems preserved by cold crosslinking is not load-bearing at room temperature, thereby limiting their application as precursors for hydrogels.
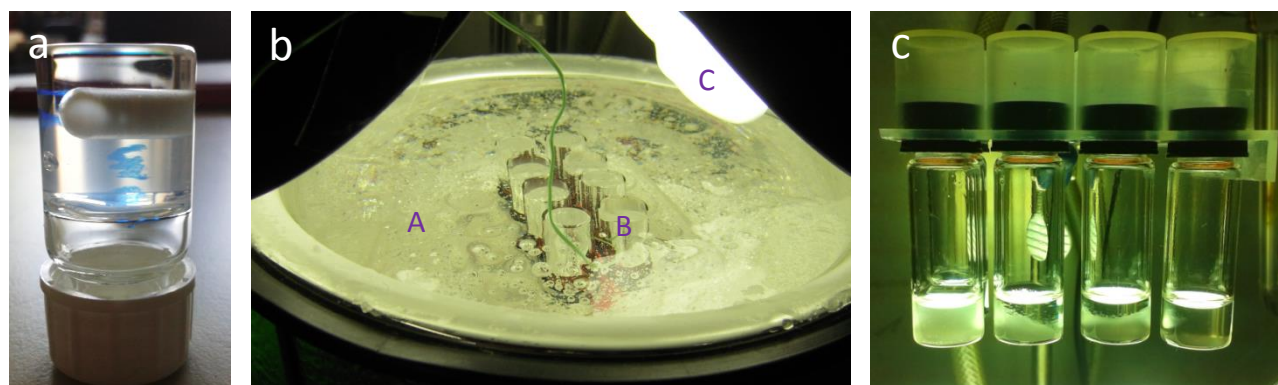

Figure V.2 (a) Physical gel of $PBLG_{51}$-toluene (4 $g \cdot L^{-1}$, $i.e.$, 0.4% w/v). (b) Cold crosslinking set up, with a Dewar vessel filled with (A) isopropanol-dry ice cooling bath (-77 °C), (B) $P(BLG_x$-co-$AG_{1-x})_n$-toluene systems being crosslinked in argon-purged glass vials maintained upside-down to allow for UV exposure via their glass bottom, and (C) UV source (here, Exo Terra ReptiGlo 5.0, a UV source which is not used in this study). (c) Room temperature crosslinking set up with $P(BLG_x$-co-$AG_{1-x})_n$-toluene systems being crosslinked in argon-purged glass vials via UV exposure with the same source, positioned below the samples.

Surprisingly, the UV-crosslinking of P(BLG$_x$-co-AG$_{1-x}$)$_n$-toluene systems at room temperature also yielded gels (Figure V.2c). These gels were slightly less stable than those crosslinked at -77 °C (Figure V.3b), yet the formation of a macroscopic gel under such conditions, is an exceptional result as chemical gels resulting from dilute solutions of low molar mass polymers (< 50,000 g·mol^{-1}) are unusual.[26] In other words, it is very unlikely that the crosslinking of loose randomly coiled polymers of molar masses as low as 10,000 g·mol^{-1} and at concentrations lower than 5 g·L^{-1} should generate a continuous network, which is a prerequisite feature to all gels.[8] Achieving a continuous and interconnected network under such conditions requires that these polymers self-assemble such that long range order is achieved. There is a precedent in the form of small organogelators, which are known to self-assemble over long distances - and sometimes hierarchically - typically resulting in supramolecular organogels.[61–64] P(BLG$_x$-co-AG$_{1-x}$)$_n$-toluene systems are liquid at room temperature, which rules out the existence of a continuous network. In Chapter IV, it was shown that P(BLG$_x$-co-AG$_{1-x}$)$_n$ are α-helical in toluene and that the high viscosity of P(BLG$_x$-co-AG$_{1-x}$)$_n$-toluene solutions is a strong indication of an end-to-end (or head-to-tail) aggregation of these α-helices.[51,65] Based on these considerations, one could postulate that the room-temperature crosslinking of P(BLG$_x$-co-AG$_{1-x}$)$_n$-toluene systems connected a somewhat fluid, loosely bound network formed by the partial aggregation of P(BLG$_x$-co-AG$_{1-x}$)$_n$ copolypeptides in toluene. If the minimum requirement for cross-linking-induced P(BLG$_x$-co-AG$_{1-x}$)$_n$ organogel formation is that the polypeptides be α-helical and somewhat aggregated, then other known helicogenic solvents for PBLG might also allow for photo-crosslinking gelation.[45] In order to verify this hypothesis and seek optimal organogel precursors for hydrogel, the room-temperature crosslinking of dilute solutions of P(BLG$_x$-co-AG$_{1-x}$)$_n$ in other helicogenic solvents, such as THF and dioxane, was explored.[48]
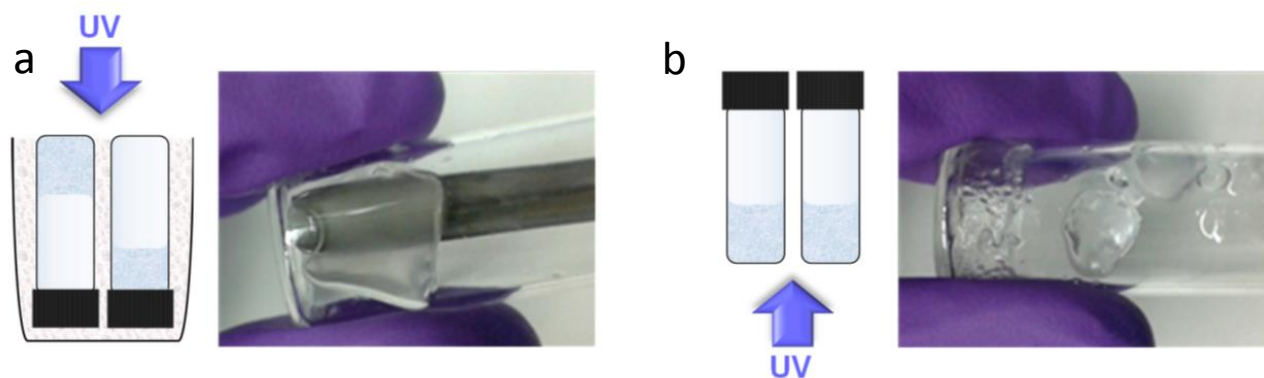

Figure V.3 (a) Crosslinked P(BLG$_x$-co-AG$_{1-x}$)$_n$-toluene at -77 °C showing good compression resistance; the schematics depict (left) P(BLG$_{0.77}$-co-LAG$_{0.23}$)$_{57}$-toluene (10 to 50 g·L^{-1}), which gels at -27 °C and remains set at the top (glass bottom) of the vial, and (right) P(BLG$_{0.76}$-co-DLAG$_{0.24}$)$_{59}$-toluene (10 to 50 g·L^{-1}) which gels at -38 °C but whose small shear modulus causes it to fall to the bottom (black lid) of the vial. (b) Room temperature crosslinked P(BLG$_x$-co-AG$_{1-x}$)$_n$-toluene showing low-compression resistance.

V.3.2 Mechanism of Photo-Crosslinking Gelation

In order to investigate this photo-crosslinking gelation of dilute systems, which is believed not to require that physical gels be formed, THF and dioxane were selected as, in addition to being helicogenic, they are known to cause aggregation of PBLG without leading to physical gelation.[45] An FTIR analysis of P(BLG$_x$-co-

AG$_{1-x}$)$_n$-dioxane solutions (Figure VI.2.a), confirmed the α-helical secondary structure of these polypeptides under dilute and semi-dilute conditions. Solutions of 10 g·L^{-1} of P(B$_L$G$_x$-co-AG$_{1-x}$)$_n$ in THF and in dioxane were successfully crosslinked at room temperature in under 20 min of UV exposure and yielded gels that showed almost no shrinkage and were mechanically stable (elastic response to mild compression). This result shows that photo-crosslinking gelation can be achieved for dilute solutions of P(B$_L$G$_x$-co-AG$_{1-x}$)$_n$ in different helicogenic solvents without the need for a pre-established physical gel network. The dioxane gels were more robust than the other gels and could be readily dried without collapsing its intricate fibrous microstructure, a collapse which visibly occurred in THF- and toluene gels (Figure V.4a, b and c).
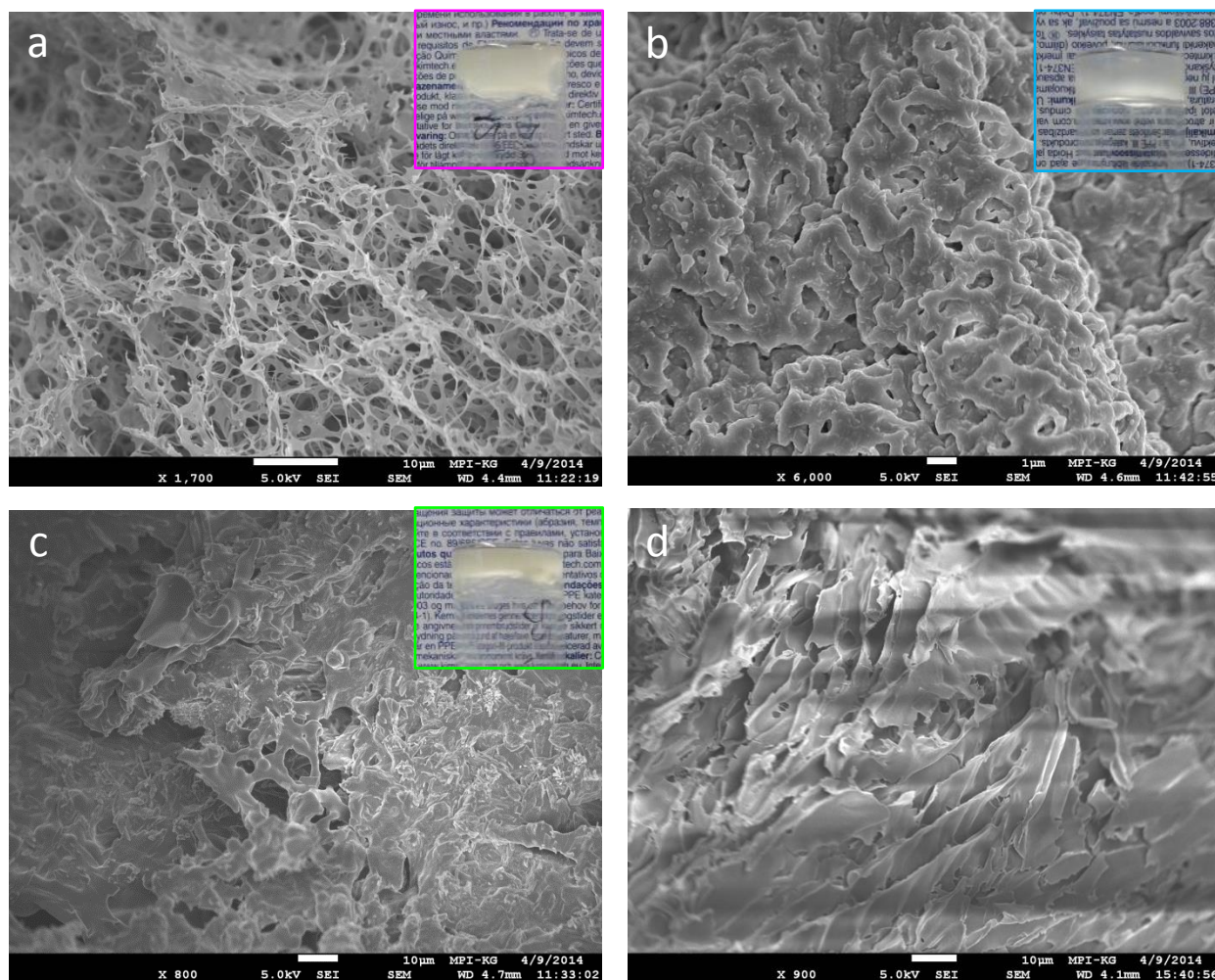
Figure V.4 SEM micrographs of vacuum-dried 10 g·L^{-1} organogels of P(B$_L$G$_x$-co-AG$_{1-x}$)$_n$ in (a) 1,4-dioxane (scale bar = 10 μm), (b) toluene (scale bar = 1 μm) and (c) THF (scale bar = 1 μm), and vial inversion picture (top right insert); and of (d) freeze-dried solution of P(B$_L$G$_x$-co-AG$_{1-x}$)$_n$ in 1,4-dioxane (10 g·L^{-1}) (scale bar = 10 μm).

P(B$_L$G$_x$-co-AG$_{1-x}$)$_n$-dioxane gels also held their shape once extracted from glass vials (Figure V.5). PB$_L$G has been reported to strongly aggregate in head-to-tail and side-by-side modes in dioxane,[66] while it merely aggregates in a head-to-tail mode in other media such as THF for instance.[45] By extrapolating this aggregation behaviour to P(B$_L$G$_x$-co-AG$_{1-x}$)$_n$, it is plausible that these copolymers formed particularly thick aggregates in dioxane, resulting in a robust and structural gel network once crosslinked. It is also possible that, the removal of dioxane (T$_m$ = 12 °C) under high vacuum caused the temperature to drop during the

evaporation stage, thereby causing the removal of dioxane to proceed *via* lyophilisation. This would help to prevent the collapse of the fibres and preserve the gel network. A comparison of the microstructures obtained from freeze dried P(BLG$_x$-*co*-AG$_{1-x}$)$_n$ in dioxane and dried P(BLG$_x$-*co*-AG$_{1-x}$)$_n$-dioxane gels provided strong evidence that such fibrous structures were not the result of lyophilisation (Figure V.4a and d).
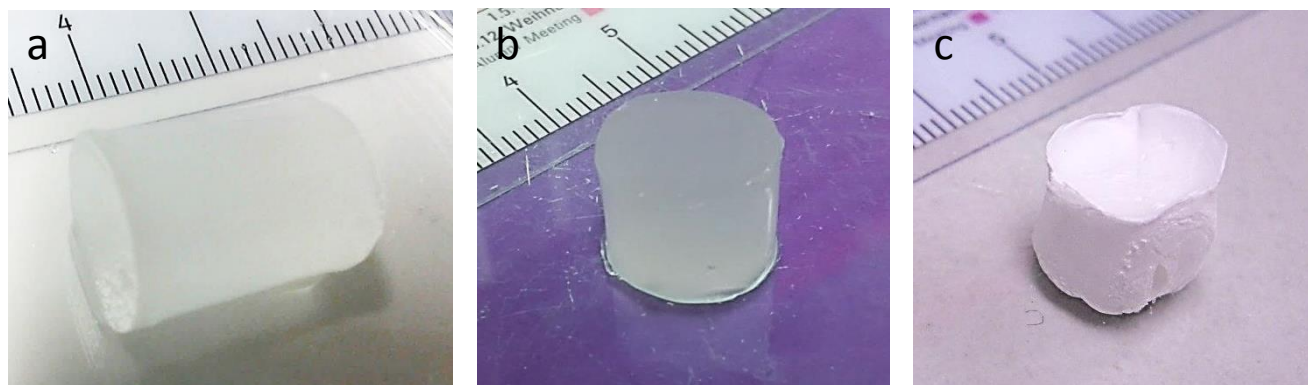

Figure V.5 Photo-crosslinked dioxane gels (10 g·L^{-1}, *i.e.* 1% w/v) after extraction from glass vial of (a) P(BLG$_{0.77}$-*co*-LAG$_{0.23}$)$_{57}$ (2 mL) and (b) P(BLG$_{0.74}$-*co*-LAG$_{0.26}$)$_{91}$ (1 mL); (c) freeze-dried P(BLG$_{0.74}$-*co*-LAG$_{0.26}$)$_{91}$ (1 mL).

The SEM analysis failed to reveal the microstructure of dried P(BLG$_x$-*co*-AG$_{1-x}$)-toluene gels (Figure V.4b), most likely due to the collapse of the gel network during the drying process. Therefore, TEM was used to investigate P(BLG$_x$-*co*-AG$_{1-x}$)-toluene gel microstructures. The dabbing procedure used to deposit gel samples onto TEM grids (Appendix A) helped achieve sufficiently thin sections as required for TEM imaging. The P(BLG$_x$-*co*-AG$_{1-x}$)$_n$-THF and -dioxane gels were too stiff to allow for the deposition of thin layers and were thus not analysed by TEM. The TEM micrographs of crosslinked P(BLG$_x$-*co*-AG$_{1-x}$)$_n$-toluene gels showed largely interconnected high aspect ratio fibrous aggregates (Figure V.6b, c, e and f) that resembled the entangled fibres observed in PBLG$_{51}$-toluene physical gels (Figure V.6a and d). These gels exhibited a higher density of fibres for higher polymer concentrations, with no significant alteration of the aspect ratios of the aggregates.

In Chapter IV, it was shown that the secondary structure and aggregation behaviour of P(BLG$_x$-*co*-AG$_{1-x}$)$_n$ and PBLG were very similar in the dry state and in solution. Besides, both homo- and copolypeptides underwent thermoreversible physical gelation. The viscosity of P(BLG$_x$-*co*-AG$_{1-x}$)$_n$-solutions and the gradual disappearance of ^{1}H-NMR signals indicated that, like PBLG, these copolypeptides aggregate in helicogenic solvents and that the level of aggregation (*e.g.*, aggregate size) increases with decreasing temperature. Based on this consideration, and the fibrous structures observed by SEM and TEM (Figure V.4 and Figure V.6), it was hypothesised that P(BLG$_x$-*co*-AG$_{1-x}$)$_n$ polymers fold into α-helices that self-assemble, into loose fibrous aggregates in helicogenic solvents (*e.g.*, THF, toluene, and dioxane) and over a broad temperature range (including room temperature), such that these aggregates can be covalently interconnected by UV-crosslinking of the AG moieties, without the need for physical gelation to occur. As such, the crosslinking stage causes the fibres to be covalently fixed and interconnected, resulting in a stable and continuous fibrous network, yielding robust gels directly from dilute solutions (Figure V.7).
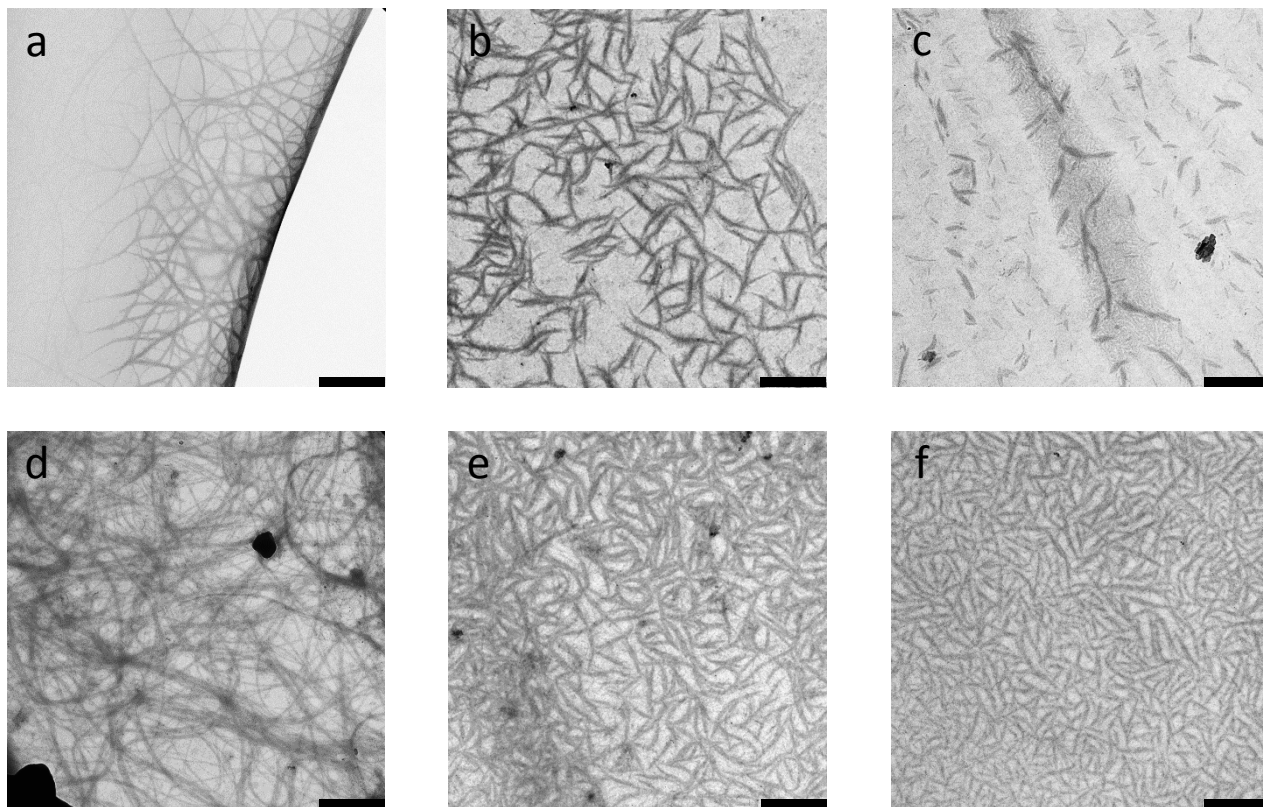
Figure V.6 TEM micrographs of toluene gels of (a) $PBLG_{51}$ (4 g·L^{-1}), (b) $P(BLG_{0.77}\text{-}co\text{-}LAG_{0.23})_{57}$ (5 g·L^{-1}), (c) $P(BLG_{0.76}\text{-}co\text{-}DLAG_{0.24})_{59}$ (5 g·L^{-1}), (d) $PBLG_{51}$ (10 g·L^{-1}), (e) $P(BLG_{0.77}\text{-}co\text{-}LAG_{0.23})_{57}$ (10 g·L^{-1}), (f) $P(BLG_{0.76}\text{-}co\text{-}DLAG_{0.24})_{59}$- (10 g·L^{-1}); (a and d) $PBLG_{51}$-toluene gels are physical gels; (b, c, d, e) the $P(BLG_x\text{-}co\text{-}AG_{1-x})_n$-toluene gels were crosslinked at -77 °C with 1,9-nonanedithiol. Scale bar = 1 µm.
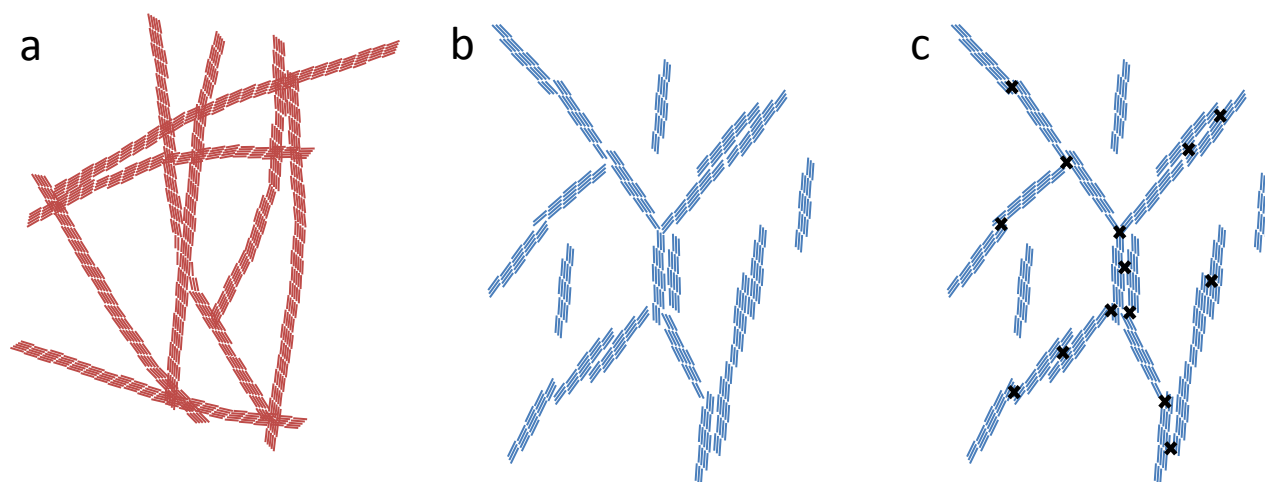
Figure V.7 Schematic illustration of (a) known PBLG-toluene gel microstructure, composed of a percolation network of long load-bearing fibres in which the PBLG α-helices (represented by red rods) are aligned parallel to the long axis, (b) postulated arrangement of $P(BLG_x\text{-}co\text{-}AG_{1-x})_n$ α-helices (represented by blue rods) into short fibres or high aspect ratio aggregates in dioxane and toluene, which are too short or unstable to generate a percolation network at room temperature, (c) same system as b after UV-crosslinking (crosslinks represented by 'x') showing how a percolation network (*e.g.*, gel) is generated.

A WAXS analysis of solutions and physical gels of $PBLG_{51}$, and of solutions and crosslinked gels of $P(BLG_x\text{-}co\text{-}AG_{1-x})_n$ in different solvents, was conducted in order to confirm the above hypothesis, but was inconclusive as no Bragg reflection was detected. Brownian motion, low concentrations, solvent-swollen fibres,[67] and an insufficient polymer-solvent contrast may explain the absence of scattering signals. In order

to circumvent such drawbacks, the glass capillaries used to hold these gels were loosely closed as to allow for partial solvent removal, in an attempt to improve the contrast while maintaining the swollen state of the gels. A selection of spectra for such samples are displayed in Figure V.8 and reveal a main peak at 2θ = 5-6°. The slightly higher *d*-spacing (1.5-1.8 nm), and lower resolution (the slightly irregular shape of the peaks was most likely caused by a greater noise) of these gel samples, compared to the pure polymers, was interpreted as the result of solvent-swollen pseudo-hexagonally packed fibres, as reported in the literature.[67–70] This result provides additional evidence to support that photo-crosslinked $P(BLG_x\text{-}co\text{-}AG_{1-x})_n$ organogels are enabled by the aggregation in solution of $P(BLG_x\text{-}co\text{-}AG_{1-x})_n$ α-helices into pseudo-hexagonally packed high aspect ratio, fibrous aggregates (Figure V.7).
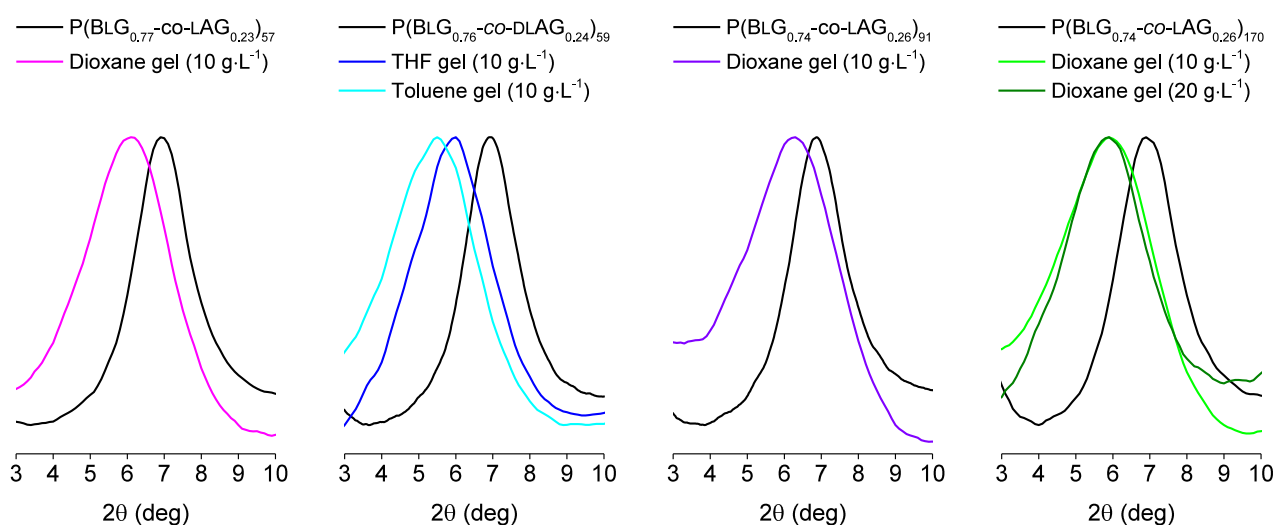

Figure V.8 [3 to 10°] 2θ portion of WAXS diffractograms of $P(BLG_x\text{-}co\text{-}AG_{1-x})_n$ polymers (black) and corresponding partially dried crosslinked gels (colour), centred around the Bragg reflection corresponding to the pseudo-hexagonal *d*-spacing at 5-7°.

V.3.3 Limits and Conditions for Photo-Crosslinking Gelation

The stoichiometry, solvent type, concentration and duration of UV exposure were varied in order to establish the ideal conditions and limits of photo-crosslinking gelation of $P(BLG_x\text{-}co\text{-}AG_{1-x})_n$. A particular focus was put on the stoichiometry of the crosslinker relative to the AG moieties. The aim to interconnect $P(BLG_x\text{-}co\text{-}AG_{1-x})_n$ polymers in order to generate a continuous network ideally dictates that one difunctional crosslinker (*i.e.*, two thiol functionalities) for two AG moieties be used. In practice, not all AG moieties need to be involved in a crosslink in order for a network to be stabilised, thereby allowing for less crosslinkers to be used. Besides, crosslinkers may also be involved in intramolecular chain crosslinks, which is detrimental to the gel stability. Based on these considerations, it may be beneficial to use less crosslinking species (< 0.5 equiv.) for 1 equiv. of AG (hypothesis (i)). However, in the context of dilute polymer systems (10 to 20 g·L^{-1}, *i.e.*, 1 to 2% w/v), the lower probability for thiol and ene groups encounter can be compensated by increasing the concentration of crosslinkers (> 0.5 equiv.) (hypothesis (ii)). To test hypotheses (i) and (ii), the following amounts of difunctional crosslinker, 1,9-nonanedithiol (thiol equivalence in bracket), were compared: 0.38 equiv. (0.75), 0.75 equiv. (1.5) and 3.75 equiv. (7.5), relative to AG (1 equiv.). Toluene

solutions (10 to 20 g·L^{-1}) of P(BLG$_{0.77}$-co-LAG$_{0.23}$)$_{57}$ and P(BLG$_{0.76}$-co-DLAG$_{0.24}$)$_{59}$ were used for this study. The P(BLG$_x$-co-AG$_{1-x}$)$_n$-toluene solutions crosslinked with 0.38 equiv. of crosslinker only led to partially formed gels, while those crosslinked with 0.75 equiv. of crosslinker led to fully formed gels, hence demonstrating the existence of a lower boundary as suggested by (ii). As for the P(BLG$_x$-co-AG$_{1-x}$)$_n$-toluene systems crosslinked with 3.75 equiv. of crosslinker, gelation did not occur, hence demonstrating the existence of a higher boundary as suggested by (i). In the rest of this study, 1.5 equiv. of thiol groups (*e.g.*, 0.75 equiv. of difunctional crosslinkers) relative to the AG moieties, was therefore used. A trifunctional crosslinker, trimethylolpropane tris(3-mercaptopropionate) (0.5 equiv., *i.e.*, 1.5 equiv. of thiol groups) was also tested (Figure V.1), but underwent ester cleavage during the deprotection step (See Section V.3.4), leading to the decomposition of the gel.

Unlike type I photoinitiators (*e.g.*, AIBN), which undergo a unimolecular bond cleavage to yield free radical species, type II photoinitiators (*e.g.*, benzophenone and derivatives) undergo a bimolecular reaction whereby their triplet excited state interacts with a hydrogen donor (*e.g.*, thiols) to generate free radicals; which is the reason why the type II was selected in this study.[71,72] Like most mercury lamps, the emission spectrum of the TQ 150 lamp used in this study exhibits a strong peak at 360 nm as well as a slightly weaker peak at 254 nm. As benzophenone absorbs intensely at 255 nm, it was chosen as a suitable type II photo-initiator.[72] Michler's ketone, a benzophenone derivative (Figure V.1), is also a type II photoinitiator and absorbs intensely at 366 nm.[73] It was, therefore, tested with the hope that it might perform faster than benzophenone and reduce the curing time. Unfortunately, Michler's ketone performed badly as no or very weak gels were obtained. In addition, the solutions turned blue, which indicates that the protonated Michler's ketone may have undergone a side reaction, most likely a nucleophilic addition with either a secondary amine (polymer) or a thiol (crosslinker).[72,74] A control sample, whithout photoinitiator, was tested but did not undergo any gelation, probably due to the fact that the direct excitation of the thiol and resulting cleavage of the labile sulfur-hydrogen bond has been shown to be less efficient in the absence of photoinitiators.[75] The coating industry, which deals with the bulk crosslinking of thick and static (*i.e.*, not mechanically stirred) systems typically recommends that photoinitiator concentrations range between 5 and 50 g·L^{-1}. Since dilute polymer systems (10 to 20 g·L^{-1}) are used here, 1 g·L^{-1} was chosen as the default benzophenone concentration. Smaller concentrations (*e.g.*, 0.3 g·L^{-1}) led to less stable, partial gels.

The present study mostly focused on dilute systems (< 20 g·L^{-1}) as the high viscosity of P(BLG$_x$-co-AG$_{1-x}$)$_n$ solutions in helicogenic solvents makes their handling increasingly difficult as their concentration increases. Nonetheless, a few samples of P(BLG$_x$-co-AG$_{1-x}$)$_n$-dioxane of relatively high concentration were prepared (Table V.1B) in order to investigate whether, like PBLG, P(BLG$_x$-co-AG$_{1-x}$)$_n$ copolypeptides abide by the Flory diagram for rod-like polymers described in Chapter IV (Figure V.9). In an effort to achieve liquid crystalline (LC) gels, the concentration was taken to 100 g·L^{-1}. Under such conditions, the gels obtained were very stiff, and showed elastomer-like mechanical responses, in that they were 'bouncy'. Moreover, the photo-crosslinking gelation of P(BLG$_{0.89}$-co-DLAG$_{0.11}$)$_{53}$, which failed at 10 and 20 g·L^{-1}, succeeded at 100

g·L^{-1}, probably due to the increased concentration of AG moieties. In addition, while little birefringence was observed for the dilute gels, 100 g·L^{-1} gels were strongly birefringent, which is an indication of a highly ordered microstructure, or liquid crystallinity in this case (Figure V.10).[19,76–78] In an experiment, a LC P(BLG$_{0.84}$-co-LAG$_{0.16}$)$_{171}$-dioxane gel was exposed to a denaturing solvent, TFA, in an attempt to supress its liquid crystallinity by unfolding the α-helices. As shown in Figure V.10 (bottom), upon contact with TFA, parts of the gel changed colour and others turned white before blending into the non-refringent black background. This indicates that the birefringence of the samples slowly diminishes without completely disappearing, probably as the result of the slow absorption of TFA into a gel that is stabilised by crosslinks.

Figure V.9 (a) photo-crosslinked P(BLG$_{0.84}$-co-LAG$_{0.16}$)$_{171}$-dioxane gel (100 g·L^{-1}); (b) photo-crosslinked dioxane gels (100 g·L^{-1}) of (left to right) P(BLG$_{0.76}$-co-DLAG$_{0.24}$)$_{59}$, P(BLG$_{0.89}$-co-DLAG$_{0.11}$)$_{53}$, P(BLG$_{0.80}$-co-LAG$_{0.20}$)$_{219}$, P(BLG$_{0.84}$-co-LAG$_{0.16}$)$_{171}$, and P(BLG$_{0.78}$-co-LAG$_{0.22}$)$_{96}$.

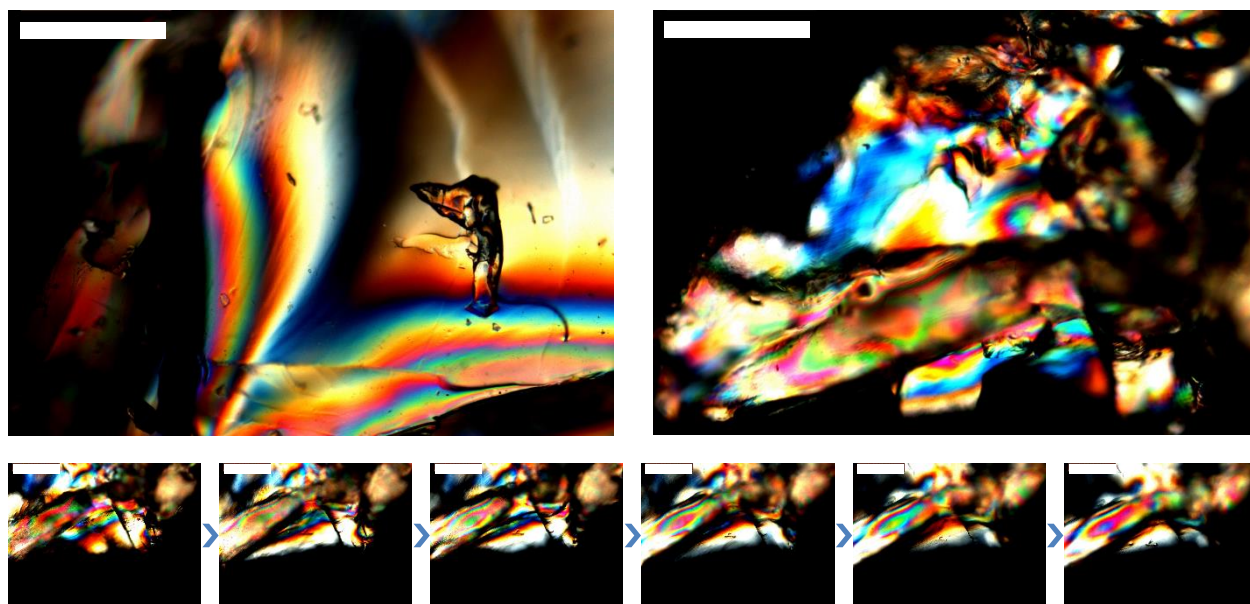**Figure V.10** Cross-polarised microscopy pictures of photo-crosslinked P(BLG$_{0.84}$-co-LAG$_{0.16}$)$_{171}$-dioxane gel (100 g·L^{-1}): (top) freshly cut gel sample, and (bottom, storyboard, left to right) same sample exposed to TFA for ~ 10 min (the pictures were taken at 1 to 2 min intervals following the exposition to TFA). Scale bars = 500 μm.

Benzylalcohol was also used as a solvent for photo-crosslinking gelation of P(BLG$_x$-co-AG$_{1-x}$)$_n$. Despite benzylalcohol being reported by Sakamoto as a helicogenic solvent in which PBLG α-helices highly aggregate, which has been shown to be a key property for photo-crosslinking gelation (Section V.3.2), no gel was obtained.[45] Surprisingly, amongst the different solvents studied by Sakamoto, benzylalcohol (ε$_r$ =

13) was the exception in a trend where the level of polypeptide aggregation decreased as the dielectric constant of the solvent increased. For comparison, ε_r(toluene) = 2.4 , ε_r(THF) = 7.6 and ε_r(dioxane) = 2.3. Most studies performed on PBLG-benzylalcohol gels focused on concentrated and liquid crystalline systems (*i.e.*, > 50 g·L^{-1}).[67,69,79,80] However, a few studies on dilute PBLG-benzylalcohol (10 g·L^{-1}) systems ascribed the gelation mechanism to a nucleation growth pathway.[67,69] Such pathway may be favoured in high dielectric constant (ε_r) solvents, whereas a phase separation pathway seems favoured in low dielectric constant (ε_r) solvents like toluene (see Chapter IV). The dipole moment of α-helices may be responsible for this difference. A future study of P(BLG$_x$-*co*-AG$_{1-x}$)$_n$-benzylalcohol systems may provide an interesting insight on the effect of the dielectric constant of the solvent in the gelation of rod-like polypeptides.

V.3.4   From Organogels to Hydrogels

The α-helicity of PBLG is key to its ability to aggregate[29,45] and to form thermoreversible physical gels.[47] Upon the debenzylation of its pendant BLG groups, PBLG yields poly-(L-glutamic acid) (PLGA), which also forms α-helices in water at a pH below the helix-coil transition (pH ~ 5-6).[1,33,34] However, PLGA helices precipitate rather than assemble into fibres. The formation of complex structures like fibres in organic solvents relies on a number of factors including α-helix-stabilising intramolecular hydrogen bonds, end-to-end aggregation of α-helices and solvent quality (*e.g.*, hydrophobicity and dielectric constant).[45] In a protic solvent like water at neutral and basic pH, the majority of the carboxylic acid groups of the L-glutamate residues are deprotonated and bare a negative charge. Electrostatic repulsion between side chains prevents poly-(L-glutamate) (PLG) from folding, thereby resulting in solvated random coils.[4,44] Upon reduction of the pH, the glutamate moieties are progressively protonated and enthalpically favoured intramolecular hydrogen bonds form.[81] The hydrophobicity of PLGA helices prevents molecular dispersion in water, and precipitation ensues.[42,43] As such, fibrous hydrogels resulting from the supramolecular assembly of PLGA α-helices have to date not been observed. Since stable and fibrous P(BLG$_x$-*co*-AG$_{1-x}$)$_n$-based organogels were prepared (Section V.3.1 and V.3.2), they were tested as precursors for new routes towards fibrous PLGA-based hydrogels were explored (Scheme V.1).

The BLG moieties in crosslinked P(BLG$_x$-*co*-AG$_{1-x}$)$_n$-toluene gels were debenzylated following route A (Section V.2.2.2). The effectiveness of the debenzylation was confirmed by FTIR (Figure V.11c). However, the resulting hydrogels were mechanically weak and typically broke into smaller pieces despite effectively swelling in water (Figure V.11a and b). In Section V.3.2, P(BLG$_x$-*co*-AG$_{1-x}$)$_n$-dioxane gels were shown to be the most robust gels prepared by the photo-crosslinking procedure. Their superior mechanical strength suggested that their network possessed good load-bearing properties, possibly as a result of the thick fibres composing it. For these reasons, P(BLG$_x$-*co*-AG$_{1-x}$)$_n$-dioxane gels were selected to investigate routes to prepare hydrogels from organogel precursors. Since the fibrous microstructure of the dioxane gels was preserved by the vacuum-drying step, the debenzylation of the BLG moieties was carried out by immersing

the dry gels (Figure V.5c) in acidic deprotection media, thereby respecting the typical deprotection procedures for PBLG-based polymers.[43,82]
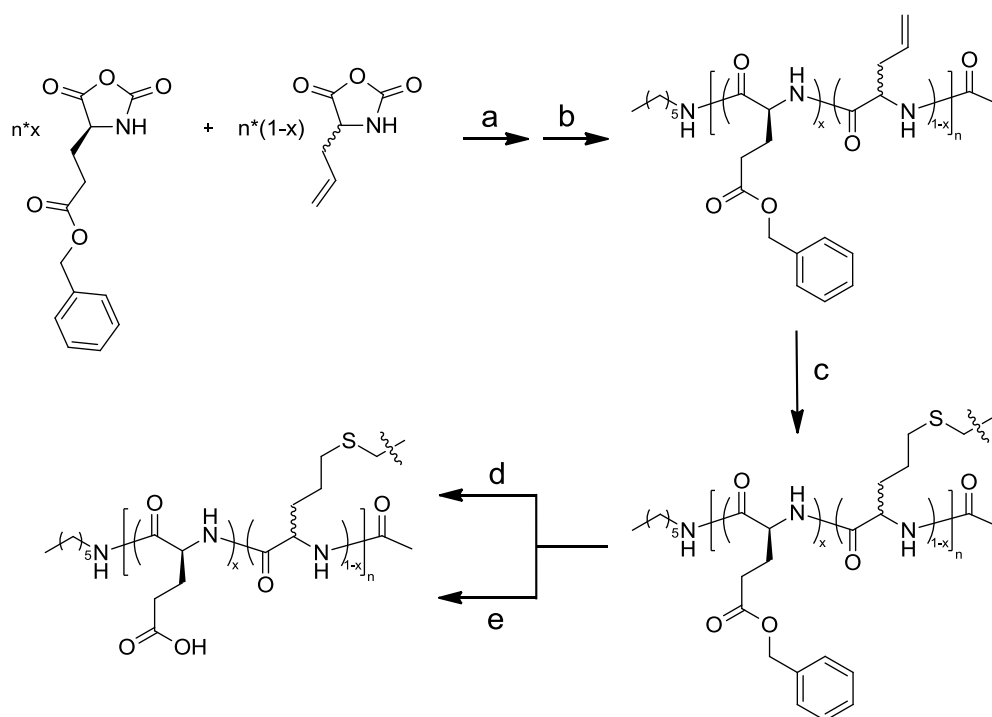
Scheme V.1 Synthesis of PLGA-based hydrogels. (a) DMF, 1-hexylamine (1 equiv.); (b) Ac$_2$O; (c) solvent (*i.e.*, 1,4-dioxane, toluene and THF), 1,9-nonanedithiol, benzophenone, hv; deprotection using (d) TFA, MSA, anisole (route A), or (e) TFA, HBr (route B).
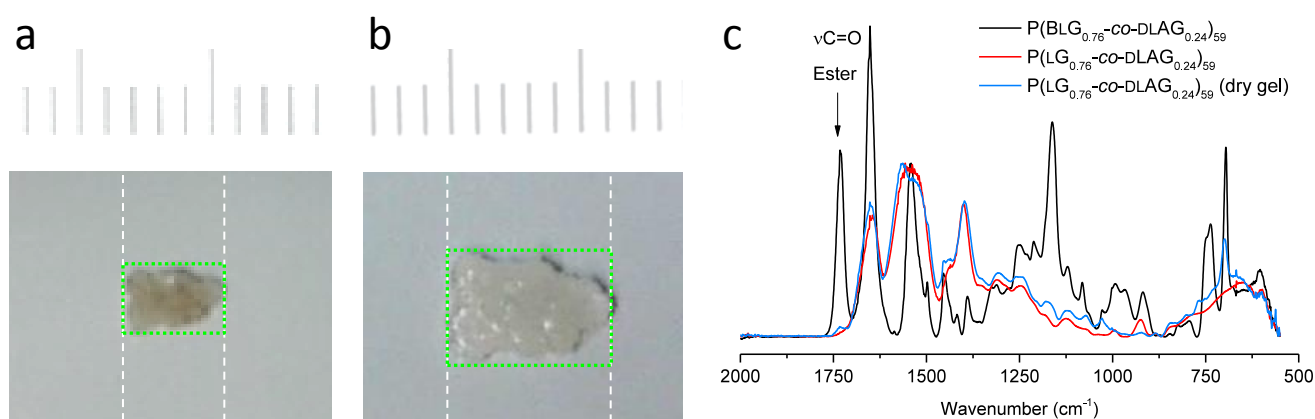

Figure V.11 Hydrogel obtained from a room-temperature crosslinked P(BLG$_{0.76}$-*co*-DLAG$_{0.24}$)$_{59}$-toluene gel (50 g·L^{-1}) following deprotection route A, (a) in its dry state (~ 2 mg), and (b) after rehydration (~ 20 mg), the scale ticks correspond to mm; (c) FTIR absorbance spectra of precursor polymer P(BLG$_{0.76}$-*co*-DLAG$_{0.24}$)$_{59}$ (black), of its deprotected counterpart P(LG$_{0.76}$-*co*-DLAG$_{0.24}$)$_{58}$ (red), and of the dry crosslinked P(LG$_{0.76}$-*co*-DLAG$_{0.24}$)$_{59}$ hydrogel (blue) (normalisation to Amide II signal at ~ 1550 cm^{-1}).

Deprotection of the carboxylic ester groups of P(BLG$_x$-*co*-AG$_{1-x}$)$_n$-dioxane gels yielded P(LG$_x$-*co*-AG$_{1-x}$)$_n$ hydrogels with high water content and with pH-responsive behaviour. This deprotection was found to be more effective using hydrobromic acid (route B) than methanesulfonic acid (route A), as confirmed by FTIR analysis of the lyophilised hydrogels (Figure V.12). Although a residual benzyl peak (< 20% as calculated from ester vC=O peak intensities of the normalised to the Amide II signal) could still be observed in the FTIR spectra, it was considered sufficiently small as to not impede the hydrogel performance. Despite the harsh

debenzylation conditions, the hydrogels showed no collapse and maintained their overall shape and volume, probably thanks to non-cleaved crosslinks that stabilise the robust fibres originally formed in the dioxane gels. As a logical consequence, the porous microstructure was also preserved, as confirmed by SEM (Figure V.13).
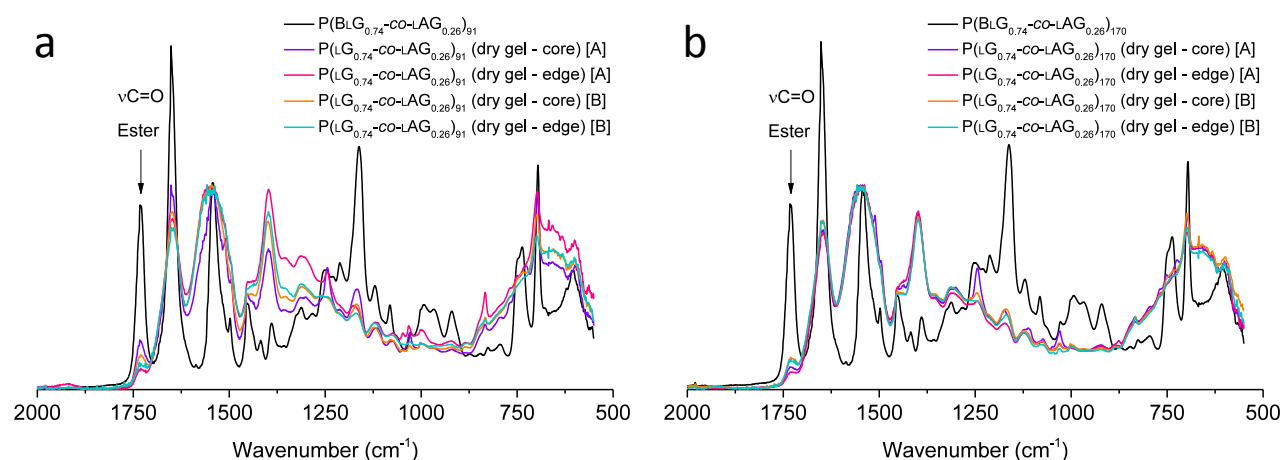

Figure V.12 FTIR spectra of freeze-dried hydrogel prepared from (a) P(BLG$_{0.74}$-*co*-LAG$_{0.26}$)$_{91}$-dioxane and (a) P(BLG$_{0.74}$-*co*-LAG$_{0.26}$)$_{170}$-dioxane (20 g·L^{-1}) gels deprotected following route A and B (in bracket in the legend); different parts of the hydrogel (core and edge) were analysed in order to check for effective deprotection (normalisation to Amide II signal).
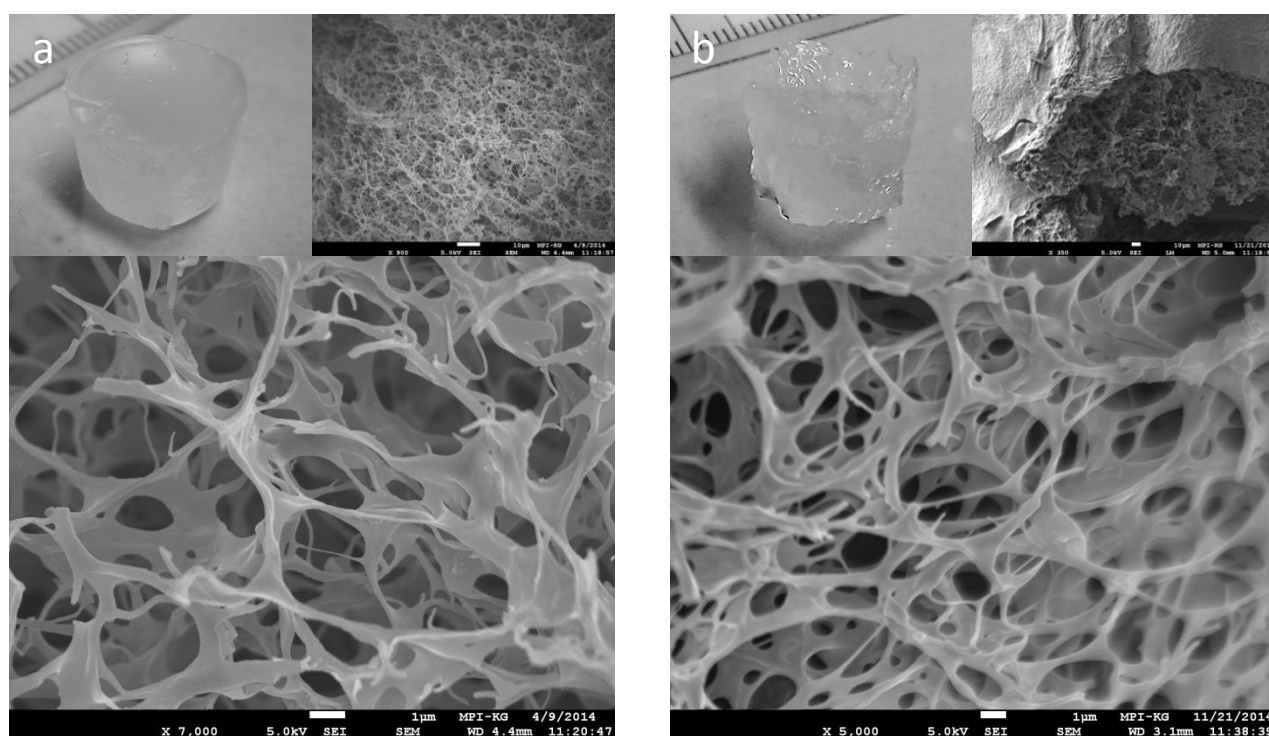

Figure V.13 SEM micrographs of (a) dried P(BLG$_{0.76}$-*co*-DLAG$_{0.24}$)$_{59}$-dioxane organogel (10 g·L^{-1}) and (b) freeze-dried P(LG$_{0.74}$-*co*-LAG$_{0.26}$)$_{170}$-water hydrogel (10 g·L^{-1}); and (top left inserts) pictures of corresponding gel. Scale bars = (bottom) 1 µm, (top) 10 µm.

V.3.5   Stimuli-Responsive Properties of P(LG$_x$-*co*-AG$_{1-x}$)$_n$ Hydrogels

P(LG$_x$-*co*-AG$_{1-x}$)$_n$ hydrogels derived from P(BLG$_x$-*co*-AG$_{1-x}$)$_n$-dioxane gels (Scheme V.1e) were able to hold up to 87 times their dry weight of water, which surpasses most PLGA-based hydrogels reported in the

literature.[17,18,40,41,83] More precisely, the swelling ratios (SR) of hydrogels derived from 10 g·L^{-1} organogels ranged between 50 and 87, and those of hydrogels derived from 20 g·L^{-1} organogels ranged between 40 and 52 (Figure V.14). This lower SR can be explained by the higher polymer concentration of the organogel precursors, which resulted in hydrogels with a denser polymer network. In addition, a higher polymer concentration led to stiffer gels, which is likely to be the result of more and / or thicker fibres, thereby limiting the extent by which the fibrous network can deform following water uptake and swelling.
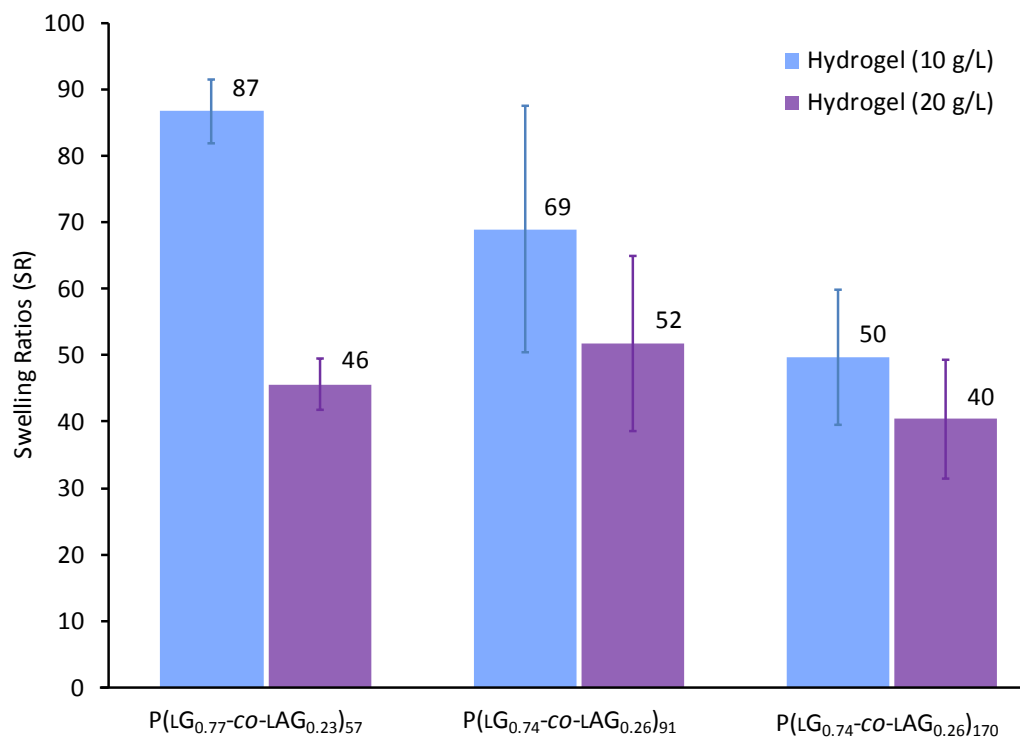

Figure V.14 Average swelling ratios (SR) of 10 to 20 g·L^{-1} (*i.e.*, 1 to 2% w/v) hydrogels; for each series, the average SR value was calculated from 3 to 5 measurements using the equation provided in Section V.2.2.3, and the error bar corresponds to the standard deviation of each series.

Interestingly, the trend by which the average SR decreased from P(LG$_{0.77}$-*co*-LAG$_{0.23}$)$_{57}$- to P(LG$_{0.74}$-*co*-LAG$_{0.26}$)$_{91}$- and to P(LG$_{0.74}$-*co*-LAG$_{0.26}$)$_{170}$-hydrogels could be correlated to the stiffness of the physical gels of the corresponding protected copolypeptides in toluene (Table IV.2). More precisely, P(BLG$_x$-*co*-AG$_{1-x}$)$_n$ copolypeptides that form stiffer physical gels in toluene upon decreasing the temperature (see Chapter IV), give rise stiffer and less water absorbent P(LG$_x$-*co*-AG$_{1-x}$)$_n$-water hydrogels (prepared *via* the procedure depicted in Scheme V.1); and *vice versa*.

The hydrogels were also tested for pH-responsiveness through immersion in acidic and basic buffer solutions. They reversibly shrunk and swelled at pH 4 and at pH 10, respectively (Figure V.15). This behaviour is caused by the pH-responsiveness of poly(L-glutamate) and its derivatives (*e.g.*, P(BLG$_x$-*co*-AG$_{1-x}$)$_n$), which fold into hydrophobic α-helices below pH 6 as demonstrated by CD spectroscopy (Figure V.16). While in the context of free polymers, such helices precipitate out of solution, in the context of gels, shrinkage takes place. This can be explained by the fact that hydrophobic poly(L-glutamic acid) helices

undergo hydrophobic interaction, thereby causing the overall gel microstructure to reversibly contract. The shrinkage in acidic conditions took place within a few minutes, while the swelling (from the shrunk state) in basic conditions took up to an hour to achieve a fully swollen gel state again. This discrepancy, or hysteresis, can be attributed to diffusion limitations in a shrunk gel.
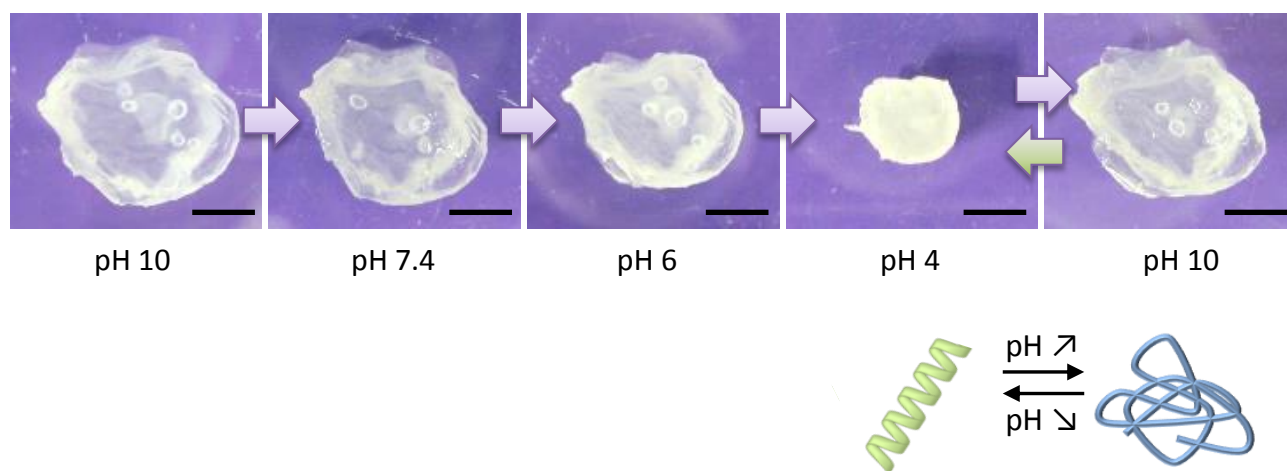

Figure V.15 P(LG$_{0.74}$-*co*-LAG$_{0.26}$)$_{170}$ hydrogel, prepared from the deprotection *via* route B of P(BLG$_{0.74}$-*co*-LAG$_{0.26}$)$_{170}$-dioxane organogel (20 g·L^{-1}), and photographed after being immersed in buffer solutions of gradually decreased pH (from pH 10 to 4), and showing reversible pH-responsiveness (from pH 4 to 10); the scale bar is 5 mm.
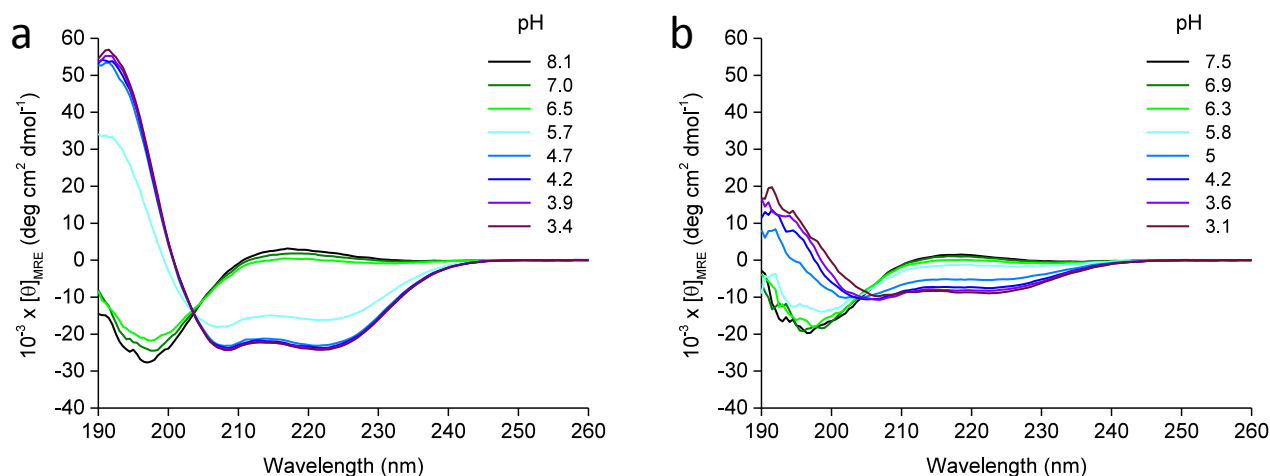

Figure V.16 CD spectra of (a) PLG$_{51}$ (*i.e.*, debenzylated PBLG$_{51}$), and (b) P(LG$_{0.76}$-*co*-DLAG$_{0.24}$)$_{58}$ (*i.e.*, debenzylated P(BLG$_{0.76}$-*co*-DLAG$_{0.24}$)$_{59}$) in Millipore water at different pH. The polypeptides were randomly coiled at pH > 6 and folded into α-helices at pH < 6.

To confirm that the pH-driven helix-coil transition is responsible for the swelling-shrinking mechanism in P(LG$_x$-*co*-AG$_{1-x}$)$_n$ hydrogels, Raman spectroscopy was performed on hydrogels that were maintained in acidic and basic buffers. The resulting Raman spectra clearly illustrate that the α-helical conformation dominated at pH 4, while random coil conformation dominated at pH 10 (Figure V.17).
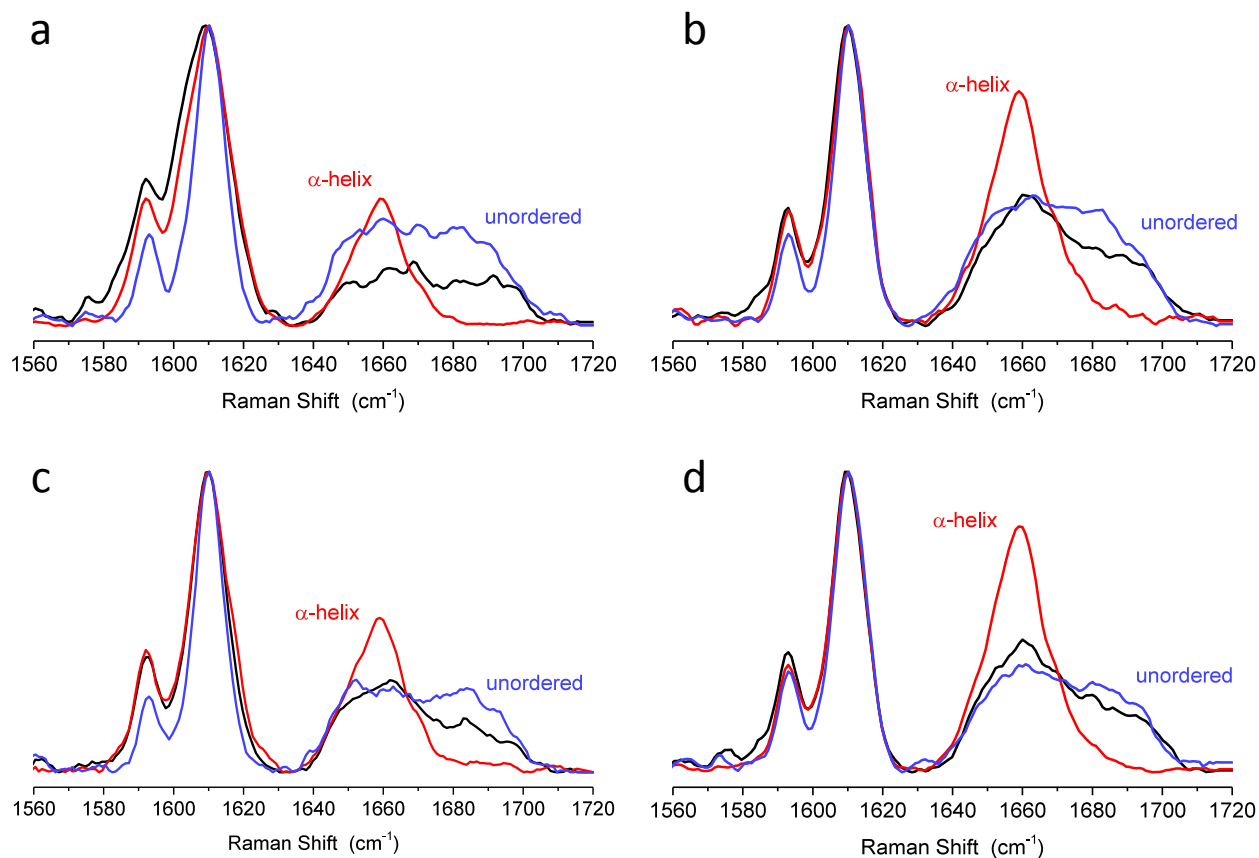
Figure V.17 Raman spectra of (top) P(LG$_{0.74}$-*co*-LAG$_{0.26}$)$_{91}$ hydrogel deprotected *via* (a) route A, and (b) route B, and (bottom) P(LG$_{0.74}$-*co*-LAG$_{0.26}$)$_{170}$ hydrogel deprotected *via* (c) route A, and (d) route B, both derived from dioxane organogels (20 g·L^{-1}). These hydrogels were analysed (black) in their dry state, (red) following 2 h immersion in pH 4 buffer solution and (blue) following 2 h immersion in pH 10 buffer solution; the peak at 1658 cm^{-1} was assigned to an α-helical conformation, and two peaks at 1665 and 1683 cm^{-1} were assigned to a disordered structure.[84]

V.4 Conclusions

A series of robust (solid-like) high water content poly(L-glutamate) (PLG)/poly(L-glutamic acid) (PLGA)-based hydrogels was synthesised. They showed reversible pH-responsiveness, which resulted from the helix-coil transition of the polypeptide chains at pH ~ 5-6. These hydrogels stand out from other PLGA gels reported in the literature as their swelling ratio in water reached 87, which is greater than what most crosslinked PLGA-based gels were reported to achieve. In addition, unlike chemical and freeze-dried gels, their porous network is fibrous in nature, which has potential for applications in regenerative medicine or even 3D cell culture, as part of a new generation of bioinspired PLGA-based extra cellular matrix mimics. These hydrogels were prepared following a novel synthetic route that consisted of the self-assembly of statistical P(BLG$_x$-*co*-AG$_{1-x}$)$_n$ copolypeptides in dioxane followed by rapid photo-crosslinking gelation (*via* UV exposure) and subsequent deprotection of the carboxylic ester functions. This organogel to hydrogel route is particularly remarkable in that it yielded gels from dilute solutions (down to 10 g·L^{-1}, *i.e.* 1% w/v) of low molar mass polypeptides (down to 11 kg·mol^{-1}).

It was shown that this unique gelation pathway is driven by the self-assembly of α-helical P(BLG$_x$-*co*-AG$_{1-x}$)$_n$ copolymers into loose fibre-like aggregates in helicogenic solvents, and that the photo-crosslinking covalently interconnects these supramolecular assemblies, thereby forming a continuous solvent-trapping network and thus a robust gel. Due to their fibrillar and porous microstructure and inherent biocompatibility, these new PLGA-based hydrogels are excellent candidates for biomedical applications. Their pH-responsiveness means that they could also be considered as sensors or bioactive materials in the context of cancers, viral, and other infectious diseases which can cause local pH changes. Cytotoxic studies ought to be considered to that effect. In addition, the highly porous and fibrous lyophilised organogels might be considered as aerogels for other applications, such as catalysis.[85]

V.5 References

(1)   Huang, J.; Heise, A. *Chem. Soc. Rev.* **2013**, *42*, 7373–7390.

(2)   Hoffman, A. S. *Adv. Drug Deliv. Rev.* **2013**, *65*, 10–16.

(3)   Deng, C.; Wu, J.; Cheng, R.; Meng, F.; Klok, H.-A. A.; Zhong, Z. *Prog. Polym. Sci.* **2014**, *39*, 330–364.

(4)   Appel, E. A.; del Barrio, J.; Loh, X. J.; Scherman, O. A. *Chem. Soc. Rev.* **2012**, *41*, 6195–6214.

(5)   Raeber, G. P. P.; Lutolf, M. P. P.; Hubbell, J. A. A. *Biophys. J.* **2005**, *89*, 1374–1388.

(6)   Wei, L.; Cai, C.; Lin, J.; Chen, T. *Biomaterials* **2009**, *30*, 2606–2613.

(7)   O'Leary, L. E. R.; Fallas, J. A.; Bakota, E. L.; Kang, M. K.; Hartgerink, J. D. *Nat. Chem.* **2011**, *3*, 821–828.

(8)   Flory, P. J. *Faraday Discuss. Chem. Soc.* **1974**, *57*, 7–18.

(9)   Petka, W. A.; Harden, J. L.; McGrath, K. P.; Wirtz, D.; Tirrell, D. A. *Science.* **1998**, *281*, 389–392.

(10)   Ye, Q.; Zuend, G.; Benedikt, P.; Jockenhoevel, S.; Hoerstrup, S. P.; Sakyama, S.; Hubbell, J. A.; Turina, M. *Eur. J. cardio-thoracic Surg.* **2000**, *17*, 587–591.

(11)   Berg, J. M.; Tymoczko, J. L.; Stryer, L. *Biochemistry*, Sixth edit.; W. H. Freeman and Company: New York, **2007**.

(12)   Zeugolis, D. I.; Khew, S. T.; Yew, E. S. Y.; Ekaputra, A. K.; Tong, Y. W.; Yung, L.-Y. L.; Hutmacher, D. W.; Sheppard, C.; Raghunath, M. *Biomaterials* **2008**, *29*, 2293–2305.

(13)   Deming, T. J. *Soft Matter* **2005**, *1*, 28–35.

(14)   Hoffman, A. S. *Adv. Drug Deliv. Rev.* **2002**, *54*, 3–12.

(15)   Peppas, N. A.; Bures, P.; Leobandung, W.; Ichikawa, H. *Eur. J. Pharm. Biopharm.* **2000**, *50*, 27–46.

(16)   Jung, J. P.; Gasiorowski, J. Z.; Collier, J. H. *Biopolymers* **2010**, *94*, 49–59.

(17)   Zhao, C.; Zhuang, X.; He, P.; Xiao, C.; He, C.; Sun, J.; Chen, X.; Jing, X. *Polymer* **2009**, *50*, 4308–4316.

(18)   Matsuoka, Y.; Kishi, R.; Sisido, M. *Polym. J.* **1993**, *25*, 919–927.

(19)   Inomata, K.; Iguchi, Y.; Mizutani, K.; Sugimoto, H.; Nakanishi, E. *ACS Macro Lett.* **2012**, *1*, 807–810.

(20)   Murakami, S.; Aoki, N.; Matsumura, S. *Polym. J.* **2011**, *43*, 414–420.

(21)   Lee, Y.-H.; Chang, J.-J.; Lai, W.-F.; Yang, M.-C.; Chien, C.-T. *Colloids Surf. B. Biointerfaces* **2011**, *86*,

409–413.

(22)   Zou, J.; Zhang, F.; Chen, Y.; Raymond, J. E.; Zhang, S.; Fan, J.; Zhu, J.; Li, A.; Seetho, K.; He, X.; Pochan, D. J.; Wooley, K. L. *Soft Matter* **2013**, *9*, 5951–5958.

(23)   Dong, C.-M.; Chen, Y. *J. Control. Release* **2011**, *152*, e13–e14.

(24)   Deming, T. J. *Adv. Mater.* **1997**, *9*, 299–311.

(25)   Kukula, H.; Schlaad, H.; Antonietti, M.; Förster, S. *J. Am. Chem. Soc.* **2002**, *124*, 1658–1663.

(26)   Truong, W. T.; Su, Y.; Meijer, J. T.; Thordarson, P.; Braet, F. *Chem. Asian J.* **2011**, *6*, 30–42.

(27)   Lutz, J.-F.; Ouchi, M.; Liu, D. R.; Sawamoto, M. *Science* **2013**, *341*, 1238149-1–8.

(28)   Merrifield, R. B. *J. Am. Chem. Soc.* **1963**, *85*, 2149–2154.

(29)   Block, H. *Poly(gamma-benzyl-L-glutamate) and other glutamic acid containing polymers*; Gordon and Breach Science Publishers Ltd., **1983**.

(30)   Tam, J. P.; Heath, W. F.; Merrifield, R. B. *J. Am. Chem. Soc.* **1983**, No. 105, 6442–6455.

(31)   Idelson, M.; Blout, E. R. *J. Am. Chem. Soc.* **1958**, *80*, 4631–4634.

(32)   Kato, Y.; Tsukadat, Y. *J. Med. Chem.* **1984**, *27*, 1602–1607.

(33)   Cheng, J.; Deming, T. J. *Top. Curr. Chem.* **2012**, *310*, 1–26.

(34)   Gooding, E. A.; Sharma, S.; Petty, S. A.; Fouts, E. A.; Palmer, C. J.; Nolan, B. E.; Volk, M. *Chem. Phys.* **2013**, *422*, 115–123.

(35)   Song, C. W.; Griffin, R.; Park, H. J. In *Cancer Drug Resistance*; Teicher, B., Ed.; Humana Press Inc., **2006**; pp 21–43.

(36)   Kato, Y.; Ozawa, S.; Miyamoto, C.; Maehata, Y.; Suzuki, A.; Maeda, T.; Baba, Y. *Cancer Cell Int.* **2013**, *13*, 1–8.

(37)   Barrientos, L. G.; Rollin, P. E. *Virology* **2007**, *358*, 1–9.

(38)   Lardner, A. *J. Leukoc. Biol.* **2001**, *69*, 522–530.

(39)   Chécot, F.; Lecommandoux, S.; Gnanou, Y.; Klok, H.-A. *Angew. Chem. Int. Ed. Engl.* **2002**, *114*, 1395–1399.

(40)   Zhao, C.; He, P.; Xiao, C.; Gao, X.; Zhuang, X.; Chen, X. *J. Appl. Polym. Sci.* **2012**, *123*, 2923–2932.

(41)   Yang, Z.; Zhang, Y.; Markland, P.; Yang, V. C. *J. Biomed. Mater. Res.* **2002**, *62*, 14–21.

(42)   Rodríguez-Hernández, J.; Lecommandoux, S. *J. Am. Chem. Soc.* **2005**, *127*, 2026–2027.

(43)   Krannig, K.-S.; Schlaad, H. *J. Am. Chem. Soc.* **2012**, *134*, 18542–18545.

(44)   Estroff, L. A.; Hamilton, A. D. *Chem. Rev.* **2004**, *104*, 1201–1218.

(45)   Sakamoto, R. *Colloid Polym. Sci.* **1984**, *262*, 788–792.

(46)   Izumi, Y.; Takezawa, H.; Kikuta, N.; Uemura, S.; Tsutsumi, A. *Macromolecules* **1998**, *31*, 430–435.

(47)   Tadmor, R.; Khalfin, R. L.; Cohen, Y. *Langmuir* **2002**, *18*, 7146–7150.

(48)   Jackson, C. L.; Shaw, M. T. *Polymer* **1990**, *31*, 1070–1084.

(49)   Tohyama, K.; Miller, W. G. *Nature* **1981**, *289*, 813–814.

(50)   Horton, J. C.; Donaldt, A. M. *Polymer.* **1991**, *32*, 2418–2427.

(51)   Chakrabarti, S.; Miller, W. G. *Biopolymers* **1984**, *23*, 719–734.

(52)   Niehoff, A.; Mantion, A.; McAloney, R.; Huber, A.; Falkenhagen, J.; Goh, C. M.; Thünemann, A. F.; Winnik, M. A.; Menzel, H. *Colloid Polym. Sci.* **2013**, *291*, 1353–1363.

(53)   Kim, K. T.; Park, C.; Vandermeulen, G. W. M.; Rider, D. A.; Kim, C.; Winnik, M. A.; Manners, I. *Angew. Chemie Int. Ed.* **2005**, *44*, 7964–7968.

(54)   Naik, S. S.; Savin, D. A. *Macromolecules* **2009**, *42*, 7114–7121.

(55)   Yamane, Y.; Kanekiyo, M.; Koizumi, S.; Zhao, C.; Kuroki, S.; Ando, I. *J. Appl. Polym. Sci.* **2004**, *92*, 1053–1060.

(56)   Huang, J.; Habraken, G.; Audouin, F.; Heise, A. *Macromolecules* **2010**, *43*, 6050–6057.

(57)   Krannig, K.-S.; Sun, J.; Schlaad, H. *Biomacromolecules* **2014**, *15*, 978–984.

(58)   Brosnan, S. M.; Schlaad, H. *Polymer* **2014**, *55*, 5511–5516.

(59)   Shukla, P. *Polymer* **1992**, *33*, 365–372.

(60)   Tipton, D. L.; Russo, P. S. *Macromolecules* **1996**, *29*, 7402–7411.

(61)   Dasgupta, D.; Guenet, J.-M. *Macromol. Chem. Phys.* **2013**, *214*, 1885–1892.

(62)   Suzuki, M.; Hanabusa, K. *Chem. Soc. Rev.* **2010**, *39*, 455–463.

(63)   Kobayashi, H.; Friggeri, A.; Koumoto, K.; Amaike, M.; Shinkai, S.; Reinhoudt, D. N. *Org. Lett.* **2002**, *4*, 1423–1426.

(64)   Abdallah, D. J.; Weiss, R. G. *Adv. Mater.* **2000**, *12*, 1237–1247.

(65)   Kiss, G.; Porter, R. S. *J. Polym. Sci. Part B Polym. Phys.* **1996**, *34*, 2271–2289.

(66)   Gupta, A. K.; Dufour, C.; Marchal, E. *Biopolymers* **1974**, *13*, 1293–1308.

(67)   Tadmor, R.; Dagan, A.; Cohen, Y. *Macromol. Symp.* **1997**, *114*, 13–22.

(68)   Jahanshahi, K.; Botiz, I.; Reiter, R.; Thomann, R.; Heck, B.; Shokri, R.; Stille, W.; Reiter, G. *Macromolecules* **2013**, *46*, 1470–1476.

(69)   Cohen, Y.; Dagan, A. *Macromolecules* **1995**, *28*, 7638–7644.

(70)   Yen, C.; Edo, S.; Oka, H.; Tokita, M.; Watanabe, J. *Macromolecules* **2008**, *41*, 3727–3733.

(71)   Arsu, N.; Aydin, M.; Yagci, Y.; Jockusch, S.; Turro, N. J. *Photochem. UV Curing New Trends* **2006**, *661*, 1–13.

(72)   Tehfe, M.-A.; Dumur, F.; Graff, B.; Morlet-Savary, F.; Fouassier, J.-P.; Gigmes, D.; Lalevée, J. *Macromolecules* **2013**, *46*, 3761–3770.

(73)   DeBoer, C. D.; Turro, N. J.; Hammond, G. S. *Org. Synth.* **1967**, *47*, 64.

(74)   Jirousek, L.; Soodak, M. *Biochem. Biophys. Res. Commun.* **1974**, *59*, 927–934.

(75)   Hoyle, C. E.; Lee, T. Y.; Roper, T. *J. Polym. Sci. Part A Polym. Chem.* **2004**, *42*, 5301–5338.

(76)   Sisido, M.; Kishi, R. *Macromolecules* **1991**, *24*, 4110–4114.

(77)   Olsen, B. D.; Segalman, R. A. *Mater. Sci. Eng. R Reports* **2008**, *62*, 37–66.

(78)   Russo, P. S.; Magestro, P.; Miller, W. G. **1987**; Vol. 3, pp 152–180.

(79)   Corstjens, T.; Rastogi, S.; Lemstra, P. **1999**, *0*, 105–110.

(80) Hill, A.; Donald, A. M. *Mol. Cryst. Liq. Cryst. Inc. Nonlinear Opt.* **1987**, *153*, 395–404.

(81) Dill, K. A. *Biochemistry* **1990**, *29*, 7133–7155.

(82) Wang, X. T.; Wang, J.; Sun, H. L.; Yu Du, X.; Ma, L. F. *J. Appl. Polym. Sci.* **2013**, *129*, 1187–1192.

(83) Zhang, Z.; Chen, L.; Deng, M.; Bai, Y.; Chen, X.; Jing, X. *J. Polym. Sci. Part A Polym. Chem.* **2011**, *49*, 2941–2951.

(84) Li-Chan, E. C. Y.; Ismail, A. A.; Sedman, J.; Van de Voort, F. R. *Handbook of Vibrational Spectroscopy*; Chalmers, J. M., Griffiths, P. R., Eds.; Wiley, **2001**.

(85) Nguyen, T.-T.-T.; Simon, F.-X.; Khan, N. A.; Schmutz, M.; Mésini, P. J. *J. Mater. Chem.* **2012**, *22*, 7712.

Chapter VI

Ongoing Projects and Future Work

The work presented in the Section VI.3.2 'Long Range Order in Emulsified Particles' is the result of a collaboration with Dr. Klaus Tauer and Dr. Chunxiang Wei (Max Planck institute of Colloids and Interfaces).

VI.1   Introduction

The investigation into the physical gelation and secondary structure of poly(γ-benzyl-L-glutamate-*co*-allylglycine) (P(BLG-*co*-AG)) polypeptides (Chapter IV) and their ability to aggregate in solution and yield fibrous gels (Chapter V) allowed to build a comprehensive study of these α-helical polypeptides and their structure-property relationships. This study was aimed at generating of a polypeptide toolbox for the preparation of biomedical and stimuli-responsive materials. Chapter V, for instance, reported the development of a robust fibrous and pH-responsive poly(L-glutamate)-based hydrogels, which could be used as extra-cellular matrix (ECM) mimics for 3D cell studies or implants.[1–4] On the other hand, polypeptide-based films can be used for tissue engineering purposes (*e.g.*, membranes, skin grafts)[5–7] or as sensors,[8–10] while fibrous microgels can be used as structural fillers that can be moulded into the desired shape or injected[11,12] to provide an support for cell growth and regenerative purposes.[1,13] It was, therefore, the intention to prepare and investigate P(BLG-*co*-AG)-based films and microgels.

As films can be prepared from any solvent in which the polypeptides are soluble, both helicogenic[14] and non helicogenic[15] solvents were investigated, the aim being to provide a diverse library of P(BLG-*co*-AG)-solvent combinations and corresponding film structures and properties. As shown in Chapter V, UV-crosslinking gelation of P(BLG-*co*-AG)-dioxane generates macroscopic gels that are 'moulded' to the shape of their transparent containers (*e.g.*, vials). As medical treatments often involve the injection of hydrogels as fillers,[7,12,16,17] structural and fibrous microgels prepared from P(BLG-*co*-AG) polypeptides may, therefore, be used for such applications. Micro-organogels were therefore prepared and studied, the long term goal being to implement the organogels to hydrogel route described in Chapter V to yield micro-hydrogels. In this chapter, the early stage results of a project aimed at utilising P(BLG-*co*-AG) polypeptides to prepare films and microgels, with a particular focus on their secondary and tertiary structures, are presented. The

fundamental knowledge established and reported in Chapters IV and V was used as a support to both design experimental approaches and provide background material to discuss and compare the results.

VI.2 Experimental

VI.2.1 Materials

The synthesis of statistical copolypeptides of γ-benzyl-L-glutamate (BLG) and allylglycine (AG), referred to as P(BLG$_x$-co-AG$_{1-x}$)$_n$ hereafter, is described in Chapter II and Appendix A, and the copolymers used for this study are gathered in Table VI.1. Other chemicals and solvents used for this study are listed in Appendix A.

Table VI.1 Molecular Characteristics of Copolypeptides Used in Chapter VI (Appendix B, P1, P2, P12 to P14, P16, and P59 to P63)

Sections		Polymer	γ-Benzyl-L-glutamate (BLG)		Allyl glycine (AG)		M_n[a]	n[a]	Đ^{app}
			Mole fraction[a]	Configu-ration	Mole fraction[a]	Configu-ration	(kg·mol^{-1})		(M_w/M_n)[b]
A VI.3.1		P(BLG$_{0.76}$-co-DLAG$_{0.24}$)$_{59}$	76%	L	24%	DL	11.4	59	1.16
		P(BLG$_{0.74}$-co-LAG$_{0.26}$)$_{170}$	74%	L	26%	L	31.9	170	1.28
	B	PBLG$_{51}$	100%	L	-	-	11.3	51	1.09
VI.3.2 C		P(BLG$_{0.78}$-co-LAG$_{0.22}$)$_{96}$	78%	L	22%	L	18.6	96	1.13
		P(BLG$_{0.80}$-co-LAG$_{0.20}$)$_{219}$	80%	L	20%	L	42.8	219	1.23
		P(BLG$_{0.84}$-co-LAG$_{0.16}$)$_{171}$	84%	L	16%	L	34.2	171	1.28
		PBLG$_{159}$	100%	L	-	-	35.0	159	1.21
		PBDG$_{155}$	100%	D	-	-	34.1	155	1.15
		P(BLG$_{0.80}$-co-DLAG$_{0.20}$)$_{209}$	80%	L	20%	DL	40.8	209	1.28
		P(BDG$_{0.81}$-co-DLAG$_{0.19}$)$_{223}$	81%	D	19%	DL	43.9	223	1.16
		P(BLG$_{0.80}$-co- BDG$_{0.20}$)$_{207}$	100%	DL	-	-	45.5	207	1.11

[a] M_n = number-average molar mass. n = number-average degree of polymerisation. Determined by ^{1}H-NMR (Appendix A).
[b] Đ^{app} = M_w/M_n = ratio of weight- over number-average molar mass (dispersity). Determined by SEC (PMMA calibration) (Appendix A).

VI.2.2 Methods

VI.2.2.1 Film Preparation

Solutions of P(BLG$_x$-co-AG$_{1-x}$)$_n$ (50 g·L^{-1}, 100 µL) were cast in PTFE wells (10 mm in diameter and 2mm deep) and left to dry at room temperature and at 65 °C. TFA, DMF, and 1,4-dioxane were used as solvents.

VI.2.2.2 Emulsion

Typically 1 mL of polypeptide-toluene solution (10 g·L^{-1}) was dispersed in 9 mL of water with a surfactant (E30) at 60 °C (for PBLG$_{51}$) or at room temperature (rt) (for P(BLG$_x$-co-AG$_{1-x}$)$_n$). The emulsion was then centrifuged (10,000 rpm, 5 minutes), and the particles were washed with distilled water and dried at rt.

See Appendix A for all analytical methods used here (i.e., FTIR, Raman, WAXS, CD, SEM).

VI.3 Results and Discussion

VI.3.1 Long Range Order in Films

TFA is a highly polar and strongly acidic denaturing solvent for polypeptides; in particular, it causes PBLG to unfold and adopt a random coil conformation.[15] It was thus selected as a non-helicogenic solvent in an attempt to generate randomly coiled $P(BLG_x\text{-}co\text{-}AG_{1-x})_n$ polypeptides and in turn films with no microscopic order, for comparison purposes with the typical secondary structures (*e.g.*, α-helices) and higher hierarchical order (*e.g.*, pseudo-hexagonal packing) investigated in Chapter IV. The following polypeptides were selected: $PBLG_{51}$ as the model α-helix (*i.e.*, reference sample), $P(BLG_{0.76}\text{-}co\text{-}DLAG_{0.24})_{59}$ because of its particularly large α' contribution (Figure IV.5), and $P(BLG_{0.74}\text{-}co\text{-}LAG_{0.26})_{170}$ as a slightly longer polymer of intermediate conformation (Table VI.1A). Against all expectations, films prepared from $P(BLG_x\text{-}co\text{-}AG_{1-x})_n$-TFA solutions exhibited strong WAXS reflection peaks, characteristic of a certain level of microscopic order (Figure VI.1). Similar diffractograms were obtained for films prepared from dioxane and toluene. The sets of peaks observed in the different diffractograms did not follow a specific trend. However, most samples exhibited a more complex organisation than the pseudo-hexagonal packing described in Chapter IV with its single peak at ~ 6-7° (Figure IV.12). Based on several studies performed on PBLG films, these peaks may be ascribed to ordered structures known as forms A, B, and C, or a combination of them.[18–21] These forms correspond to more (form B) or less (form A and C) ordered variations of the arrangement of α-helices into pseudo-hexagonal lattices. The lack of trend and consistency between samples may be attributed to the sample preparation technique, which did not take into consideration (i) the orientation of the films in the X-ray beam path and (ii) the inherent differences between solvents (*e.g.*, surface tension, volatility) which may have led to different drying rates, film thicknesses, local stresses and inhomogeneities.
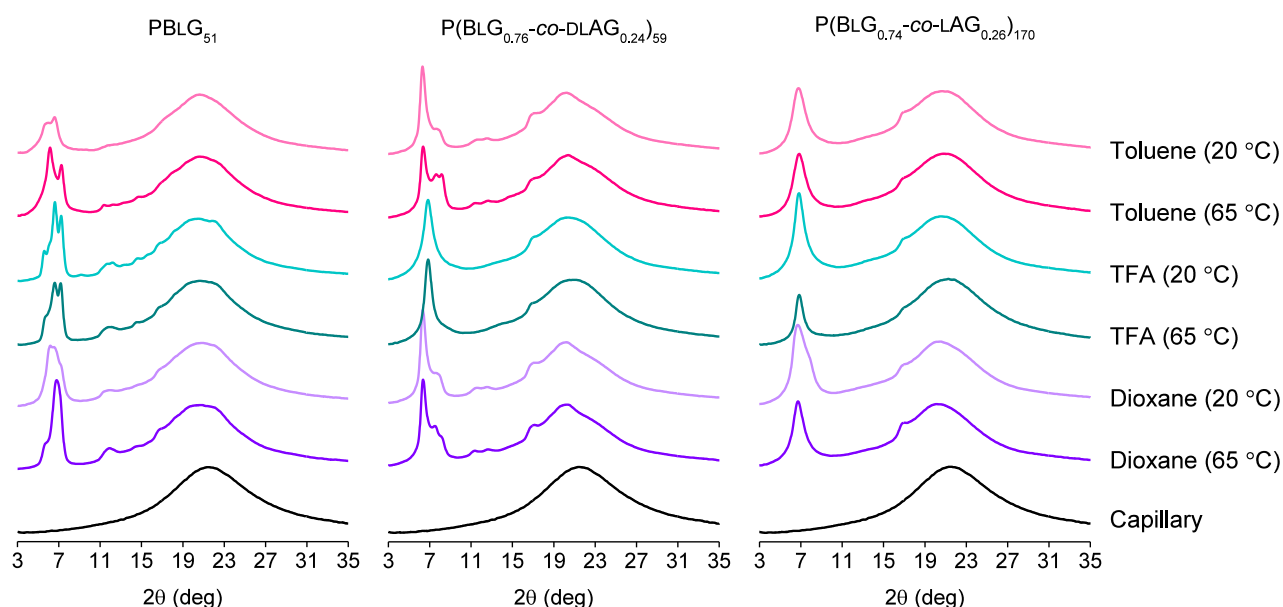

Figure VI.1 WAXS diffractograms of films cast from $P(BLG_x\text{-}co\text{-}AG_{1-x})_n$ solutions (50 g·L^{-1}) exhibiting peaks that can be ascribed to different sub-types of hexagonal packing (*e.g.*, pseudo-hexagonal, form A, B or C).

In order to complement the WAXS study with a secondary structure analysis, the formation of films from P(BLG$_x$-*co*-AG$_{1-x}$)$_n$ solutions was monitored by FTIR (Figure VI.2 and IV.2). While these polypeptides assumed an α-helical conformation at all stages of the film formation in dioxane and toluene, their conformation in TFA changed during the drying process. As expected, at 50 g·L^{-1}, and most likely at lower concentrations too, the polypeptides were randomly coiled in TFA, as suggested by a broad and undefined Amide I band with a hump at 1640 cm^{-1}. As the solution dried and the polypeptide concentration increased, an α-helical peak (~ 1650 cm^{-1}) appeared at approximately 400 g·L^{-1} (concentration calculated from a TFA peak at 1774 cm^{-1}) and grew as the solvent evaporated further. A likely explanation is that TFA removal and increasing polymer-polymer interactions induced the folding of polypeptide chains into α-helices.[15]
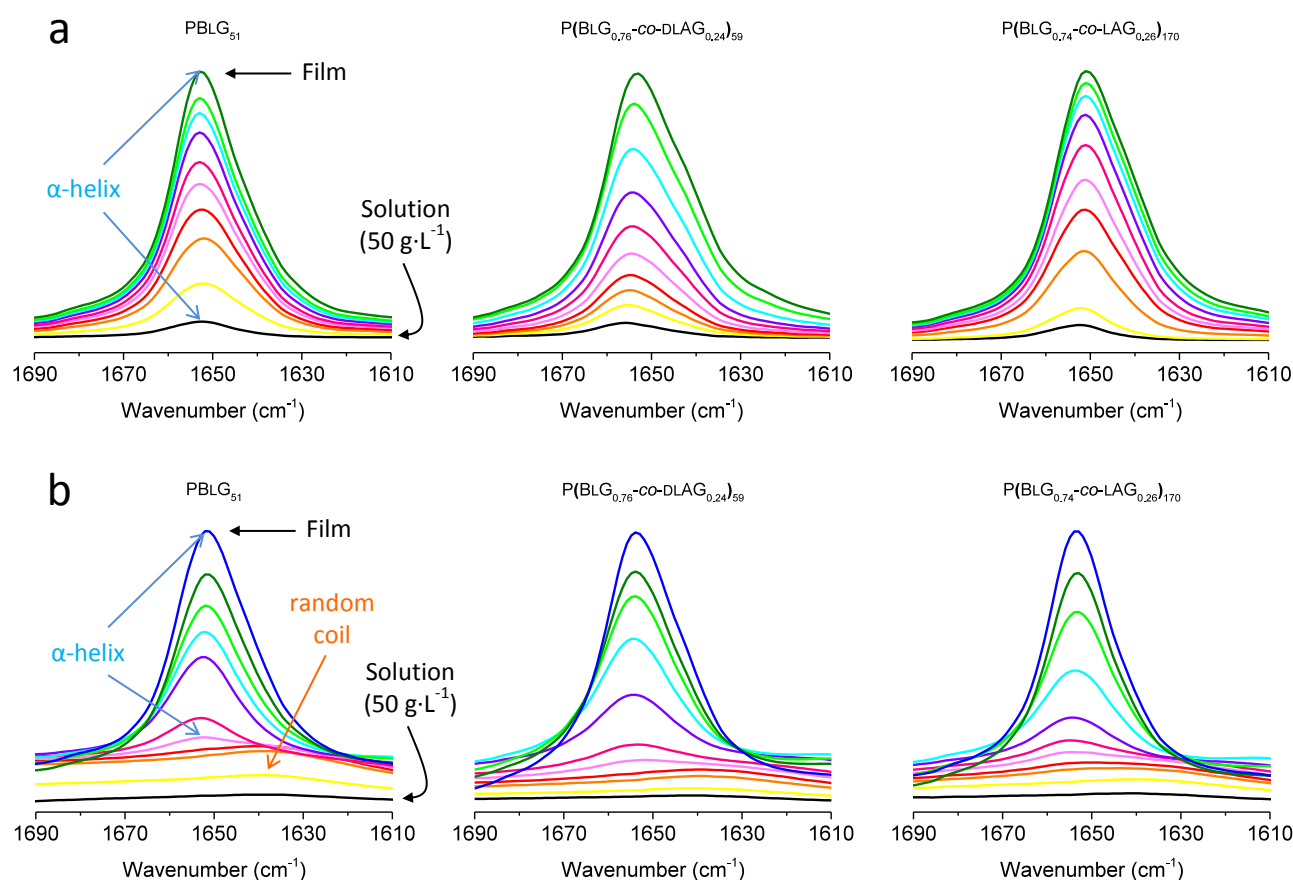
Figure VI.2 FTIR-monitored Film formation of P(BLG$_x$-*co*-AG$_{1-x}$)$_n$ solutions (50 g·L^{-1}) in (a) dioxane and (b) TFA. The black spectra correspond to the initial solutions (*i.e.*, concentration = 50 g·L^{-1}); the coloured spectra correspond to the drying solutions (*i.e.*, concentration > 50 g·L^{-1}) that were left to dry until a film was formed ((a) dark green or (b) dark blue spectra). In dioxane (a), the Amide I bands are composed of a main peak at approximately 1650 cm^{-1} (α helix) and a shoulder - more pronounced for the copolymers - at approximately 1640 cm^{-1} (α' conformation); based on Chapter IV, these bands are characteristic of a mostly α-helical conformation. In TFA (b), the Amide I bands are not clearly defined at low concentration: only a broad hump at approximately 1640 cm^{-1} (probably indicative of a random coil conformation) can be observed; from concentration ≥ 400 g·L^{-1}, an α-helix peak at 1650 cm^{-1} appears and gradually dominates the Amide I band.

Interestingly, once normalised and compared to one another, the Amide I bands of different films prepared from the same polypeptide exhibited relative fluctuations, not only between the α and α' peaks, but also between the Amide I band itself and reference peaks (Figure VI.3 and VI.4). Like for WAXS, these

fluctuations did not seem to follow a particular trend, with the exception of films prepared from TFA at room temperature. For these samples, the α' peaks were consistently the most prominent in both FTIR and Raman spectroscopy. It is altogether surprising that sample preparation alone can cause Amide I bands to undergo such a level of fluctuations between samples prepared from the same polypeptide. These fluctuations may be interpreted as the result of slightly different α-helical conformations (*e.g.*, more or less 'perfect' helices) caused by different preparation methods (*e.g.*, solvent, drying rate). Alternatively, these fluctuations may also suggest that different packings (*e.g.*, pseudo-hexagonal, form A, B or C), along with their corresponding crystal lattices, inter-chain interactions and geometrical constraints, may differently affect local polarities, polarizabilities, and bond orientations. This may lead to more or less Raman- or FTIR-active bond vibrations. The latter hypothesis is in line with the WAXS study, which showed that the packing of α-helices varied with the preparation method (Figure VI.1). Despite these fluctuations, the relative height of the amide I bands (averaged over all film samples for each polypeptide) with respect to the reference peak (which is proportional the BLG mole fraction only) is agreement with the BLG/AG mole fraction ratio of all tested polypeptides (Figure VI.3 and VI.4).
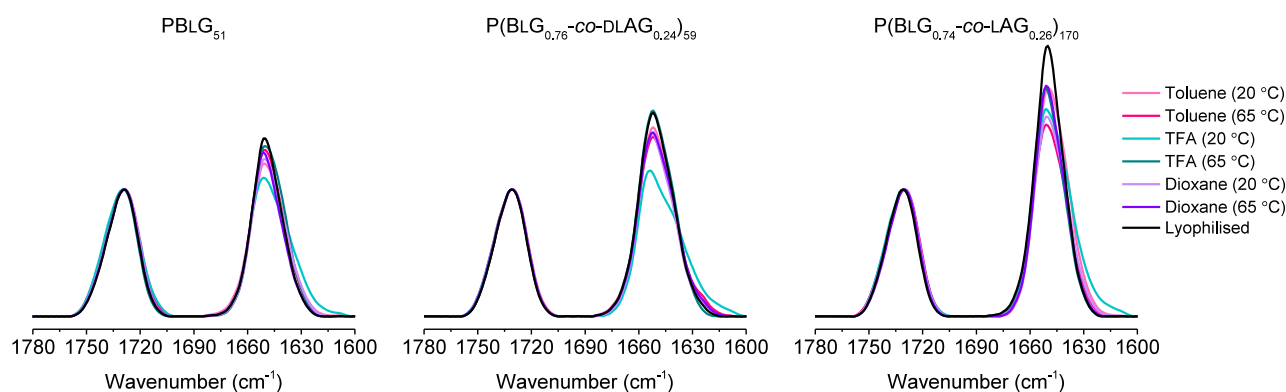

Figure VI.3 Partial FTIR spectra centred around the Amide I band (~ 1680 to 1620 cm^{-1}) of films cast from P(BLG$_x$-*co*-AG$_{1-x}$)$_n$ solutions (50 g·L^{-1}) and dried at 20 or 65 °C. Each spectrum was normalised to the 1730 cm^{-1} peak, which corresponds to the ν(C=O) of the ester group of the BLG moiety.[22–26] Despite the fluctuations in peak height and α/α' peak intensity ratio, the mean Amide I band increased with respect to the reference peak (1730 cm^{-1}) with increasing AG content.
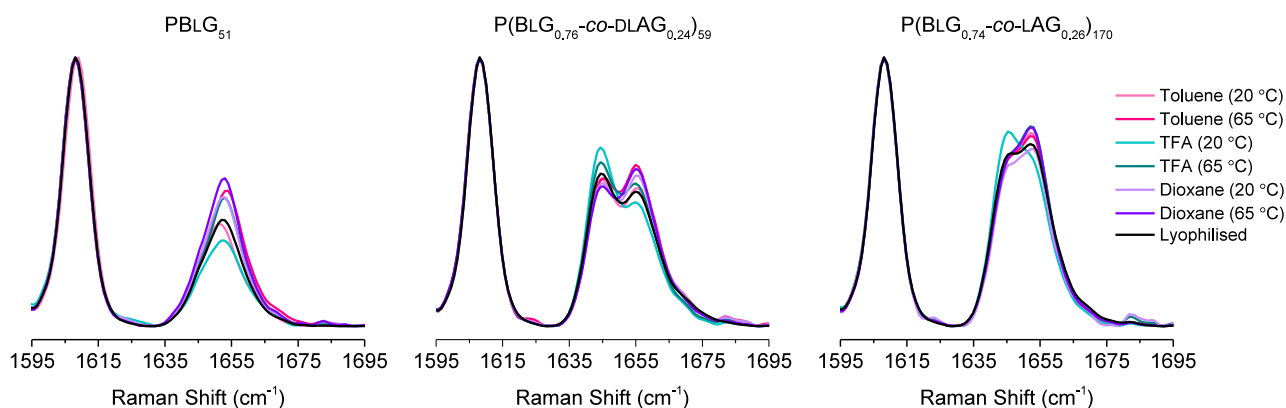

Figure VI.4 Partial Raman spectra centred around the Amide I band (~ 1620 to 1680 cm^{-1}) of films cast from P(BLG$_x$-*co*-AG$_{1-x}$)$_n$ solutions (50 g·L^{-1}) and dried at 20 or 65 °C. Each spectrum was normalised to the 1610 cm^{-1} peak, which corresponds to the ν(C-C) of the phenyl group of the BLG moiety.[22–26] Despite the fluctuations in peak height and α/α' peak intensity ratio, the mean Amide I band increased with respect to the reference peak (1610 cm^{-1}) with increasing AG content.

Further work, with a particular focus on the orientation of the samples and rigorously devised sample preparation methods, is recommended. In particular, it may be interesting to undertake a study of oriented films, prepared by the application of a mechanical stress, a magnetic or electric field. Analytical methods suited to the characterization of anisotropic samples, such as polarised Raman and WAXS analysis with control over the sample orientation, shall be favoured. In addition, SEM should be used to search for potential film morphologies in connection with the study on anisotropic morphologies of emulsified particles presented hereafter (Section VI.3.2).

VI.3.2 Long Range Order in Emulsified Particles

In order to supplement the study on the physical gelation of $P(BLG_x\text{-}co\text{-}AG_{1-x})_n$ solutions (Chapter IV), microgels from $PBLG_{51}$, $P(BLG_{0.78}\text{-}co\text{-}LAG_{0.22})_{96}$, $P(BLG_{0.80}\text{-}co\text{-}LAG_{0.20})_{219}$, and $P(BLG_{0.84}\text{-}co\text{-}LAG_{0.16})_{171}$ (Table VI.1B) were prepared. As emulsions generally produce featureless spherical micro-particles, it was surprising to observe regular spiral-like morphologies on most particles (Figure VI.5). In addition, these spirals were clockwise (or right-handed). It is common knowledge that, as a result of geometrical constraints and the associated dihedral angles of the polypeptide backbone,[27] the chirality of the α-helix is controlled by the chirality of the amino acids that compose it: while L amino acids give rise to right-handedness, D amino acids give rise to left-handedness.[28] Based on the L stereo-regularity of their repeat units, and as attested by CD spectroscopy (Figure IV.10), all analysed polypeptides from Table VI.1B were right-handed α-helices. Therefore, efforts to determine whether the α-helical chirality is the critical factor for the chirality of the spirals were made. For this, a new set of 'mirror image' α-helical polypeptides was synthesised and characterised (Table VI.1C).
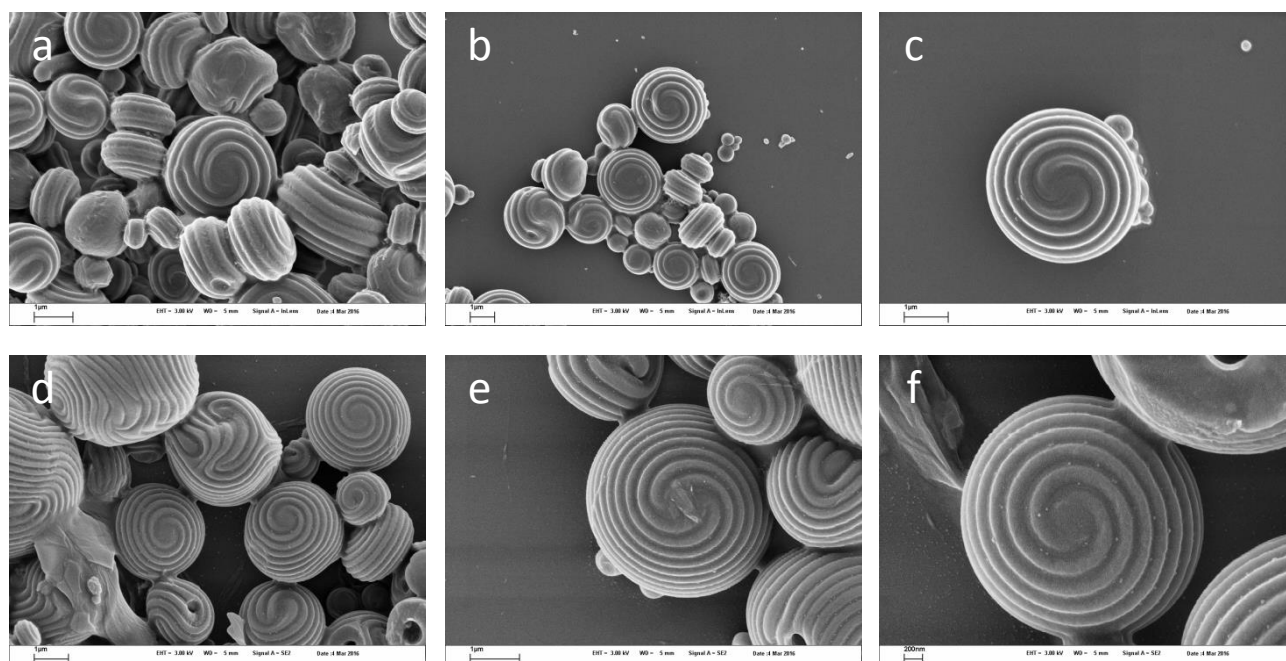

Figure VI.5 Particles prepared from $P(BLG_{0.80}\text{-}co\text{-}LAG_{0.20})_{219}$-toluene in water emulsions. The emulsions carried out at (a, b, and c) 60 °C led to smaller particles than those carried out at (d, e, and f) room temperature; this result is typical of emulsions. Scale bars = (a to e) 1 μm, (f) 200 nm.

A CD spectroscopic analysis showed that PBLG$_{159}$ and P(BLG$_{0.80}$-*co*-DLAG$_{0.20}$)$_{209}$, which are composed of a majority of L residues, are right-handed α-helices as attested by the minima at 208 and 222 nm. In contrast, their respective mirror images, PBDG$_{155}$ and P(BDG$_{0.81}$-*co*-DLAG$_{0.19}$)$_{223}$, which are composed of a majority of D residues, are left-handed α-helices as attested by the maxima at 208 and 222 nm (Figure VI.7a). The Raman spectra of PBLG$_{159}$ and its mirror image PBDG$_{155}$ were almost identical, and so were the spectra of P(BLG$_{0.80}$-*co*-DLAG$_{0.20}$)$_{209}$ and its mirror image P(BDG$_{0.81}$-*co*-DLAG$_{0.19}$)$_{223}$ (Figure VI.6). This result illustrates that, from a secondary structure aspect, each set of enantiomers consists of near-perfect conformational mirror images. While CD spectroscopy can distinguish between enantiomers (*i.e.*, the orbital transitions of chiral samples, measured by CD, correspond to the absorption of either the left- or right-polarised light, depending on the enantiomer), this is not the case of Raman spectroscopy in a standard set up (*e.g.*, the vibrational energy of νC=O in a right- or left-handed α-helical conformation is identical), which explains why enantiomers exhibited identical Raman spectra and 'opposite' CD spectra.
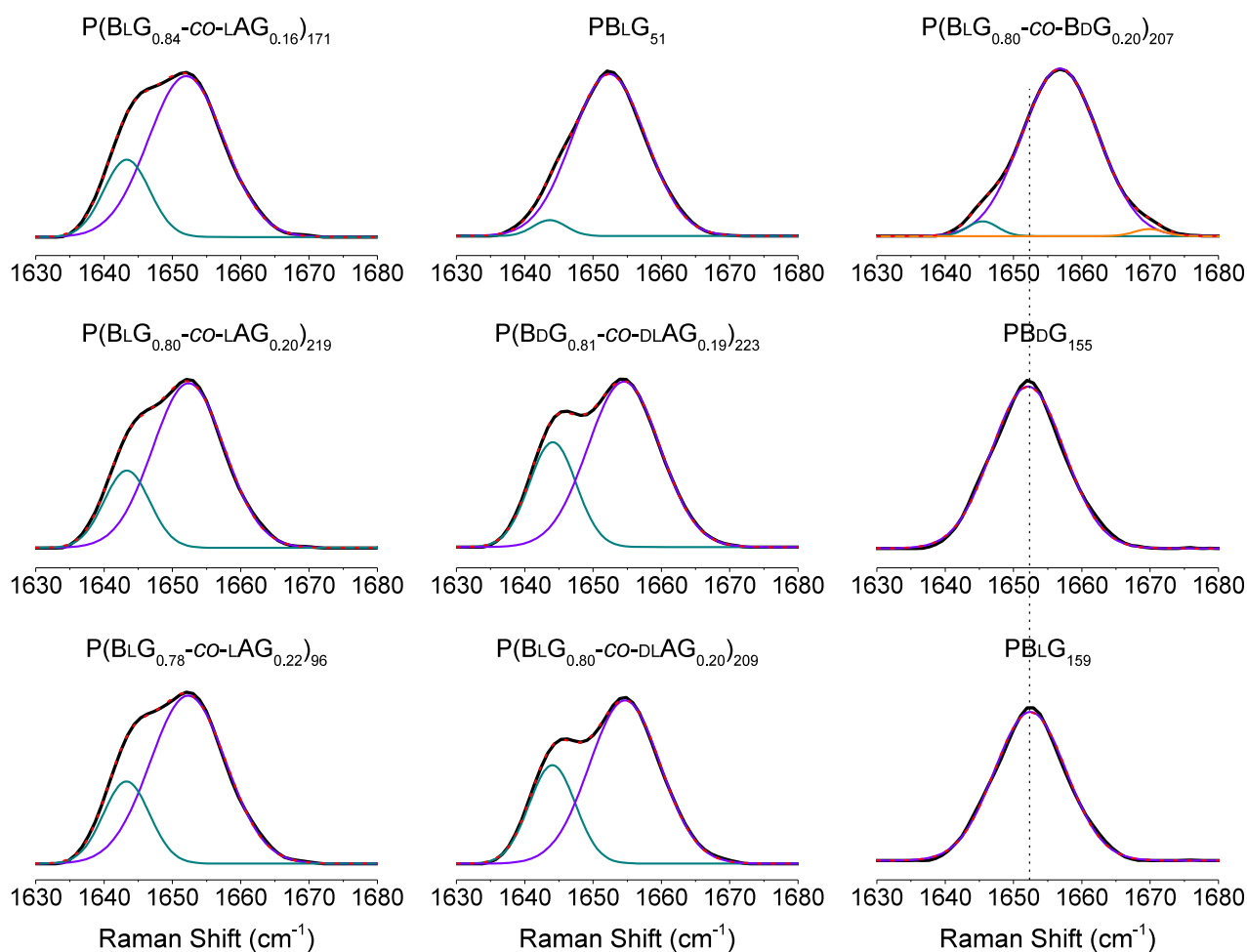

Figure VI.6 Amide I bands (black) from Raman spectra of the series of polypeptides investigated as part of the emulsion study (Table VI.1B and C). The deconvoluted Amide I bands show: a single peak at ~ 1652 cm^{-1} (α-helix, violet) for PBLG$_{159}$ and PBDG$_{155}$; a set of two peaks of identical height ratio, at ~ 1654 cm^{-1} (α-helix, violet) and ~ 1644 cm^{-1} (α' conformation, green) for P(BLG$_{0.80}$-*co*-DLAG$_{0.20}$)$_{209}$ and P(BDG$_{0.81}$-*co*-DLAG$_{0.19}$)$_{223}$; and a main peak at 1657 cm^{-1} (α-helix, violet), along with two smaller peaks at 1645 cm^{-1} (α' conformation, green) and 1670 cm^{-1} (β sheet, orange) for P(BLG$_{0.80}$-*co*-BDG$_{0.20}$)$_{207}$. The three spectra in the left column were analysed in Chapter IV. The peak assignment is discussed in more details in Chapter IV.
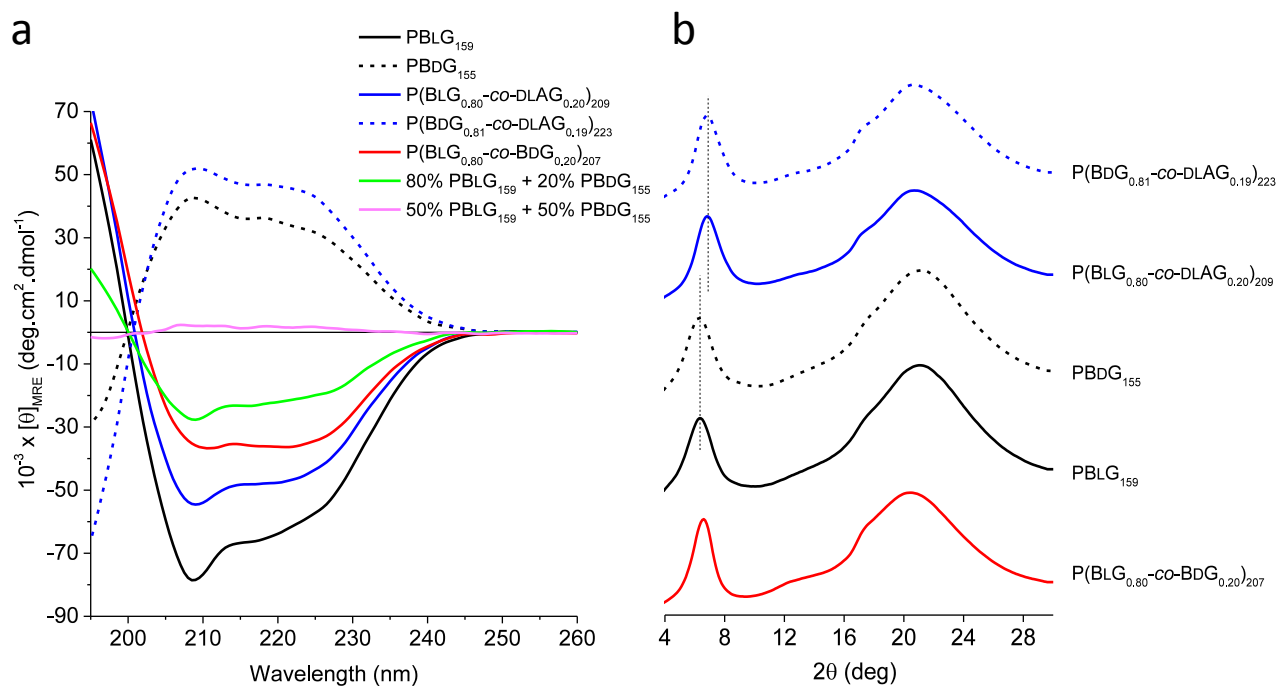
Figure VI.7 Characterisation of the series of polypeptides investigated as part of the emulsion study (Table VI.1C). (a) CD spectroscopy in HFIP at 0.05 g·L^{-1}; the two minima and maxima at 208 and 222 nm and their relative intensities are characteristic of a right-handed and left-handed α-helical conformation, respectively; CD spectra of particles are available in Appendix B. (b) WAXS diffractograms of the lyophilised polypeptides: the peak at 6–7° (~ 1.3-1.4 nm) is indicative of a pseudo-hexagonal arrangement of α-helical polymers; the shoulder at 17° (~ 0.5 nm) corresponds to the α-helical pitch; the broad peak centred around 21° is the amorphous halo. As predicted and explained in Chapter IV, the polypeptides composed of 100% of BLG (BDG by extension) units exhibited slightly larger d-spacing than those composed of a mixture of BLG and AG (BDG and AG by extension); the difference is highlighted by the vertical dotted lines.

As expected, the particles resulting from the emulsion of PBLG$_{159}$ and P(BLG$_{0.80}$-*co*-DLAG$_{0.20}$)$_{209}$ exhibited right-handed (or clockwise) spirals, whereas those from PBDG$_{155}$ and P(BDG$_{0.81}$-*co*-DLAG$_{0.19}$)$_{223}$ exhibited left-handed (or counterclockwise) spirals (Figure VI.8). This result confirms that the chirality of the spirals is controlled by that of the polypeptides. As a rather logical consequence, P(BLG$_{0.80}$-*co*-BDG$_{0.20}$)$_{207}$, which is composed of a mixture of L and D enantiomers, exhibited a lower overall helicity compared to its pure PBLG and PBDG counterparts (Figure VI.7a) and produced particles with far less defined spiral morphologies (Figure VI.8e). It should be noted that although a small percentage of β-sheet conformation was observed for P(BLG$_{0.80}$-*co*-BDG$_{0.20}$)$_{207}$ by Raman spectroscopy (Figure VI.6), its contribution to the overall secondary structure was not significant enough to be detected by CD and WAXS (Figure VI.7b) and that the α-helical conformation was thus thought to predominates. The α-helical peak of P(BLG$_{0.80}$-*co*-BDG$_{0.20}$)$_{207}$ corresponded to a higher Raman shift (1657 cm^{-1}) than the α-helical peak of homopolymers PBLG$_{159}$ and PBDG$_{155}$ (1652 cm^{-1}). This may be caused by intramolecular hydrogen bonds that are part of a geometrically strained right-handed α-helix, or by a mixed conformation composed of left-handed and right-handed α-helical segments. The latter option is not consistent with (i) WAXS diffractograms, which showed a well defined pseudo-hexagonal arrangement (Figure VI.7b), and (ii) a monomodal CD trace (Figure B.38), indicative of an effective statistical copolymerisation and randomly distributed BLG and BDG residues.
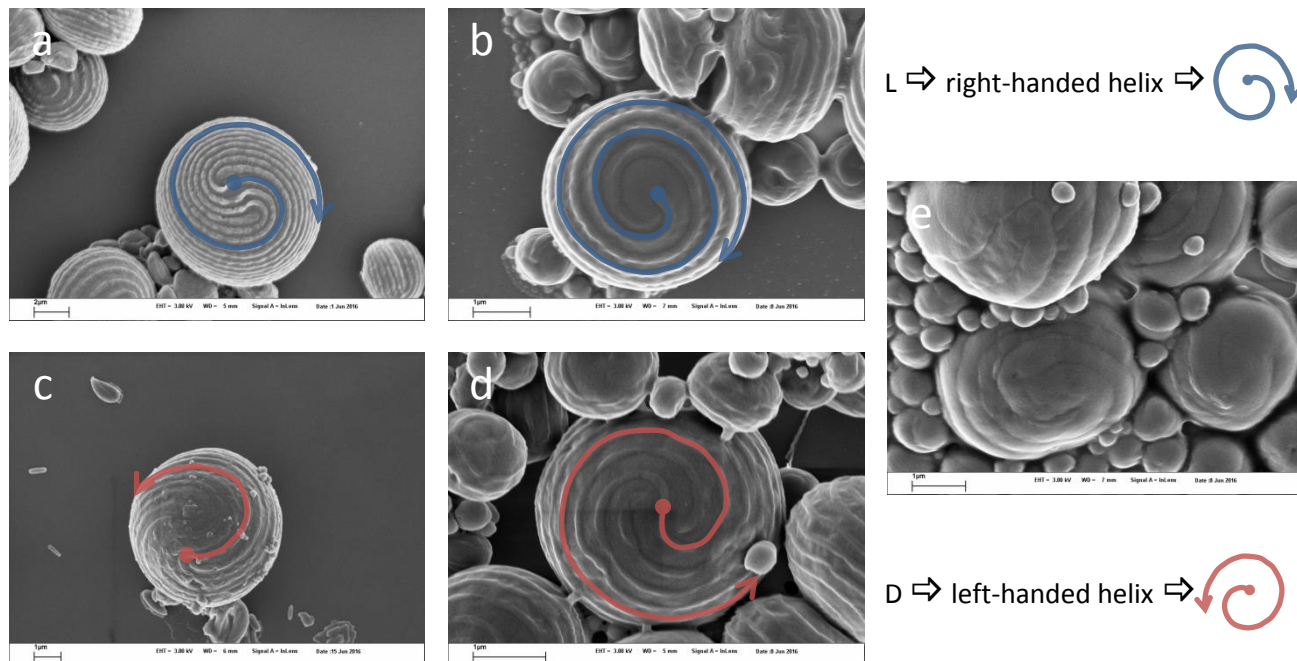
Figure VI.8 Particles resulting from polypeptide-toluene in water emulsions (60 °C) of (a) PB$_L$G$_{159}$, (b) P(B$_L$G$_{0.80}$-*co*-$_{DL}$AG$_{0.20}$)$_{209}$, (c) PB$_D$G$_{155}$, (d) P(B$_D$G$_{0.81}$-*co*-$_{DL}$AG$_{0.19}$)$_{223}$, and (e) P(B$_L$G$_{0.80}$-*co*-B$_D$G$_{0.20}$)$_{207}$. Spiral ridges were highlighted in blue or red to make it easier to visualise the direction of the spirals, which was either (a and b) clockwise, or (c and d) counterclockwise. Although a spiral-like pattern can be noticed for (e) it is not sharp and regular enough to make out a direction. Scale bars = (a) 2 µm, (b to e) 1 µm.

The mechanism by which these spirals form is not fully understood yet. Interestingly, the first studies to mention similar features focused on the crystallisation of linear polymers with no chiral centres (*e.g.*, polyethylene, polymethylene oxide, polyethylene oxide). These morphologies were then considered to be the result of crystal lattice distortions caused by screw dislocations, during the crystallisation of polymers either from solutions or in bulk (Figure VI.9b).[29–31] This explanation was, however, later challenged by Keith et al., who argued that long-range deformations of chain-folded polymer crystals cannot be solely attributed to dislocation mechanisms, but would also require a cooperative process, such as shear stress-driven distortion of bond angles.[32] Since the polymers studied were non chiral, the spiral direction did not receive any particular attention. A more recent study by Akagi et al., however, reported the synthesis of chiral helical polyacetylene in nematic liquid crystals (LCs) as the polymerisation solvent.[33] More precisely, the study showed that the chirality of the LC solvents (R or S) was transmitted to the polymer over the long range. R and S LC solvents gave rise to counterclockwise and clockwise polymer chains, respectively, as demonstrated by CD spectroscopy (positive and negative Cotton effect, respectively), and formed helical fibrils which were bundled with the same screw directions as the chiral nematic LCs. These bundled fibres formed spiral morphologies at the next hierarchical level, *i.e.* in the microscopic-near macroscopic regime (Figure VI.9a). Another study, by Malthete at al., similarly showed that mesogenic disk-like molecules could, through the formation of columnar and nematic mesophases, transmit their chirality over several hierarchical levels, to yield clockwise and counterclockwise spirals (Figure VI.9d).[34] These last two examples demonstrate that whether the chirality is intrinsic to the building block or transmitted by a solvent (in the same way as a negative film yields a positive photography), it can

be hierarchically transferred, thereby yielding highly ordered structures, such as clockwise or counterclockwise spirals. In a more recent study, Bellomo et al. further extended this body of work by showing that spiral-like composite morphologies were obtained from using concentrated LC phases of PEO-modified polylysine as templates for the formation of well-ordered silica structures.[35] Hexagonal silica crystals were obtained when highly concentrated polypeptide template-solutions were used (> 40 wt%), sometimes with a 'central screw dislocation' (*i.e.*, a spiral morphology) (Figure VI.9c). They also showed that this spiral feature could be suppressed by using a mixture of D- and L-polypeptides, and that both the spiral and platelet morphologies gave way to disordered composites when DL-random polypeptides or polypeptides with high dispersity (Đ > 1.4) were used. However, neither was the direction of the spirals discussed, nor were pure D-polypeptide template-solutions tested. A parallel may be drawn between this last example and the suppression of well-defined spiral features by the use of the DL-statistical copolypeptide $P(BLG_{0.80}\text{-}co\text{-}BDG_{0.20})_{207}$.
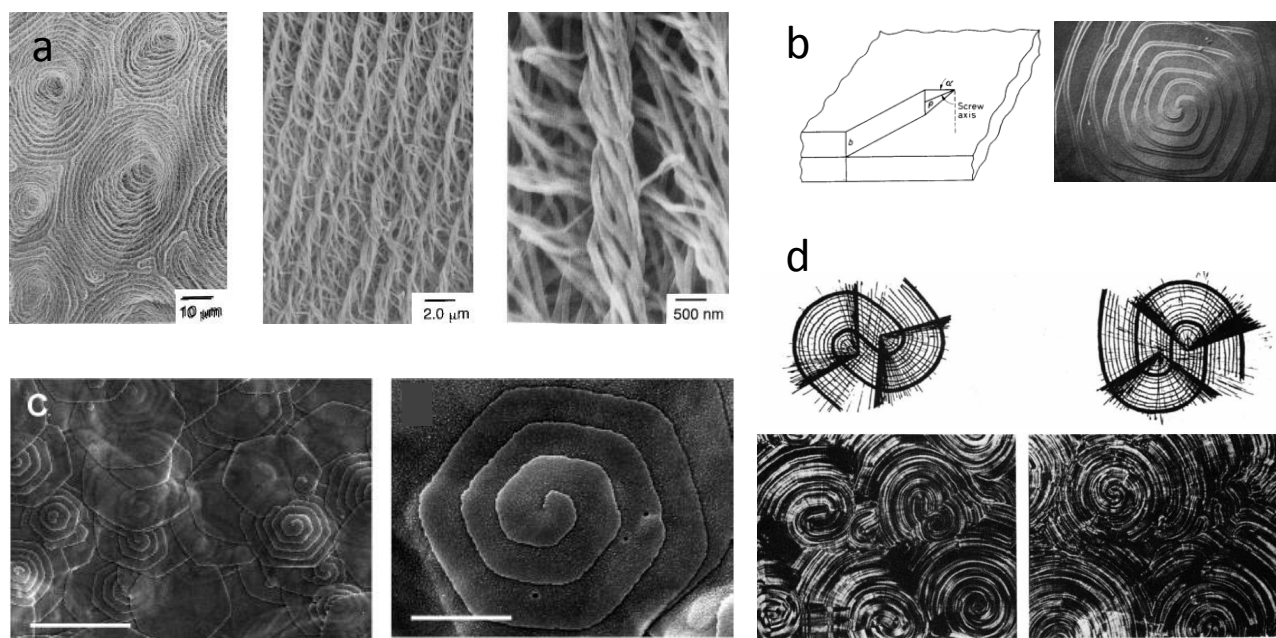

Figure VI.9 Examples of spiral morphologies from the literature. (a) SEM micrographs of a polyacetylene film synthesised with (R)-chiral nematic liquid crystal; reprinted from *Science, 282, Akagi et al., Helical Polyacetylene Synthesized with a Chiral Nematic Reaction Field, 1683-1686, 1998,* with permission from AAAS.[33] (b) Schematic diagram of step associated with screw dislocation and SEM micrograph of shadowed surface replica of bulk crystallised (at 56 °C) polyethylene oxide; reprinted from *Polymer, 5, Barnes et al., Morphology of polymer crystals: Screw dislocations in polyethylene, polymethylene oxide and polyethylene oxide, 283-292, 1964,* with permission from Elsevier.[30] (c) SEM top view image of (left) silica-ethylene glycol-side chain-modified polylysine (n = 264) (85 wt.%polypeptide) composite hexagonal plates (scale bar = 10 μm), and (right) close-up of a silica-ethylene glycol-side chain-modified polylysine (n = 264) (65 wt% polypeptide) composite hexagonal plate (scale bar = 2 μm); reprinted from *Journal of the American Chemical Society, 128, Bellomo et al., Monoliths of Aligned Silica-Polypeptide Hexagonal Platelets, 2276-2279, 2006,* with permission from the American Chemical Society.[35] (d) Enantiomeric spirals of columnar mesophases of (left) (+)- and (right) (-)-hexasubstituted triphenylene (x100 magnification); reprinted from *Nature, 298, Malthête et al., Macroscopic evidence of molecular chirality in columnar mesophases, 46-48, 1982,* with permission from Macmillan Publishers Ltd.[34]

Based on the different methods reported in the literature to prepare polymer crystals with screw-like or spiral morphologies, it could be thought that the P(BLG$_x$-*co*-AG$_{1-x}$)$_n$-based spirals may result from (i) stress-driven crystallisation, which takes place as the particles undergo an inhomogeneous drying on a flat surface (vertical stress, leading to the screw-like crystallisation to start at the top of the particle),[32] or (ii) poor-solvent-driven crystallisation through the use of water as the continuous medium and washing solvent.[30] As far as the direction of the spirals is concerned, one could imagine that α-helices may be endowed with a slight twist (left- or right-handed, depending on the helix and polypeptide chirality, either D or L), which is transmitted - through the pseudo-hexagonal packing step - to higher hierarchical levels, such as fibres or LC phases depending on the concentration. Aside from the aforementioned literature examples, the 'helical-twist' model was also proposed for collagen fibrils.[36–39] This example is particularly relevant to the present study because, like PBLG, PBDG and P(BG$_x$-*co*-AG$_{1-x}$)$_n$ polypeptides, collagen strands fold into helices (PPII and triple helices), which in turn self-assemble into pseudo-hexagonal lattices.[40] In the case of the polypeptides analysed in this study, although a slight tilt or twist might be hardly noticeable at the fibril level (*i.e.*, organogels) or may be lost in other geometries (*e.g.*, films), one could postulate that this nanoscale twist could be transmitted (as spirals) to the micro/macroscale level in the context of crystallisation on non-planar, spherical surfaces. In fact, on some particles, slightly twisted fibre bundles were noticeable, thereby supporting this 'nano-twist' hypothesis (Figure VI.10). Interestingly a physical study by Grason showed that there is a connection between packing in twisted filament bundles and packing on positively curved surfaces.[41] Besides, such phenomenon has already been reported for β-sheets, which often form twisted ribbons at higher hierarchical levels.[42] At this stage of the study, this explanation remains speculative but could be tested in the future by methodically designed experiments complemented by computer simulations.

Figure VI.10 Particles resulting from polypeptide-toluene in water emulsions of (a and b) PBDG$_{155}$, and (c) PBLG$_{159}$. Scale bars = (a and c) 2 μm, (b) 1 μm.

It is also worth noting that out of all the polypeptides tested, P(BLG$_{0.80}$-*co*-LAG$_{0.20}$)$_{219}$ produced the best-defined spirals. One would have rather expected the best results to be obtained from the 'model' polypeptides, *i.e.*, PBLG$_{51}$ (Figure VI.11a), PBLG$_{159}$ and PBDG$_{155}$, which are the best-defined α-helices from a conformational aspect (Figure VI.6). The presence of fibres embedded in-between the ridges of the spirals observed on some PBLG$_{159}$ and PBDG$_{155}$ particles helped formulate an explanation for this. As demonstrated

in Chapter IV, the gelation in toluene of rod-like α-helical polymers such as PBLG and P(BLG$_x$-*co*-AG$_{1-x}$)$_n$ takes place upon decreasing the temperature and generates solvent-trapping fibres (T$_{gel}$ available in Table IV.2). This happens when dilute solutions cross the isotropic to LC-isotropic boundary (Figure IV.15), which occurs at room temperature for PBLG (and by extension to PBDG) and at lower temperatures for P(BLG$_x$-*co*-AG$_{1-x}$)$_n$ (and by extension to P(BDG$_x$-*co*-AG$_{1-x}$)$_n$). This potentially means that as the PBLG$_{159}$ and PBDG$_{155}$ particles cooled down and dried, a competition between spiral-generating-crystallisation and fibre-forming-gelation took place, thereby resulting in these characteristic hybrid features. In addition, the quality of the spirals was also lower for P(BLG$_{0.78}$-*co*-LAG$_{0.22}$)$_{96}$ and P(BLG$_{0.84}$-*co*-LAG$_{0.16}$)$_{171}$ (Figure VI.11b and c). In comparison to P(BLG$_{0.80}$-*co*-LAG$_{0.20}$)$_{219}$ (T$_{gel}$ = -12 °C), P(BLG$_{0.78}$-*co*-LAG$_{0.22}$)$_{96}$ is shorter and P(BLG$_{0.84}$-*co*-LAG$_{0.16}$)$_{171}$ has a higher T$_{gel}$ (-8 °C), properties which may have been the main cause for the imperfect spirals in Figure VI.11b and c.

These observations and interpretations suggest that the best-defined spirals should derive from α-helical P(BG$_x$-*co*-AG$_{1-x}$)$_n$, preferably enantiomerically pure (*e.g.*, BLG and LAG, or possibly BDG and DAG), and most likely with a sufficiently low T$_{gel}$ and a sufficiently high chain length (*n*). However, other parameters, such as emulsion temperature, stirring speed or drying temperature and rate, might also affect the resulting features. Therefore, should one be interested in defining the parameter ranges leading to the best-defined spirals, would a software-supported design of experiment be recommended.
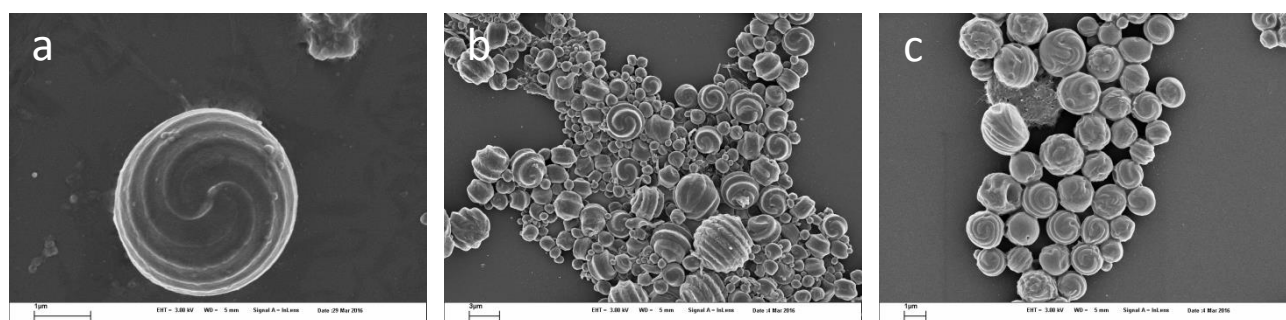

Figure VI.11 Particles resulting from polypeptide-toluene in water emulsions of (a) PBLG$_{51}$, (b) P(BLG$_{0.84}$-*co*-LAG$_{0.16}$)$_{171}$, and (c) P(BLG$_{0.78}$-*co*-LAG$_{0.22}$)$_{96}$. Scale bars = (a and e) 1 µm, (b) 3 µm.

VI.4   Conclusions

The P(BLG$_x$-*co*-AG$_{1-x}$)$_n$ polypeptides studied in Chapter IV for their interesting gelation properties were emulsified and produced particles with highly regular spiral morphologies. It was demonstrated that the direction of these spirals was controlled by the chirality of the polypeptides. Notably, PBLG$_n$ and P(BLG$_x$-*co*-AG$_{1-x}$)$_n$, which are composed of a majority of L residues, and thus have a right-handed α-helical conformation, gave rise to particles exhibiting clockwise spirals. Vice-versa, PBDG$_n$ and P(BDG$_x$-*co*-AG$_{1-x}$)$_n$, which are composed of a majority of D residues, and thus have a left-handed α-helical conformation, gave rise to particles exhibiting counterclockwise spirals. These spirals could be partly suppressed by the use of polypeptides of lower helicity, such as a copolymers of BLG and BDG residues. The transmission of the chirality from a molecular level (*i.e.*, polypeptide chain) to higher hierarchical levels (*i.e.*, micron-sized

particles), was proposed to occur via the existence of a chiral nano-twist in the α-helix axis that was 'amplified' upon pseudo-hexagonal packing - through LC phase crystallisation or fibre formation - and was transcribed into microscopic chiral spirals in the context of a crystallisation on a non-planar, spherical surface. This hypothesis was inspired by several examples reported in the literature, including collagen fibrils, and was supported by the twisted bundles of fibres observed on some particles. Additional experimental work in parallel with a modelling study is recommended to provide further evidence for this hypothesis.

Although it might seem unclear how such morphologies might be useful in the context of biomedical applications, they provide a unique platform for the fundamental study and understanding of how conformational information at a nanoscale level can be transmitted to the micro-/macroscale level through a hierarchical organisation. As such, $P(B_LG_x\text{-}co\text{-}AG_{1-x})_n$ may be used as model polymers to study and elucidate structure-property relationships in natural materials. Like in the study by Bellomo et al., these spiral-particles may be also used as templates for the synthesis of ordered inorganic systems (*e.g.*, mineralisation), with a view to studying or replicating the formation of charophytes algae or other similar species for instance (*e.g.*, diatoms).[43] Likewise, twisted bundles of $P(B_LG_x\text{-}co\text{-}AG_{1-x})_n$ fibres may be used as models to study the anisotropic orientation of actin filaments in stressed matrix architectures formed during *in vitro* tissue growth.[44] They might even be used as a toolbox to test mathematical geometries and illustrate the connections and differences between packing in twisted filament bundles and packing on positively curved surfaces.[41] In addition, the easy and affordable synthesis of organic $P(B_LG_x\text{-}co\text{-}AG_{1-x})_n$ polymers and their simple processing (*i.e.*, by emulsion) into chiral spherical particles, with unique CD spectral 'fingerprints', may find some application as high-end fillers in coatings used for counterfeit purposes.

The study of $P(B_LG_x\text{-}co\text{-}AG_{1-x})_n$-based films showed sample preparation-dependant conformations and packing. Both the emulsion and film studies would benefit from being conducted in parallel as their results might be connected, since they both investigate the outcome of the drying process of $P(B_LG_x\text{-}co\text{-}AG_{1-x})_n$-solutions, with the difference that one is performed on spherical surfaces and the other on flat surfaces. As such, films might represent interesting control samples. It is, therefore, recommended that the film study is continued with a particular focus on stress-driven anisotropic organisation and resulting morphologies. The development of films and microgels for biomedical applications, as initially planned, may also benefit from the results of these fundamental studies.

VI.5   References

(1)   Jung, J. P.; Gasiorowski, J. Z.; Collier, J. H. *Biopolymers* **2010**, *94*, 49–59.

(2)   Lowe, S. B.; Tan, V. T. G.; Soeriyadi, A. H.; Davis, T. P.; Gooding, J. J. *Bioconjug. Chem.* **2014**, *25*, 1581–1601.

(3)   Li, Y.; Qin, M.; Cao, Y.; Wang, W. *Sci. China Physics, Mech. Astron.* **2014**, *57*, 849–858.

(4)   Aggeli, A.; Boden, N.; Carrick, L. M.; Mcleish, T. C. B.; Nyrkova, I. A.; Semenov, A. N. In *Molecular Gels*; Springer Netherlands, **2006**; pp 99–130.

(5)   Stenzel, K. H.; Miyata, T.; Rubin, A. L. *Annu. Rev. Biophys. Bioeng.* **1974**, *3*, 231–253.

(6)   Zhu, J.; Hu, J.; Marchant, R. E. In *Biomimetic Biomaterials*; Elsevier, **2013**; pp 238–275.

(7)   Maude, S.; Ingham, E.; Aggeli, A. *Nanomedicine* **2013**, *8*, 823–847.

(8)   Sivakumar, M.; Tominaga, R.; Koga, T.; Kinoshita, T.; Sugiyama, M.; Yamaguchi, K. *Sci. Technol. Adv. Mater.* **2005**, *6*, 91–96.

(9)   Kato, Y.; Ozawa, S.; Miyamoto, C.; Maehata, Y.; Suzuki, A.; Maeda, T.; Baba, Y. *Cancer Cell Int.* **2013**, *13*, 1–8.

(10)   Yu, G.; Yan, X.; Han, C.; Huang, F. *Chem. Soc. Rev.* **2013**, *42*, 6697.

(11)   Vashist, A.; Vashist, A.; Gupta, Y. K.; Ahmad, S. *J. Mater. Chem. B* **2014**, *2*, 147.

(12)   Deming, T. J. *Wiley Interdiscip. Rev. Nanomedicine Nanobiotechnology* **2014**, *6*, 283–297.

(13)   Jiang, Y.; Chen, J.; Deng, C.; Suuronen, E. J.; Zhong, Z. *Biomaterials* **2014**, *35*, 4969–4985.

(14)   Sakamoto, R. *Colloid Polym. Sci.* **1984**, *262*, 788–792.

(15)   Dupré, D. B.; Duke, R. W.; Hines, W. A.; Samulski, E. T. *Mol. Cryst. Liq. Cryst.* **1977**, *40*, 247–259.

(16)   Truong, W. T.; Su, Y.; Meijer, J. T.; Thordarson, P.; Braet, F. *Chem. Asian J.* **2011**, *6*, 30–42.

(17)   Gangloff, N.; Luxenhofer, R. *Hierarchical Macromolecular Structures: 60 Years after the Staudinger Nobel Prize II*; Percec, V., Ed.; Advances in Polymer Science; Springer International Publishing: Cham, **2013**; Vol. 262.

(18)   Watanabe, J.; Imai, K.; Gehani, R.; Uematsu, I. *J. Polym. Sci. Polym. Phys. Ed.* **1981**, *19*, 653–665.

(19)   McKinnon, A. J.; Tobolsky, A. V. *J. Phys. Chem.* **1968**, *72*, 1157–1161.

(20)   Cohen, Y.; Dagan, A. *Macromolecules* **1995**, *28*, 7638–7644.

(21)   Yen, C. C.; Tokita, M.; Park, B.; Takezoe, H.; Watanabe, J. *Macromolecules* **2006**, *39*, 1313–1315.

(22)   Koenig, J. L.; Sutton, P. L. *Biopolymers* **1971**, *10*, 89–106.

(23)   Iconomidou, V. A.; Chryssikos, G. D.; Gionis, V.; Willis, J. H.; Hamodrakas, S. J. *Insect Biochem. Mol. Biol.* **2001**, *31*, 877–885.

(24)   Wilser, W. T. *J. Chem. Phys.* **1975**, *62*, 720.

(25)   Profit, A. A.; Vedad, J.; Saleh, M.; Desamero, R. Z. B. *Arch. Biochem. Biophys.* **2015**, *567*, 46–58.

(26)   David, C.; D'Andrea, C.; Lancelot, E.; Bochterle, J.; Guillot, N.; Fazio, B.; Maragò, O. M.; Sutton, A.; Charnaux, N.; Neubrech, F.; Pucci, A.; Gucciardi, P. G.; de la Chapelle, M. L. *Vib. Spectrosc.* **2012**, *62*, 50–58.

(27)   Berg, J. M.; Tymoczko, J. L.; Stryer, L. *Biochemistry*, Sixth edit.; W. H. Freeman and Company: New York, **2007**.

(28)   Czarniecka, K.; Samulski, E. T. *Mol. Cryst. Liq. Cryst.* **1981**, *63*, 205–214.

(29)   Keller, A. *Die Makromol. Chemie* **1959**, *34*, 1–28.

(30) Barnes, W. J.; Price, F. P. *Polymer* **1964**, *5*, 283–292.

(31) Sears, G. W. *Polym. Lett.* **1964**, *2*, 1117–1120.

(32) Keith, H. D.; Passaglia, E. *J. Res. Natl. Bur. Stand. Sect. A Phys. Chem.* **1964**, *68A*, 513–518.

(33) Akagi, K. *Science* **1998**, *282*, 1683–1686.

(34) Malthête, J.; Jacques, J.; Tinh, N. H.; Destrade, C. *Nature* **1982**, *298*, 46–48.

(35) Bellomo, E. G.; Deming, T. J. *J. Am. Chem. Soc.* **2006**, *128*, 2276–2279.

(36) Piez, K. A.; Trus, B. L. *Biosci. Rep.* **1981**, *1*, 801–810.

(37) Wess, T. J.; Hammersley, A. P.; Wess, L.; Miller, A. *J. Mol. Biol.* **1998**, *275*, 255–267.

(38) Orgel, J. P. R. O.; Irving, T. C.; Miller, A.; Wess, T. J. *Proc. Natl. Acad. Sci.* **2006**, *103*, 9001–9005.

(39) Bozec, L.; van der Heijden, G.; Horton, M. *Biophys. J.* **2007**, *92*, 70–75.

(40) Okuyama, K.; Miyama, K.; Mizuno, K.; Bächinger, H. P. *Biopolymers* **2012**, *97*, 607–616.

(41) Grason, G. M. *Rev. Mod. Phys.* **2015**, *87*, 401–419.

(42) Lu, H.; Wang, J.; Song, Z.; Yin, L.; Zhang, Y.; Tang, H.; Tu, C.; Lin, Y.; Cheng, J. *Chem. Commun.* **2014**, *50*, 139–155.

(43) Chassagne-Manoukian, M.; Haddoumi, H.; Cappetta, H.; Charrière, A.; Feist, M.; Tabuce, R.; Vianey-Liaud, M. *Geobios* **2013**, *46*, 371–379.

(44) Bidan, C. M.; Kollmannsberger, P.; Gering, V.; Ehrig, S.; Joly, P.; Petersen, A.; Vogel, V.; Fratzl, P.; Dunlop, J. W. C. *J. R. Soc. Interface* **2016**, *13*, 20160136.

Summary and Outlook

The development and study of a series of statistical copolypeptides and materials prepared from them were reported. The main achievements and suggestions for future work are summarised below.

Secondary Structure and Physical Gelation

Statistical copolypeptides of γ-benzyl-L-glutamate (BLG) and allylglycine (AG), noted P(BLG-*co*-AG), were synthesised by ring opening polymerisation (ROP) of amino acid *N*-carboxyanhydrides (NCA) and analysed. The choice of amino acids was mainly based on the ability for PBLG homopolymers to fold into α-helices that can self-assemble to form physical and thermoreversible gels at room temperature in helicogenic solvents such as toluene. AG was chosen as a functionalisable comonomer. The properties, composition and structure of the synthesised polypeptides were thoroughly investigated. Their random architecture was confirmed by NMR, and their ability to form physical gels at low temperature (between -38 and -8 °C) in toluene was demonstrated by rheology. The gelation temperature was found to be affected by both the AG molar fraction and the chain length (n). Raman and FTIR spectroscopy were used to study the secondary structure of the polypeptides. For an AG molar fraction below 26%, P(BLG-*co*-AG) polypeptides were mostly α-helical, despite minor defects caused by the presence of AG and identified as portions of the α-helix that lacked intramolecular hydrogen bonds. A WAXS study showed that both P(BLG-*co*-AG) and PBLG α-helices were pseudo-hexagonally packed in the dry state. The collected results helped established that P(BLG-*co*-AG) and PBLG have a similar conformation and packing behaviour, but that the presence of AG drastically modifies the gelation temperature and rheology of the polypeptides.

In this study, the conditions and limits within which statistical copolypeptides self-assemble into physical organogels, without the assistance of blocks or self-assembly-inducing end group moieties,[1] were determined. This work may inspire design rules for statistical copolypeptide hydrogelators, which would set a precedent in the field of self-assembled polypeptide hydrogels, currently dominated by block and sequence-controlled architectures, and small amphiphilic peptides. Future work should focus on the preparation and study of statistical copolypeptides that can directly form hydrogels. In particular, a third comonomer should be considered. For instance a compact amino acid such as glycine may help tighten the helical conformation while offering a hydrophobic core, which may assist with the self-assembly in water in the same way that collagen self-assembles. Star topology and gradient architectures, using the 1,2,3-tris(aminomethyl)benzene (TAB) initiator used in Chapter III, may also be considered as a way to drive supramolecular assembly in water.[2–4]

Summary

Fibrillar Hydrogels Derived From Organogels

P(BLG-*co*-AG) organogels, stable at room temperature, were prepared by crosslinking AG moieties with dithiol crosslinkers. Robust, solid-like organogels were generated from very dilute P(BLG-*co*-AG) solutions (*i.e.*, down to 10 g·L^{-1} in toluene, THF or dioxane) despite rather short polymer chains (50 < *n* < 220). An SEM, TEM and WAXS study showed that, like PBLG, crosslinked P(BLG-*co*-AG) gels were composed of a network of fibres, themselves formed by pseudo-hexagonally packed α-helices, like in physical gels of PBLG. Moreover, an FTIR study confirmed that the conformation of P(BLG-*co*-AG), like PBLG, was α-helical in solution too (*e.g.*, in toluene and dioxane). These results indicate that P(BLG-*co*-AG) polypeptides behave similarly to PBLG in helicogenic solvents, in that they fold into α-helices that aggregate in a head-to-tail and side-by-side fashion. By crosslinking these loosely bound aggregates, a fibrous network is formed, *i.e.*, an organogel. Although such organogels fall into the 'chemical gel' category (*i.e.*, crosslinked gel), their formation initially relied on some level of self-assembly; this makes them stand out from traditional gel categories. P(BLG-*co*-AG)-dioxane organogels were the most robust and were thus used to prepare hydrogels by debenzylating the BLG units to yield L-glutamic acid (LGA) moieties. The resulting hydrogels retained the fibrous structure, and were highly absorbent (swelling ratio up to 87) and pH-responsive. Most importantly, this is the first demonstration of PLGA-based hydrogels displaying such fibrous features. The pH responsiveness was the result of the helix-coil transition of PLGA and P(LGA-*co*-AG) polypeptides that takes place under mildly acidic conditions (pH ~ 5 to 6).

Fibrous structures being of great interest to tissue engineers, future work should include biocompatibility and cell growth assays.[5] The lyophilised organogels, which are highly porous and fibrous might be considered as aerogels for applications such as catalysis.[6] Concentrated P(BLG-*co*-AG)-dioxane organogels (100 g·L^{-1}) were birefringent, which implies that rather than a fibrous structure, the polypeptide helices in these gels are ordered in a liquid crystalline phase. Provided debenzylation is effective on such concentrated gels, the resulting hydrogels, or membranes, may be used as collagen-mimetic biocompatible templates for biomineralisation; for instance to generate bone mimics.[7] For optimal results, the concentrated gels might be pre-orientated through mechanical shear stress or under electric or magnetic fields.[8,9]

New Morphologies

Particles with highly regular spiral morphologies were obtained from PBLG- and P(BLG-*co*-AG)-toluene in water emulsions. A CD and Raman spectroscopic study demonstrated that the direction of these spirals was controlled by the chirality of the polypeptides. More specifically, PBLG and P(BLG-*co*-AG), which are composed of a majority of L residues and thus have a right-handed α-helical conformation, gave rise to particles exhibiting clockwise spirals. Vice-versa, PBDG and P(BDG-*co*-AG), which are composed of a majority of D residues and thus have a left-handed α-helical conformation, gave rise to particles exhibiting

counterclockwise spirals. The transmission of the chirality from a molecular level (*i.e.*, polypeptide) to higher hierarchical levels (*i.e.*, micron-sized particles), is as yet not fully understood. Literature and SEM evidence suggests that this process may occur *via* the existence of a chiral 'nano-twist' along the α-helix axis that is 'amplified' upon pseudo-hexagonal packing through LC phase crystallisation or fibre formation.

These morphologies provide a unique platform for the fundamental study and understanding of how conformational information at a nanoscale level can be transmitted to the micro-/macroscale through hierarchical organisation. Such systems might be used as models to reproduce or better understand natural systems such as actin filaments,[10] charophyte algae,[11] diatoms, or even naturally twisted collagen bundles.[12] Future work should aim to determine the process by which the chirality is transmitted to higher hierarchical levels with the help of CD and oriented Raman spectroscopy, WAXS and electron microscopy.

Ring Opening Polymerisation of NCA

The aforementioned polypeptides were synthesised by ROP of NCA with primary amine initiators in order to ensure that the polymerisation proceeds *via* the controlled pathway known as normal amine mechanism (NAM). Tertiary amines can be used to catalyse the ROP of NCA but the resulting polymerisation proceeds *via* the uncontrolled pathway known as activated monomer mechanism (AMM). It was shown that primary ammonium chlorides and primary amines could be combined with tertiary amines to initiate a controlled ROP of NCA, provided the molar fraction of tertiary amine was below a certain threshold (typically, < 1.5 equiv., relative to primary ammonium chlorides, and < 0.8 equiv. relative to primary amines). An extensive kinetic study by SEC and FTIR, complemented by NMR analyses, was used to produce time-conversion plots and to determine chain lengths and polydispersity indices (Đ) throughout the polymerisation reactions. The polymerisation rate could be controlled by the HCl to total amine ratio and the polymerisation could even be paused and resumed by altering this ratio during the reaction. These results, along with the time-conversion plot analysis, strongly suggest that both NAM and AMM contribute to the overall mechanism of this newly established primary ammonium/tertiary amine-mediated ROP of NCA, and also to the more traditional primary amine-initiated ROP of NCA (with or without the addition of a tertiary amine).

Future work should focus on the identification of the actual reactions kinetics and their parameters in order to confirm the proposed AMM-NAM-mixed mechanism. It is also worth stressing that the AMM pathway is known to favour stereospecificity[13] (*i.e.*, tacticity resulting from the copolymerisation of D and L monomers) as well as to be affected by the nucleophilicity of *N*-acylated NCA chain ends[14] (which may vary with the nature of the NCA). As such, the copolymerisation of NCAs by primary amine/tertiary amine-initiated ROP of NCA ought to be thoroughly investigated for different types of comonomers (*e.g.*, BLG-, BDG-, LAG-, DAG-, LLeu- and LPhe-NCAs), particularly in terms of the resulting polypeptide compositions and monomeric unit distributions (*e.g.*, random, periodic, gradient or block). If the resulting copolypeptides show some stereospecificity or an architecture that differs from true randomness, this new ROP method

may be used to generate 'pseudo-sequences', which may assist with the synthesis of new polypeptide hydrogelators, as mentioned earlier in this summary.

References

(1)   Kim, K. T.; Park, C.; Vandermeulen, G. W. M.; Rider, D. A.; Kim, C.; Winnik, M. A.; Manners, I. *Angew. Chemie Int. Ed.* **2005**, *44*, 7964–7968.

(2)   Higashi, D.; Yoshida, M.; Yamanaka, M. *Chem. - An Asian J.* **2013**, *8*, 2584–2587.

(3)   Mazzier, D.; Maran, M.; Polo Perucchin, O.; Crisma, M.; Zerbetto, M.; Causin, V.; Toniolo, C.; Moretto, A. *Macromolecules* **2014**, *47*, 7272–7283.

(4)   Besenius, P.; Portale, G.; Bomans, P. H. H.; Janssen, H. M.; Palmans, A. R. A.; Meijer, E. W. *Proc. Natl. Acad. Sci. U.S.A* **2010**, *107*, 17888–17893.

(5)   Jung, J. P.; Gasiorowski, J. Z.; Collier, J. H. *Biopolymers* **2010**, *94*, 49–59.

(6)   Nguyen, T.-T.-T.; Simon, F.-X.; Khan, N. A.; Schmutz, M.; Mésini, P. J. *J. Mater. Chem.* **2012**, *22*, 7712.

(7)   de Campos Vidal, B.; Silveira Mello, M. L. *Mater. Res.* **2001**, *4*, 169–173.

(8)   Inomata, K.; Iguchi, Y.; Mizutani, K.; Sugimoto, H.; Nakanishi, E. *ACS Macro Lett.* **2012**, *1*, 807–810.

(9)   Block, H. *Poly(gamma-benzyl-L-glutamate) and other glutamic acid containing polymers*; Gordon and Breach Science Publishers Ltd., **1983**.

(10)   Bidan, C. M.; Kollmannsberger, P.; Gering, V.; Ehrig, S.; Joly, P.; Petersen, A.; Vogel, V.; Fratzl, P.; Dunlop, J. W. C. *J. R. Soc. Interface* **2016**, *13*, 20160136.

(11)   Chassagne-Manoukian, M.; Haddoumi, H.; Cappetta, H.; Charrière, A.; Feist, M.; Tabuce, R.; Vianey-Liaud, M. *Geobios* **2013**, *46*, 371–379.

(12)   Grason, G. M. *Rev. Mod. Phys.* **2015**, *87*, 401–419.

(13)   Kricheldorf, H. R.; Mang, T. *Die Makromol. Chemie* **1981**, *182*, 3077–3098.

(14)   Kricheldorf, H. R.; Chemie, M. **1979**, *109*, 97–109.

Appendix A

Experimental Section

A.1   Materials

A.1.1.1   NCA Reagents

The amino acids γ-benzyl-L-glutamate (L-glutamic acid γ-benzyl ester) (BLG) (≥99%) and L-leucine (99.7%) were purchased from Sigma-Aldrich. The amino acids L- and DL-allylglycine (AG) (98%) were purchased from BoaoPharma. The amino acid γ-benzyl-D-glutamate (5-benzyl D-glutamate) (BDG) (>98%) was purchased from TCI Chemicals. The amino acid L-phenylalanine (≥99%) was purchased from Alfa Aesar. Triphosgene (98%) and α-pinene (98%) were purchased from Sigma-Aldrich.

A.1.1.2   Solvents and Solutions

Anhydrous N,N-dimethylformamide (DMF) (99.8%), anhydrous 1,4-dioxane (99.8%), deuterated chloroform (CDCl$_3$) (99.96 atom % D), deuterated dimethyl sulfoxide (DMSO-d$_6$) (99.9 atom % D), acetone (99.9%) and deuterium oxide (D$_2$O) (99.9 atom % D) were purchased from Sigma-Aldrich. Anhydrous toluene (99.85%), anhydrous ethanol (99.5%), anhydrous tetrahydrofuran (THF) (99.5%), dichloromethane (DCM) (99.5%), 1,1,1,3,3,3-hexafluoro-2-propanol (HFIP) (99.9%) and deuterated 1,1,1-trifluoroacetic acid (TFA-d) (99.5 atom % D) were purchased from Acros Organics. Deuterated toluene (toluene-d$_8$) (99.5 atom % D) was purchased from VWR. 1,1,1-Trifluoroacetic acid (TFA) (≥99.9%) and N-Methyl-2-pyrrolidone (NMP) (99.97%) were purchased from Roth. Buffer solutions pH 4 (citric acid/sodium hydroxide/hydrogen chloride) and pH 10 (boric acid/potassium chloride/sodium hydroxide) were purchased from Merck.

A.1.1.3   Other Reagents and Standards

1-Hexylamine (HexA) (99%), benzylamine (BnA) (99%), hexamethylenediamine (HexDA) (98%), acetic anhydride (Ac$_2$O) (99%), maleic anhydride (MalO) (99%), 1-pyrenemethylamine hydrochloride (PyA·HCl)

(95%), 1-pyrenemethanol (PyOH) (98%), 18-crown-6 (≥99%), 1,2,3-tris(bromomethyl)benzene, hydrazine hydrate (50-60%), phtalamide potassium salt (98%), heptadecafluoroundecanoyl chloride (HepdF-COCl) (≥97%), N,N-diisopropylethylamine (DIPEA) (99.5%), benzophenone (99%), Michler's ketone (98%), 1,9-nonanedithiol (95%), hydrobromic acid (HBr) (33% in acetic acid), methanesulfonic acid (MSA) (99.5%), butylated hydroxytoluene (BHT) (≥99%) and PSS polystyrene standards (PS2M and PS4M) were purchased from Sigma-Aldrich. Fuming hydrochloric acid (HCl) (32%) was purchased from Roth. Triethylamine (TEA) (99%) was purchased from Acros Organics.

A.2 Synthesis

All relevant NMR spectra are available in Appendix B.

A.2.1 NCAs

A.2.1.1 γ-Benzyl-L-glutamate NCA (BLG-NCA) and γ-Benzyl-D-glutamate NCA (BDG-NCA)

Typically, 7.5 g (1 equiv.) of D- or L-glutamic acid γ-benzyl ester was placed in a flame-dried and nitrogen-purged round bottom flask. It was dried under high vacuum for 12 hours and dissolved in 150 mL dry THF. Under vigorous stirring, triphosgene (3.75 g, 0.4 equiv.) was added and the mixture was heated to 50 °C for 3 h, or at least 1 h after the mixture has become completely translucent (yellowish). The mixture was reduced to about 20 mL under reduced pressure and precipitated in 200 mL re-distilled heptanes under inert atmosphere. The precipitate was filtered, washed with heptanes, and dried under high vacuum for 1 h. It was then re-dissolved in 20 mL of anhydrous THF, precipitated, filtered, washed and dried for at least 12 h. Recrystallisation was not performed but could be effective using dioxane and ethyl acetate (1:1). The NCAs were then stored under inert atmosphere at -25 °C.

Yield = 94%

Melting point = 93-94 °C

^{1}H-NMR (CDCl$_3$, 300 MHz): δ (ppm) 7.42-7.21 (m, 5H), 6.72 (s, 1H), 5.13 (s, 2H), 4.38 (t, J = 6.0 Hz, 1H), 2.59 (t, J = 6.9 Hz, 2H), 2.34-2.01 (m, 2H)

^{13}C-NMR (CDCl$_3$, 75 MHz): δ (ppm) 172.4, 169.4, 152.0, 135.2, 128.7, 128.6, 128.3, 67.1, 56.9, 29.8, 26.9

A.2.1.2 L-Allylglycine NCA (LAG-NCA) and DL-Allylglycine NCA (DLAG-NCA)

The procedure used to synthesise L or DLAG-NCA was identical to the one used for BLG-NCA (above), with the exception that α-pinene (4 equiv. relative to AG amino acid) was added to the reaction mixture prior to adding triphosgene.

Yield = 61%

Melting point (LAG-NCA) = 43-45 °C; melting point (DLAG-NCA) = 89-91 °C

^{1}H-NMR (CDCl$_3$, 300 MHz): δ (ppm) 6.75 (s, 1H), 5.74 (ddt, J = 10.3, 7.6, 7.1 Hz, 1H), 5.35-5.17 (m, 2H), 4.40 (dd, J = 7.1, 4.5 Hz, 1H), 2.80-2.42 (m, 2H)

^{13}C-NMR (CDCl$_3$, 75 MHz): δ (ppm) 169.1, 152.8, 130.0, 121.5, 57.4, 35.8

A.2.1.3   L-Leucine NCA (LLeu-NCA)

The procedure used to synthesise LLeu-NCA was identical to the one used for B$_L$G-NCA (above), with the exception that 8.55 g (0.5 equiv.) of triphosgene was used for 7.5 g (1 equiv.) of L-leucine.

Yield = 79%

Melting point = 76-78 °C

^{1}H-NMR (CDCl$_3$, 300 MHz): δ (ppm) 7.09 (s, 1H), 4.35 (dd, J = 8.8, 3.9 Hz, 1H), 1.94-1.58 (m, 3H), 0.98 (t, J = 6.2 Hz, 6H)

^{13}C-NMR (CDCl$_3$, 75 MHz): δ (ppm) 170.1, 153.2, 56.3, 40.9, 25.1, 22.8, 21.6

A.2.1.4   L-Phenylalanine NCA (LPhe-NCA)

The procedure used to synthesise LPhe-NCA was identical to the one used for B$_L$G-NCA (above), with the exception that 4.5 g (0.5 equiv.) of triphosgene was used for 5 g (1 equiv.) of L-Phenylalanine.

Yield = 83%

Melting point = 90-91 °C

^{1}H-NMR (CDCl$_3$, 300 MHz): δ (ppm) 7.39-7.12 (m, 5H), 6.51 (s, 1H), 4.53 (dd, J = 7.4, 4.3 Hz, 1H), 3.24 (dd, J = 14.1, 4.2 Hz, 1H), 3.01 (dd, J = 14.1, 7.6 Hz, 1H)

^{13}C-NMR (CDCl$_3$, 75 MHz): δ (ppm) 169.0, 152.3, 134.0, 129.4, 129.3, 128.0, 59.0, 37.8

A.2.2   Initiators

A.2.2.1   Benzylamine Hydrochloride (BnA·HCl)

3 mL of BnA (1 equiv.) was dissolved in 7 mL of DCM. Under vigorous stirring, 3 mL of fuming HCl (12.1 N) (1.1 equiv.) was added dropwise. The precipitate was filtered, washed with DCM and recrystallised from a minimum of dry ethanol to yield pearly-white needles. The latter were dried under high vacuum for 24 h.

Yield: 85%

^{1}H-NMR (DMSO-d$_6$, 600 MHz): δ (ppm) 8.64 (s, 3H), 7.37-7.53 (m, 5H), 3.99 (s, 2H)

^{13}C-NMR (DMSO-d$_6$, 151 MHz): δ (ppm) 134.31, 129.16, 128.69, 128.52, 42.25

A.2.2.2   1,2,3-Tris(aminomethyl)benzene Trihydrochloride (TAB·3HCl)

The synthesis of TAB·3HCl was based on an adapted procedure from Grawe et al.[1] and Mitchell et al.[2].
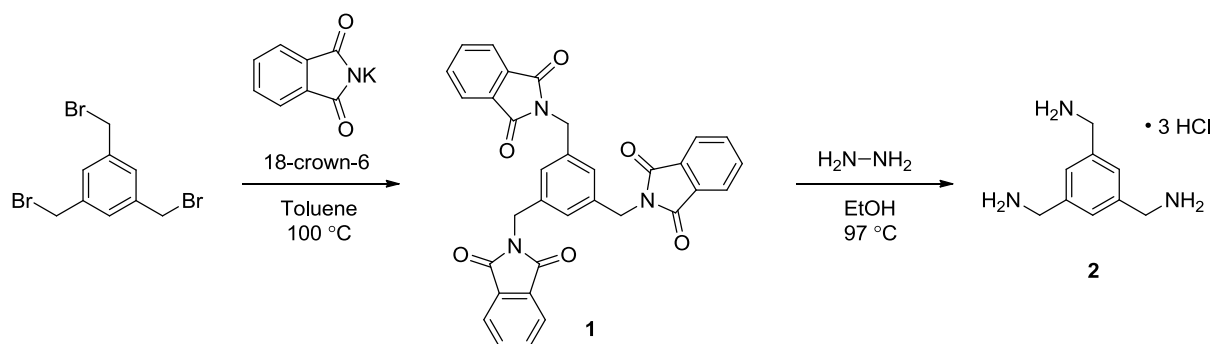
I.   Synthesis of Intermediate Product (**1**)

1,2,3-Tris(bromomethyl)benzene (3.50 g, 1 equiv.), phtalamide potassium (6.54 g, 3.6 equiv.) and 18-crown-6 (0.78 g, 0.3 equiv.) were suspended in 45 mL of toluene in a flame-dried and nitrogen-purged round bottom flask. The mixture was refluxed for 24 h at 100 °C. 40 mL of distilled water was added and the mixture was allowed to phase separate. The aqueous layer was pipetted out and extracted 3 times with DCM. The organic layers were collected and dried over $MgSO_4$, filtered, and evaporated to dryness under reduced pressure. The residue was re-dissolved in a minimum of DCM under moderate heat and purified by column chromatography using a DCM/acetone (20:1) eluent.

*R_f(**1**) = 0.6*

Yield: 75 %

^{1}H-NMR (CDCl$_3$, 300 MHz): δ (ppm) 7.70-7.82 (m, 12H), 7.35 (s, 3H), 4.78 (s, 6H)

^{13}C-NMR (CDCl$_3$, 75 MHz): δ (ppm) 167.99, 137.44, 134.06, 132.22, 127.95, 123.52, 41.34

II.   Synthesis of TAB·3HCl (**2**)

The purest fractions containing **1** were collected and evaporated to dryness under reduced pressure. **1** (1.16 g, 1 equiv.) was then slurried with 70 mL of dry ethanol into a flame-dried and nitrogen-purged flask. Under vigorous stirring, 0.8 mL of hydrazine (6 equiv.) was added dropwise. The mixture was refluxed for 16 h at 97 °C. 3.5 mL of distilled water was then added. The mixture was then acidified with fuming HCl (12.1 N) down to pH ~ 3. The precipitate was filtered, washed with ethanol/water (95:5, pH ~ 3), and the filtrates were collected and evaporated to dryness under reduced pressure. The residue was slurried in acidic water, filtered, washed with ethanol/water (95:5, pH ~ 3), and the filtrate was evaporated again. The residue was recrystallised from dioxane/water (20:1).

Yield: 38 %

^{1}H-NMR (D$_2$O, 300 MHz): δ (ppm) 7.58 (s, 3H), 4.28 (s, 6H)

^{13}C-NMR (CDCl$_3$,75 MHz): δ (ppm) 134.97, 130.39, 42.88

A.2.3   Polypeptides

A.2.3.1   Primary Amine-Initiated Polymerisations

PBLG, PLLeu, PLPhe and copolymers of BLG and AG were synthesised by polymerisation of α-amino acid *N*-carboxyanhydride (NCA) monomers. Typically (*e.g.*, sample P(BLG$_{0.80}$-*co*-LAG$_{0.20}$)$_{219}$), BLG-NCA (1.25 g, 4.75 mmol, n·x equiv.) and AG-NCA (0.168 g, 1.2 mmol, n·(1-x) equiv.), were dried under high vacuum for 1 hour and dissolved in 40 mL of dry DMF (typical concentration ranges between 60 and 120 g·L^{-1}) under inert atmosphere in a flame-dried flask. The mixture was cooled down in ice for 20 min and the initiator solution (0.1 M 1-hexylamine in DMF, 0.4 mL, 0.04 mmol, 1 equiv.) was added. The reaction medium was then evacuated (1 mbar) after 1 hour and stirred at room temperature for 3-5 days. Polymerisation was terminated by addition of acetic or maleic anhydride (> 50·n equiv), stirred for another 20 min and then precipitated in cold methanol. The product was collected by centrifugation (9000 rpm, 5 min), re-precipitated (in methanol or diethyl ether), washed, dried under high vacuum for 12 h, and freeze-dried (*i.e.*, lyophilised) from 1,4-dioxane. It was found that impurities (*e.g.*, terminating agent excess, solvent stabilisers, technical grade solvents impurities) had a tendency to accumulate in polypeptides; for this reason, an additional dialysis step (in THF) was sometimes performed prior to lyophilising.

The solubility of PLLeu and PLPhe polymers in DMF was relatively poor. The turbidity of the polymerisation medium increased with increasing degree of polymerisation. In order to maintain the polymerisation homogeneous, an alternative solvent mixture of Chloroform (2 parts) and DMF (1 part) was found to improve the solubility of the polymers.

Typical Yields > 80%

See section A.2.3.4 for chemical shifts.

A.2.3.2   Primary Ammonium/Tertiary Amine-mediated Polymerisations (Chapter III)

The procedure used for polymerisations initiated by a mixture of primary ammonium chloride and tertiary amine was identical to the one used for primary amine-initiated polymerisations (Section A.2.3.1). The initiator solution consisted of a primary ammonium chloride (typically, 0.02 to 0.2 M) and a tertiary amine (typically, 0.2 to 1.5 equiv. relative to primary ammonium species, *i.e.*, 0.005 to 0.3 M) dissolved in DMF (unless otherwise mentioned, see Section B.3). Not being soluble in DMF, the primary ammonium chloride TAB·3HCl was dissolved in DMSO instead. A polymerisation control, comparing PyA·HCl in DMSO and PyA·HCl in DMF as initiator solutions, showed that the introduction of a small amount of DMSO in the polymerisation medium had little effect of the polymerisation outcome (Appendix B, P37 and P39).

Typical Yields > 70%

See section A.2.3.4 for chemical shifts.

A.2.3.3   Debenzylation

The deprotection procedure varies with the type of polypeptide. Anisole and MSA were added to a solution of P(BLG-*co*-AG) in TFA (100 g·L^{-1}), such that the final TFA/anisole/MSA volume ratio of 45:10:45 was achieved (deprotection route A). HBr was added to a solution of PBLG in TFA (100 g·L^{-1}), such that the final TFA/HBr ratio of 75:25 was achieved (deprotection route B). The mixtures were stirred in ice for 30 min and then at room temperature for another 30 min. The polymers were precipitated in diethyl ether, collected by centrifugation (9000 rpm, 5 min), dissolved in a NaHCO$_3$-saturated aqueous solution to get rid of the excess of acid for 12 h, dialysed against distilled water for 48 h, and freeze-dried.

Typical Yields > 70%

See section A.2.3.4 for chemical shifts.

A.2.3.4   Chemical Shifts of Polypeptides

The chemical shifts of the synthesised polypeptides typically vary depending on the composition and type of initiator or terminating agent (see Appendix B for supporting data). A comprehensive list is provided hereafter:

- *PBLG$_{51}$ (P1): ^{1}H NMR (TFA-d, 400 MHz): δ (ppm) 7.26-7.24 (br, 255H), 5.60-5.13 (br, 102H), 4.69-4.66 (br, 51H), 3.29 (br, 2H), 2.58-1.94 (br, 593H), 1.53-1.50 (br, 2H), 1.36-1.34 (br, 6H), 0.86-0.83 (br, 3H)*

- *PLG$_{51}$ (P1-D): ^{1}H NMR (TFA-d, 400 MHz): δ (ppm) 4.53-4.25 (br, 51H), 3.34-3.14 (br, 2H), 2.58-1.85 (br, 204H), 1.57-1.47 (br, 2H), 1.38-1.21 (br, 6H), 0.94-0.82 (br, 3H)*

- *P(BLG$_{0.76}$-co-DLAG$_{0.24}$)$_{59}$ (P2): ^{1}H NMR (TFA-d, 400 MHz): δ (ppm) 7.28-7.26 (br, 225H), 5.62 (br, 14H), 5.19-5.06 (br, 118H), 4.74-4.57 (br, 59H), 3.29 (br, 2H), 2.57-1.98 (br, 211H), 1.54-1.51 (br, 2H), 1.36-1.28 (br, 6H), 0.88-0.85 (br, 3H)*

- *P(LG$_{0.76}$-co-DLAG$_{0.24}$)$_{58}$ (P2-D): ^{1}H NMR (TFA-d, 400 MHz): δ (ppm) 5.86-5.66 (br, 14H), 5.28-5.06 (br, 28H), 4.54-4.19 (br, 58H), 3.27-3.09 (br, 2H), 2.68-1.78 (br, 207H), 1.57-1.40 (br, 2H), 1.33-1.14 (br, 6H), 0.90-0.80 (br, 3H)*

- *P(BLG$_{0.77}$-co-LAG$_{0.23}$)$_{57}$ (P3): ^{1}H NMR (TFA-d, 400 MHz): δ (ppm) 7.29-7.27 (br, 220H), 5.60 (br, 13H), 5.19-5.06 (br, 114H), 4.74-4.57 (br, 57H), 3.30 (br, 2H), 2.59-1.99 (br, 205H), 1.55-1.51 (br, 2H), 1.37-1.28 (br, 6H), 0.88-0.85 (br, 3H)*

- *P(BLG$_{0.89}$-co-DLAG$_{0.11}$)$_{53}$ (P4): ^{1}H NMR (TFA-d, 400 MHz): δ (ppm) 7.25-7.23 (br, 235H), 5.59 (br, 6H), 5.16-5.02 (br, 106H), 4.71-4.53 (br, 53H), 3.27 (br, 2H), 2.53-1.94 (br, 203H), 1.51-1.48 (br, 2H), 1.33-1.25 (br, 6H), 0.85-0.82 (br, 3H)*

- *P(BLG$_{0.74}$-co-LAG$_{0.26}$)$_{170}$ (P12): ^{1}H NMR (TFA-d, 400 MHz): δ (ppm) 7.20 (br, 625H), 5.54 (br, 45H), 5.14-5.00 (br, 340H), 4.70-4.50 (br, 170H), 3.23 (br, 2H), 2.51-1.93 (br, 593H), 1.53-1.47 (br, 2H), 1.34-1.22 (br, 6H), 0.80 (br, 3H)*

- $P(BLG_{0.80}\text{-}co\text{-}LAG_{0.20})_{219}$ (P13): ^1H NMR (TFA-d, 400 MHz): δ (ppm) 7.20 (br, 875H), 5.54 (br, 44H), 5.14-5.00 (br, 438H), 4.70-4.50 (br, 219H), 3.23 (br, 2H), 2.51-1.93 (br, 791H), 1.53-1.47 (br, 2H), 1.34-1.22 (br, 6H), 0.80 (br, 3H)

- $P(BLG_{0.84}\text{-}co\text{-}LAG_{0.16})_{171}$ (P14): ^1H NMR (TFA-d, 400 MHz): δ (ppm) 7.20 (br, 715H), 5.54 (br, 28H), 5.14-5.00 (br, 342H), 4.70-4.50 (br, 171H), 3.23 (br, 2H), 2.51-1.93 (br, 631H), 1.53-1.47 (br, 2H), 1.34-1.22 (br, 6H), 0.80 (br, 3H)

- $P(BLG_{0.74}\text{-}co\text{-}LAG_{0.26})_{91}$ (P15): ^1H NMR (TFA-d, 400 MHz): δ (ppm) 7.22 (br, 335H), 5.56 (br, 24H), 5.15-5.02 (br, 182H), 4.73-4.52 (br, 91H), 3.23 (br, 2H), 2.55-1.94 (br, 319H), 1.54-1.48 (br, 2H), 1.33-1.23 (br, 6H), 0.81 (br, 3H)

- $P(BLG_{0.78}\text{-}co\text{-}LAG_{0.22})_{96}$ (P16): ^1H NMR (TFA-d, 400 MHz): δ (ppm) 7.20 (br, 375H), 5.54 (br, 21H), 5.14-5.00 (br, 192H), 4.70-4.50 (br, 96H), 3.23 (br, 2H), 2.51-1.93 (br, 345H), 1.53-1.47 (br, 2H), 1.34-1.22 (br, 6H), 0.80 (br, 3H)

- "star"-$(PBLG_{15})_2$ (P18B): ^1H NMR (TFA-d, 400 MHz): δ (ppm) 7.44-7.03 (br, 155H), 5.25-4.96 (br, 62H), 4.77-4.55 (br, 31H), 3.35-3.14 (br, 4H), 2.69-1.81 (br, 130H), 1.57-1.43 (br, 4H), 1.40-1.20 (br, 4H)

- star-$(PBLG_{40})_3$ (P36): ^1H NMR (TFA-d, 600 MHz): δ (ppm) 7.31-7.08 (br, 303H), 6.45 (d, J = 12.6 Hz, 3H), 6.32 (d, J = 12.6 Hz, 3H), 5.20-4.88 (br, 120H), 4.72-454 (br, 60H), 4.42 (d, J = 15.4 Hz, 3H), 4.20 (d, J = 14.9 Hz, 3H), 2.60-1.80 (br, 240H)

- star-$(PLG_{43})_3$ (P49-D): ^1H NMR (TFA-d, 600 MHz): δ (ppm) 7.10 (s, 3H), 6.34 (d, J = 12.3 Hz, 3H), 5.97 (d, J = 12.2 Hz, 3H), 4.48 (d, J = 14.1 Hz, 3H), 4.35-4.20 (br, 129H), 2.39-1.76 (br, 516H)

- star-$(P(LG_{0.93}\text{-}co\text{-}LAG_{0.07})_{39})_3$ (P52-D): ^1H NMR (TFA-d, 600 MHz): δ (ppm) 7.10 (s, 3H), 6.33 (d, J = 12.3 Hz, 3H), 5.97 (d, J = 12.2 Hz, 3H), 5.81-5.65 (br, 8H), 5.20-5.05 (br, 16H), 4.50 (d, J = 13.7 Hz, 3H), 4.45-4.10 (br, 117H), 2.60-1.77 (br, 452H)

A.2.4 Microscale Chemistry

The large number of experiments performed in order to produce conclusive results required that both polymerisations and gel samples be scaled down, in order to minimise costs and reduce waste. This resulted in the need to work with extremely small volumes and masses, especially in regard to low concentration gels, and initiator, catalyst, crosslinker and internal standard solutions. The strategies used to remain as accurate and precise as possible are described hereafter. Stock solutions were prepared and used whenever possible. Liquid reagents that had to remain dry, such as initiator and catalyst were weighed by precision balance in purged flasks using purged 1 mL syringes and using narrow needles in order to allow for dropwise feed. Volumes of 0.05 to 1 mL were handled with 1 mL syringes. Volumes < 0.05 mL were handled with precision syringes (Hamilton or NanoFil, glass body, PTFE joints) or with micropipettes (with a pre-calibration for each type of solvent). Solid samples of > 10 mg were weighed by precision scale; for samples < 10 mg, stock solutions were used instead.

A.3 Analytical Instrumentation and Methods

A.3.1 Nuclear Magnetic Resonance

Proton and carbon nuclear magnetic resonance (^{1}H-NMR and ^{13}C-NMR, respectively) spectra of small compounds (*e.g.*, NCAs, initiators) were recorded on a Bruker Avance 300 MHz spectrometer (at 300 MHz and 75 MHz, respectively) or on a Bruker DPX-400 spectrometer (at 400 MHz and 100 MHz, respectively). Unless mentioned otherwise the number of scans was 128 for ^{1}H-NMR and 1024 for ^{13}C-NMR.

^{1}H-NMR spectra of the P1 to P18 polypeptides series were recorded on a Bruker DPX-400 spectrometer (at 400 MHz); the line broadening (lb) value was set to 1.0, the number of scans was at least 128, and the acquisition time was set to 2 s.

^{1}H-NMR, ^{13}C-NMR and HSQC spectra of the P18 to P63 polypeptides series were recorded on a Bruker Avance III 600 MHz spectrometer (at 600 MHz and 151 MHz, respectively); the number of scans was at least 32 for ^{1}H-NMR and 256 for ^{13}C-NMR, and the acquisition time was set to 3 s.

The ^{19}F-NMR spectrum of P18A in THF-d_8 was recorded on a Varian spectrometer (at 376 MHz) in [1]H-non-decoupled mode.

For the ^{13}C and ^{1}H experiments, the polypeptides were analysed in TFA-d, and the NCAs in CDCl$_3$.

A.3.2 Temperature Sweep ^{1}H-NMR (Chapter IV)

A Bruker Avance 500 MHz spectrometer was used for the acquisition of ^{1}H-NMR spectra for the gelation experiments in deuterated toluene (toluene-d_8); the number of scans was 32, and the acquisition time was set to 6 s. Solutions of polypeptides (20 g·L^{-1}) were initially measured at 40 °C and the temperature was gradually decreased by steps of 5 °C, down to -40 °C for P(BLG$_x$-*co*-AG$_{1-x}$)$_n$ copolypeptides and down to 0 °C for PBLG$_{51}$. For each temperature, the sample temperature was allowed to equalise for 5 min before the measurement was performed. The spectra of all temperature sweep measurements are in Appendix B.

A.3.3 Circular Dichroism Spectroscopy

Circular dichroism (CD) spectra were recorded on a JASCO J-715 spectrometer. Aqueous polypeptide solutions were prepared with Millipore water and their concentration was ~ 0.2 g·L^{-1}. Organic polypeptide solutions were prepared with HFIP and their concentration was ~ 0.05 g·L^{-1}.

The results were expressed as molar ellipticity ([θ] in mdeg) or as its normalised equivalent, mean residue ellipticity ([θ]$_{MRE}$ in deg·cm^2·dmol^{-1}) as a function of the wavelength (nm). [θ]$_{MRE}$ was normalised to the concentration of chiral species (*i.e.*, total concentration of monomeric residues in mol·L^{-1}) and to the cuvette width (2 mm).

A.3.4   Scanning Electron Microscopy

Scanning electron microscopy (SEM) images were taken with a Leo 1550 Gemini (Carl Zeiss AG, Germany) microscope operating at 5 to 10 kV. The samples were loaded on carbon-coated stubs and sputtered with gold palladium alloy prior to imaging.

A.3.5   Transmission Electron Microscopy (Chapter V)

Transmission electron microscopy (TEM) was performed on a EM 912 Omega microscope (Zeiss AG) operating at an accelerating voltage of 120 kV. The TEM gel samples were prepared by dabbing 200 mesh carbon-coated copper grids onto the gels and leaving the grids to dry under laminar air flow.

A.3.6   Atomic Force Microscopy

Atomic Force Microscopy (AFM) was performed on thin polypeptide and collagen films. The latter were scanned using a Nano Surfaces atomic force microscopy from Bruker operating at a scanning speed of 0.6 Hz, an amplitude set point range of 300 to 420 mV, an integral gain range of 0.5 to 6 and a proportional gain range of 5 to 60.

A.3.7   Size Exclusion Chromatography

Size exclusion chromatography (SEC), also known as gel permeation chromatography (GPC), with simultaneous UV and RI detection was performed in a solution of NMP with LiBr (0.5 wt%) at a flow rate of 0.8 mL·min^{-1} at 70 °C, on two 300 x 8 mm^2 PSS-GRAM columns (7 µm particle size, 100 and 1000 Å porosity). Poly(methyl methacrylate) (PMMA) standards (PSS, Mainz, Germany; M_p from 505 to 898,000 g·mol^{-1}) were used for calibration. The UV detector was set to measure UV absorptions taking place at 270 nm (*e.g.*, compounds containing benzyl functions) for most measurements. For the polymers initiated by a pyrene-containing initiator, the detector was set to 340 nm, a wavelength at which pyrene absorbs, but not benzyl groups.

SEC in water was performed with a 0.1 M aqueous solution of NaNO$_3$, at a flow rate of 0.8 mL·min^{-1}, on two PSS-Suprema columns 300 x 8 mm^2 (10 µm particle sizes, 30 and 3000 Å porosity). Poly(ethylene oxide) (PEO) standards (PSS, Mainz, Germany; M_p from 238 to 969,000 g·mol^{-1}) were used for calibration.

The samples were dissolved in the eluent solution (1.5 to 3.5 g·L^{-1}) and filtered (0.45 µm filters) prior to being injected on the column (100 µL per injection).

A.3.8   Polymerisation Kinetics Followed by SEC (Chapter III)

In the kinetics studies reported in chapter III, a large polystyrene (PS2M) was used as the internal standard to measure the polymerisation conversions. Other internal standards can also be used, such as smaller species, like BHT, or even larger polymers, like PS4M (Figure A.1). The advantage of BHT and polystyrene as internal standard for SEC measurements is their strong absorption in the UV range.
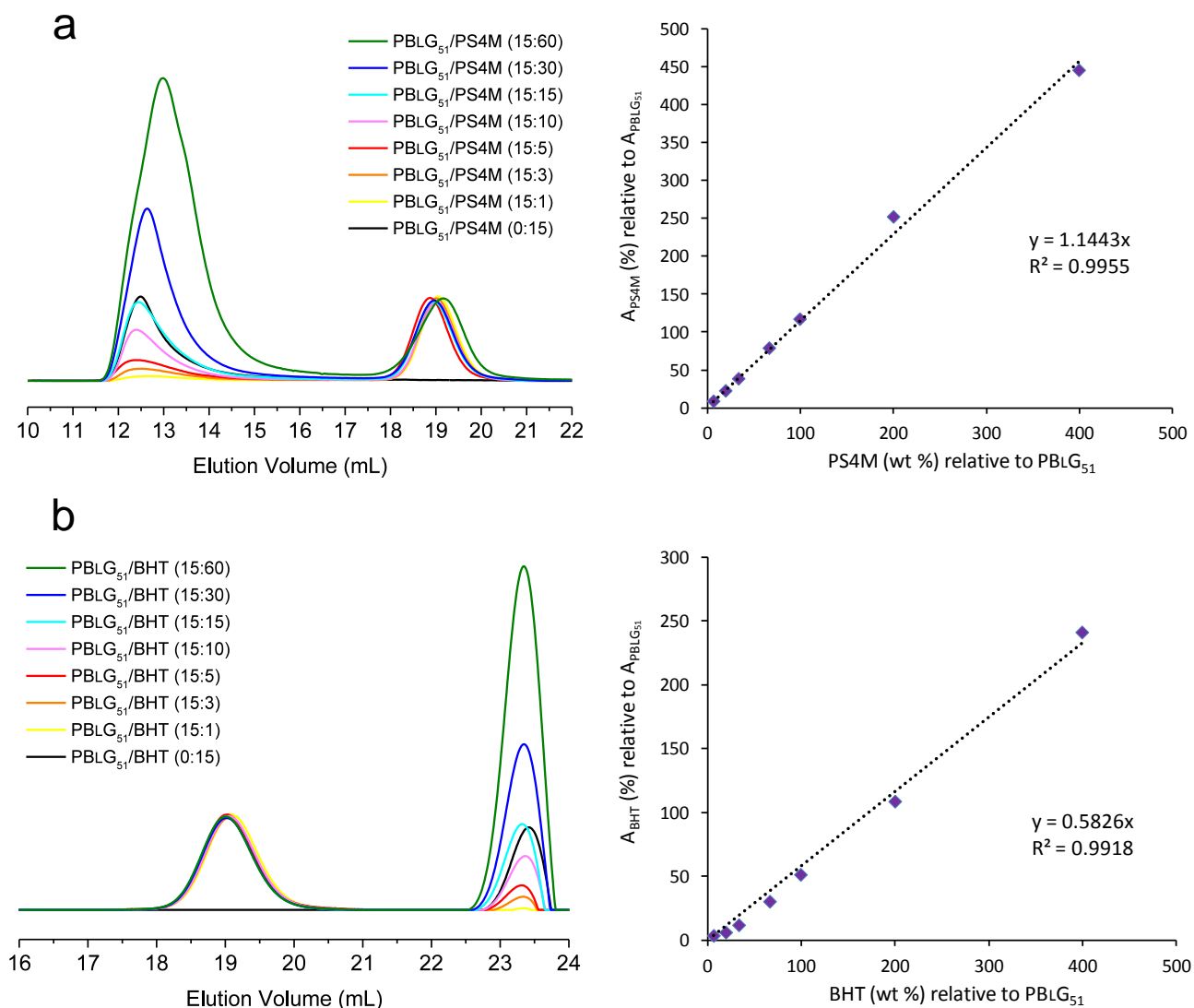
Figure A.1 (a) PBLG$_{51}$/PS4M and (b) PBLG$_{51}$/BHT calibration series: (left) SEC traces (RI signal) with PBLG$_{51}$/standard weight ratios in bracket, (right) calibration curve where the internal standard ((a) PS4M and (b) BHT) to PBLG$_{51}$ ratio of the areas under the elution peaks are plotted as a function of the measured internal standard ((a) PS4M and (b) BHT) to PBLG$_{51}$ weight ratios.

A.3.9 Attenuated Total Reflectance Fourier Transform Infrared Spectroscopy

Attenuated total reflectance Fourier transform infrared (ATR-FTIR) spectroscopy, sometimes simply referred to as FTIR in the present study, was performed on a Bruker Vertex 70 fitted with PLATINUM ATR. Liquid samples were placed directly on the ATR diamond under a mixture of dry air and nitrogen flow. Solid samples were mechanically pressed against the ATR diamond using the apparatus lever. The spectra were acquired and processed with OPUS. Unless otherwise mentioned, the number of scans was 32, the built-in atmospheric correction function was turned on, and the background was automatically subtracted; in the case of liquid samples, the background was the solvent used for the sample.

The spectra were they processed as follows: portions of interest (*e.g.*, 1758-1815 cm^{-1}) of the spectra were isolated ('cut' function), baseline corrected ('concave rubberband correction', 1 to 3 iteration), and fitted with Gaussian functions ('curve fit' function). For kinetic studies, the areas under the

peaks of interest were extracted to calculate monomer conversions. For secondary structure studies, normalisation to a reference peak was applied.

A.3.10 Polymerisation Kinetics Followed by ATR-FTIR (Chapter III)

At regular interval during polymerisation reactions, the monomer (NCA) conversion was measured by sampling ~ 0.05 mL of reaction medium using nitrogen-purged 1mL syringes and placing the sample directly onto the ATR diamond in a nitrogen-purged chamber of the FTIR apparatus. To minimise the exposure of polymerisation samples to the moisture in the atmosphere, the number of scans used was 16 for all samples and calibration solutions. The conversion was measured from the area under a characteristic NCA peak (see Section III.2.2.2). Calibration curves were used order to accurately calculate NCA concentrations from the absorbance peaks at 1785-1790 cm^{-1} that corresponds to the vibrational energy of the (N-)C=O stretch within NCA. The calibration curves for LLeu-NCA and LPhe-NCA are given in Figure A.2, and the one for BLG-NCA is given in Figure III.3.
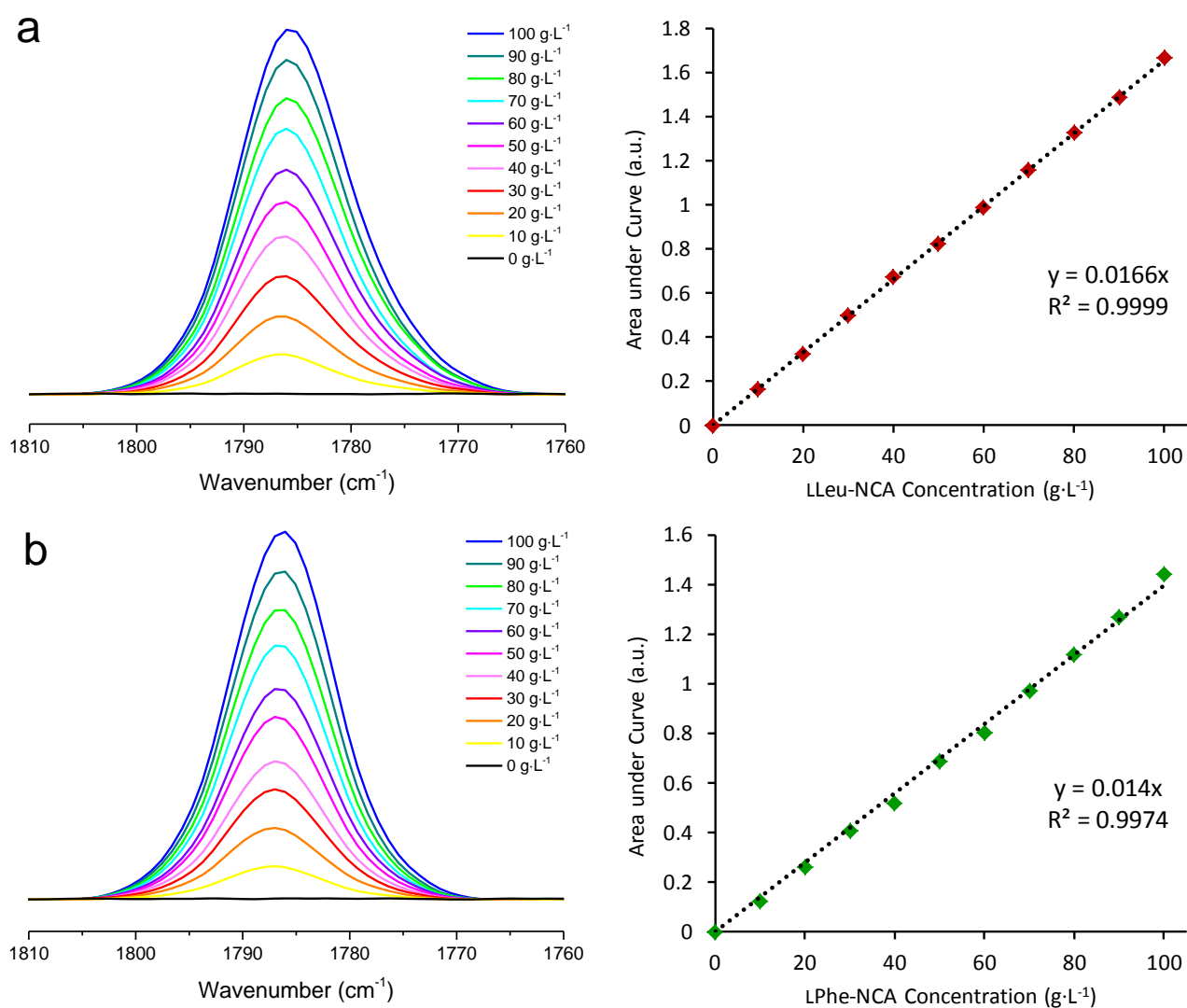
Figure A.2 FTIR calibration series for (a) LLeu-NCA and (b) LPhe-NCA: (left) FTIR absorbance peaks corresponding to NCA (N-)C=O stretch; (right) calibration curve where the area under the 1785-1790 cm^{-1} peaks is plotted as a function of the measured NCA concentrations.

A.3.11   Raman Spectroscopy

Raman spectroscopy was performed on a UHTS 300 (WITec, Ulm, Germany) equipped with a Nd:YAG laser (λ = 532 nm) and a piezoscanner (P-500, Physik Instrumente, Karlsruhe, Germany). The spectra were acquired with a CCD detector (DU401-BV, Andor, Belfast, UK) placed behind a grating spectrograph (1800 groves per mm, UHTS 300, WITec, Ulm, Germany). The laser beam was focused through a 10× (Nikon, NA = 0.2) microscope objective. ScanCtrlSpectroscopyPlus software (version 1.38, Witec) was used for the measurement and OPUS 7.0 for the spectra processing. The 1703-1592 cm^{-1} portion of the spectra was isolated ('cut' function), baseline corrected ('concave rubberband correction', 2 iterations), smoothed ('smooth' function, number of smoothing point 9), normalised and fitted with Gaussian functions ('curve fit' function, Levenberg-Maquardt algorithm).

The analysed polymers were mechanically compacted, a technique which was found to reduce noise and improving spectral quality (Figure A.3), probably as the result of an increase in the 'concentration' or density of polymer chains within the laser path.
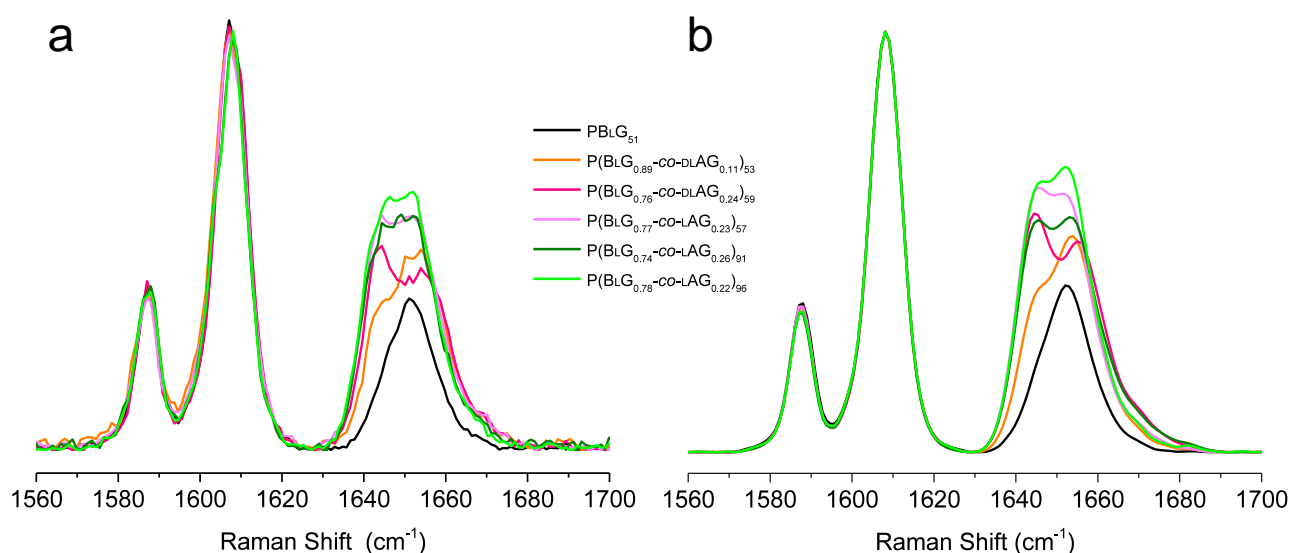
Figure A.3 Amide I band of dry PBLG and P(BLG$_x$-co-AG$_{1-x}$)$_n$ copolypeptides: (a) non compacted, and (b) compacted and showing an improved signal-to-noise ratio.

A.3.12   Wide-Angle X-Ray Scattering

Wide angle X-ray scattering (WAXS) was performed on a Nanostar X-ray diffractometer (Bruker AXS) operating at 40 kV and 35 mA (Cu Kα radiation, λ = 1.5418 Å). Dry polymer samples were placed in sealed borosilicate glass capillaries (about 1.5 mm diameter), normal to the X-ray beam path. The sample to detector distances used for this study were approximately 4 and 8 cm (intrinsic 2θ error of 0.08°). The beam centre and exact distance were calculated using a corundum standard. The scattering patterns were collected during 7200 s of exposure time per sample and recorded by a position sensitive area 2D detector (HI-STAR, Bruker AXS, Karlsruhe, Germany). The 2D patterns were then integrated using Bruker AXS SAXS-offline software (V4.1.16).

A.3.13 Differential Scanning Calorimetry (Chapter IV)

Differential scanning calorimetry (DSC) measurements were performed with a Mettler Toledo DSC1/TC100. Polypeptide-toluene gel samples (20 to 50 $g \cdot L^{-1}$) were placed in sealed aluminium crucibles and loaded in the DSC apparatus. The programs generally consisted of a ramp from room temperature to 60 °C, a 2 min isotherm at 60 °C, a ramp from 60 to -40 °C, a 2 min isotherm at -40 °C, and a ramp from -40 to 60 °C. The heating and cooling rates were either (-)5 or (-)10 $K \cdot min^{-1}$. Depending on the aim of the measurement an additional quenching ramp, from 60 to -40 °C at a cooling rate of -40 $°C \cdot min^{-1}$, followed by a normal heating ramp of -40 to 60 °C (to measure the effect of a fast cooling) could be added to the program.

A.4 References

(1)   Grawe, T.; Schrader, T.; Zadmard, R.; Kraft, A. *J. Org. Chem.* **2002**, *67*, 3755–3763.

(2)   Mitchell, M. S.; Walker, D. L.; Whelan, J.; Bosnich, B. *Inorg. Chem.* **1987**, *26*, 396–400.

Appendix B

Supporting Information

B.1   NCAs

This section contains supporting data relative to the NCAs that were used to synthesise the polypeptides discussed in this thesis. Table B.1 provides an overview of these NCAs, their abbreviation, and the figure in which their NMR spectra can be found.

Table B.1 List of NCAs and the figures for their ^{1}H-NMR and ^{13}C-NMR spectra (M_n are in Da or g·mol^{-1}). Whether an NCA was used in a specific chapter rather than all or most of them, is highlighted in the 'Chapter' column.

Chapter	Abbr.	NCA	M_n (Da)	Figures	
				^{1}H-NMR	^{13}C-NMR
	BLG-NCA	γ-benzyl-L-glutamate	263.25	B.1	B.2
VI	BDG-NCA	γ-benzyl-D-glutamate	263.25	B.3	B.4
	LAG-NCA	L-allylglycine	141.12	B.5	B.6
	DLAG-NCA	DL-allylglycine	141.12	B.7	B.8
III	LLeu-NCA	L-Leucine	157.17	B.9	B.10
III	LPhe-NCA	L-Phenylalanine	191.18	B.11	B.12
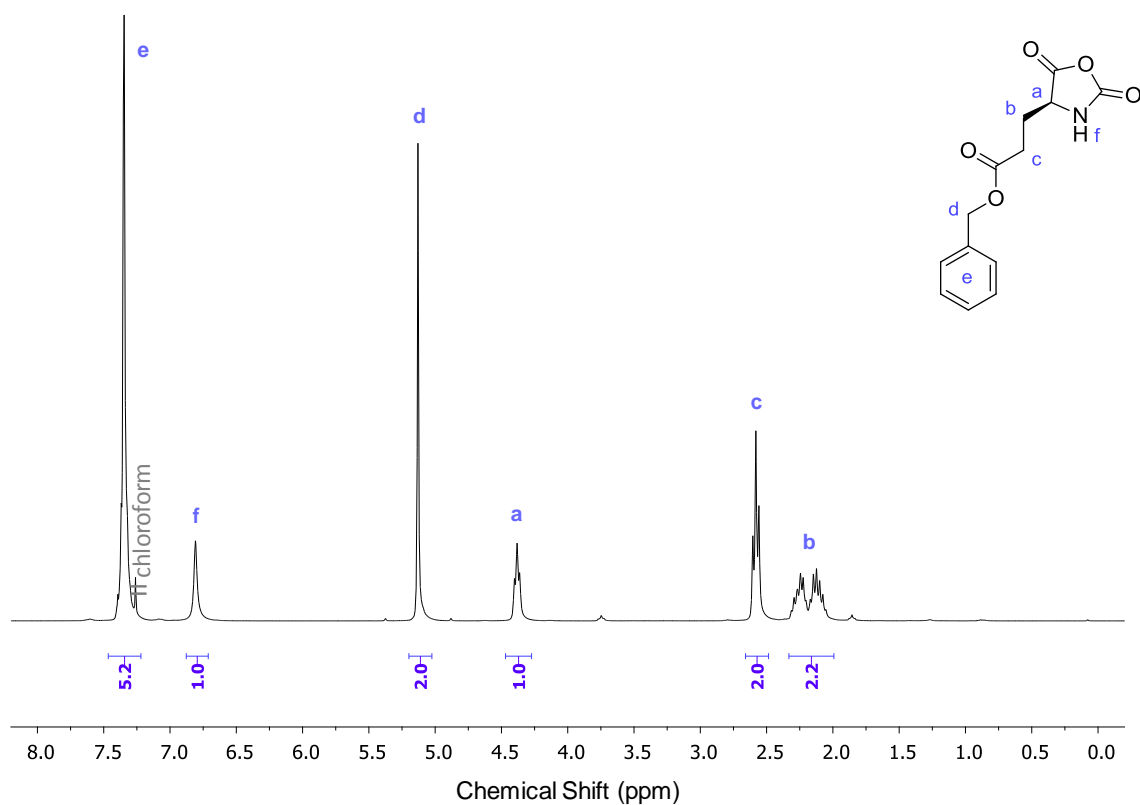
Figure B.1 ^{1}H-NMR spectrum (CDCl$_3$, 300 MHz) of B∟G-NCA.
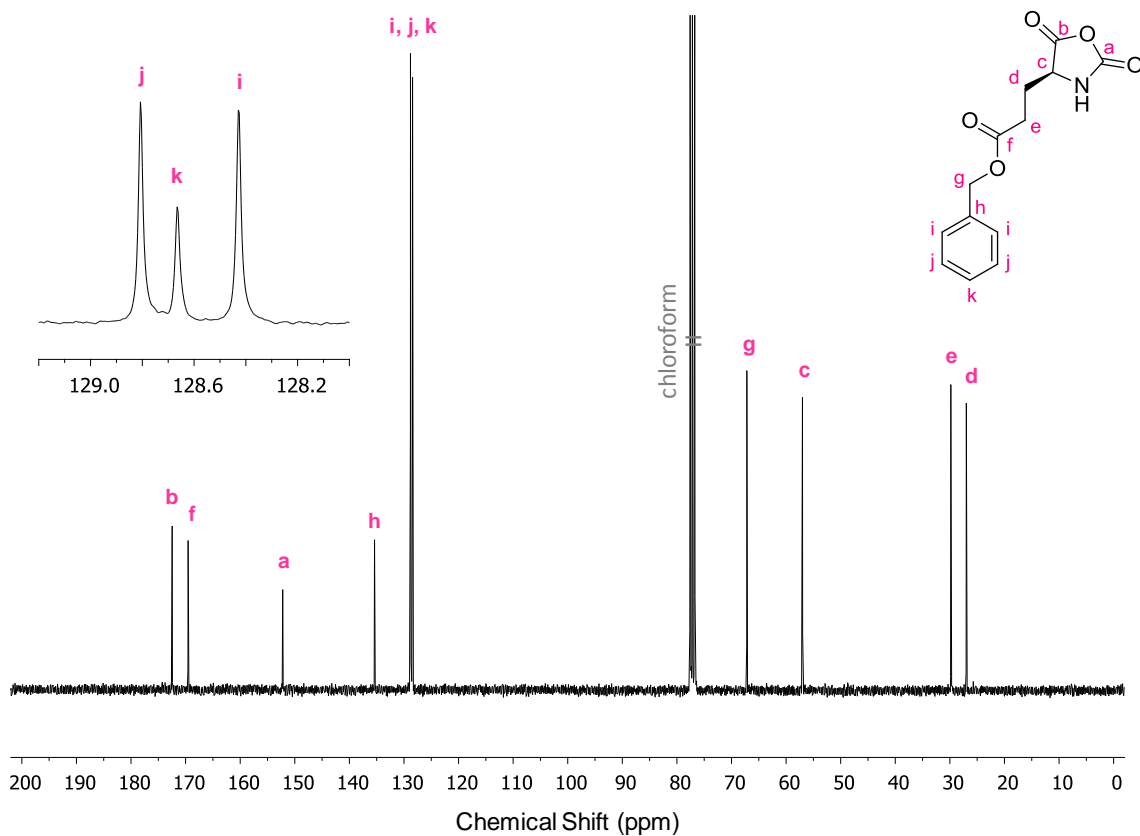
Figure B.2 ^{13}C-NMR spectrum (CDCl$_3$, 75 MHz) of B∟G-NCA.
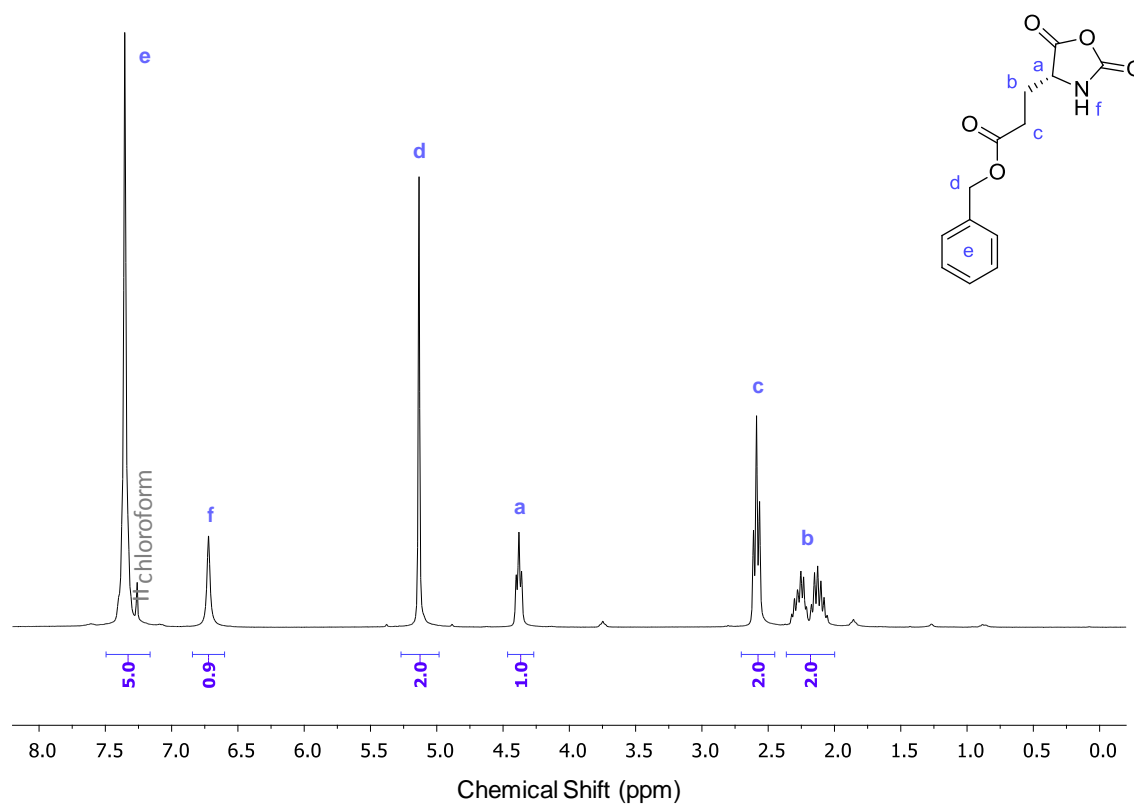
Figure B.3 ^{1}H-NMR spectrum (CDCl$_3$, 300 MHz) of BDG-NCA.
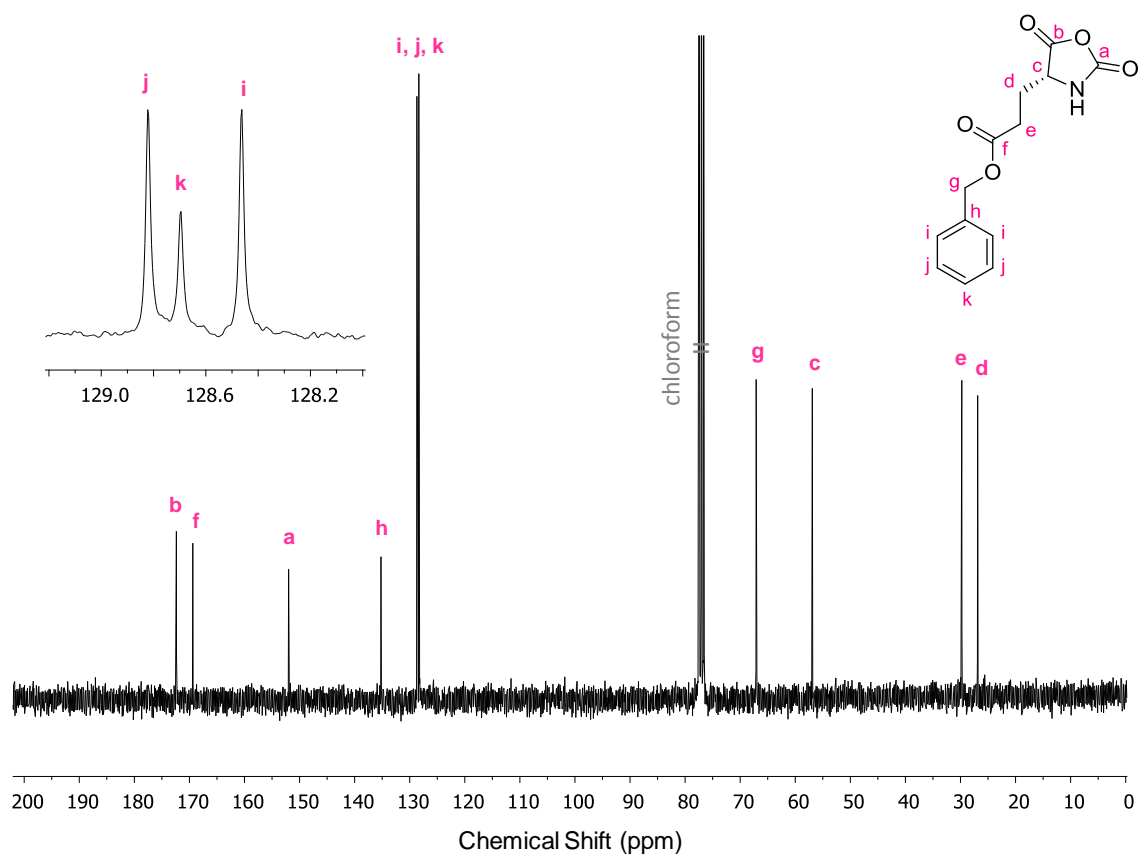
Figure B.4 ^{13}C-NMR spectrum (CDCl$_3$, 75 MHz) of BDG-NCA.
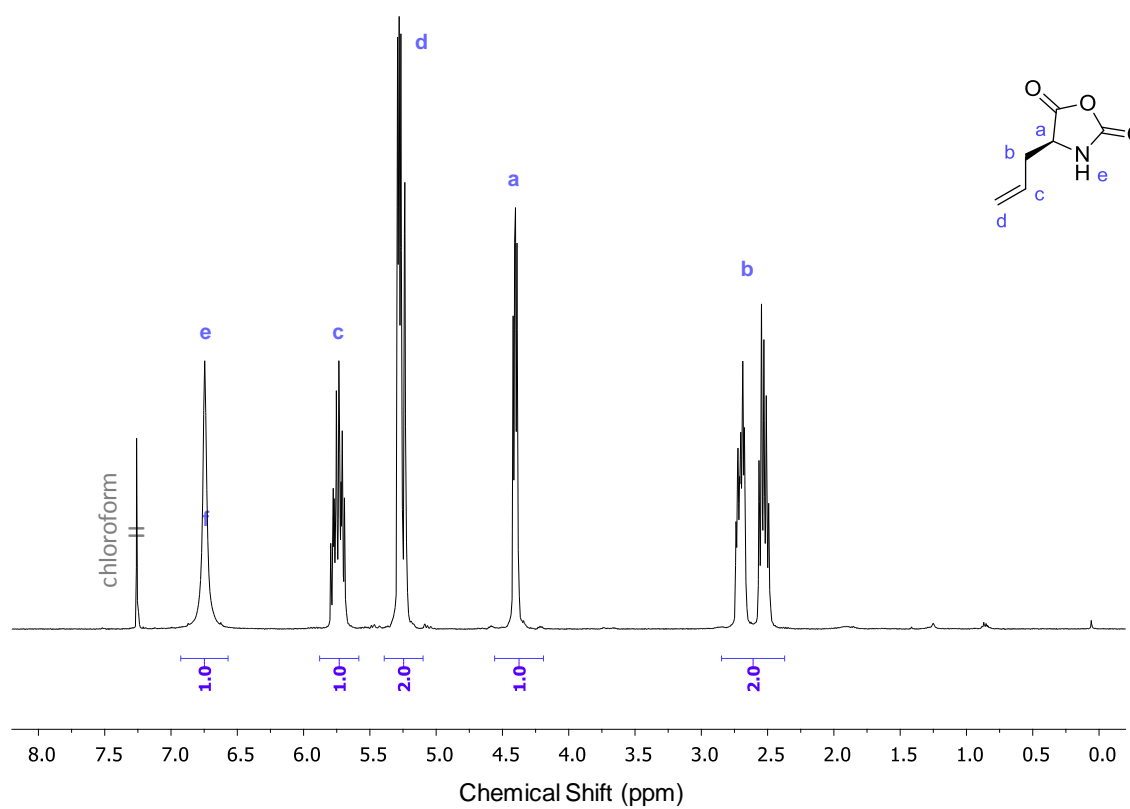
Figure B.5 ^{1}H-NMR spectrum (CDCl$_3$, 400 MHz) of ʟAG-NCA.
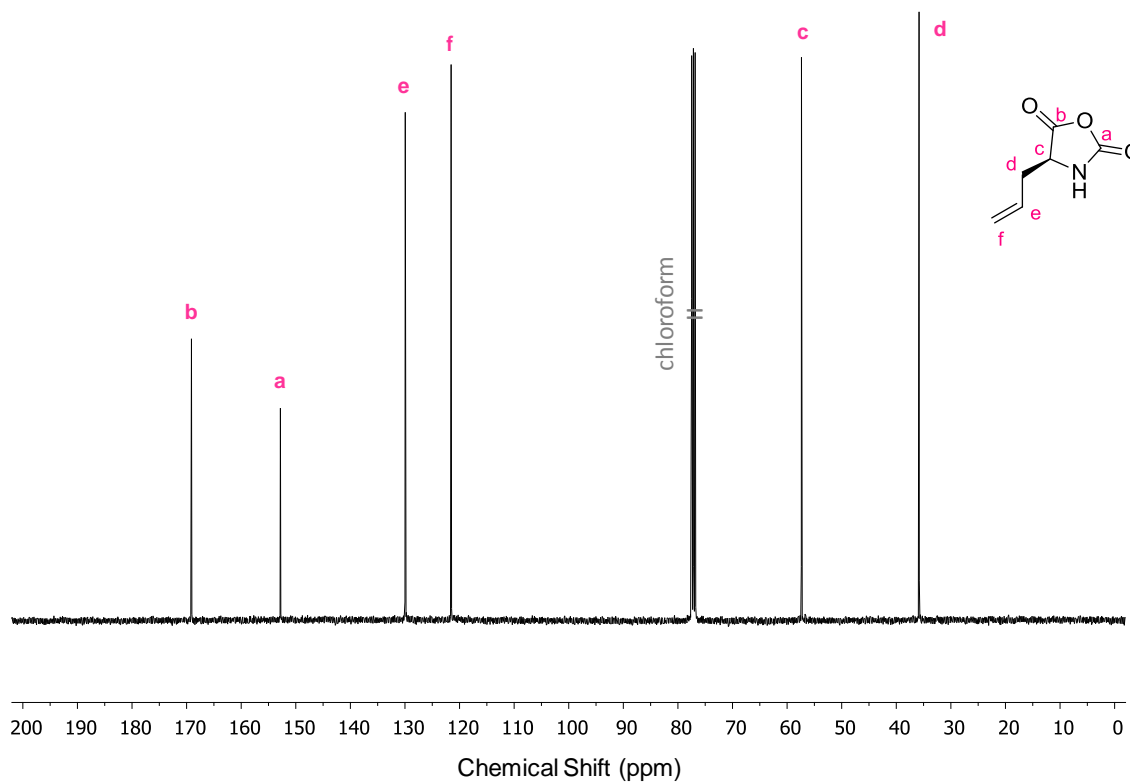
Figure B.6 ^{13}C-NMR spectrum (CDCl$_3$, 100 MHz) of ʟAG-NCA.
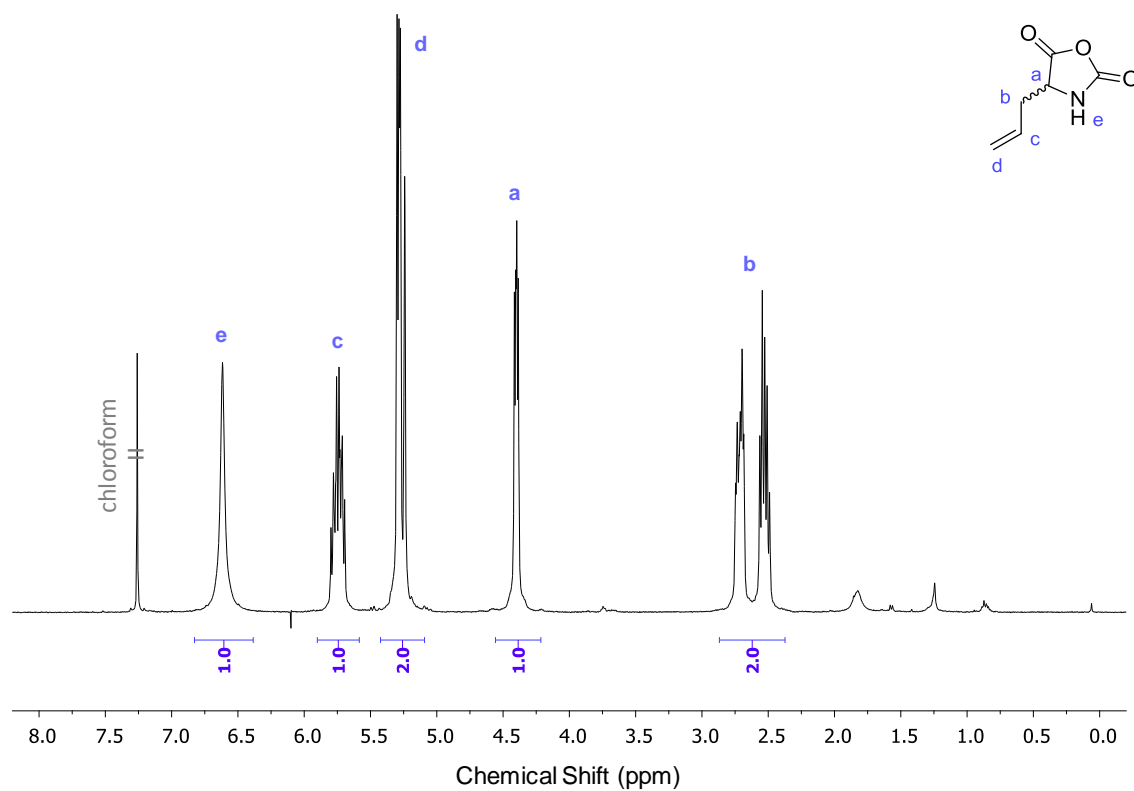
Figure B.7 ^{1}H-NMR spectrum (CDCl$_3$, 400 MHz) of DLAG-NCA.
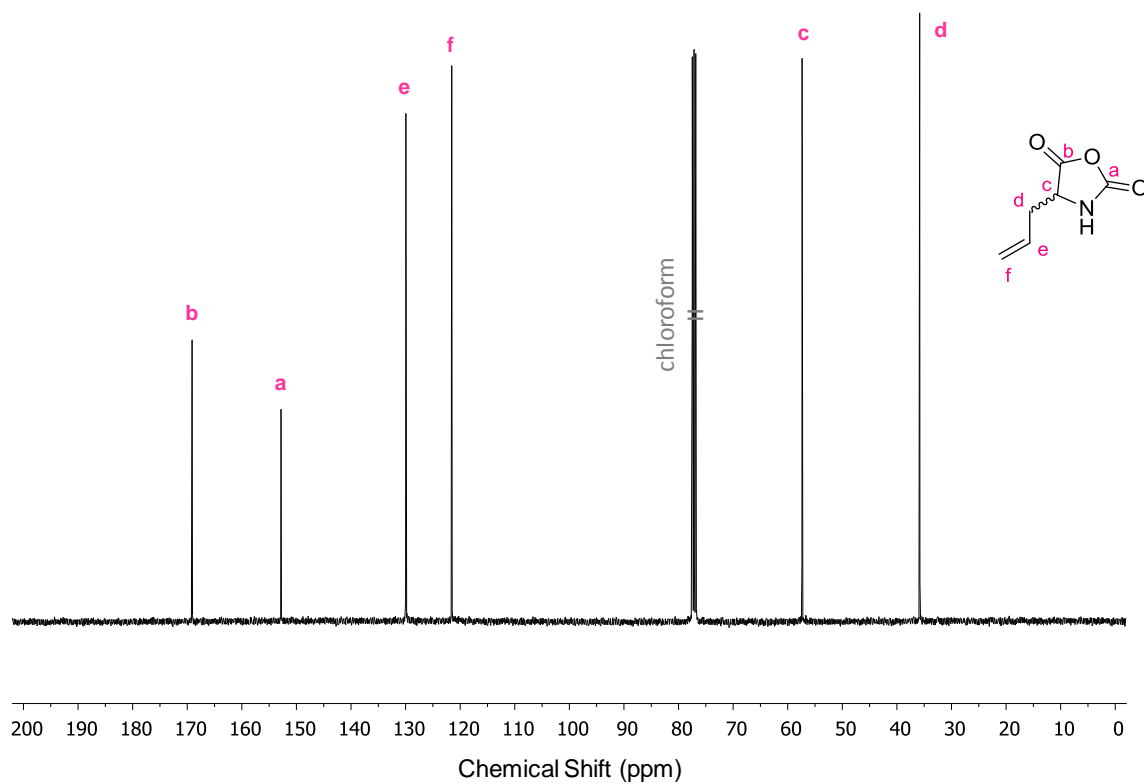
Figure B.8 ^{13}C-NMR spectrum (CDCl$_3$, 100 MHz) of DLAG-NCA.
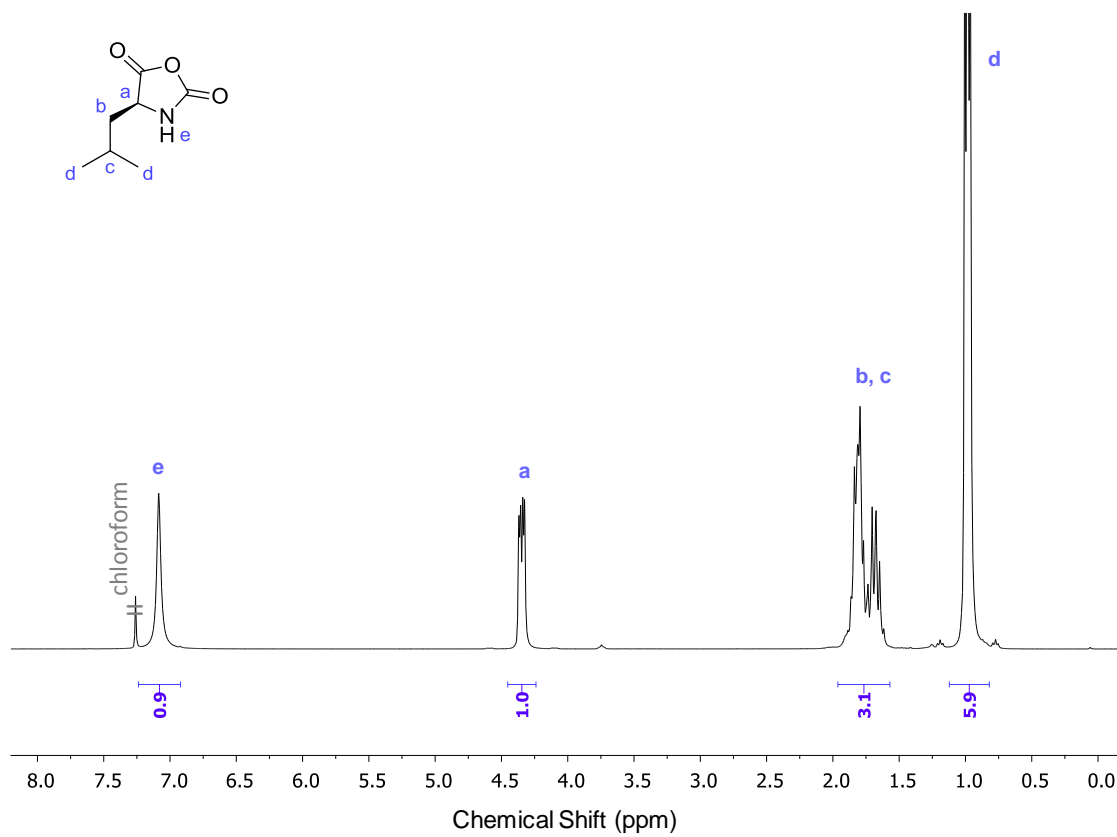
Figure B.9 ^{1}H-NMR spectrum (CDCl₃, 300 MHz) of ʟLeu-NCA.
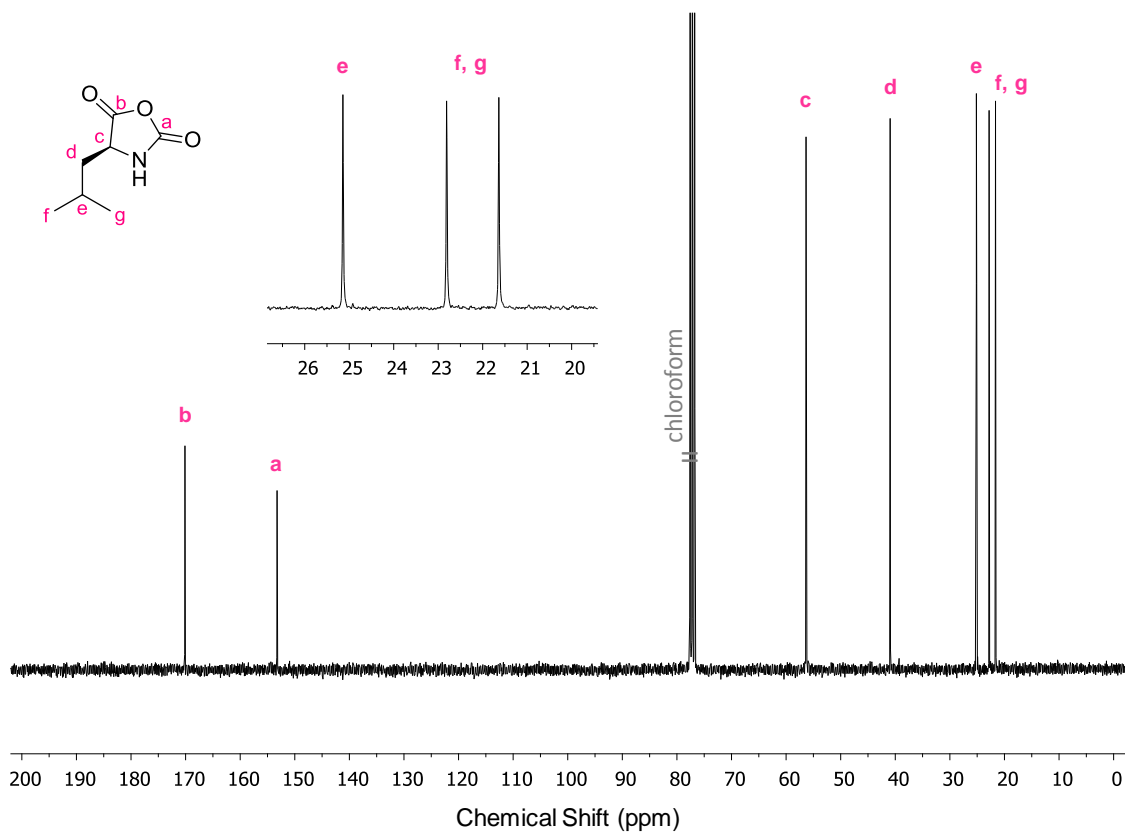
Figure B.10 ^{13}C-NMR spectrum (CDCl₃, 75 MHz) of ʟLeu-NCA.
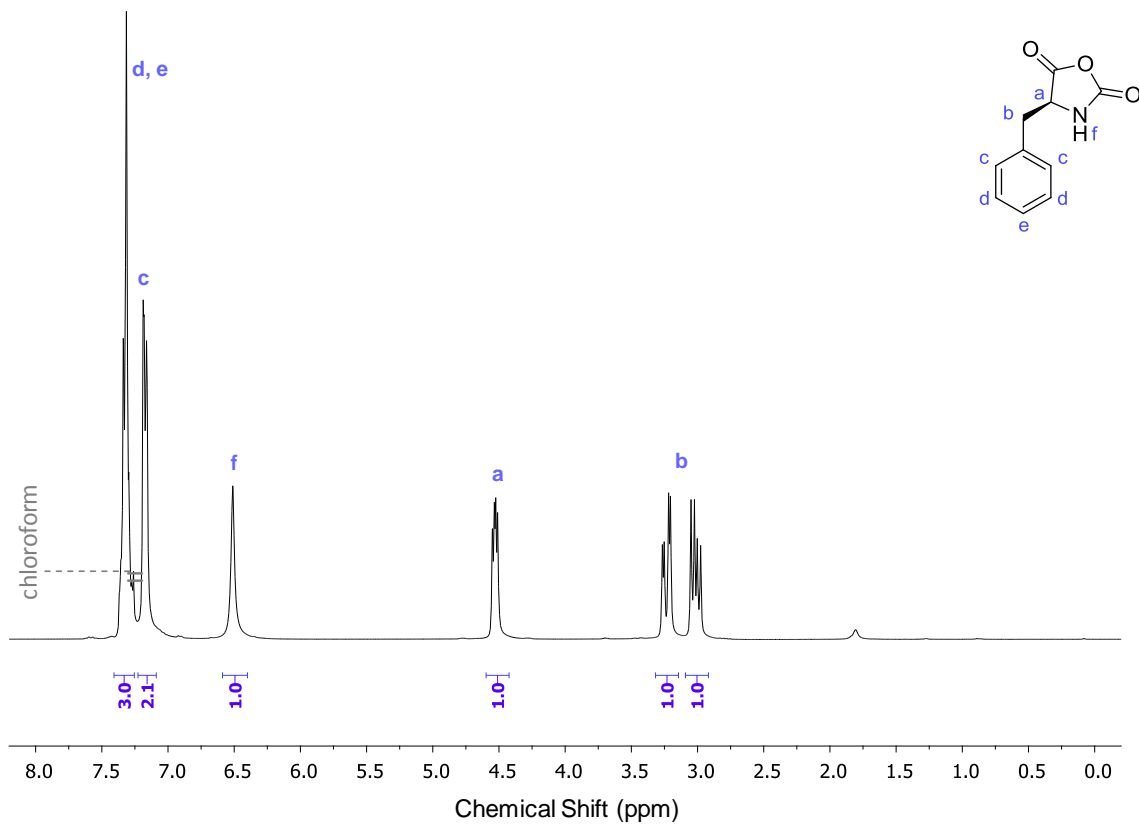
Figure B.11 ^{1}H-NMR spectrum (CDCl$_3$, 300 MHz) of ʟPhe-NCA in CDCl$_3$.
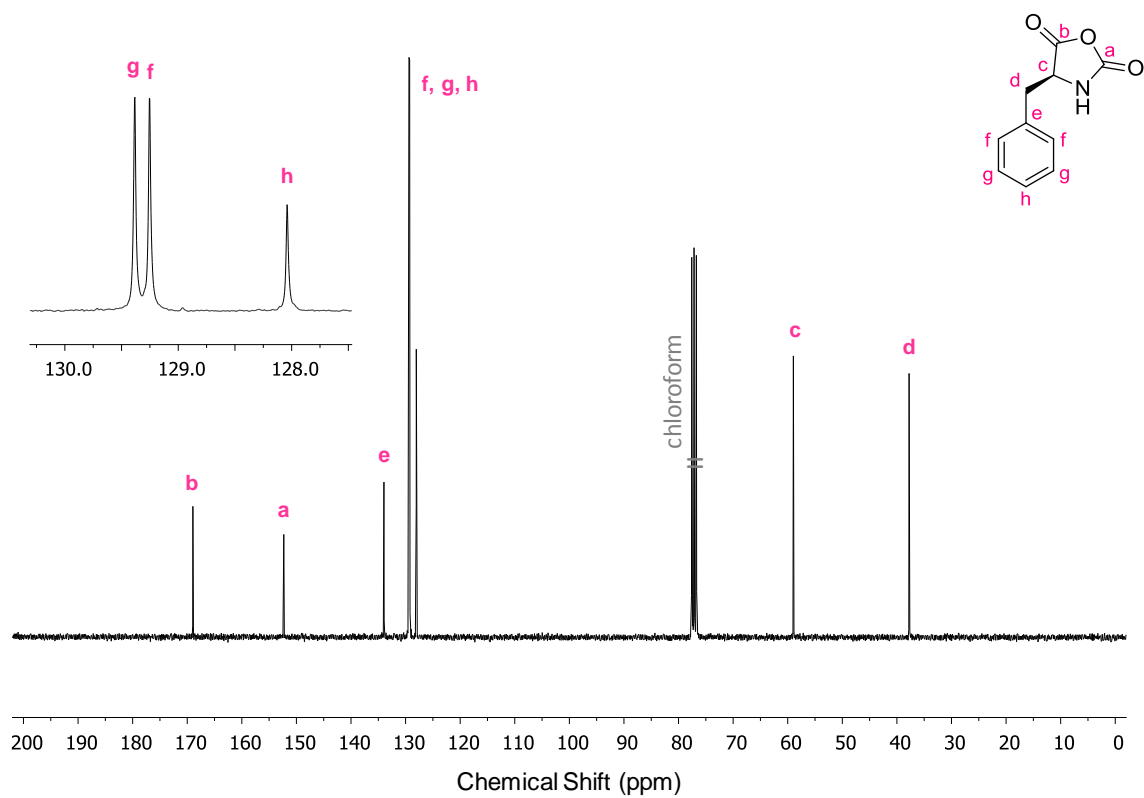
Figure B.12 ^{13}C-NMR spectrum (CDCl$_3$, 75 MHz) of ʟPhe-NCA.

B.2 Polypeptides

This section contains supporting data relative to the polypeptides that were analysed in Chapter II, IV, V, and VI. Table B.2 provides an overview of these polypeptides, their composition, their reference (*i.e.*, Pxx), and the figure in which their NMR spectrum and SEC trace can be found (See Figure II.1 for abbreviations).

Table B.2 List of polypeptides, their properties, and figure references for their ^{1}H-NMR spectra and SEC traces (M_n are in kDa or kg·mol^{-1}); synthesis and chemical shifts are in Appendix A. Whether a polypeptide was used in a specific chapter rather than all or most of them is highlighted in the 'Chapter' column. All copolypeptides are statistical (random-like) copolypeptides.

Chapter	Entry	Polypeptide	Initiator	Terminating Agent	NMR M_n (kDa)	Figure	SEC M_n^{app} (kDa)	Figure	n	BG (%)	AG (%)	SEC $Đ^{app}$ (M_w/M_n)
	P1	PBLG$_{51}$	HexA	Ac$_2$O	11.3	**B.13**	8.5	**II.7**	50	100	0	1.09
	P1-D	PLG$_{51}$	*Derived from P1***		6.7	**B.37**	8.9	**B.40**	-	-	-	1.74
	P2	P(BLG$_{0.76}$-*co*-DLAG$_{0.24}$)$_{59}$	HexA	Ac$_2$O	11.4	**B.14**	10.5	**II.7**	50	75	25	1.16
II	**P2-D**	P(LG$_{0.76}$-*co*-DLAG$_{0.24}$)$_{58}$	*Derived from P2***		7.2	**II.10**	6.2	**B.40**	-	-	-	2.1
	P3	P(BLG$_{0.77}$-*co*-LAG$_{0.23}$)$_{57}$	HexA	Ac$_2$O	11.1	**B.15**	8.9	**II.7**	50	75	25	1.25
	P4	P(BLG$_{0.89}$-*co*-DLAG$_{0.11}$)$_{53}$	HexA	Ac$_2$O	11.0	**B.16**	10.4	**II.7**	50	88	12	1.18
	P12	P(BLG$_{0.74}$-*co*-LAG$_{0.26}$)$_{170}$	HexA	Ac$_2$O	31.9	**B.17**	28.0	**II.7**	150	75	25	1.28
	P13	P(BLG$_{0.80}$-*co*-LAG$_{0.20}$)$_{219}$	HexA	Ac$_2$O	42.8	**B.18**	27.4	**II.7**	150	80	20	1.23
	P14	P(BLG$_{0.84}$-*co*-LAG$_{0.16}$)$_{171}$	HexA	Ac$_2$O	34.2	**B.19**	21.6	**II.7**	150	85	15	1.28
	P15	P(BLG$_{0.74}$-*co*-LAG$_{0.26}$)$_{91}$	HexA	Ac$_2$O	17.2	**B.20**	12.7	**II.7**	75	75	25	1.21
	P16	P(BLG$_{0.78}$-*co*-LAG$_{0.22}$)$_{96}$	HexA	Ac$_2$O	18.6	**B.21**	12.7	**II.7**	75	80	20	1.13
II	**P18A**	*"star"*-(PBLG$_{15}$)$_2$	HexDA	HepdF-COCl	7.6	**II.12**	9.1	**B.39**	50	100	0	1.19
II	**P18B**	*"star"*-(PBLG$_{15}$)$_2$	HexDA	Ac$_2$O	6.8	**II.11**	8.4	**B.39**	50	100	0	1.19
II	**P33**	*star*-(PBLG$_{20}$)$_3$	TAB·3HCl*	MalO	13.6	**B.22**	9.2	**B.39**	60	100	0	1.09
II	**P36**	*star*-(PBLG$_{40}$)$_3$	TAB·3HCl*	MalO	26.8	**B.23**	18.7	**B.39**	150	100	0	1.08
II	**P36-D**	*star*-(PLG$_{40}$)$_3$	*Derived from P36***		16.0	**B.24**	24.0	**B.40**	-	-	-	1.46
	P40	*"star"*-(P(BLG$_{0.50}$-*co*-LAG$_{0.50}$)$_{73}$)$_2$	HexDA	MalO	23.4	**II.8**	16.7	**B.39**	300	50	50	1.27
III	**P49**	*star*-(PBLG$_{42}$)$_3$	TAB·3HCl*	MalO	28.1	**B.25**	19.3	**B.39**	150	100	0	1.19
II	**P49-D**	*star*-(PLG$_{43}$)$_3$	TAB·3HCl*	MalO	17.1	**B.26**	20.1	**B.40**	-	-	-	1.51
III	**P50**	*star*-(P(BLG$_{0.79}$-*co*-LAG$_{0.21}$)$_{36}$)$_3$	TAB·3HCl*	MalO	21.6	**B.27**	-	-	150	75	25	-
II	**P50-D**	*star*-(P(LG$_{0.80}$-*co*-LAG$_{0.20}$)$_{37}$)$_3$	*Derived from P50***		14.1	**B.28**	15.5	**B.40**	-	-	-	1.60
III	**P51**	*star*-(P(BLG$_{0.79}$-*co*-LAG$_{0.21}$)$_{36}$)$_3$	TAB·3HCl*	Ac$_2$O	21.4	-	-	-	150	75	25	-
II	**P51-D**	*star*-(P(LG$_{0.80}$-*co*-LAG$_{0.20}$)$_{37}$)$_3$	*Derived from P51***		13.9	**B.29**	18.2	**B.40**	-	-	-	1.95
III	**P52**	*star*-(P(BLG$_{0.93}$-*co*-LAG$_{0.07}$)$_{40}$)$_3$	TAB·3HCl*	MalO	25.6	**B.30**	-	-	150	88	12	-
II	**P52-D**	*star*-(P(LG$_{0.93}$-*co*-LAG$_{0.07}$)$_{39}$)$_3$	*Derived from P52***		15.3	**B.31**	18.9	**B.40**	-	-	-	1.5
	P59	PBLG$_{159}$	HexA	Ac$_2$O	35.0	**B.32**	30.6	**B.38**	150	100	0	1.21
VI	**P60**	PBDG$_{155}$	HexA	Ac$_2$O	34.1	**B.33**	40.4	**B.38**	150	100	0	1.15
VI	**P61**	P(BLG$_{0.80}$-*co*-BDG$_{0.20}$)$_{207}$	HexA	Ac$_2$O	45.5	**B.34**	26.9	**B.38**	200	80L/20D	0	1.11
VI	**P62**	P(BDG$_{0.81}$-*co*-DLAG$_{0.19}$)$_{223}$	HexA	Ac$_2$O	43.9	**B.35**	39.9	**B.38**	200	80	20	1.16
VI	**P63**	P(BLG$_{0.80}$-*co*-DLAG$_{0.20}$)$_{209}$	HexA	Ac$_2$O	40.8	**B.36**	34.9	**B.38**	200	80	20	1.28

* Initiated by ammonium chloride salts (1 equiv.) and TEA (0.5 equiv.) according to the primary ammonium/tertiary amine-mediated ROP procedure reported in Chapter III and Appendix A. ** Debenzylation according to the procedure reported in Appendix A.

B.2.1 ^{1}H-NMR Spectra of Polypeptides
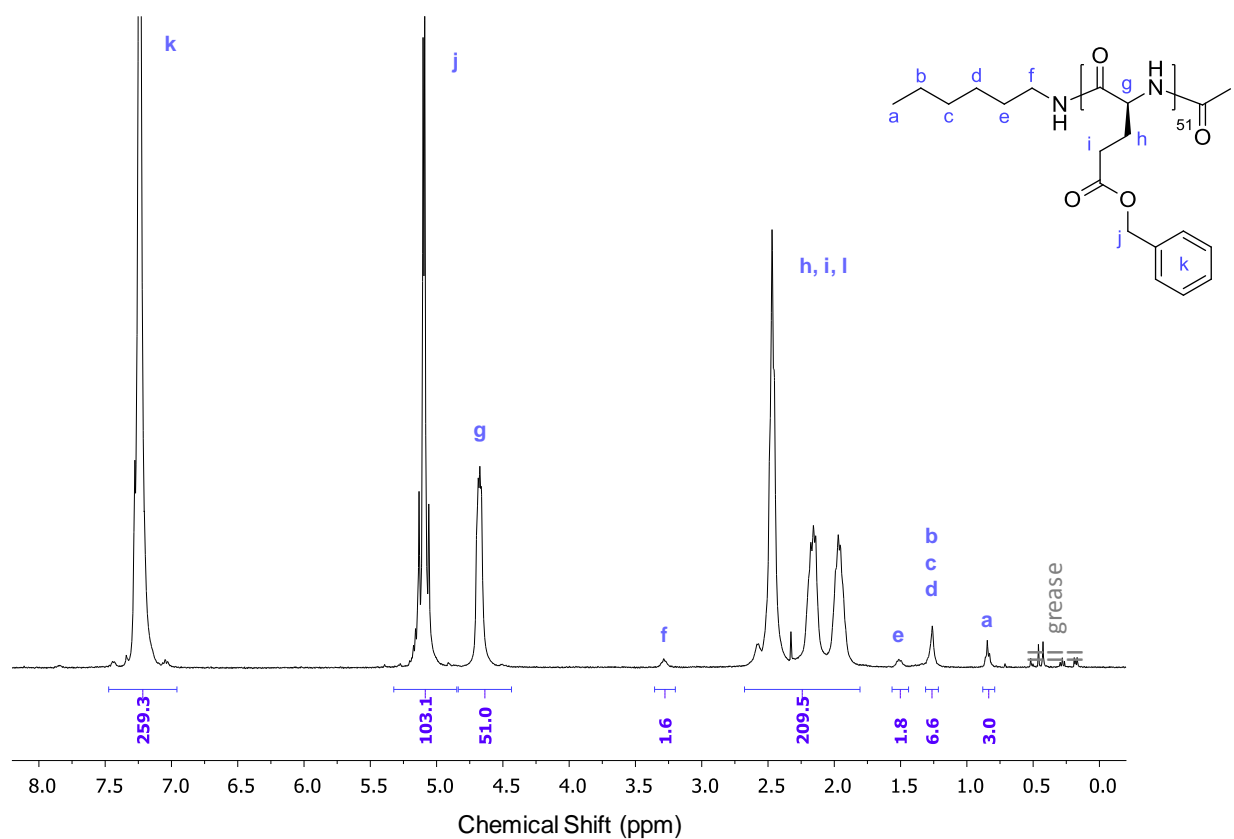
Figure B.13 ^{1}H-NMR spectrum (TFA-d, 400 MHz) of PBLG$_{51}$ (P1).
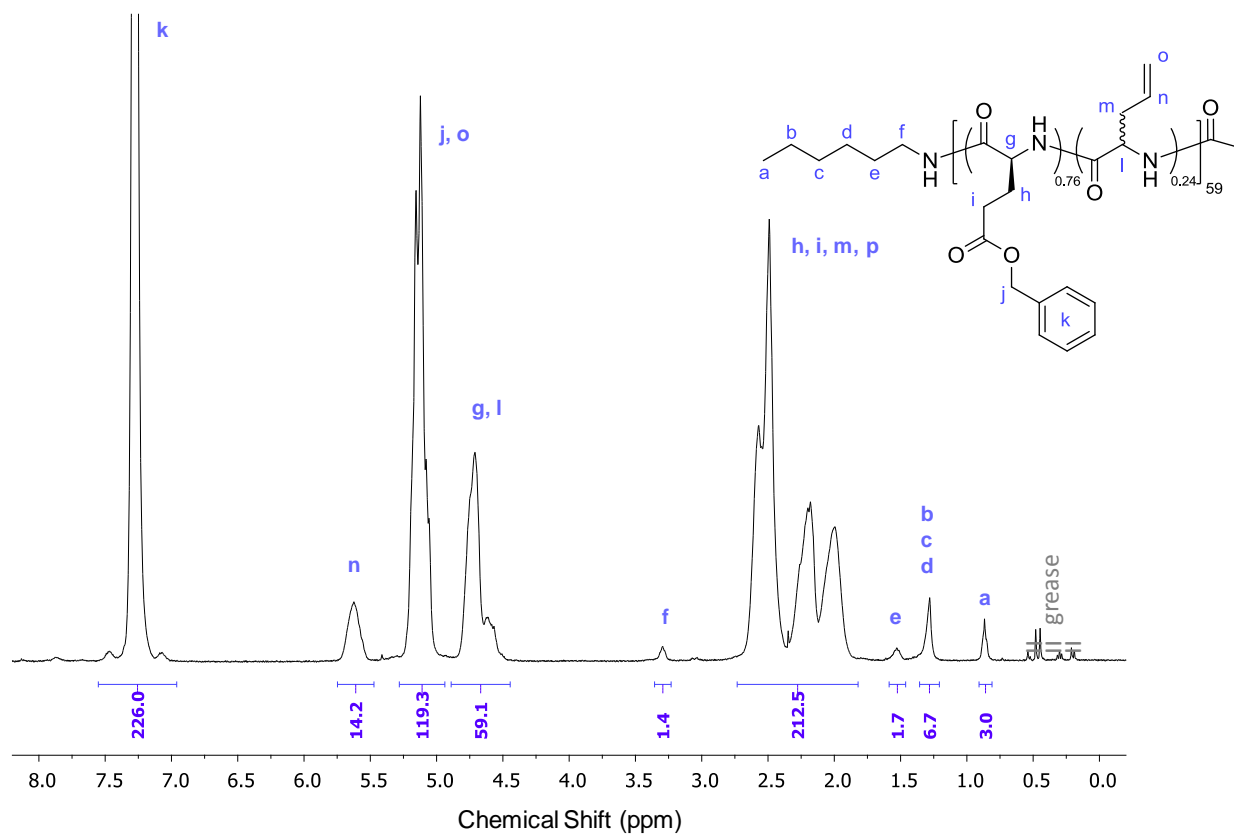
Figure B.14 ^{1}H-NMR spectrum (TFA-d, 400 MHz) of P(BLG$_{0.76}$-co-DLAG$_{0.24}$)$_{59}$ (P2).
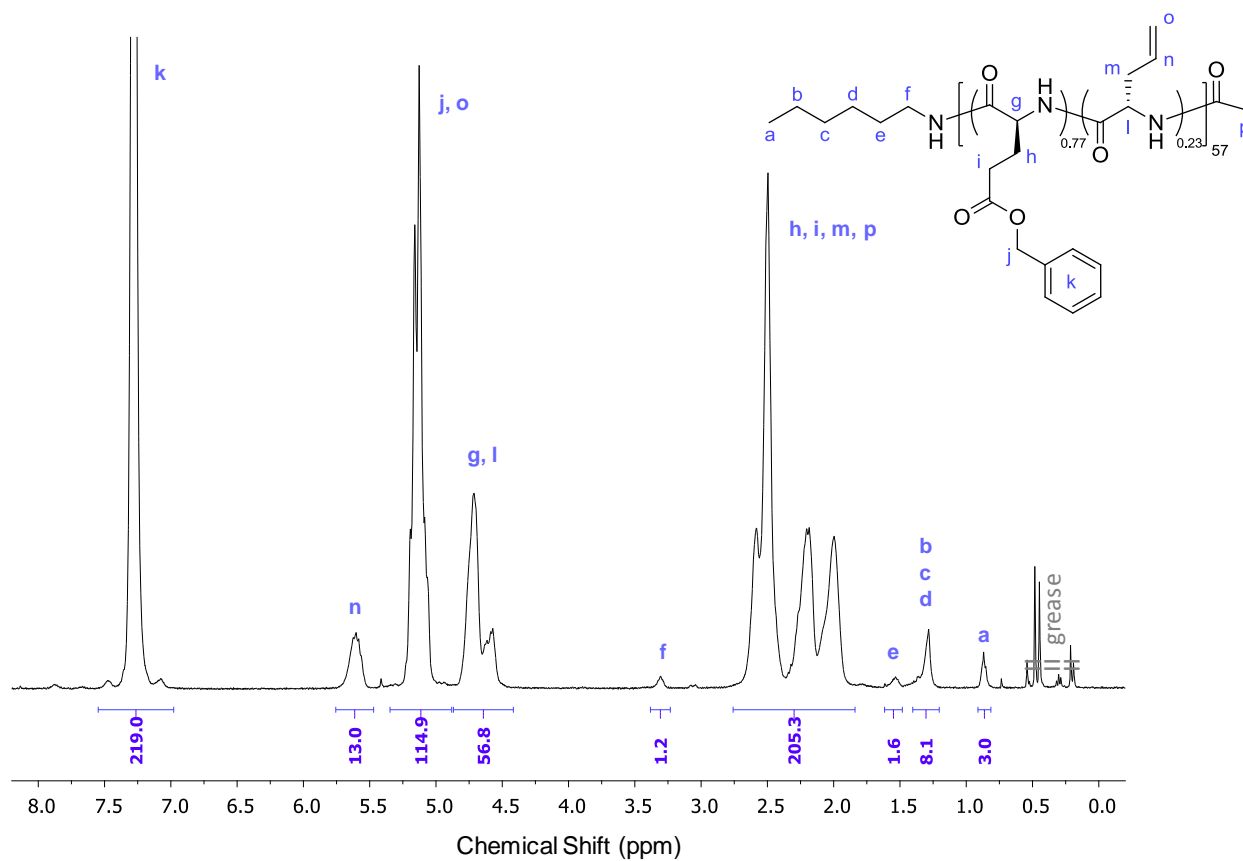
Figure B.15 ^{1}H-NMR spectrum (TFA-d, 400 MHz) of P(BLG$_{0.77}$-*co*-LAG$_{0.23}$)$_{57}$ (P3).
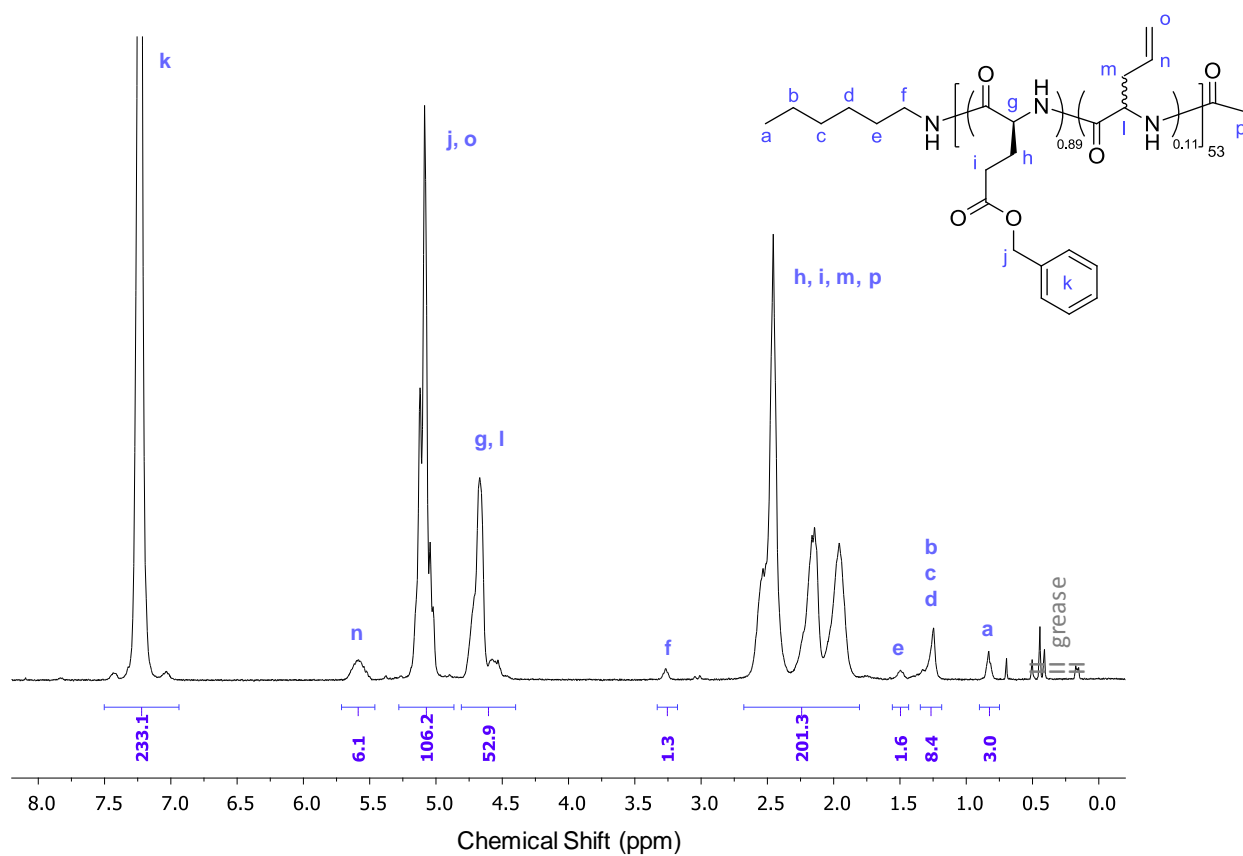
Figure B.16 ^{1}H-NMR spectrum (TFA-d, 400 MHz) of P(BLG$_{0.89}$-*co*-DLAG$_{0.11}$)$_{53}$ (P4).
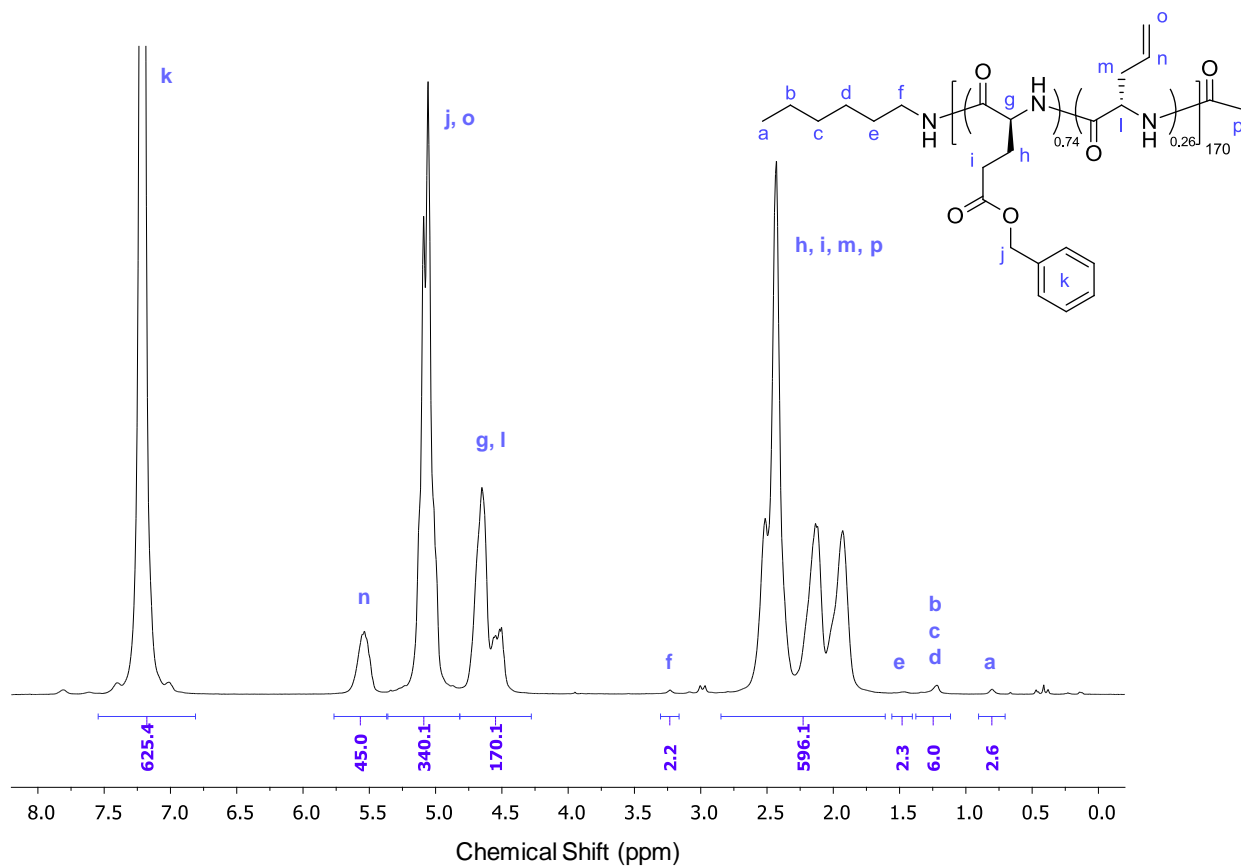
Figure B.17 ^{1}H-NMR spectrum (TFA-d, 400 MHz) of P(B<small>L</small>G$_{0.74}$-*co*-LAG$_{0.26}$)$_{170}$ (P12).
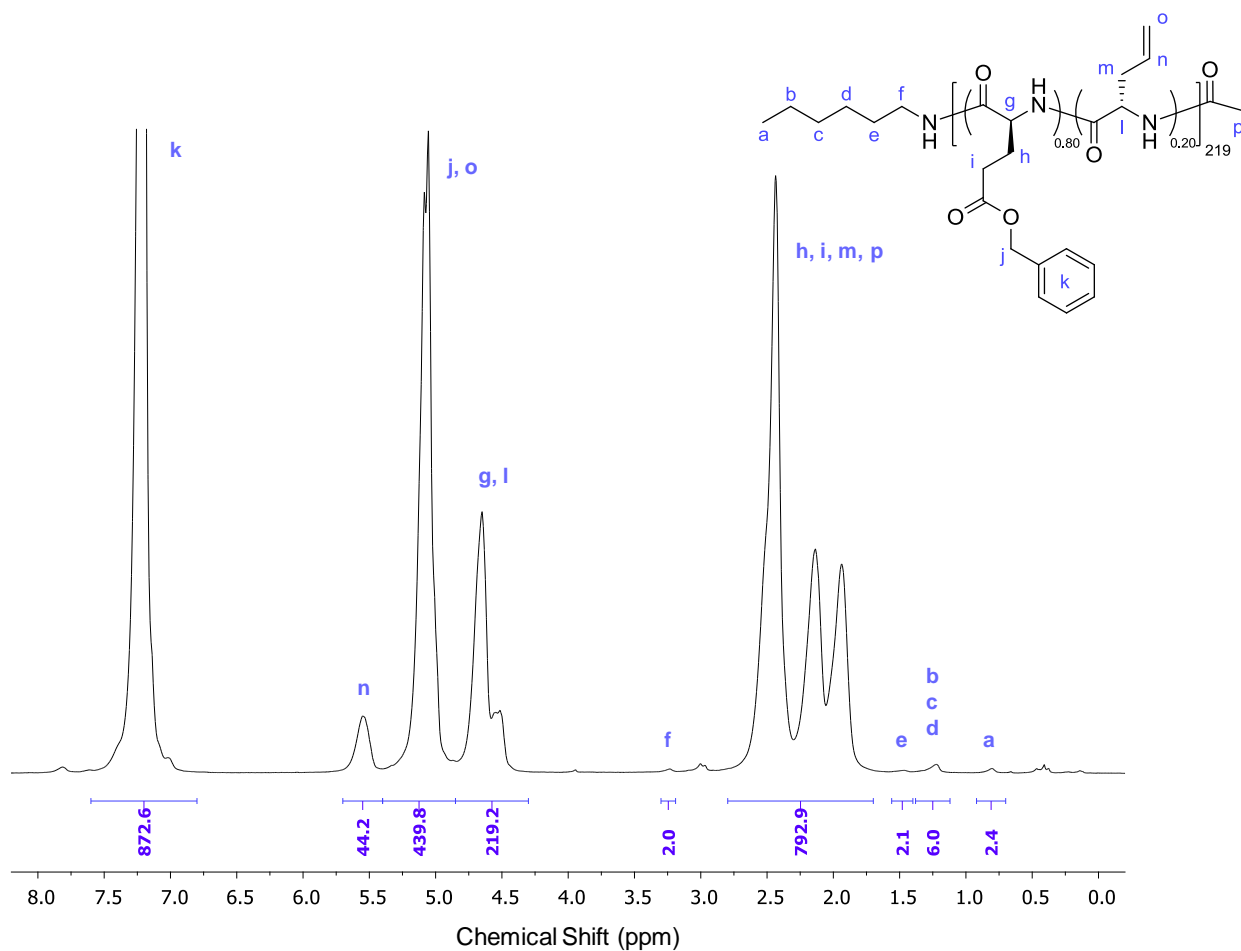
Figure B.18 ^{1}H-NMR spectrum (TFA-d, 400 MHz) of P(B<small>L</small>G$_{0.80}$-*co*-LAG$_{0.20}$)$_{219}$ (P13).
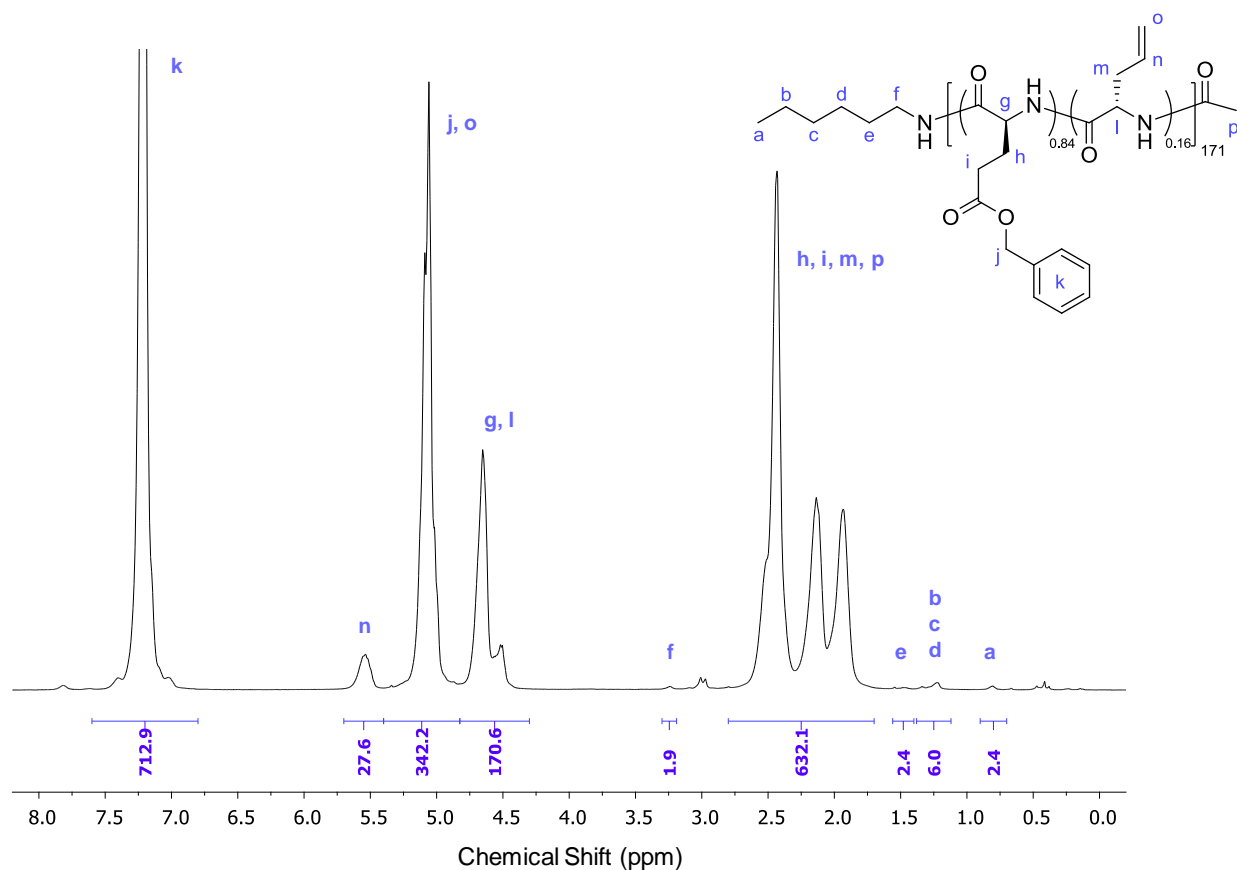
Figure B.19 ^{1}H-NMR spectrum (TFA-d, 400 MHz) of P(BLG$_{0.84}$-*co*-LAG$_{0.16}$)$_{171}$ (P14).
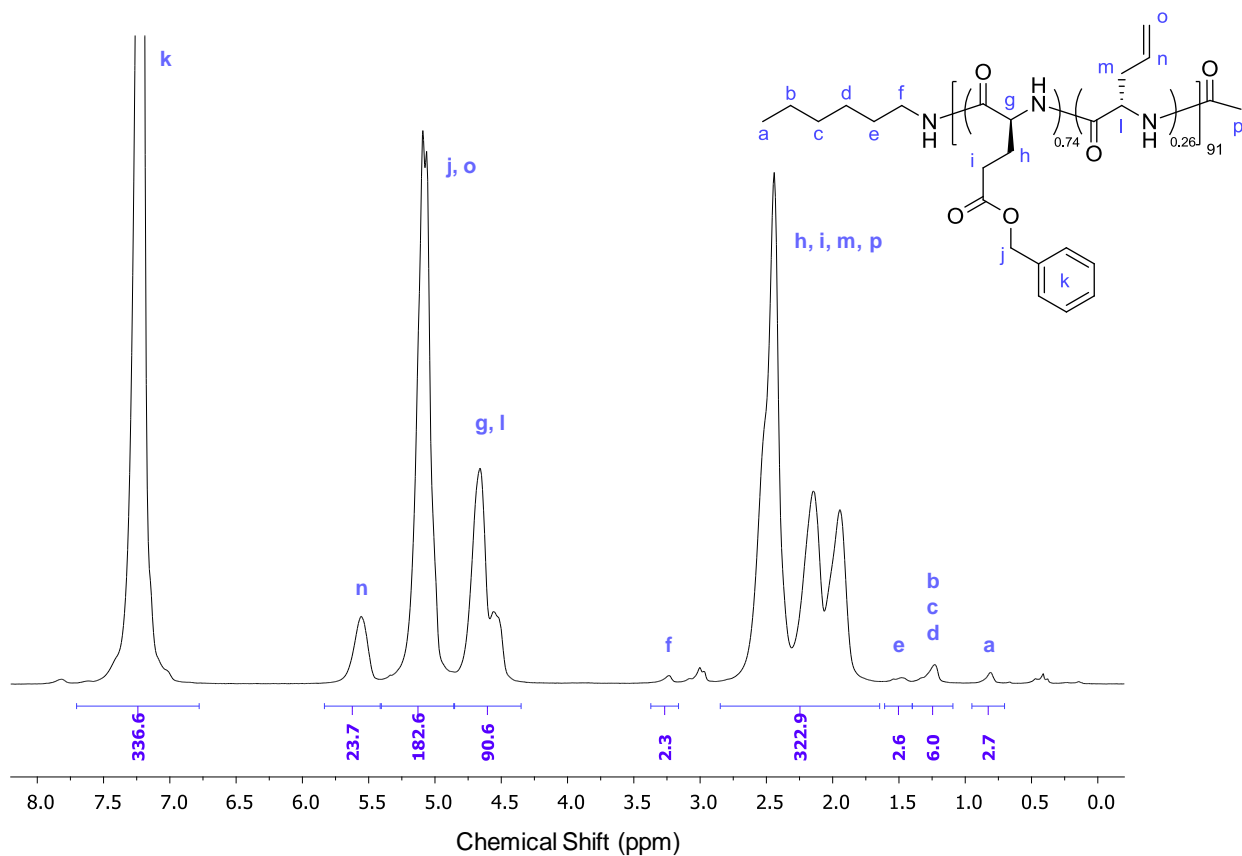
Figure B.20 ^{1}H-NMR spectrum (TFA-d, 400 MHz) of P(BLG$_{0.74}$-*co*-LAG$_{0.26}$)$_{91}$ (P15).
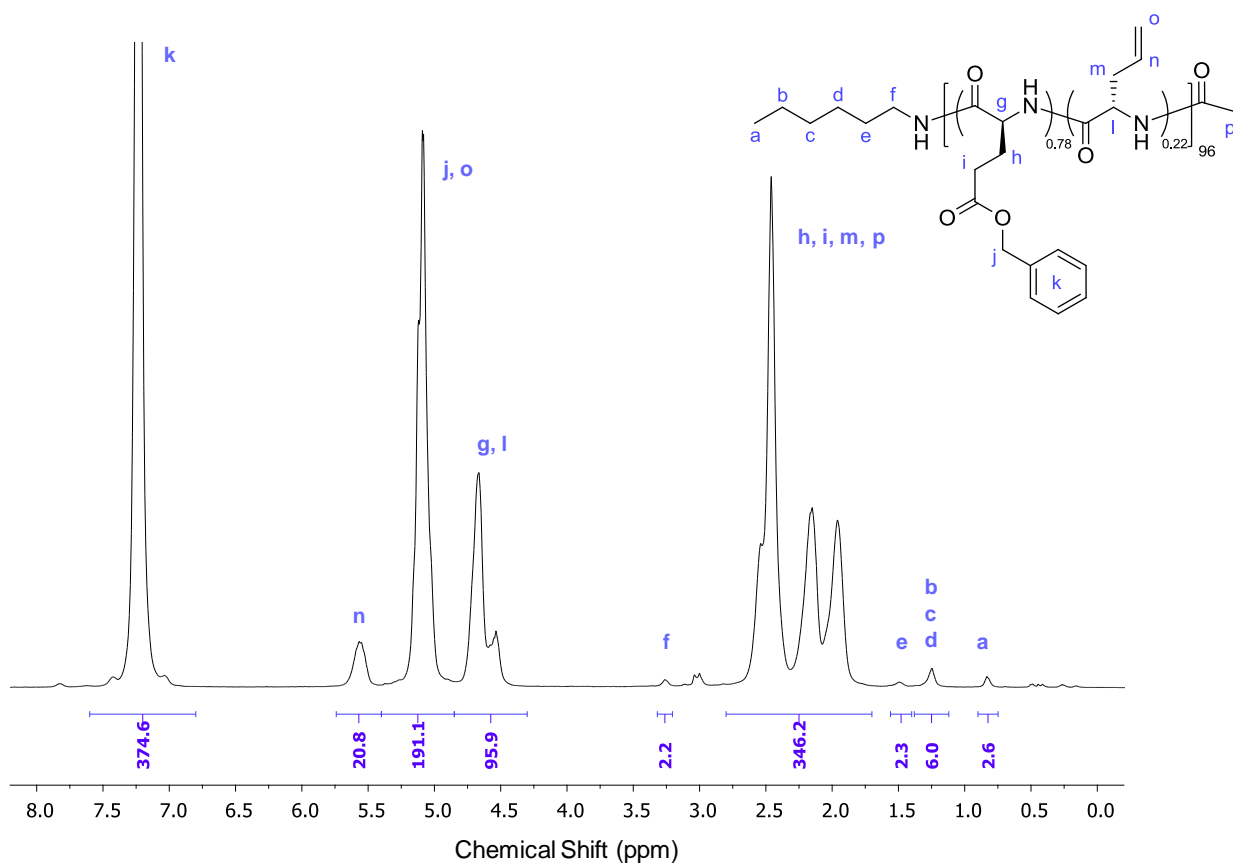
Figure B.21 ^{1}H-NMR spectrum (TFA-d, 400 MHz) of P(BLG$_{0.78}$-*co*-LAG$_{0.22}$)$_{96}$ (P16).
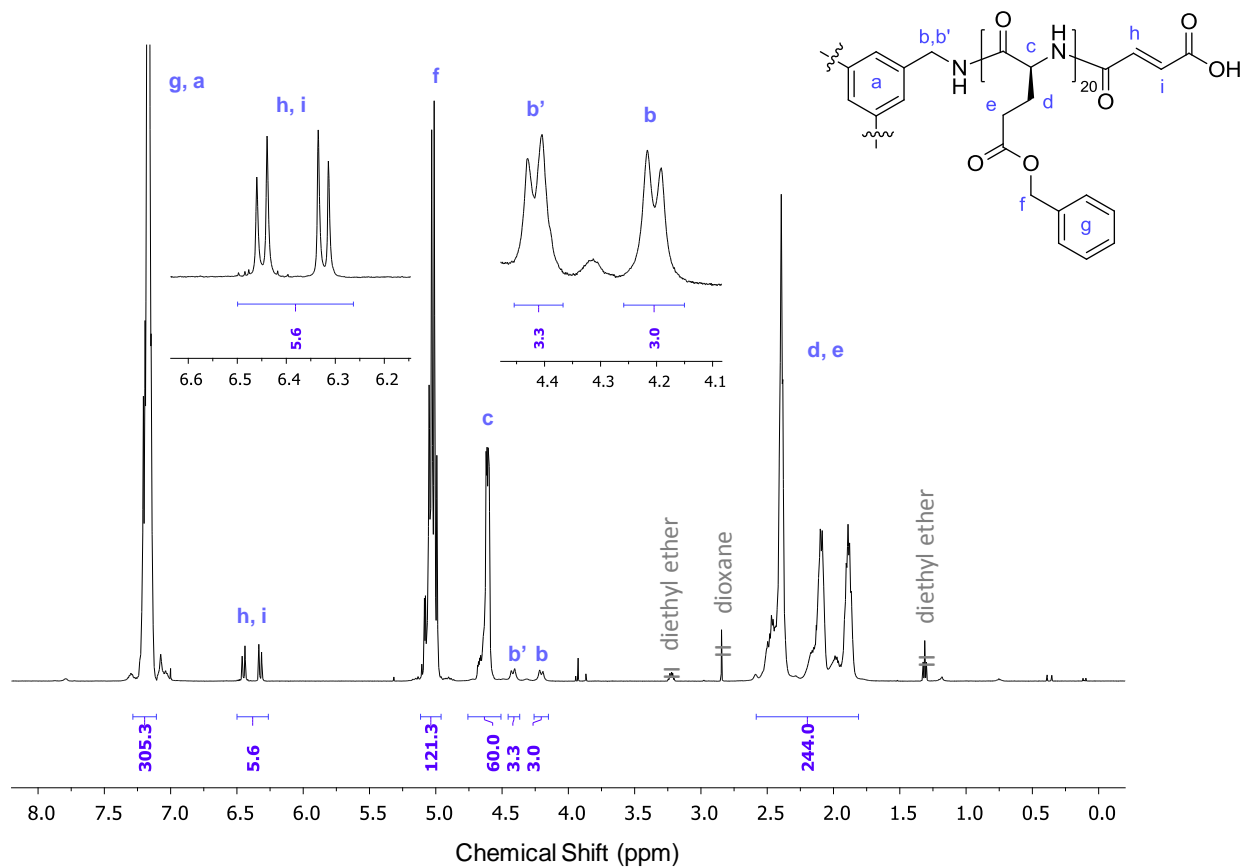
Figure B.22 ^{1}H-NMR spectrum (TFA-d, 600 MHz) of *star*-(PBLG$_{20}$)$_3$ (P33).
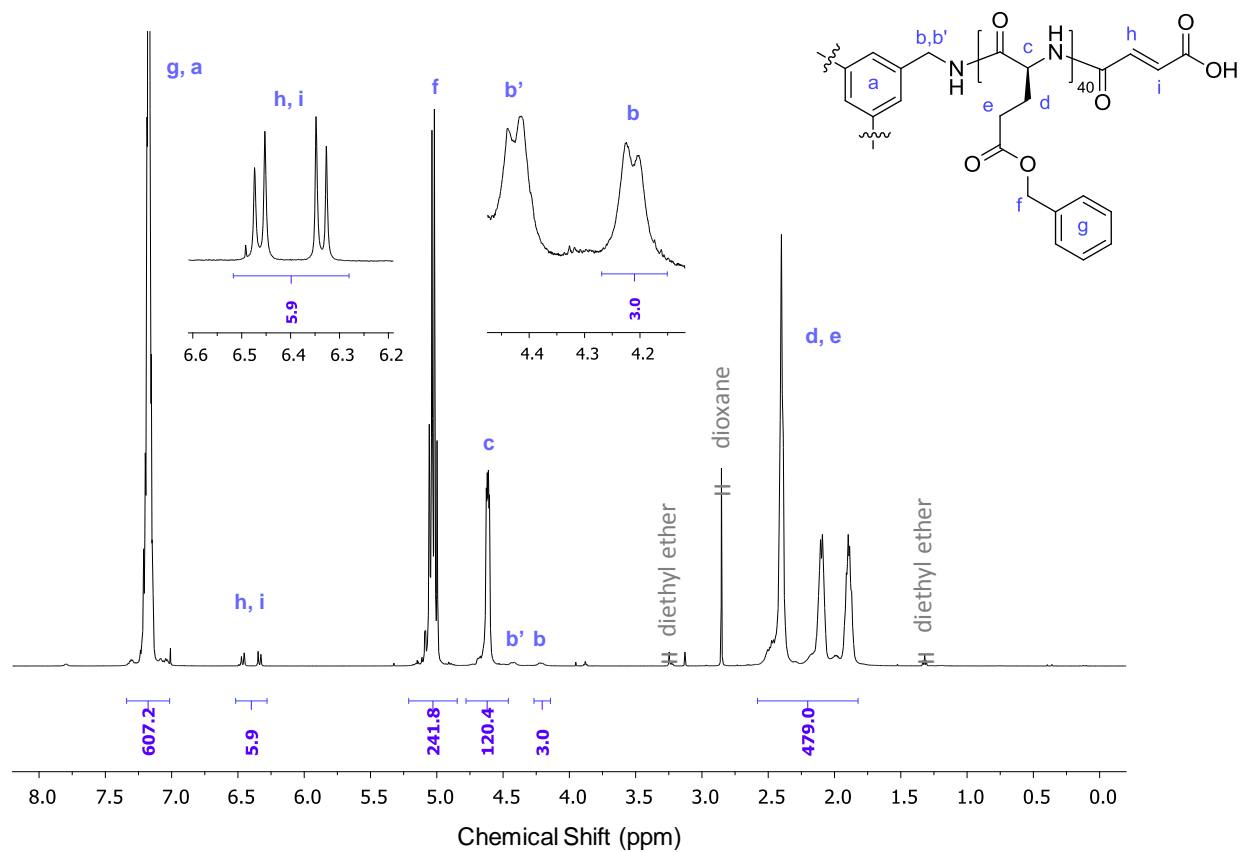
Figure B.23 ^{1}H-NMR spectrum (TFA-d, 600 MHz) of *star*-(PB∟G$_{40}$)$_3$ (P36).
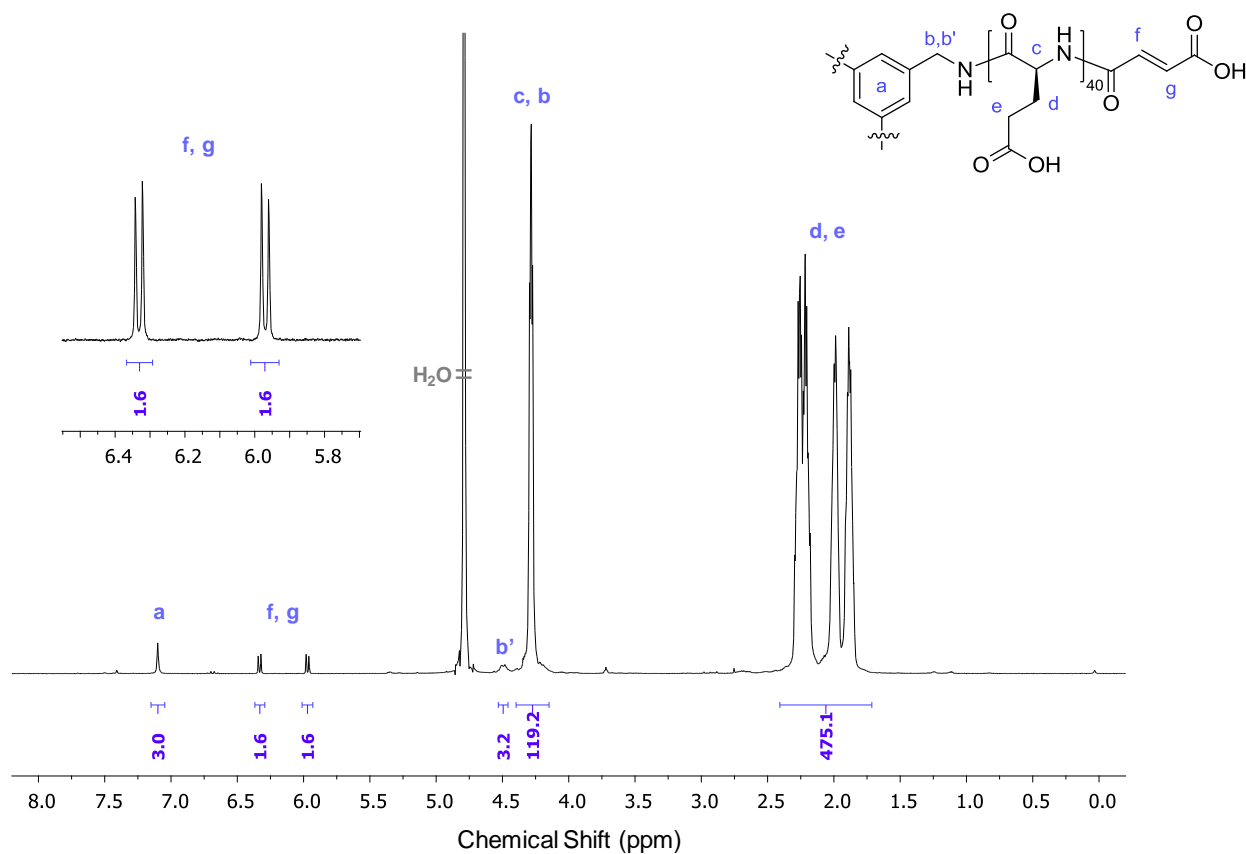
Figure B.24 ^{1}H-NMR spectrum (D$_2$O, 600 MHz) of *star*-(P∟G$_{40}$)$_3$ (P36-D).
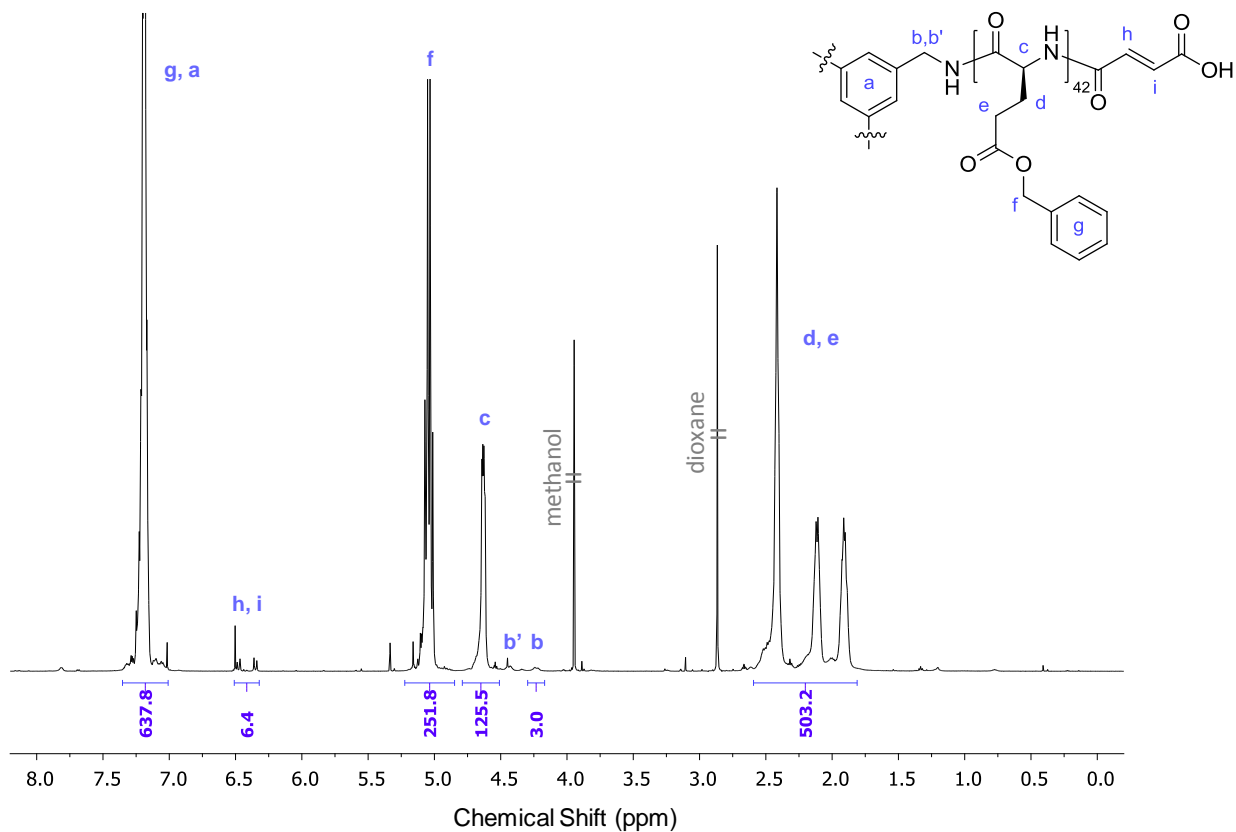
Figure B.25 ^{1}H-NMR spectrum (TFA-d, 600 MHz) of *star*-(PB$_L$G$_{42}$)$_3$ (P49).
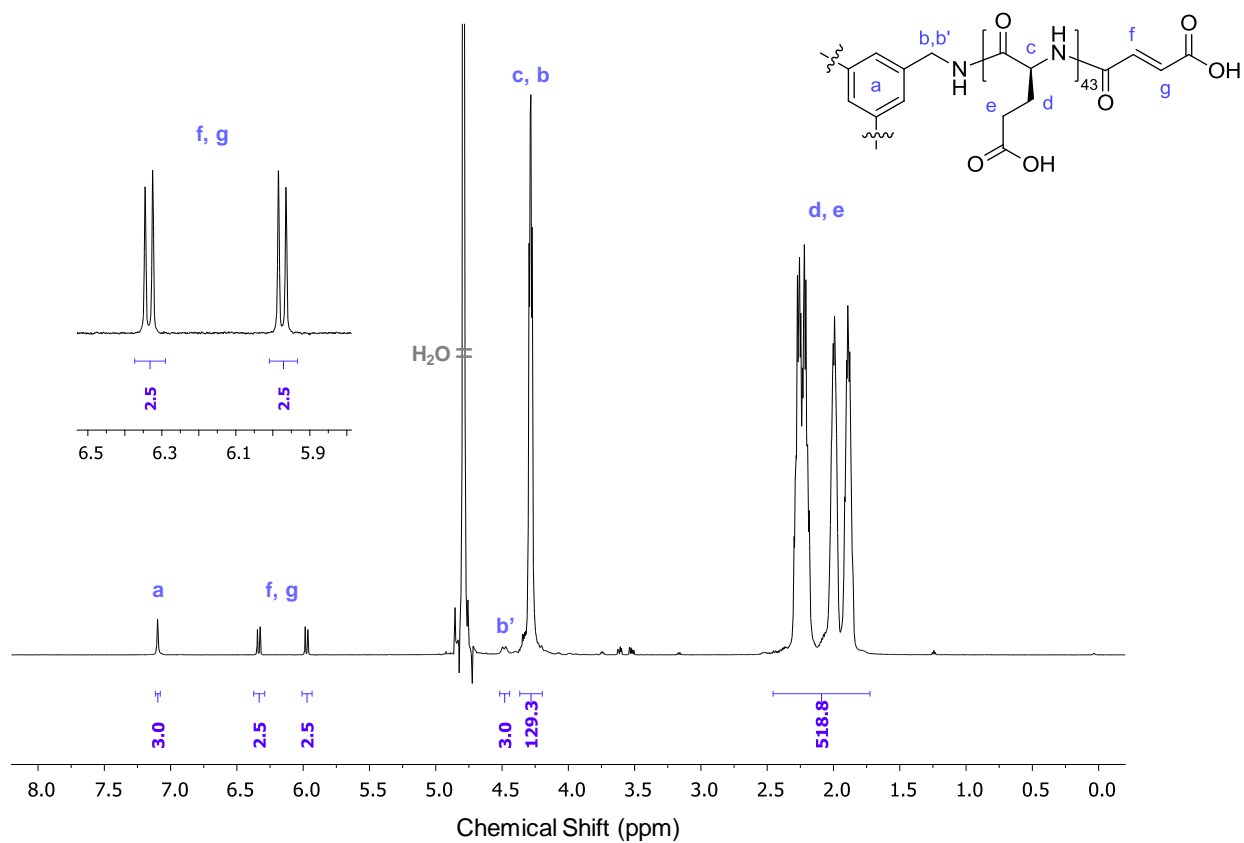
Figure B.26 ^{1}H-NMR spectrum (D$_2$O, 600 MHz) of *star*-(P$_L$G$_{43}$)$_3$ (P49-D).
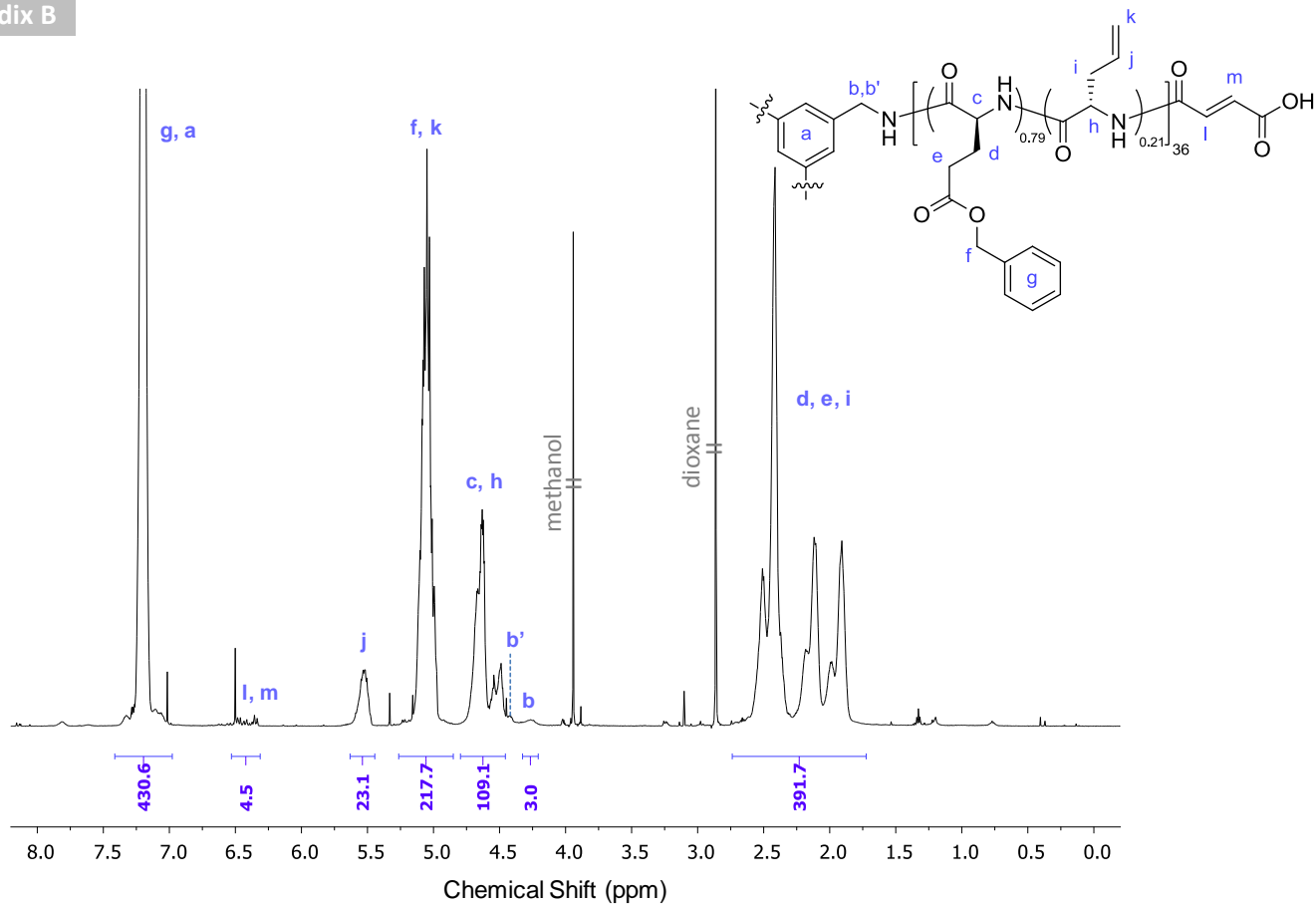
Figure B.27 ^{1}H-NMR spectrum (TFA-d, 600 MHz) of *star*-(P(BLG$_{0.79}$-*co*-LAG$_{0.21}$)$_{36}$)$_3$ (P50).
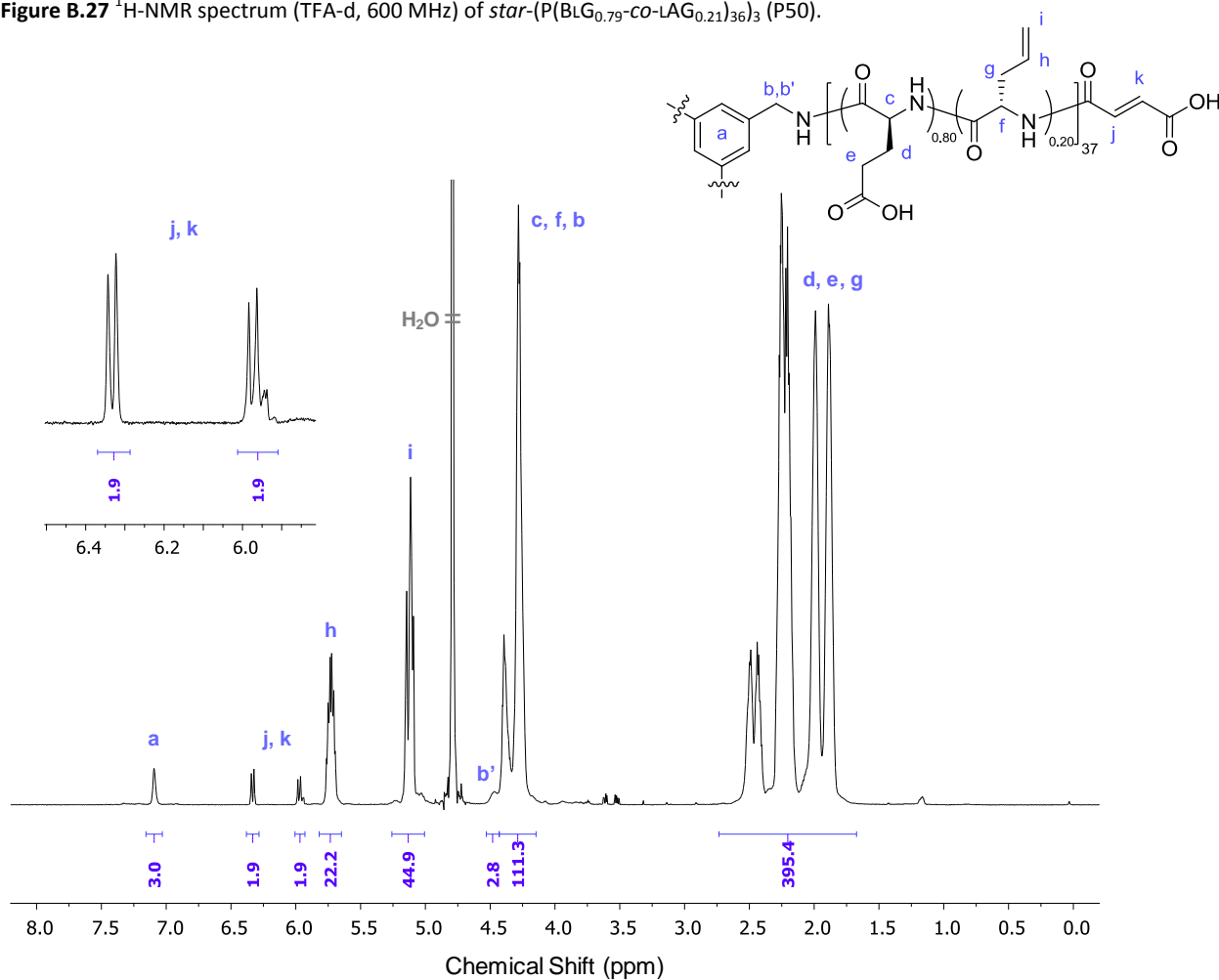
Figure B.28 ^{1}H-NMR spectrum (D$_2$O, 600 MHz) of *star*-(P(BLG$_{0.80}$-*co*-LAG$_{0.20}$)$_{37}$)$_3$ (P50-D).
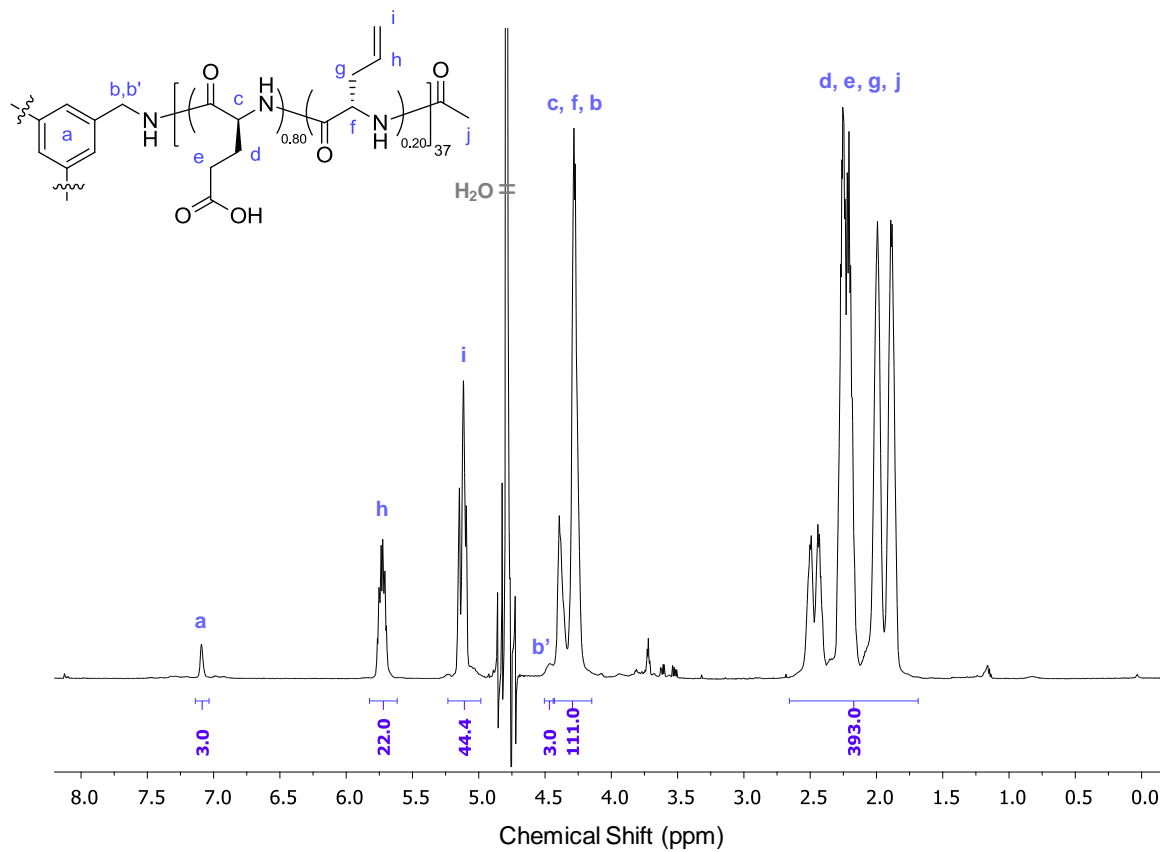
Figure B.29 ^{1}H-NMR spectrum (D$_2$O, 600 MHz) of *star*-(P(B$_L$G$_{0.80}$-*co*-LAG$_{0.20}$)$_{37}$)$_3$ (P51-D).
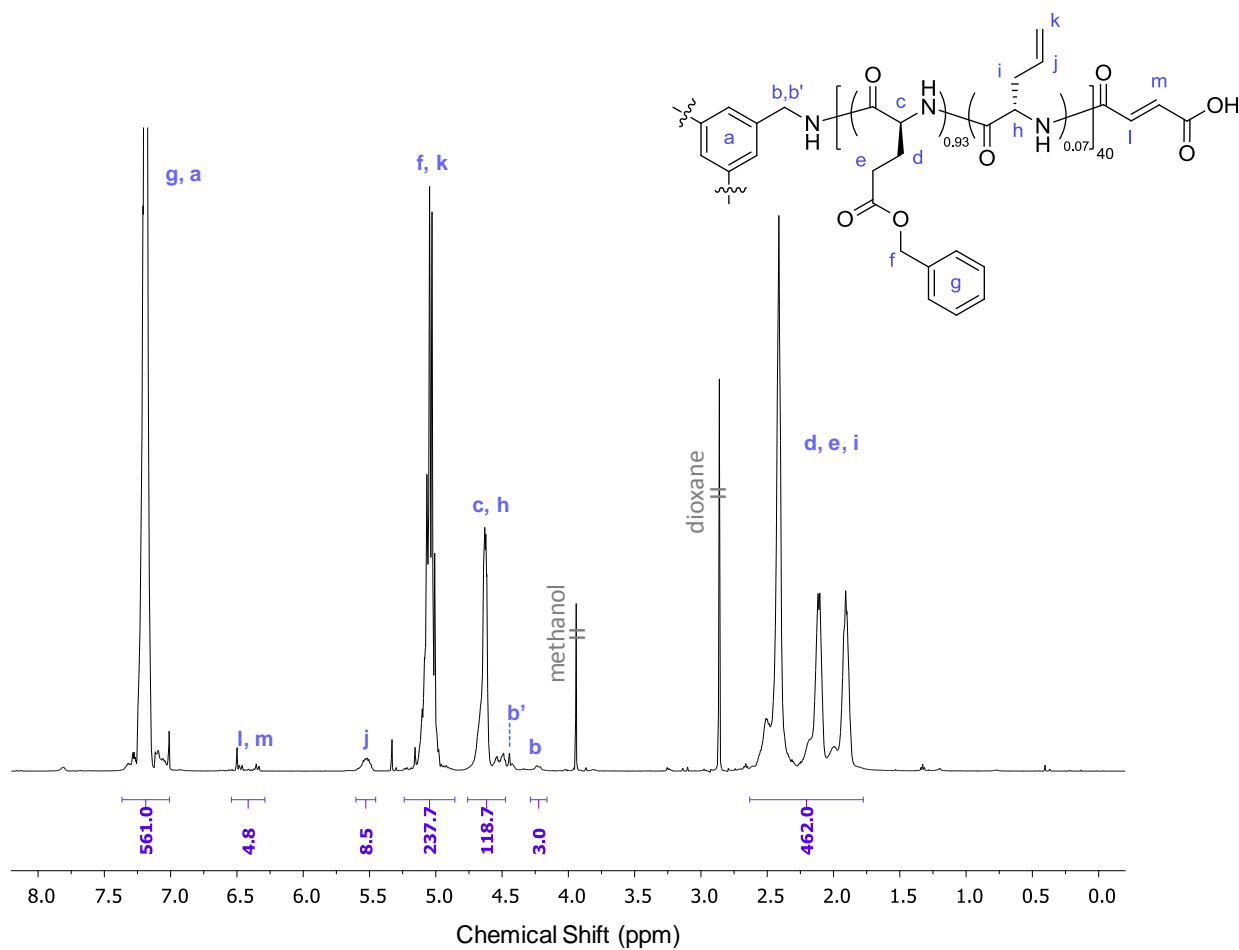
Figure B.30 ^{1}H-NMR spectrum (TFA-d, 600 MHz) of *star*-(P(B$_L$G$_{0.93}$-*co*-LAG$_{0.07}$)$_{40}$)$_3$ (P52).
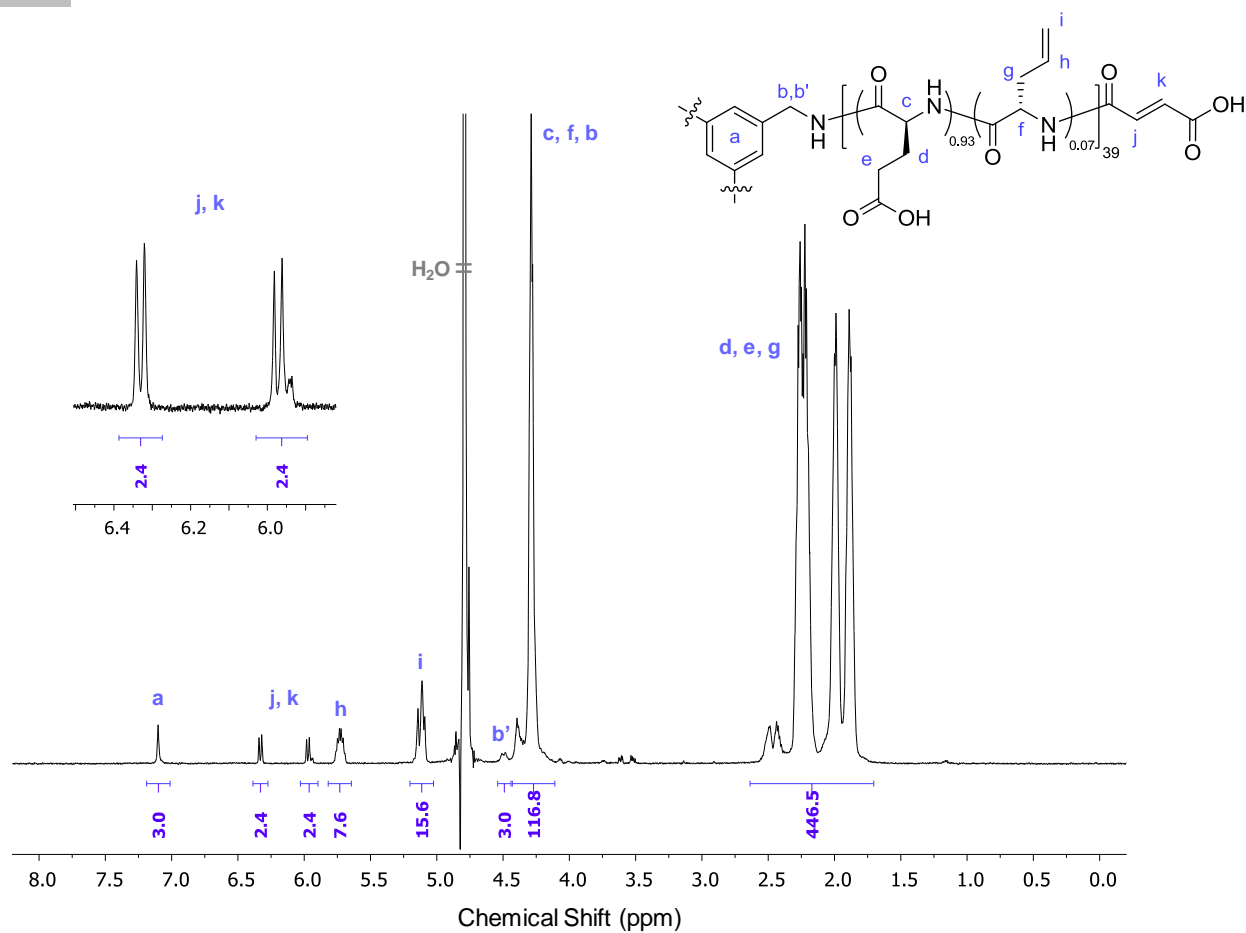
Figure B.31 ^{1}H-NMR spectrum (D$_2$O, 600 MHz) of *star*-(P(LG$_{0.93}$-*co*-LAG$_{0.07}$)$_{39}$)$_3$ (P52-D).
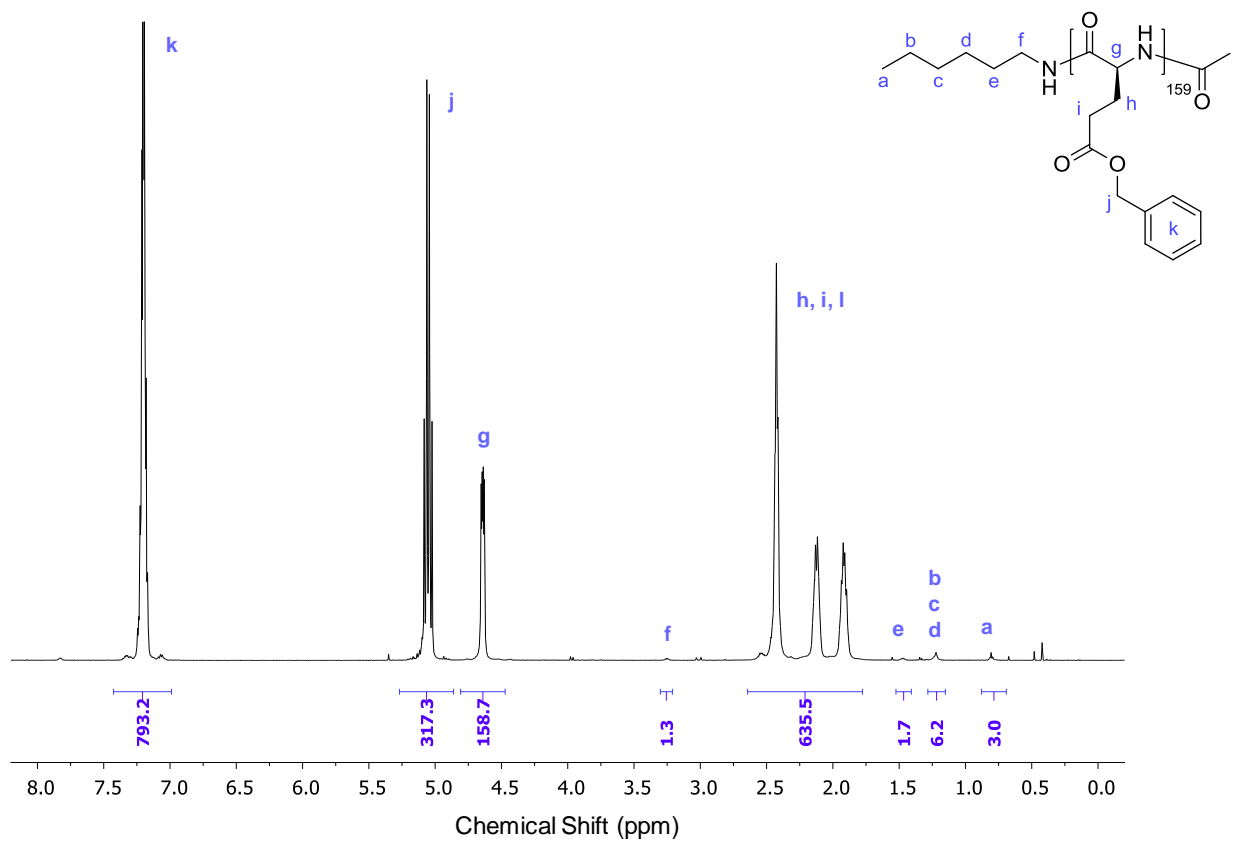
Figure B.32 ^{1}H-NMR spectrum (TFA-d, 600 MHz) of PBLG$_{159}$ (P59).
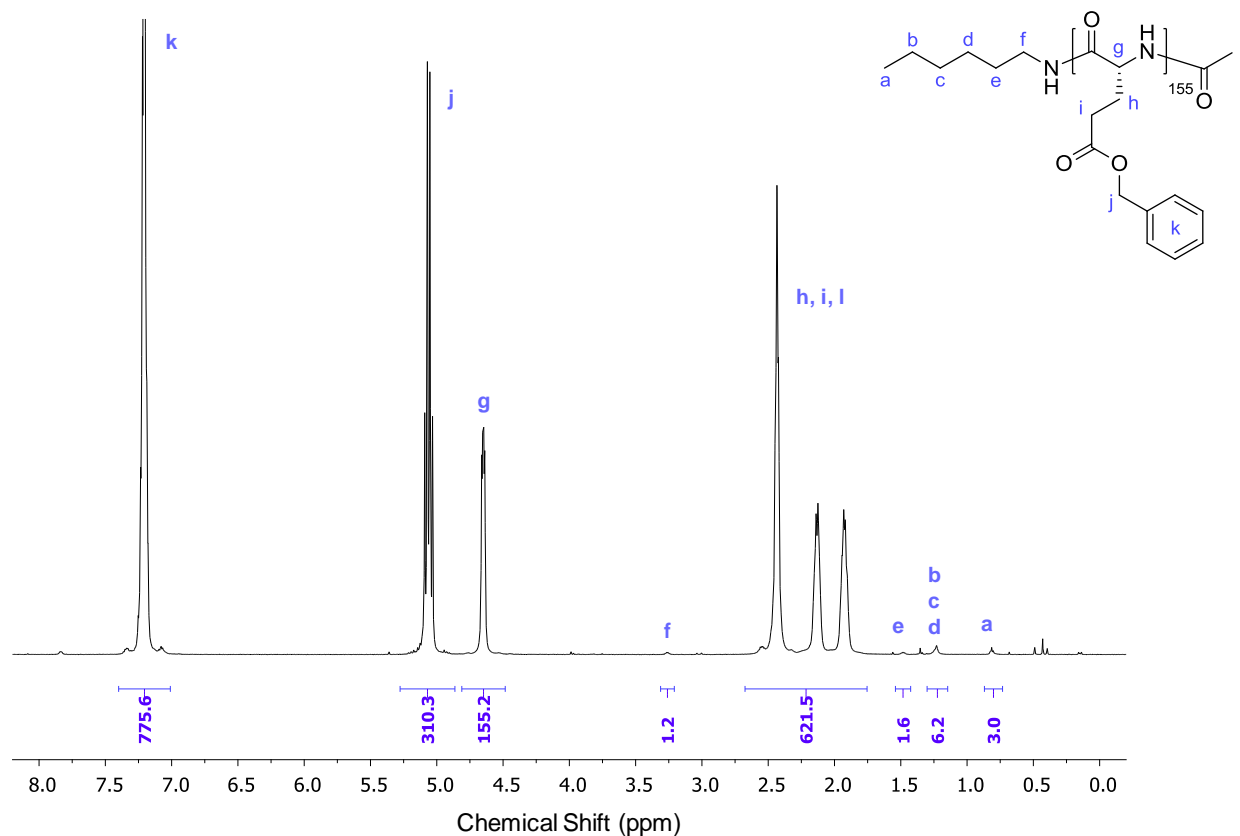
Figure B.33 ^{1}H-NMR spectrum (TFA-d, 600 MHz) of PB$_D$G$_{155}$ (P60).
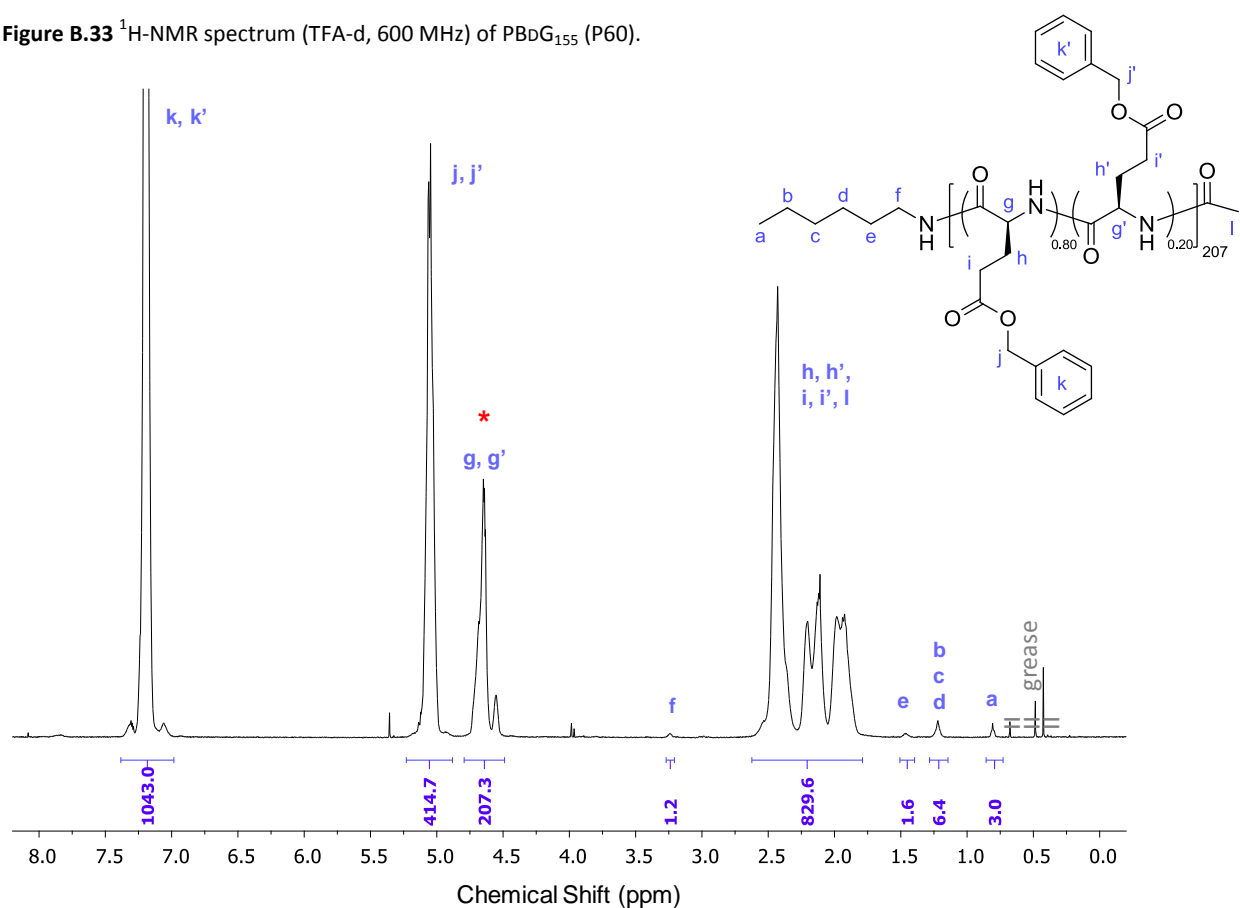
Figure B.34 ^{1}H-NMR spectrum (TFA-d, 600 MHz) of P(B$_L$G$_{0.80}$-*co*-B$_D$G$_{0.20}$)$_{207}$ (P61); * the splitting of the C$_\alpha$ (4.46-4.79 ppm) is likely caused by the clashing of two opposite conformations (*i.e.*, a B$_L$G-induced right-handed helix and B$_D$G-induced left-handed helix) and cannot be used to quantify the B$_L$G/B$_D$G molar ratio, given that the C$_\alpha$ of each homopolymer comes out at the same chemical shift (4.57-4.70 ppm) (Figure B.32 and B.33); the values indicated for their molar fractions is based on the monomer feed ratio.
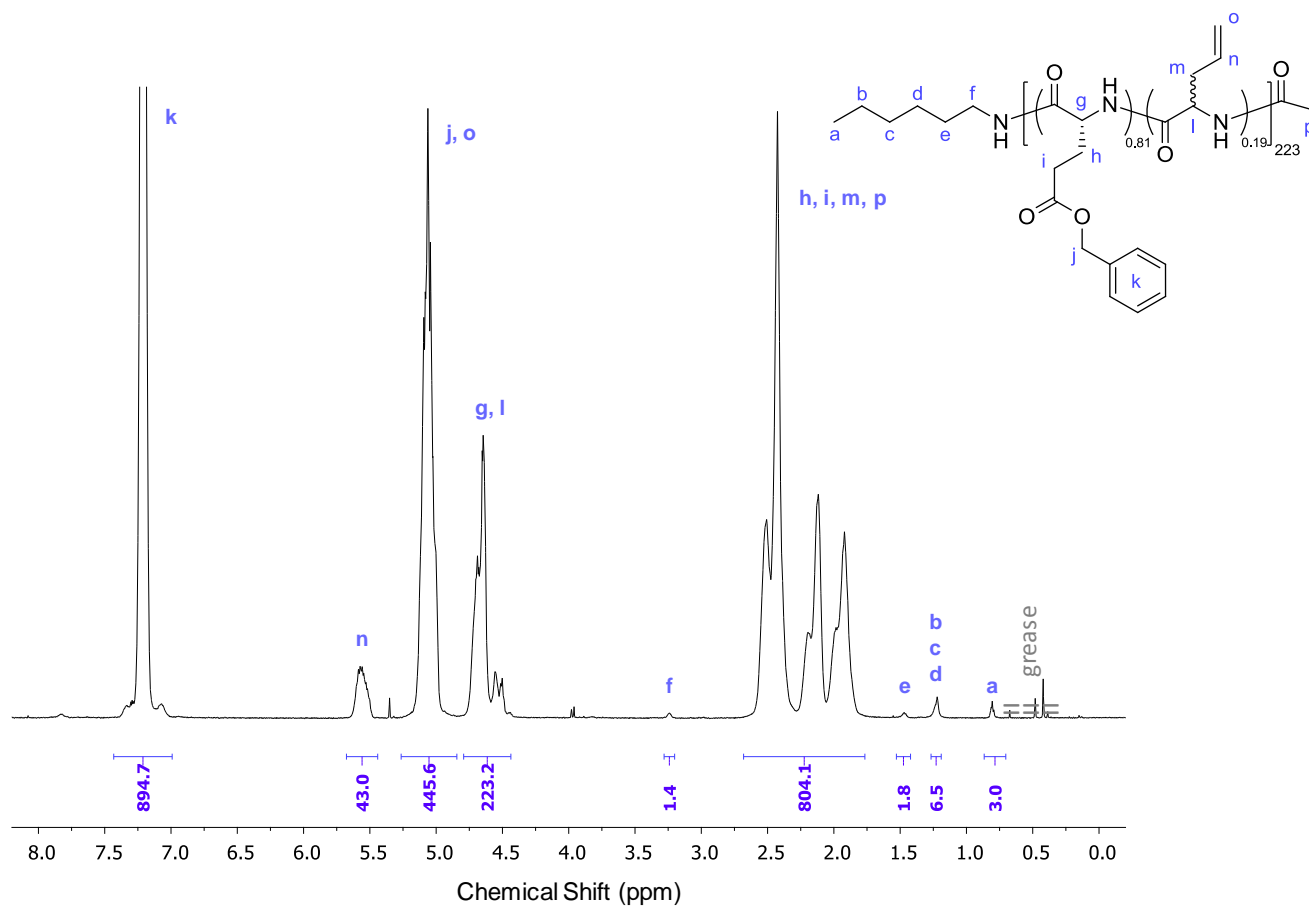
Figure B.35 ^{1}H-NMR spectrum (TFA-d, 600 MHz) of P(BDG$_{0.81}$-*co*-DLAG$_{0.19}$)$_{223}$ (P62).
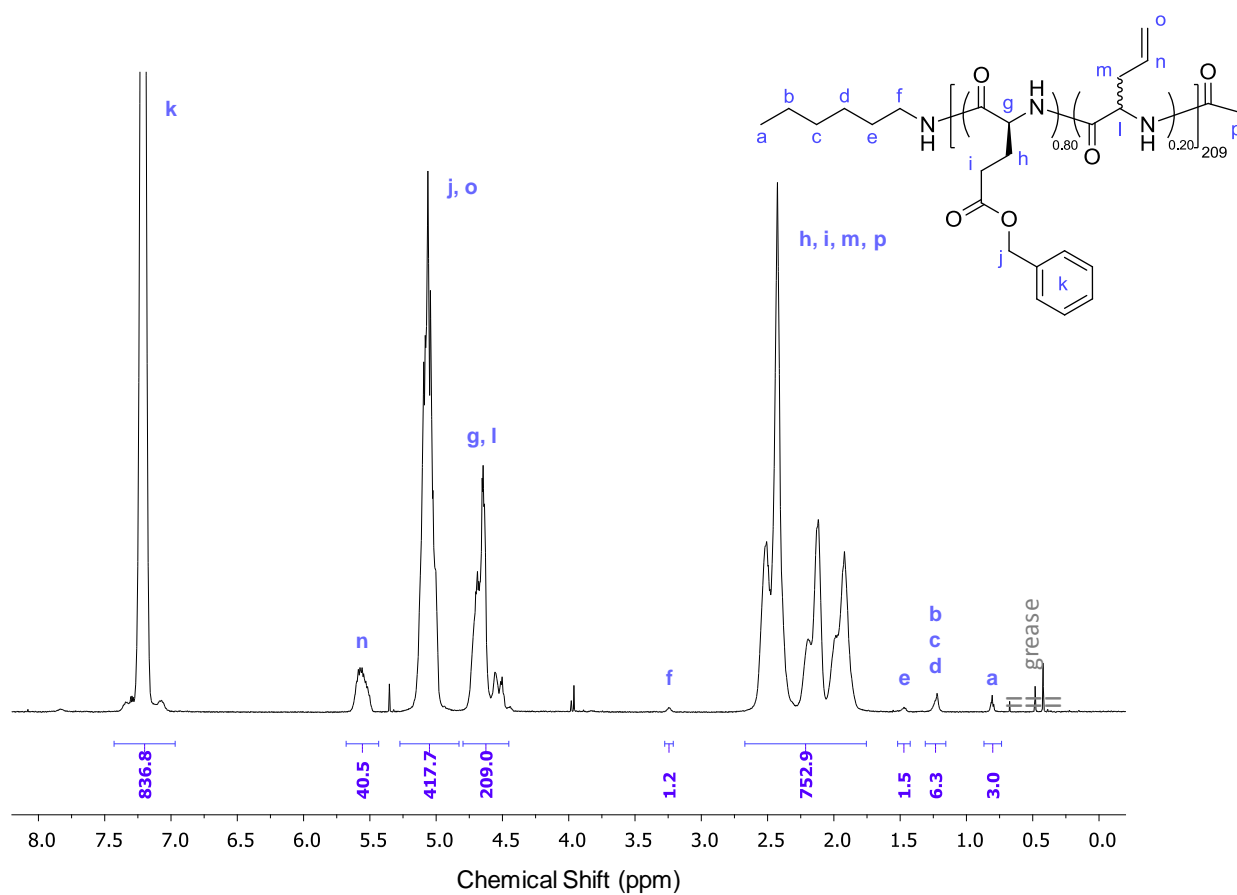

Figure B.36 ^{1}H-NMR spectrum (TFA-d, 600 MHz) of P(BLG$_{0.80}$-*co*-DLAG$_{0.20}$)$_{209}$ (P63).
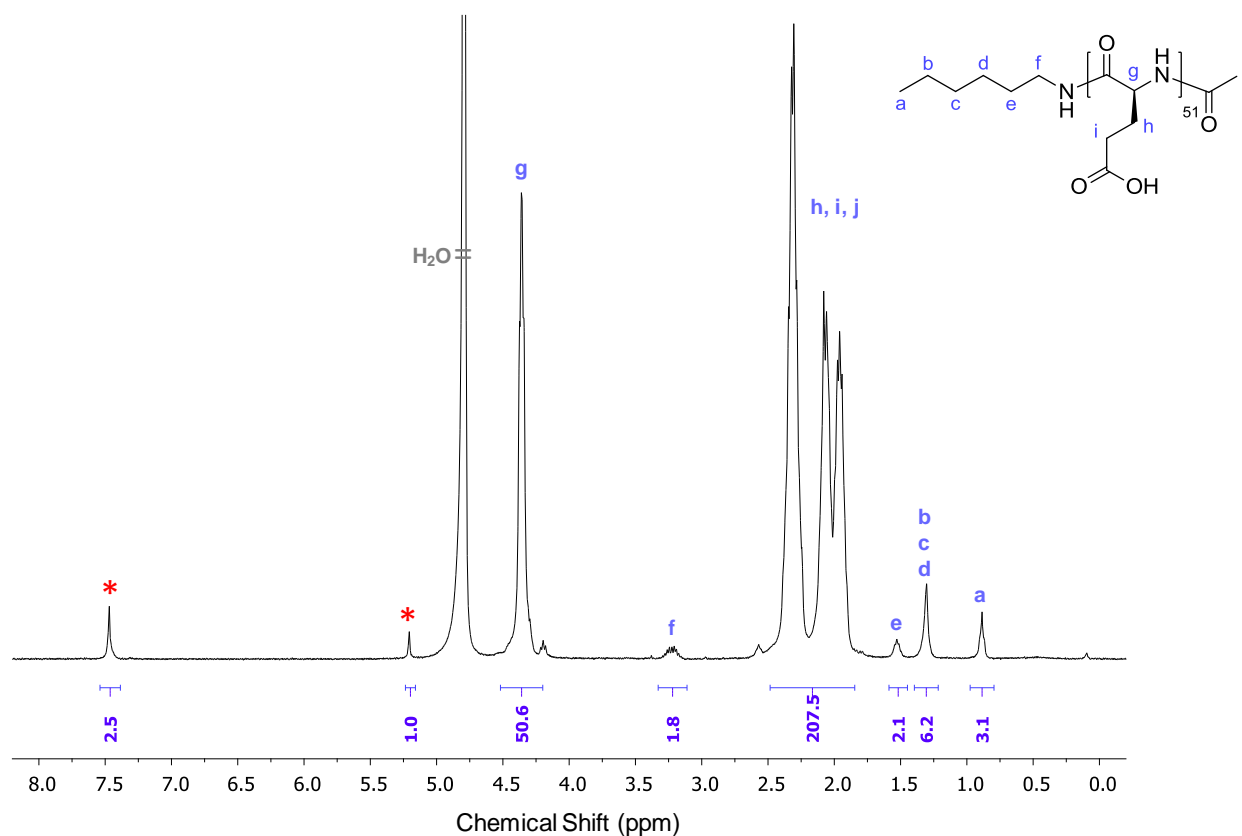
Figure B.37 ^{1}H-NMR spectrum (D$_2$O, 400 MHz) of PB$_L$G$_{51}$ (P1-D); the peaks assigned to the * symbol correspond to residual B$_L$G units (0.5 remaining B$_L$G units on average per chain), more precisely the benzyl ring (5H) at ~ 7.5 ppm and the CH$_2$ (ester) (2H) at ~ 5.2 ppm.

B.2.2   SEC Traces of Polypeptides

The SEC traces of a selection of polypeptides are displayed in the following figures. Other SEC traces can be found in Figure II.7.

Figure B.38 SEC (NMP, PMMA calibration) traces of P(BG$_x$-co-AG$_{1-x}$)$_n$ polypeptides synthesised for the study on emulsions reporter in Chapter VI (*i.e.*, P59 to P63); P1 (black) and P13 (grey) traces are added for comparison.

Figure B.39 SEC (NMP, PMMA calibration) traces of P(BLG$_x$-co-AG$_{1-x}$)$_n$ polypeptides with a star topology (P18A, P18B, P33, P36, P40, and P49).
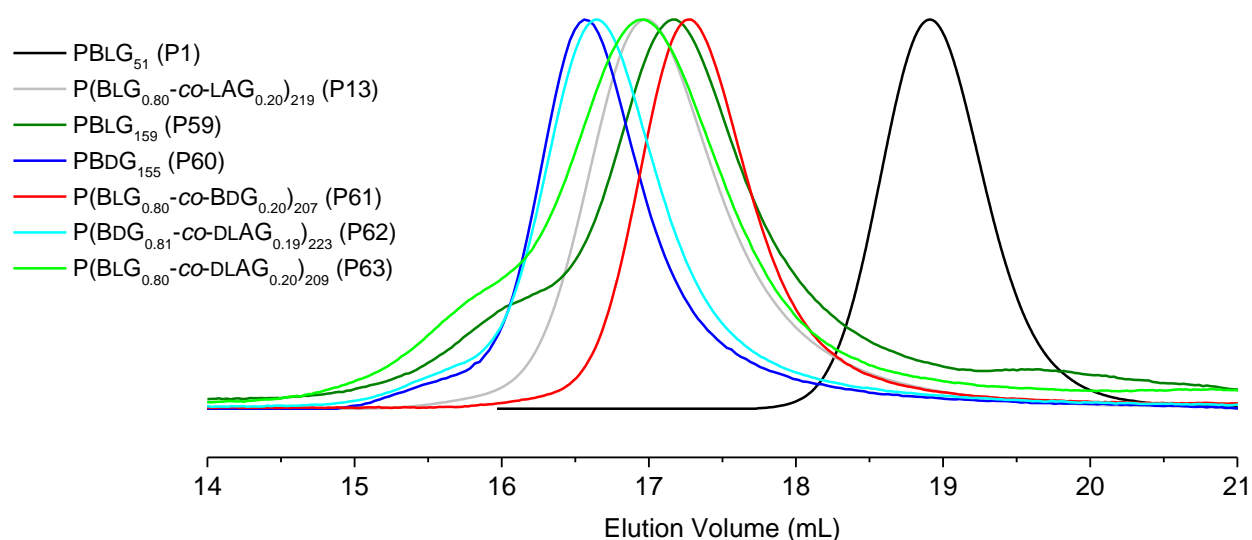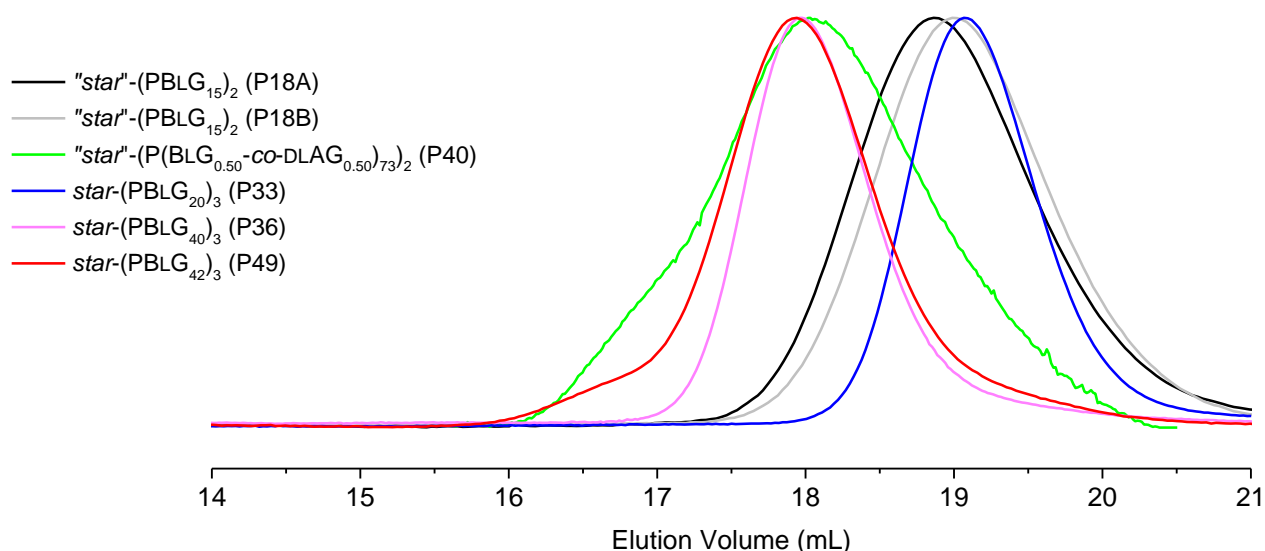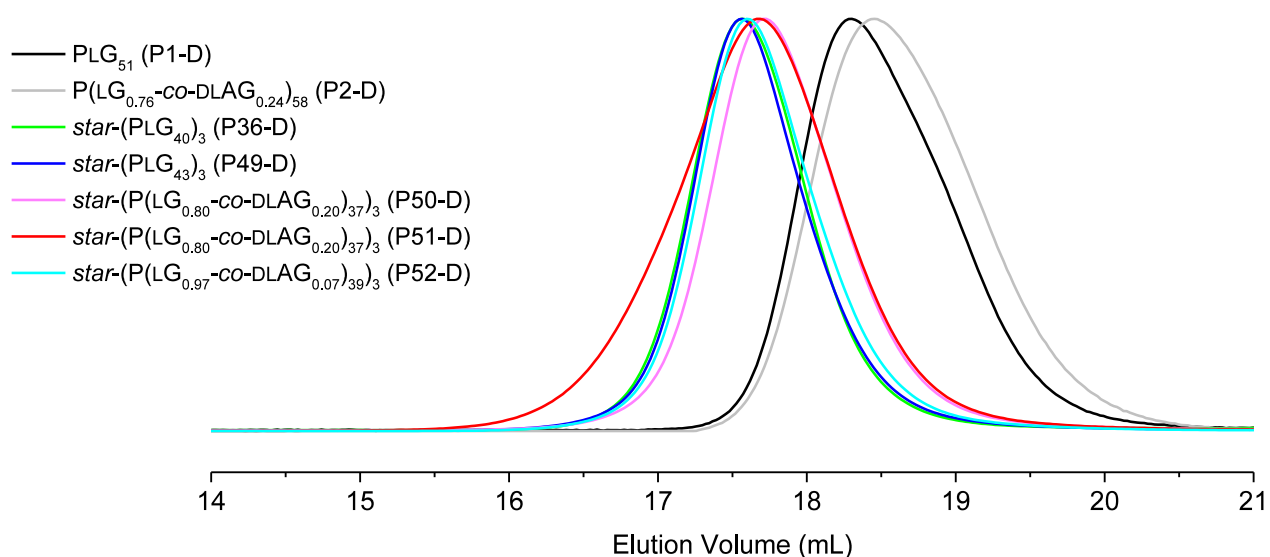

Figure B.40 SEC (D$_2$O, PEO calibration) traces of P(LG$_x$-co-AG$_{1-x}$)$_n$ polypeptides (P1-D, P2-D, P36-D, and P49-D to P52-D).

In Figure B.38, it is unclear why the traces of PBLG$_{159}$ and P(BLG$_{0.80}$-co-DLAG$_{0.20}$)$_{209}$ are slightly bimodal as a number of causes could explain this secondary peak (*e.g.*, impurity on the SEC column, AMM contribution). Nevertheless, the particles obtained from these polypeptides showed distinct spiral features (results reported in Chapter VI), which indicates that the process by which the polypeptide chirality is transmitted to a higher level of hierarchy can still occur despite a slightly bimodal molar mass distribution. The molar mass distribution of *"star"*-(P(BLG$_{0.50}$-co-LAG$_{0.50}$)$_{73}$)$_2$ is broader than other polypeptides, which could be explained by its low solubility in the eluent used for the SEC column (Figure B.39). Finally, although the dispersities in water SEC may seem rather large (Table B.2), it is simply characteristic of the method. All debenzylated polypeptides exhibited a narrow and largely monomodal molar mass distribution (Figure B.40).

B.3   Polymerisations Followed by SEC (Chapter III)

This section contains supporting data relative to kinetic studies and polymerisations followed by SEC, the results of which are reported in Chapter III. Table B.3 provides an overview of these polymerisations, their reaction conditions, their reference (*i.e.*, Pxx-y), and the figure in which their NMR spectra, SEC traces and conversion plots can be found (see Figure II.1 for abbreviations). All reactions were terminated by maleic anhydride in order to determine the M_n throughout the reaction, as to ensure that the M_n^{app} calculated from SEC measurements followed the same trend, which was the case for all reactions (Figure B.41).

Table B.3 List of polymerisations of BₗG-NCA followed by SEC; unless otherwise mentioned (in the comment column), the polymerisations were run at room temperature (rt) in DMF and terminated after 7 d (168 h); the initiator mixture (primary ammonium chloride and tertiary amine) was in DMSO. The Ðᵃᵖᵖ column provides an upper or lower boundary (*i.e.*, maximum or minimum) for the dispersity which was monitored at regular time intervals during the polymerisation. The internal standard was either added to the polymerisation medium (in) or to each individual SEC sample (out). The polymerisations are grouped in either white or blue blocks, each block indicating that the polymerisations were run in parallel (hence subjected to the same conditions).

Entry	NCA equiv.	Initiator (Ini)	Ini Equiv.	Tertiary Amine (TA)	TA Equiv.	NCA conc. (g·L⁻¹)	Internal Standard	SEC Ðᵃᵖᵖ (Mw/Mn)	NMR n *	SEC n **	n (SEC) at	Comment	Figure or Table (T/)
P25	150	TAB·3HCl	1	-	-	60	out	< 1.05	-	23	168 h		**III.4**
P26	150	TAB·3HCl	1	TEA	0.5	60	out	< 1.12	160	111	168 h		**II.4, III.4, B.41**
P27	150	-	-	TEA	0.5	60	out	> 1.90	> 1k	-	168 h	Large *n*	**II.6, III.4**
P28	150	TAB·3HCl	1	TEA	0.5	60	out	< 1.12	105	76	168 h	50 °C	**III.4, B.41**
P29	150	TAB·3HCl	1	TEA	0.5	60	out	< 1.19	162	100	168 h	NMP	**B.41**
P30	150	TAB·3HCl	1	TEA	0.5	60	out	-	-	-	168 h	NMP, 50 °C #	-
P31	150	TAB·3HCl	1	-	-	200	out	< 1.12	141	98	168 h		**B.41**
P32	150	TAB·3HCl	1	TEA	0.5	200	out	< 1.11	206	127	168 h		**B.41**
P34	150	PyA·HCl	1	TEA	1.5	100	in	> 1.80	-	102	120 h	See P56	**III.5**
P37	150	PyA·HCl	1	TEA	0.2	100	in	< 1.15	118	81	168 h		**B.41, B.42**
P38	150	PyA·HCl	1	TEA	0.2	100	out	< 1.11	128	81	168 h		**B41**
P39	150	PyA·HCl	1	TEA	0.2	100	in	< 1.09	102	75	168 h	Initiator in DMF	**B41**
P41-0	150	PyA·HCl	1	-	-	100	in	< 1.08	89	50	168 h		**III.5, B.42**
P41-50	150	PyA·HCl	1	TEA	0.5	100	in	< 1.08	113	96	168 h		**III.5, B.42, B.45**
P41-70	150	PyA·HCl	1	TEA	0.7	100	in	< 1.08	130	100	168 h		**III.5, B.42**
P41-90	150	PyA·HCl	1	TEA	0.9	100	in	< 1.10	131	101	168 h		**III.5, B.42**
P41-110	150	PyA·HCl	1	TEA	1.1	100	in	< 1.08	124	101	168 h		**III.5, B.42**
P42	150	PyA·HCl	1	DIPEA	0.5	100	in	< 1.09	124	97	168 h		**T/III.2**
P43	150	PyA·HCl	1	TEA	0.5	100	in	< 1.09	119	98	168 h	Stop-and-go	**III.6**

* Final n (after work-up) was determined by ¹H-NMR. ** n was determined by SEC at the time indicated in the following column. # P30 was unsuccessful.
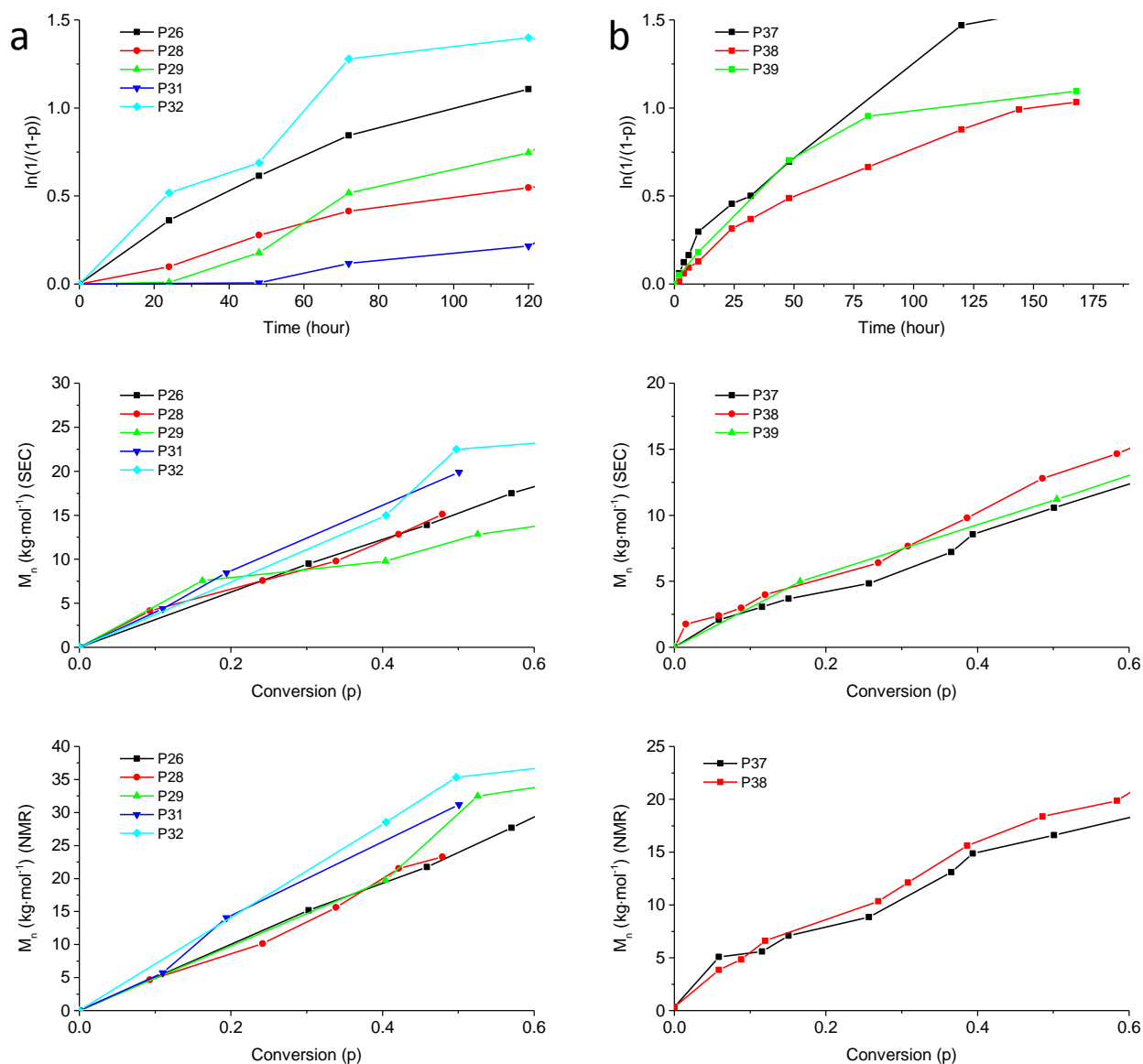
Figure B.41 M_n-conversion and first order time-conversion plots for the series of polymerisations of BʟG-NCA (100 equiv.) in DMF initiated by: (a) TAB·3HCl/TEA (1:0.5 equiv.) (P26, P28, P29 and P32) or TAB·3HCl (1 equiv.) (P31); and (b) PyA·HCl/TEA (1:0.2 equiv.) (P37 to P39). Monomer conversions were determined by SEC, and M_n was determined by both SEC and ^{1}H-NMR (Section III.2.2.1).
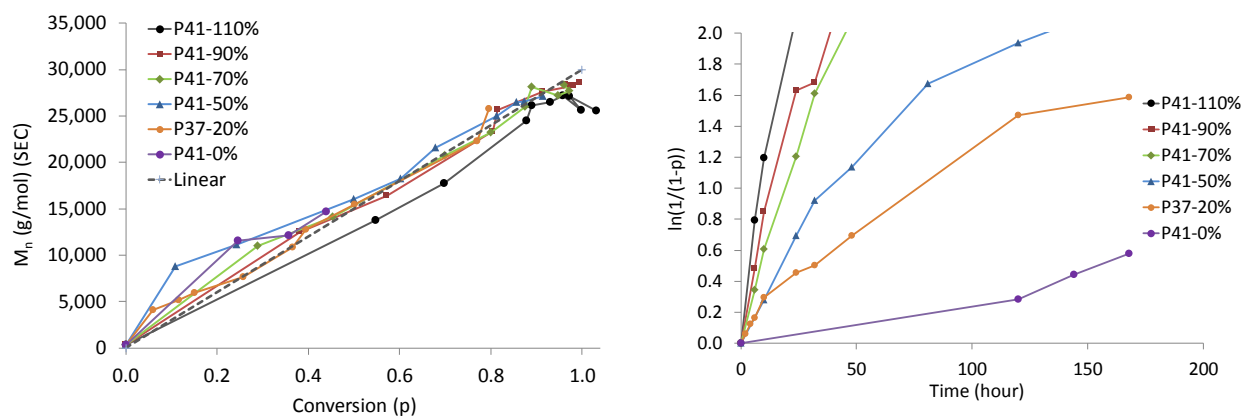

Figure B.42 M_n-conversion and first order time-conversion plots for the polymerisations of BʟG-NCA (100 equiv.) in DMF initiated by PyA·HCl/TEA (1:x equiv.) for different molar fractions of TEA (x = 0, 0.2, 0.5, 0.7, 0.9 and 1.1 equiv.) (P37 and P41-0 to P41-110). Monomer conversions and M_n were determined by SEC (Section III.2.2.1).

B.4 Polymerisations Followed by FTIR (Chapter III)

This section contains supporting data relative to kinetic studies and polymerisations followed by FTIR, the results of which are reported in Chapter III. Figure B.4 provides an overview of these polymerisations, their reaction conditions, their reference (*i.e.*, Pxx-y), and the figure in which their NMR spectra and SEC traces can be found (see Figure II.1 for abbreviations). All reactions were terminated by maleic anhydride in order to determine the M_n throughout the reaction, as to ensure that the M_n^{app} provided by SEC followed the same trend, which was the case for all reactions.

Table B.4 List of polymerisations of NCAs followed by FTIR; unless otherwise mentioned (in the comment column), the polymerisations were run at room temperature (rt) in DMF and terminated after 5 d (120 h), and the NCA concentration was 100 g·L^{-1}. The initiator mixture was in DMF. The Đ^{app} column provides an upper or lower boundary (*i.e.*, maximum or minimum) for the dispersity (measured at ~ 4h, 24h, 50h and 72h). The polymerisations are grouped in either white or blue blocks, each block indicating that the polymerisations were run in parallel (hence subjected to the same conditions).

Entry	NCA	NCA equiv.	Initiator (Ini)	Ini Equiv.	Tertiary Amine (TA)	TA Equiv.	SEC Đ^{app} (M_w/M_n)	NMR n *	SEC n **	n (SEC) at	Comment	Figure
P44-A	BLG	100	BnA	1	-	-	< 1.08	93	82	73 h		**III.7, III.8**
P44-B	BLG	100	BnA·HCl	1	-	-	< 1.55	96	43	73 h	bimodal	**III.7, III.8**
P44-C	BLG	100	BnA·HCl	1	TEA	0.5	< 1.08	82	73	73 h		**III.7, III.8**
P44-D	BLG	100	-	-	TEA	0.5	> 1.80	-	180	73 h		**III.7, III.8**
P45-A	LLeu	100	BnA	1	-	-	-	-	-	73 h	No RI signal	**III.7, III.8**
P45-B	LLeu	100	BnA·HCl	1	-	-	-	-	-	73 h	No RI signal	**III.7, III.8**
P45-C	LLeu	100	BnA·HCl	1	TEA	0.5	-	-	-	73 h	No RI signal	**III.7, III.8**
P45-D	LLeu	100	-	-	TEA	0.5	-	-	-	73h	No RI signal	**III.7, III.8**
P46-A	LPhe	100	BnA	1	-	-	-	-	-	73 h	No RI signal	**III.7, III.8**
P46-B	LPhe	100	BnA·HCl	1	-	-	-	-	-	73 h	No RI signal	**III.7, III.8**
P46-C	LPhe	100	BnA·HCl	1	TEA	0.5	-	-	-	73 h	No RI signal	**III.7, III.8**
P46-D	LPhe	100	-	-	TEA	0.5	-	-	-	73 h	No RI signal	**III.7, III.8**
P47-A'	BLG	100	HexA	1	-	-	< 1.20	93	86	49 h	25 °C	**B.43**
P47-E	BLG	100	BnA	1	TEA	0.5	< 1.20	84	58	49 h	25 °C	**III.9**
P47-A	BLG	100	BnA	1	-	-	< 1.22	95	67	49 h	25 °C	**III.9, B.43, B.44**
P53	BLG	100	PyOH	1	-	-	> 1.23	-	18	53 h	bimodal	**B.43**
P54	BLG	100	PyOH	1	TEA	0.5	> 1.70	245	226	53 h		**B.43**
P55-80	BLG	100	BnA	1	TEA	0.8	< 1.45	79	69	53 h		**III.9**
P55-100	BLG	100	BnA	1	TEA	1	< 1.65	80	55	53 h		**III.9**
P55-150	BLG	100	BnA	1	TEA	1.5	< 1.79	111	52	53 h		**III.9**
P56	BLG	150	PyA·HCl	1	TEA	1.5	> 1.65	-	97	50 h	Repeat P34	
P57-50C	BLG	100	BnA·HCl	1	TEA	0.5	< 1.17	64	50	50 h	50 °C	**III.10**
P57-80C	BLG	100	BnA·HCl	1	TEA	0.5	< 1.18	38	26	50 h	80 °C	**III.10**
P57-5%	BLG	100	BnA·HCl	1	TEA	0.5	< 1.16	79	52	50 h	50 g·L^{-1}	**III.10**
P57-20%	BLG	100	BnA·HCl	1	TEA	0.5	< 1.18	89	64	50 h	200 g·L^{-1}	**III.10**
P58	BLG	100	BnA·HCl	1	TEA	1.5	< 1.25	91	70	50 h		**III.10**

* Final n (after work-up) was determined by ^{1}H-NMR. ** n was determined by SEC at the time indicated in the following column.
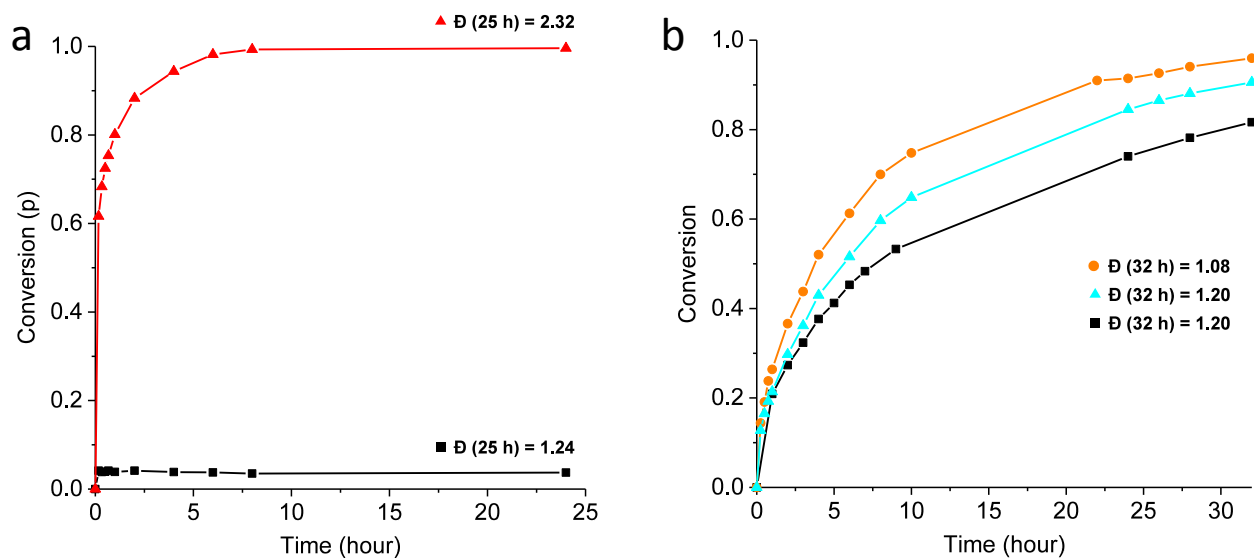
Figure B.43 Time-conversion plots for (a) the polymerisations of BʟG-NCA (100 equiv.) in DMF initiated by (a) ■ PyOH (1 equiv.) (P53), and ▲ PyOH/TEA (1:1.5 equiv.) (P54), and (b) ■ BnA (1 equiv.) and run at rt (20 °C) (P44-A), ▲ HexA (1 equiv.) and run at 25 °C (P47-A'), and ● BnA (1 equiv.) and run at 25 °C (P47-A). Monomer conversions were determined by FTIR spectroscopy (Section III.2.2.2); the polymer dispersities at 25 h and 32 h were determined by SEC.
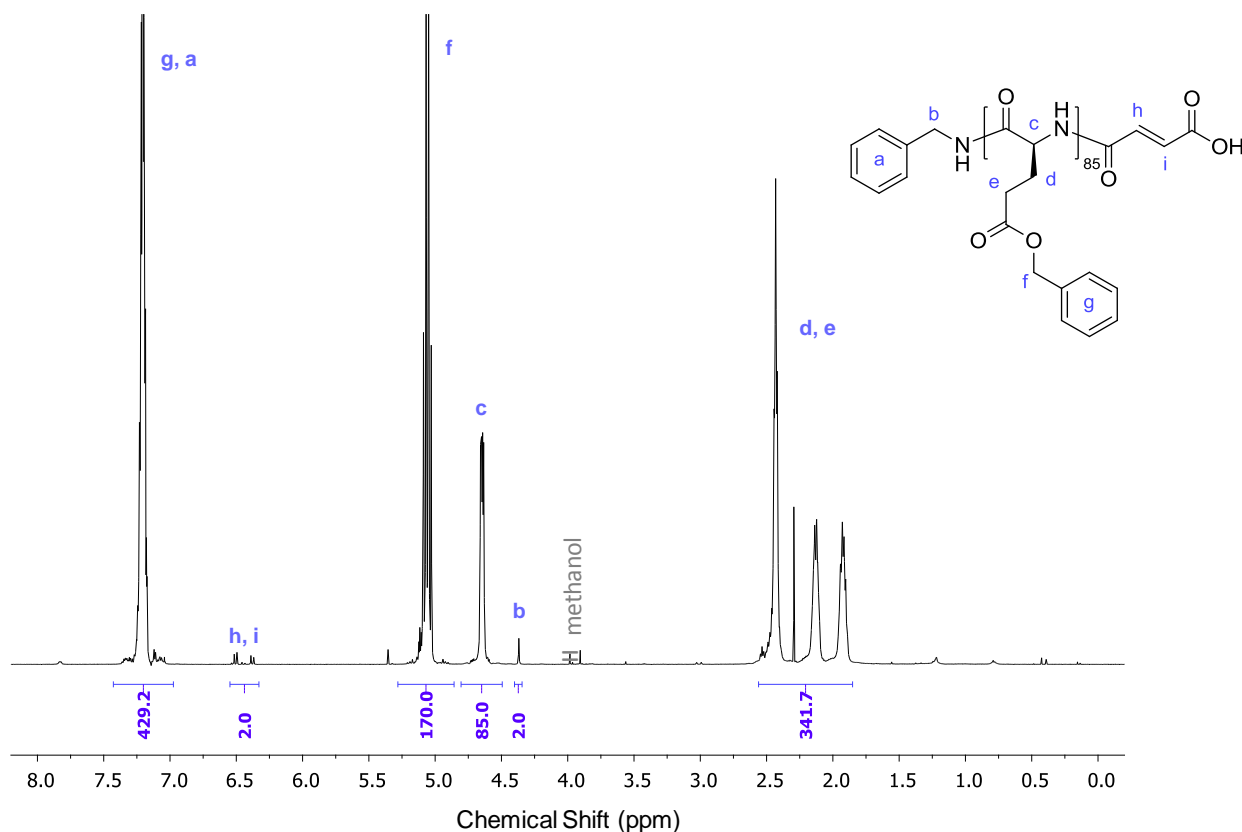

Figure B.44 ^{1}H-NMR spectrum (TFA-d, 600 MHz) of PBʟG$_{85}$ (P47A-32h); the spectrum is representative of BnA- or BnA·HCl/TEA-initiated polymerisations.
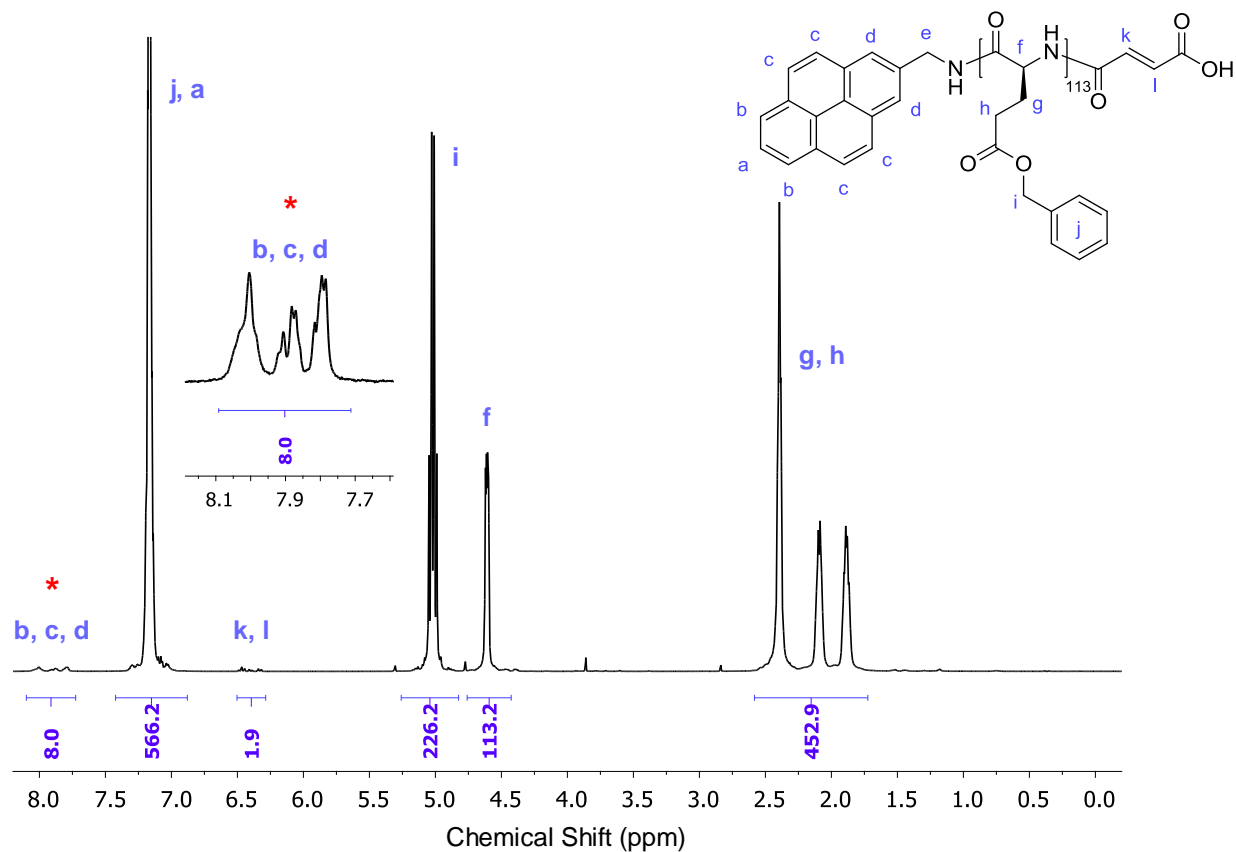
Figure B.45 ^{1}H-NMR spectrum (TFA-d, 600 MHz) of PBLG₁₁₃ (P41-50%); the spectrum is representative of PyA·HCl/TEA-initiated polymerisations. * The peaks at ~ 8 ppm corresponds to the pyrene end group; it was assumed that only the protons noted b, c and d belonged to this set of peaks, however, a debenzylation experiment would help confirm this assignment.

B.5 ^{1}H-NMR Temperature Sweep Experiment (Chapter IV)

During a physical gelation, line broadening, loss of spectral resolution, and signal disappearance can be observed by ^{1}H-NMR measurements. A temperature-sweep NMR experiment illustrates this phenomenon for dilute polypeptide solutions in toluene-d₈ (Figure B.46 and B.47).
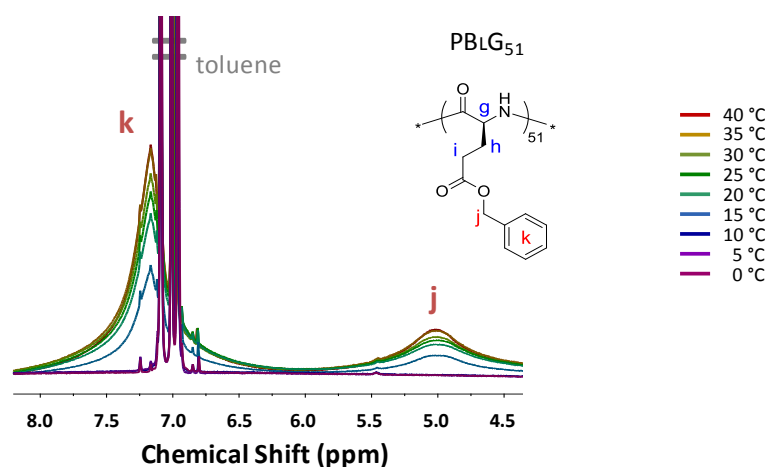

Figure B.46 [4.5 - 8 ppm] Portions of ^{1}H-NMR spectra of PBLG₅₁ in toluene-d₈ (20 g·L⁻¹), taken at incrementally decreased temperatures, from 40 °C to 0 °C; all spectra were normalised to the toluene signal at 7.01 ppm

Figure B.47 [4.5 - 8 ppm] Portions of ^{1}H-NMR spectra of P(BLG$_x$-co-AG$_{1-x}$)$_n$ copolypeptides in toluene-d$_8$ (20 g·L^{-1}), taken at incrementally decreased temperatures, from 40 °C to -40 °C; all spectra were normalised to the toluene signal at 7.01 ppm

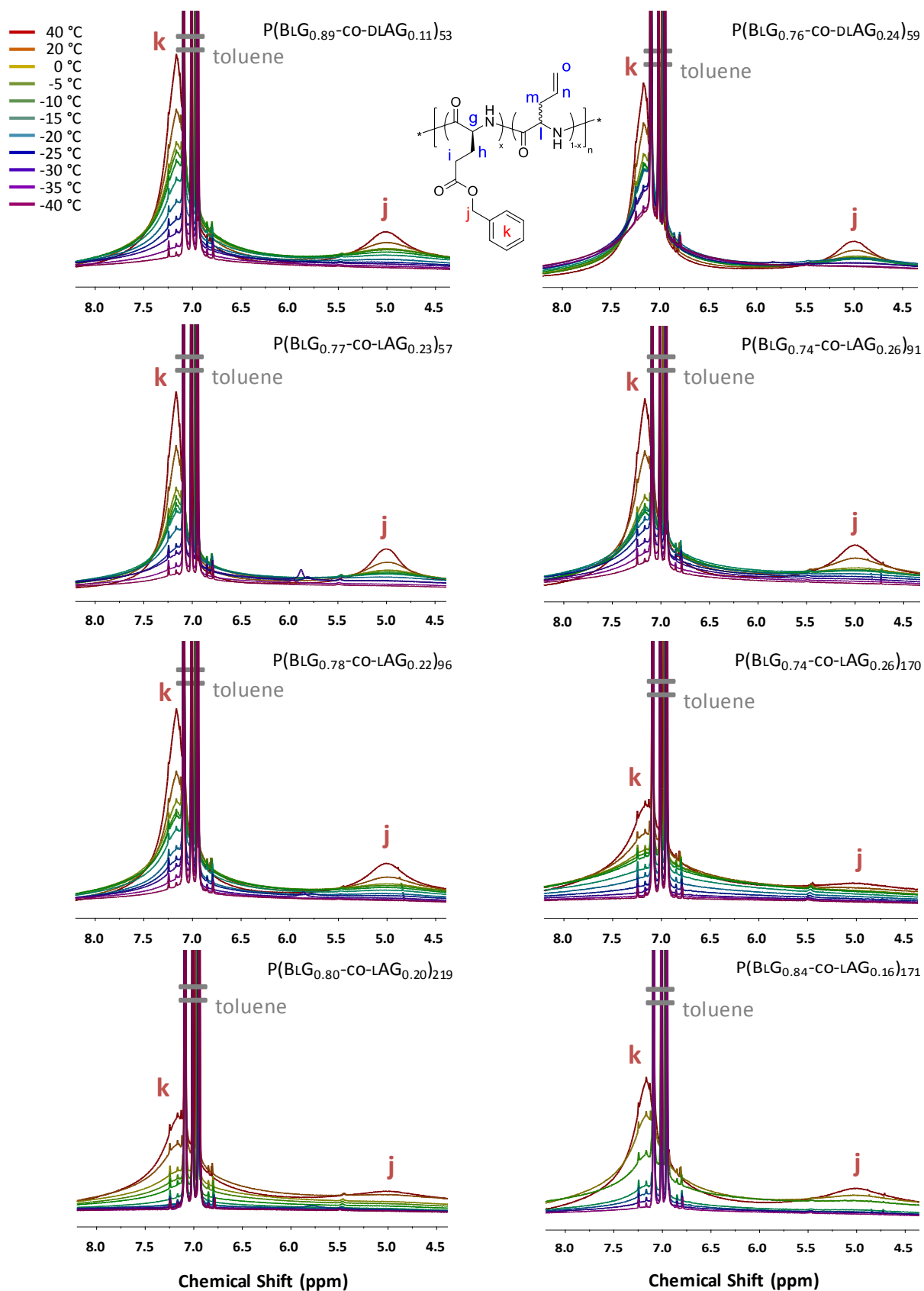A good correlation was found between the disappearance of the benzene peak, noted k, and the gelation temperature measured by rheology (Table B.5).

Table B.5 Properties of PBLG and P(BLG$_x$-co-AG$_{1-x}$)$_n$ copolypeptides studied in toluene (rheology) or toluene-d$_8$ (^{1}H-NMR) at 20 g·L^{-1}.

Copolypeptides	Cross-over Modulus (Stiffness)[a]	Cross-over Temperature (T$_{gel}$)[a]	Complex Viscosity (η^*) at 20 °C[a]	Temperature at which benzyl signal disappears in ^{1}H-NMR ($\pm$ 5 °C)[b]
	(Pa)	(°C)	(mPa·s)	(°C)
PBLG$_{51}$	5	39	5900	10
P(BLG$_{0.89}$-co-DLAG$_{0.11}$)$_{53}$	26	-26	520	-40
P(BLG$_{0.76}$-co-DLAG$_{0.24}$)$_{59}$	27	-38	630	< -40
P(BLG$_{0.77}$-co-LAG$_{0.23}$)$_{57}$	30	-27	150	-40
P(BLG$_{0.74}$-co-LAG$_{0.26}$)$_{91}$	96	-35	780	< -40
P(BLG$_{0.78}$-co-LAG$_{0.22}$)$_{96}$	54	-23	620	-40
P(BLG$_{0.74}$-co-LAG$_{0.26}$)$_{170}$	158	-23	2270	-35
P(BLG$_{0.80}$-co-LAG$_{0.20}$)$_{219}$	444	-12	3000	-20
P(BLG$_{0.84}$-co-LAG$_{0.16}$)$_{171}$	331	-8	1450	-20

[a] *Determined by rheometry.* [b] *Determined by ^{1}H-NMR.*

B.6 Emulsified particles (Chapter VI)

Particles produced from P(BG$_x$-co-AG$_{1-x}$)$_n$-toluene in water emulsions were dispersed in water and analysed by CD spectroscopy (Figure B.48). Although a Cotton effect can be observed between particles of opposite chirality, other particles only showed a weak CD signal. It may be due to the preparation method, for instance weights may have been overestimated due to the weight contribution of residual toluene.
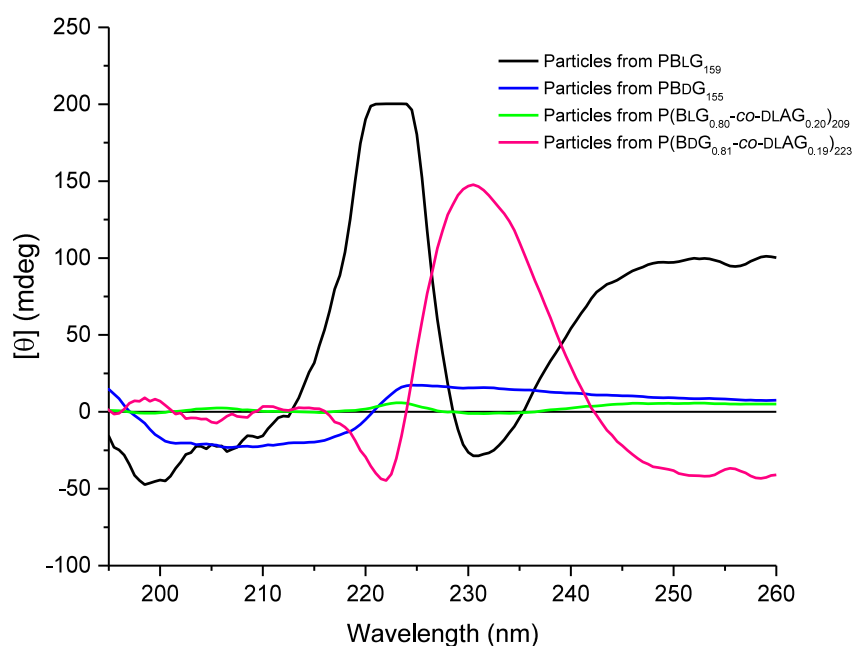

Figure B.48 CD spectra of particles with spiral features reported in Chapter VI. The particles were re-dispersed in Millipore water (0.4 g·L^{-1}) prior to the measurement.
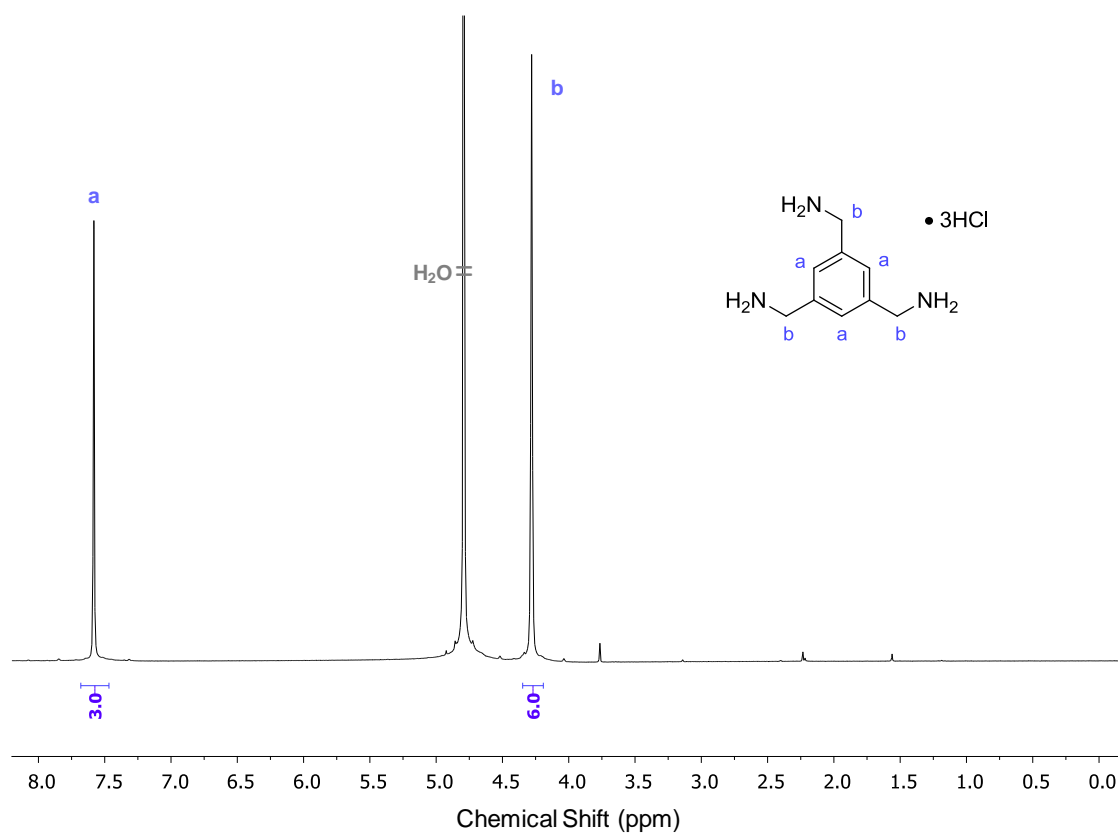
B.7 Additional Data

Figure B.49 ^{1}H-NMR spectrum (D$_2$O, 300 MHz) of TAB·3HCl.

Appendix C

List of Publications and Conference Contributions

C.1 Journal Publications

Physical Gelation of α-Helical Copolypeptides

<u>C. D. Vacogne</u>, M. Schopferer and H. Schlaad, *Biomacromolecules*, **2016**, *17*, 2384-2391

Primary Ammonium/Tertiary Amine-Mediated Controlled Ring Opening Polymerisation of Amino Acid *N*-Carboxyanhydrides

<u>C. D. Vacogne</u> and H. Schlaad, *Chem. Commun.*, **2015**, *51*, 15645-15648

Fibrillar Gels *via* the Self-Assembly of Poly(ʟ-Glutamate)-Based Statistical Copolymers

<u>C. D. Vacogne</u>, S. M. Brosnan, A. Masic and H. Schlaad, *Polym. Chem.*, **2015**, *28*, 4995-5134 [Front Cover]

C.2 Conference Contributions

250th American Chemical Society (ACS) National Meeting, Boston, August 2015 (presentation)

<u>C. D. Vacogne</u> and H. Schlaad, Controlling NCA Ring Opening Polymerisation to Achieve Well-Defined Hydrogels

European Polymer Federation (EPF) Congress, Dresden, June 2015 (presentation)

<u>C. D. Vacogne</u>, H. Schlaad, S. M. Brosnan, A. Masic, A Supramolecular Assembly Route Towards Stimuli-Responsive Poly(l-glutamate) Hydrogels

Tag der Chemie (TDC), Berlin, June 2015 (poster and presentation)

<u>C. D. Vacogne</u>, H. Schlaad, S. Brosnan, A. Masic, A Supramolecular Assembly Route Towards Stimuli-Responsive Poly(l-glutamate) Hydrogels [Poster Prize]

IMPRS on Multiscale Bio-Systems Workshop, Berlin, 2014 - 2016 (4 events) (poster and presentation)

<u>C. D. Vacogne</u>, New Synthetic Routes Towards Well-Defined Polypeptides, Morphologies and Hydrogels